



Computation-based Science and Technology Research Center
&
Department of Physics

# Scattering meson and baryon resonances in lattice QCD

SRIJIT PAUL

A dissertation submitted to The Cyprus Institute in partial fulfillment of the requirements for the degree of Doctor of Philosophy and submitted to the University of Wuppertal in partial fulfillment of the requirements for the degree of Doctor Rerum Naturalium.

JUNE 2019

# Scattering Meson and Baryon resonances in lattice QCD


**Srijit Paul**

Supervisors: Prof. Giannis Koutsou
Prof. Thomas Lippert

Computation-based Science and Technology Research Center
The Cyprus Institute
&
Fakultät für Mathematik und Naturwissenschaften
Bergischen Universität Wuppertal

This dissertation is submitted for the degree of
*Doctor of Philosophy*

June 2019

This project has received funding from the European Union's Horizon 2020 research and innovation programme under grant agreement No' 642069

The PhD thesis can be quoted as follows:

urn:nbn:de:hbz:468-20190820-152722-0
[http://nbn-resolving.de/urn/resolver.pl?urn=urn%3Anbn%3Ade%3Ahbz%3A468-20190820-152722-0]

DOI: 10.25926/hrjk-fe50
[https://doi.org/10.25926/hrjk-fe50]

**Doctoral candidate:**

Srijit PAUL

**Doctoral Thesis Title:**

Scattering meson and baryon resonances in lattice QCD

The present Doctoral Dissertation was submitted in partial fulfillment of the requirements for the Degree of Doctor of Philosophy

**Examination Committee:**

Assist. Prof. Giannis KOUTSOU
The Cyprus Institute, Supervisor

Prof. Thomas LIPPERT
University of Wuppertal, Supervisor

Prof. Constantia ALEXANDROU
The Cyprus Institute

Prof. Dirk PLEITER
University of Regensburg

Prof. Stefan MEINEL
University of Arizona

Prof. Francesco KNECHTLI
University of Wuppertal

I would like to dedicate this thesis to my loving parents for their constant emotional support and motivation.

# Declaration

I hereby declare that except where specific reference is made to the work of others, the contents of this dissertation are original and have not been submitted in whole or in part for consideration for any other degree or qualification in this, or any other university. This dissertation is my own work and contains nothing which is the outcome of work done in collaboration with others, except as specified in the text and Acknowledgements.

Srijit Paul
June 2019

# Acknowledgements

I am grateful to my supervisors Prof. Constantia Alexandrou, Assist. Prof. Giannis Koutsou, Prof. Thomas Lippert, and Prof. Dirk Pleiter for their continuous support in numerous direct and indirect ways, as well as for helping me define my objectives and giving an unbiased opinion on every aspect of my research. I would like to acknowledge Prof. Pleiter for providing access to the HPC ecosystem at the Forschungszentrum Jülich, which is one of the leading super-computing centers in the world. I am also very thankful to IBM Research labs for providing me access to their latest super-computing prototypes at IBM Research labs in Zurich.

Assist. Prof. Koutsou has assisted me in a way that has made me more self-confident in solving complex physics and programming issues. Prof. Alexandrou has been a constant lighthouse, shaping the direction of my research throughout my graduate studies. In conjunction, I am thankful to Dr. Marcus Petschlies from the University of Bonn for being available all throughout the days and Dr. Luka Leskovec from Jefferson Lab for being available all throughout the nights. Apart from this, I would like to acknowledge Prof. John Negele and Dr. Andrew Pochinsky from the Massachusetts Institute of Technology and Prof. Stefan Meinel from the University of Arizona for their persistent efforts in discussing and sharing their valuable opinions on various aspects of my research. Dr. Pochinsky has helped me with the scripting language QLUA developed on top of the core USQCD repositories. At The Cyprus Institute, I am thankful to Dr. Jacob Finkenrath, Dr. Kyriakos Hadjiyannakou, Dr. Andreas Athenodorou and Dr. Charis Chrysotomou for keeping the research environment fertile and open to new avenues of research.

I acknowledge the funding from HPC-LEAP, a European Joint Doctorate program coordinate by Prof. Alexandrou. I am thankful for all the administrative help provided by Dr. K. Kleovolou and J Song at the Graduate School of The Cyprus Institute and Dr. N. Savva and C. Leontiou as HPC-LEAP project managers.

I am grateful to Prof. Kostas Orginos for providing the gauge field ensemble for the $\pi\pi$ project, which was generated using resources provided by XSEDE (supported by National Science Foundation Grant No. ACI-1053575). In addition, I acknowledge the use of computational resources of the supercomputers EDISON and CORI at the National Energy Research

Scientific Computing Center (NERSC), a DOE Office of Science User Facility supported by the Office of Science of the U.S. Department of Energy under Contract No. DE-AC02-05CH11231. Also, access to these computational resources was provided under the project *mp133* at NERSC. I am also thankful to the computational resources at the Phi clusters of the Cy-Tera for the production of Ising configurations for the Machine learning project.

Furthermore, it would have been impossible without the constant emotional support from my mother (Mrs. Chandrani Paul [ma]) and my father (Mr. Uttam Kumar Paul [baba]). And last but definitely not the least I would like to thank Maneesha (Manu) for always being there when sometimes she has every right not to.

# Abstract

We study meson and baryon resonances in QCD using lattice techniques. Specifically, we investigate the systems where two incoming stable hadrons strongly interact to form a resonance which then later decays to produce the same outgoing stable hadrons except for a difference in the phase. This phase shift encodes information about the resonance. On the lattice, the Lüscher formalism connects the infinite volume phase shift to finite volume spectra. In order to obtain the spectra on the lattice, we compute the necessary correlation functions involving the two-hadron operator and the single-hadron operator which have the quantum numbers of the resonance. We develop a new method to compute these two-point correlation functions to reduce their computational costs which is prohibitively expensive using conventional methods. Using this new method, we obtain the spectra and compute the relevant phase shifts which enable us to extract the resonance parameters. This method also facilitates the computation of three-point correlation functions with an electromagnetic current insertion. Therefore, we extend our analysis, to compute these three-point functions, which is related to the infinite volume transition form factor and resonant photocoupling through the Briceno, Hansen, Walker-Loud formalism. In this thesis, we present results from applying this method to extract the lowest-lying $\rho$ meson resonance parameters ($m_\rho, g_{\rho\pi\pi}$) in the $\pi\pi$ channel, transition form factor ($\mathcal{V}_{\pi\gamma\to\pi\pi}(s,q^2)$) for a range of center of mass energies ($\sqrt{s}$) and photon virtualities ($q^2$), and resonant photocoupling ($g_{\rho\pi\gamma}$), as well as the first results for the lowest-lying $\Delta$ baryon resonance parameters ($m_\Delta, g_{\Delta\pi N}$) in the $\pi N$ channel[1].

[1]Common thesis between The Cyprus Institute and the University of Wuppertal in partial fulfillment of the PhD requirements for a dual degree within the European Joint Doctorate Program High Performance Computing for Life Sciences, Engineering And Physics (HPC-LEAP). The project has received funding from the European Union's Horizon 2020 research and innovation programme under grant agreement No' 642069.

# Abstract

In dieser Arbeit werden Meson und Baryon Resonanzen in QCD mit Gittermethoden studiert. Der Fokus ist hier bei auf die Untersuchung der Systeme gelegt bei dennen stabile Hadrons mit der Starken-Wechselwirkung interagieren. Diese Interaktion auch als Resonanz bezeichnet fuehrt zu einem Phasenschift der ausgehenden Teilchen. Mit der Differenz der Phase können nun Ausagen über die Art der Resonanz getroffen werden. Aus dem sogenannten Lüscher Formalismus folgt nun das die infinite Volumenphase mit dem finiten Volumenspektrum zusammenhängt, welches auf dem Gitter bestimmt werden kann. Für dies werden die Berechnung bestimmter Korrelations Funktionen benötigt, die das Hadronensystem beschreiben können.

In dieser Arbeit haben wir eine neue Methode entwickelt um diese Zwei-Punkt-Korrelations Funktionen zu bestimmen. Diese Methode reduziert den erheblichen numerischen Aufwand der Berechnung im Vergleich zu den konventionelen Methoden. Mit Hilfe des von uns entwickelten Verfahren wurden die Hadronenspektren und die jeweiligen Phasenshifts bestimmt, so dass die entsprechenden Resonanzparameter berechnet werden konnten. Darüber hinaus kann das Verfahren zur Bestimmung von Drei-Punkt Korrelations Funktionen unter Einbezug des elektromagnetischen Strom benutzt werden. Die Drei-Punkt Funktionen können nun mit dem Briceno-Hansen-Walker-Loud Formalismus zur die Bestimmung der Photonkopplung der Resonanz benutzt werden.

In dieser Arbeit bestimmen wir der Parameter der ersten Rho-Resonanz ($m_\rho, g_{\rho\pi\pi}$), für den Pion-Pion Kanal, fuer den sogenannten Transition Form Faktor ($\mathcal{V}_{\pi\gamma\to\pi\pi}(s,q^2)$) für verschiedene Energien im Massenmittelpunkt-Frame ($\sqrt{s}$) und verschiedene Photonenvirtualitäten ($q^2$), die resonante Photonbindung, so wie Resultate ($m_\Delta, g_{\Delta\pi N}$) fuer die erste Delta-Baryon Resonanz im Nukleon-Pionen Kanal.[2].

[2]Verbreitet Diplomarbeit zwischen dem Cyprus Institute und der Universität Wuppertal zur teilweisen Erfüllung der Promotionsvoraussetzungen für ein duales Studium im Rahmen des europäischen gemeinsamen Promotionsprogramms High Performance Computing for Life Sciences, Ingenieurwesen und Physik (HPC-LEAP). Das Projekt wurde aus Forschungsmitteln der Europäischen Union für Horizont 2020 finanziert und Innovationsprogramm im Rahmen der Finanzhilfevereinbarung Nr. 642069

# Table of contents

# List of figures

# List of tables

# Chapter 1

# Introduction

The physical world can be most accurately described by the four fundamental forces (interactions) of nature namely, gravitational, weak, electromagnetic and strong force in order of their strengths. Among these four forces, most observable macroscopic phenomena can be described by the gravitational and electromagnetic forces, while most of the visible mass is due to the strong force. The Standard Model is the most comprehensive unified description of three of the four forces; weak, electromagnetic and strong forces. The Standard model can be thought of as a theory of interactions between fermions divided into categories: *quarks* and *leptons*, mediated by vector bosons. (*force carriers*). This zoo of particles can be visualized as in Fig. (1.1).

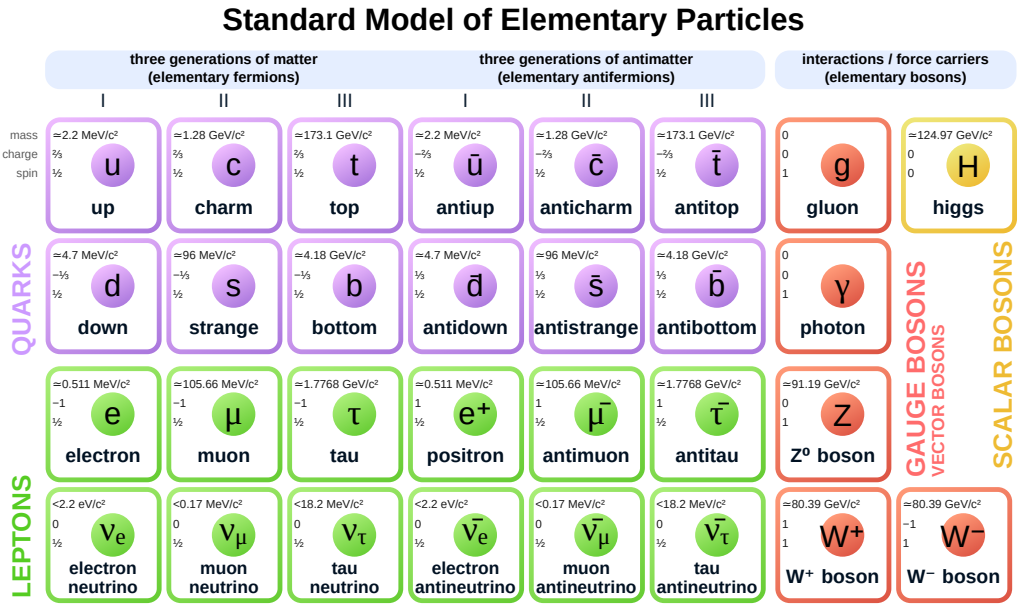


Fig. 1.1 The particle zoo of standard model [248]

In this description of elementary particles, all the fermions interact via the weak interactions, and all but neutrinos interact via the electromagnetic interactions and only quarks interact via the strong interactions. The force carriers for weak interactions are the $W^{\pm}$ and $Z$ bosons, for electromagnetic interactions are the photons and for strong interactions are the gluons. In addition, the recently discovered [1, 63] scalar boson called Higgs boson is responsible for the mass of elementary particles through Higgs mechanism [131, 92, 120]. While most mass of the observable universe comes from composite particles protons and neutrons, jointly called nucleons, only 1% of their mass is due to their constituent quarks, and the rest is primarily due to strong interactions [254]. Such composite particles which interact via strong interactions are called *hadrons*. The vast majority of hadrons observed in nature are not stable under the strong interactions, but decay and have a short life-time, and therefore defined as *resonances*.

This thesis investigates the theory of strong interactions to understand the properties of resonances. We utilize non-perturbative lattice techniques to study the resonances. The outline of the thesis can be discussed as follows:

- In Chapter 1, we start by discussing the origin of Quantum Chromodynamics, and motivate the QCD action with an inclination towards discretizing it later. In this context, we also emphasize on the two most defining properties of the strong force and outline the regime of our investigation for which the lattice techniques are the best available tools.

- Since the primary areas of investigation in the thesis are resonances, we establish the framework of scattering in Chapter 2 by briefly summarizing the scattering $S$-matrix formalism in quantum field theory, and exploring the pole structure of the $S$-matrix with an example. Furthermore, we extend the example towards resonance photoproduction by virtue of the Watson's theorem and conclude the Chapter by motivating the need for a non-pertubative treatment to characterize the resonances from the first principles.

- Chapter 3 introduces various lattice techniques relevant to the thesis which includes different discretization schemes, numerical algorithms for lattice simulations and a generic overview on the different sources of errors. As a forward looking approach in applying novel techniques for the study of statistical systems, in this chapter, we also present a novel study for using unsupervised learning for identifying phase transitions in the Ising model.

- Equipped with the language of lattice techniques, in Chapter 4, we present schematically the methodologies to extract finite volume spectra starting from designing of the

interpolators, projecting them into different irreps on the lattice, ingredients for computing the correlation functions between these interpolators and finally the variational method to obtain the energies. Next, we briefly review the Lüscher formalism which connects these energies to infinite volume phase shifts and consequently the resonant parameters. The importance of Lüscher analysis becomes apparent, when we shed light on the interpretation of the spectrum of a resonant state, through a simple example. After this, we concisely describe the Briceno, Hansen, Walker-Loud formalism which relates the three point functions on the lattice and the resonance phase shifts to the infinite volume transition form factor and resonant photocoupling.

- We apply all these techniques to study the low-lying meson $\rho$ resonance and its photoproduction in Chapter 5.

- Similarly we study the low lying $\Delta$ baryon resonance in Chapter 6.

Results from this thesis have been presented in 3 journal publications (1 is still in submission) and 6 proceedings for presentations at various conferences, as listed below.

1. L. Leskovec, C. Alexandrou, G. Koutsou, S. Meinel, J. W. Negele, **S. Paul**, M. Petschlies, A. Pochinsky, G. Rendon, S. Syritsyn, "A study of the radiative transition $\pi\pi \to \pi\gamma^*$ with lattice QCD," C16-07-24 Proceedings, 34th International Symposium on Lattice Field Theory (Lattice 2016): Southampton, UK, July 24-30, 2016. [arXiv:1611.00282 [hep-lat]] [159].

2. C. Alexandrou, L. Leskovec, S. Meinel, J. W. Negele, **S. Paul**, M. Petschlies, A. Pochinsky, G. Rendon, S. Syritsyn, "*P*-wave $\pi\pi$ scattering and the $\rho$ resonance from lattice QCD," Phys.Rev. D96 (2017) no.3, 034525 [arXiv:1704.05439 [hep-lat]] [11].

3. **S. Paul**, C. Alexandrou, L. Leskovec, S. Meinel, J. W. Negele, M. Petschlies, A. Pochinsky, G. Rendon, S. Syritsyn, "$\pi\pi$ *P*-wave resonant scattering from lattice QCD ," C17-06-18.1 Proceedings, EPJ Web Conf. 175 (2018) 05022, 35th International Symposium on Lattice Field Theory (Lattice 2017): Granada, Spain, June 18-24, 2017.[DOI:10.1051/epjconf/201817505022] [208].

4. C. Alexandrou, L. Leskovec, S. Meinel, J. W. Negele, **S. Paul**, M. Petschlies, A. Pochinsky, G. Rendon, S. Syritsyn, "$\pi\gamma \to \pi\pi$ transition and the $\rho$ radiative decay width from lattice QCD," Phys.Rev. D98 (2018) no.7, 074502 [arXiv:1807.08357 [hep-lat]] [12].

5. L. Leskovec, C. Alexandrou, S. Meinel, J. W. Negele, **S. Paul**, M. Petschlies, A. Pochinsky, G. Rendon, S. Syritsyn, "A Lattice QCD study of the $\rho$ resonance ," C18-05-29 Proceedings, 13th Conference on the Intersections of Particle and Nuclear Physics:29 May - 03 Jun 2018. Palm Springs, California, USA [arXiv:1810.01927 [hep-lat]] [160].

6. L. Leskovec, C. Alexandrou, S. Meinel, J. W. Negele, **S. Paul**, M. Petschlies, A. Pochinsky, G. Rendon, S. Syritsyn, "Calculating the $\rho$ radiative decay width with lattice QCD ," Proceedings, 36th International Symposium on Lattice Field Theory (Lattice 2018): Michigan, USA, July 22-28, 2018. [arXiv:1811.10034 [hep-lat]] [161].

7. G. Rendon, C. Alexandrou, L. Leskovec, S. Meinel, J. W. Negele, **S. Paul**, M. Petschlies, A. Pochinsky, G. Silvi, S. Syritsyn, "$K\pi$ scattering and the $K^*(892)$ resonance in $2+1$ flavor QCD ," Proceedings, 36th International Symposium on Lattice Field Theory (Lattice 2018): Michigan, USA, July 22-28, 2018. [arXiv:1811.10750 [hep-lat]] [215].

8. **S. Paul**, G. Silvi, C. Alexandrou, L. Leskovec, S. Meinel, J. W. Negele,, M. Petschlies, A. Pochinsky, G. Rendon, S. Syritsyn, "Towards the P-wave nucleon-pion scattering amplitude in the $\Delta(1232)$ channel ," Proceedings, 36th International Symposium on Lattice Field Theory (Lattice 2018): Michigan, USA, July 22-28, 2018. [arXiv:1812.01059 [hep-lat]] [209].

9. C. Alexandrou, C. Chrysostomou, A. Athenodorou, **S. Paul** "Unsupervised identification of the phase transition on the 2D-Ising model," [arXiv:1903.03506v1] [8].

## 1.1 Quantum Chromodynamics

### 1.1.1 Historical development

Historically, our understanding of the strong interactions can be traced back to the first hint of the existence of color charge in experiments, namely when the $\Delta^{++}$ was discovered in 1951 [59]. Within the of quark model, which was first developed first by successively joining together the concepts of spin, isospin, strangeness and the eightfold way, the flavor and spin components of the $\Delta^{++}$ baryon is represented as, $|\Delta^{++}\rangle = |u_\uparrow u_\uparrow u_\uparrow\rangle$, which is clearly a highly symmetric configuration, requiring the introduction of additional quantum numbers, since the $\Delta^{++}$ is a fermion. In 1965, after fourteen years of its discovery, the color charge was introduced as a new quantum number with the group SU(3) [116, 127]. During these

fourteen formative years, quarks were theoretically proposed by Gell-Mann [111] and Zweig [257, 258] in 1964, while in 1968, quarks (partons) were first interpreted as point-like constituents of the proton by Bjorken [40, 39, 38] and Feynman [97] through their (near-) scaling behaviour of the structure functions measured in deep inelastic electron-proton scattering at SLAC [42]. This discovery raised further questions, namely whether a new force holds the quarks together inside a proton. In the quest to answer this question, C.L Smith pointed out that one can measure the total fraction of proton momentum carried by quarks [167], and the subsequent experiments showed that this fraction is only half of the total. This was the first indirect evidence for the existence of gluons, which were later formally confirmed by studying jet-physics in experiments [130, 91] and in theory [79, 227].
In the theoretical domain, the development of renormalizable non-Abelian gauge theories by Hooft [234] in 1971 and the realization of Parisi that the key to constructing a field theory of strong interactions would be asymptotic freedom [204], followed by Symanzik showing the conditions for asymptotic freedom in scalar field theory [230], were connected by Politzer [213], Gross and Wilczek [117] and finally formalized into a quantum field theory of strong interactions by Fritzsch, Gell-Mann and Leutwyler [106] in 1973, known as Quantum Chromodynamics(QCD).
QCD, when probed at high energies (short wavelengths) in deep inelastic scattering experiments is weakly coupled and the partons (quarks and gluons) are described as *asymptotically free*, which only scatter off one another through relatively small quantum corrections that can be systematically calculated. But at longer wavelengths (low energies), of the order of the size of a proton $\approx 1fm = 10^{-15}m$, strongly *confined* towers of hadron resonances emerge, with string-like potentials building up if we try to separate their partonic constituents. Therefore, QCD is uniquely characterized by two defining properties namely, *asymptotic freedom* and *confinement*. Nonetheless, both of these features are encoded within the definition of the Lagrangian of QCD.

### 1.1.2 QCD action

In this section we define the QCD action from the QCD Lagrangian. The SU(3) gauge invariant QCD Lagrangian is motivated from first principles.
In order to construct a theory satisfying local gauge symmetry, we consider a continuous group of gauge transformations (also called local gauge transformations of the second kind), represented by a set of SU(3) matrices $\Lambda(x)$ and a quark of flavor $q$, represented by $\psi^{\alpha}_{c,q}(x)$ with SU(3) color index $c = 1,2,3$ and Dirac spinor index $\alpha = 0,1,2,3$. Suppressing all

indices in the following, the field $\psi(x)$ transforms like,

$$\psi(x) \to \psi'(x) = \Lambda(x)\psi(x). \tag{1.1}$$

For arbitrary space-time points $x$ and $y$, let $V_x$ denote the vector space of quark fields $\psi(x)$ at $x$, and $V_y$ as vector space of quark fields $\psi(y)$ at $y$. For local gauge invariance, we need to define a function $U$ along any curve from $x$ to $y$, such that $U(\Lambda(x)\psi(x)) = \Lambda(y)U(\psi(y))$. This mapping preserves probability and is independent of the local choice of basis. This function is called a *parallel transporter*, $U(x,y) : V_x \to V_y$. Let $\mathscr{C}_{yx}$ be some curve in space-time from $x$ to $y$. It may be parametrized as follows,

$$c(s),\ s \in [0,1],\ c(0) = x,\ c(1) = y.$$

Then,

$$U(\mathscr{C}_{yx})\psi(x) \in V_y. \tag{1.2}$$

If we define $y = \lim_{a\to 0}(x + a\hat{\mu})$, where $\mu$ is a unit vector in the direction of $\mu^*$, then we can write $U(x,y) \equiv U(\mathscr{C}_{yx})$, which transform as $U(x,y) \to U'(x,y) = \Lambda(x)U(x,y)\Lambda(y)^{-1}$, which is a probability preserving unitary basis transformation. Using $U(x,y)$ we can define a *covariant* derivative in the direction of $\mu$ by the limiting procedure:

$$D_\mu \psi(x) = \lim_{a\to 0} \frac{1}{a}[U(x, x + a\hat{\mu})\psi(x + a\hat{\mu}) - \psi(x)] \tag{1.3}$$

Since, $U(x,y)$ is a SU(3) matrix and a continuous function of its arguments, for infinitesimal $a$ it can be represented as,

$$U(x, x + a\hat{\mu}) = \exp\left(-igaA^b_\mu(x + \frac{a}{2}\hat{\mu})T_b + \mathscr{O}(a^3)\right). \tag{1.4}$$

Here $g$ is the bare gauge coupling and $A^b_\mu$, $b = 1, 2, \cdots, 8$ [1] are real-valued fields for each generator $T_b$ of the transformation group SU(3). The matrices $T_b = \frac{\lambda_b}{2}$ where $\lambda_b$ are Gell-Mann matrices discussed in the Appendix A.

Expanding Eq. (1.4) in $a$ and inserting it into definition Eq. (1.3) yields, in the limit $a \to 0$, for the continuum covariant derivative associated with the local SU(3) gauge symmetry,

$$D_\mu = \partial_\mu - igA^b_\mu T_b, \tag{1.5}$$

[1] for SU(N) this has $N^2 - 1$ real-valued components

which has the correct gauge transformation properties and where $A^b_\mu$ represents the gauge potential. Thus, we have defined a locally gauge invariant kinetic term for the quark fields. To define a locally gauge invariant kinetic term for the gauge potential, we follow ideas from the curvature tensor definition in general relativity, defining a *field strength* tensor as,

$$F^b_{\mu\nu} = \partial_\mu A^b_\nu - \partial_\nu A^b_\mu + g f_{bcd} A^c_\mu A^d_\nu. \tag{1.6}$$

where $f_{bcd}$ are called structure constants of the symmetry group SU(3) given in Appendix A. Geometrically this can be interpreted as the *plaquette* [186] defined as,

$$\begin{aligned} U_\square(x;\mu,\nu) = U(x,x+a\hat{\mu})U(x+a\hat{\mu},x+a\hat{\nu}+a\hat{\mu}) \\ \times U(x+a\hat{\nu}+a\hat{\mu},x+a\hat{\nu})U(x+a\hat{\nu},x) \end{aligned} \tag{1.7}$$

The plaquette can be made locally gauge invariant if we take its trace. Inserting Eq. (1.4) in Eq. (1.7) and using the Baker-Campbell-Haussdorff formula to expand to $a^6$ we get,

$$\mathrm{Re}(\mathrm{Tr}(U_\square(x;\mu,\nu))) = \mathrm{Tr}[1] - \frac{1}{4} g^2 a^4 F^{\mu\nu}_b F^b_{\mu\nu} + \mathscr{O}(a^6). \tag{1.8}$$

Now we can write the QCD Lagrangian density that is renormalizable, conserves parity and is invariant under time reversal,

$$\mathscr{L}_{QCD}[\psi,\bar{\psi},A] = -\frac{1}{4} F^{\mu\nu}_b F^b_{\mu\nu} + \bar{\psi}(i\gamma^\mu D_\mu - m_q)\psi \tag{1.9}$$

with $\bar{\psi} = \psi^\dagger \gamma_0$ being the antiquark field. The fermionic part contains the covariant Dirac operator $\mathbb{M} \equiv i\gamma^\mu D_\mu - m_q$ with quark mass $m_q$. The Dirac gamma matrices $\gamma^\mu$ satisfy anti-commutation relation $\{\gamma^\mu,\gamma_\nu\} = 2g_{\mu\nu}$. In Minkowski space-time the metric tensor is $g_{\mu\nu} = \mathrm{diag}(-1,1,1,1)$.
Thus, the QCD action with Minkowski space-time metric can be written as,

$$\mathscr{S}^M_{QCD}[\psi,\bar{\psi},A] = \int d^4x_M \mathscr{L}_{QCD} \tag{1.10}$$

### 1.1.3 QCD Path Integral

For the purpose of this thesis, QCD as introduced above is quantized via the path integral formulation [95, 96] where quark fields $\psi$ are *Grassmann* variables. The expectation of a physical observable $\hat{O}[\psi,\bar{\psi},A]$ is then formally given by the following functional integral

following the convention of Ref. [212],

$$\langle \hat{O} \rangle = \frac{1}{\mathscr{Z}} \int \mathscr{D}A \mathscr{D}\psi \mathscr{D}\bar{\psi}\, O[\psi, \bar{\psi}, A]\, e^{iS^M_{QCD}[\psi,\bar{\psi},A]} \tag{1.11}$$

with partition function given by,

$$\mathscr{Z} = \int \mathscr{D}A \mathscr{D}\psi \mathscr{D}\bar{\psi}\, e^{iS^M_{QCD}[\psi,\bar{\psi},A]}. \tag{1.12}$$

The gauge invariance of the physical observable is preserved in a fixed gauge because the integrand and the measure in Eq. (1.11) is gauge-invariant in that fixed gauge.

### 1.1.4 QCD: Energy scale dependence description

Having written down the Lagrangian, one may proceed to construct the QCD Feynman rules and calculate observables. The question is how do we extract the *asymptotically free* behaviour at high energies and *confining* behaviour at low energies. These two mutually exclusive behaviours depict that the parameters of the theory, or the degrees of freedom, are dependent on the energy scale. At high energies, as the coupling $g << 1$, perturbative treatment of the QCD Lagrangian is applicable and perturbative loop corrections give rise to UV divergences [117] which need to be treated through a regularization procedure. In order to keep the observables independent of the regularization scheme, regularization follows redefining of the parameters of the theory as renormalized parameters which depend on the renormalization scale $\mu$ (energy scale). The quantity which best captures the dependence of the coupling ($g(\mu)$) on the renormalization scale is $\alpha_s(\mu) = g^2(\mu)/4\pi$. At next-to-leading order (NLO) in the perturbative expansion, the $\beta$-function of QCD which is defined as the change of the coupling $g$ with respect to the logarithm of the energy scale $\mu$, is [213, 117],

$$\beta(g) \equiv \mu \frac{\partial}{\partial \mu} g(\mu) = -\frac{g^3}{16\pi^2}\left(11 - \frac{2N_f}{3}\right) + \mathscr{O}(g^5), \tag{1.13}$$

where $N_f$ is the number of dynamical quarks, typically between 2(first family) to 6(first, second and third family). Since the $\beta$-function is always negative for $N_f \leq 16$, the interactions between quarks and gluons vanishes at high energies. Thus, we show the defining characteristics of *asymptotic freedom* of QCD is included in the theory. Equation (1.13) can be solved for $\alpha_s(\mu)$ in terms of a subtraction point $\Lambda_{QCD}$,

$$\alpha_s(\mu) = \frac{12\pi}{(33 - 2N_f)\log(\mu^2/\Lambda^2_{QCD})} \tag{1.14}$$

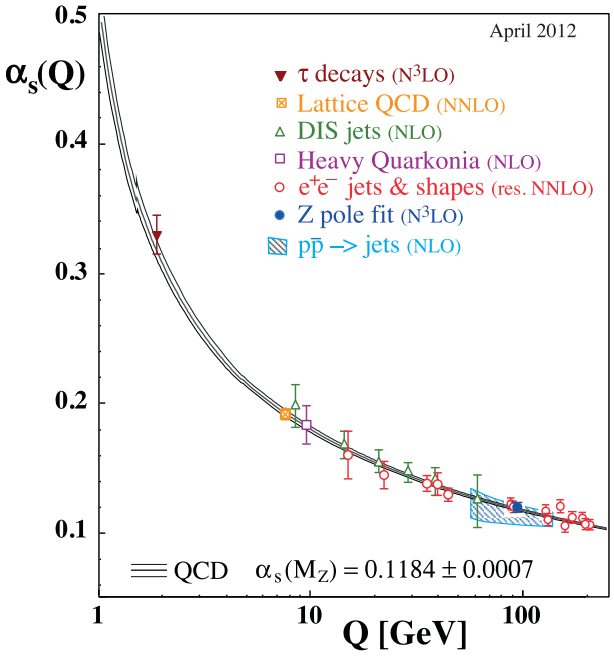


Fig. 1.2 The coupling of QCD as a function of a characteristic energy scale $\mu = Q$, obtained from matching the QCD perturbative calculation to a given order (as given in brackets) to the experimental measurements of several quantities. There is also one point which is obtained by matching to a lattice QCD calculation [31].

In Fig. 1.2, as $\mu$ approaches $\Lambda_{QCD}$, the strength of the interaction quickly diverges, illustrating the fact the standard perturbative tools fail and non-pertubative effects become important. Thus, we successfully extracted the *confining* behaviour at low energies. Experimentally $\Lambda_{QCD} \approx 200$ MeV which is of the order of the inverse size of the light hadrons. This is consistent with our realization of hadrons being composed of strongly interacting constituents when low-energy probes are used. In fact at low energies, these hadrons are the effective degrees of freedom of QCD, and the details of their properties and interactions, although sensitive to the short distance theory of QCD, can be studied in a systematic low-energy expansion. In the low to medium energy limit, major contribution towards building hadrons from quarks is from $u$, $d$ and $s$ quarks as $m_c \approx 1.3\,\text{GeV}$.
In the next chapter, we briefly review the theory of elastic scattering, to study the formation of hadron resonances non-perturbatively.

# Chapter 2

# Scattering Theory

## 2.1 Introduction

Numerous past, ongoing and planned scattering experiments around the world are being carried out to study the strong interactions. These experiments investigate different aspects of QCD at various energy scales. Scattering cross-section from one of the early experiments is shown in Fig. (2.1).

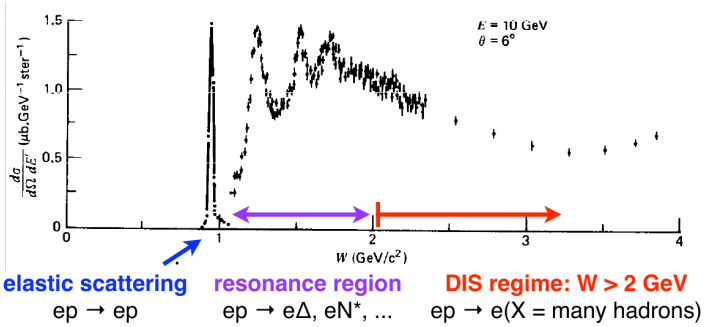


Fig. 2.1 Differential cross-section of $e^- p$ scattering as function of the invariant mass of the proton decay products $W$. The electron energy is 10 GeV and the detector was placed at 6° with respect to the electron beam axis. The elastic scattering peak at $W = m_p$ has been scaled down by a factor 8.5 [104].

Experiments at higher energies($> 2$ GeV) probe the deep inelastic regime, where the objective is to study the consequences of asymptotic freedom of quarks. On the other hand, experiments at lower energies ($< 2$ GeV) aim at exploring the hadronic physics which is attributed to the confining property of QCD.

In this chapter, the main objective is to provide a description for elastic low-energy scattering relevant to the study of hadronic physics.

## 2.2 *S*-matrix formalism

Since, we want to study scattering of particles with relativistic energies, we need the to study scattering within the framework of quantum field theory. We begin by defining the probability $P$ of the incoming states to go to outgoing states, in terms of one-particle state $|\phi\rangle$ as :

$$P = \left| {}_{\text{out}}\langle \{p_1, p_2, \ldots, p_{n'}\} | \{q_1, q_2, \ldots, q_n\} \rangle_{\text{ in}} \right|^2 \tag{2.1}$$

Here we have considered $n$ incoming states $q_1, q_2, \cdots$ scattering into $n$ outgoing $p_1, p_2, \cdots$ states, where $p_1, p_2 \cdots p_n'$ represent the momenta of the outgoing states in 4-momentum space, and $q_1, q_2 \cdots q_n$ represent the momenta of the ingoing states in 4-momentum space. These states are eigenstates of the total Hamiltonian $H$, which can be written as $H = H_0 + V$ where $H_0$ is the free Hamiltonian and $V$ is the interacting potential. These asymptotically free *in* and *out* states (eigen states of the free Hamiltonian $H_0$ in limits $T = \infty$ and $T = -\infty$) are related by the limit of a sequence of unitary operators. This limiting unitary operator is called the $S - matrix$. In 4-momentum space this can represented as,

$$\begin{aligned} {}_{\text{out}}\langle \{p_1, p_2, \ldots, p_{n'}\} | \{q_1, q_2, \ldots, q_n\} \rangle_{\text{ in}} &\equiv \langle \{p_1, p_2, \ldots, p_{n'}\} | S | \{q_1, q_2, \ldots, q_n\} \rangle \\ &= \lim_{T \to \infty} \left\langle \{p_1, p_2, \ldots, p_{n'}| e^{-i2HT} | \{q_1, q_2, \ldots, q_n\} \right\rangle , \end{aligned} \tag{2.2}$$

where the two states on the right of the equality are defined at a common time reference frame. These asymptotically free states consist of several non-interacting particles that transforms under the inhomogenous Lorentz group as a direct product of one-particle states, which are labelled by their four momenta $p^\mu$, spin $l$ with $z-$component $m$, and an additional discrete label $n$ for the particle type, which includes a specification of its mass, spin and charge. Since $S$-matrix is defined in the limiting case, if the incoming particles do not interact, then $S$ is just the identity matrix. Therefore, it is convenient to isolate the interactive part of the $S$-matrix into the $T$-matrix,

$$iT \equiv S - \mathbb{I} \tag{2.3}$$

Furthermore, due to momentum-conservation the expectation value of the $T$-matrix is proportional to a four-dimensional delta-function, so all of the physics can be encapsulated in the Lorentz invariant scattering amplitude, $M$, defined by,

$$\langle \{p_1, p_2, \ldots, p_{n'}\} | iT | \{q_1, q_2, \ldots, q_n\} \rangle = (2\pi)^4 \delta^{(4)} (p_{out} - q_{in})\, iM \tag{2.4}$$

where $p_{out} = \sum_i^{n'} p_i$ and $q_{out} = \sum_i^{n} q_i$. In typical theoretical calculations, the amplitude $M$ is computed for physically relevant scattering particles, which is then connected to quantities that can be measured in experiments. In order to illustrate the multitude of properties of the $S$-matrix we take the example of scattering of 2 spin-zero particles of equal masses into 2 spin-zero particles (also represented as $2 \to 2$) of equal masses in the next parts of the chapter.

### 2.2.1 Case study: $2 \to 2$ scattering with equal masses

The kinematics of the system can be described in a Lorentz invariant way using 2 variables (3 4-momenta implies 12 independent components, then 4 on-mass-shell conditions $|\vec{p}_i|^2 = m_i^2$ and 3 Lorentz Boosts and 3 rotations reduces the independent components to 2 kinematic variables). A convenient choice of variables could be from the Lorentz invariant *Mandelstam* variables ($s$,$t$ and $u$). These variables are defined as,

$$s = (p_1 + p_2)^2 \quad = (p_3 + p_4)^2 \qquad (2.5)$$

$$t = (p_1 - p_3)^2 \quad = (p_2 - p_4)^2 \qquad (2.6)$$

$$u = (p_1 - p_4)^2 \quad = (p_2 - p_3)^2 \qquad (2.7)$$

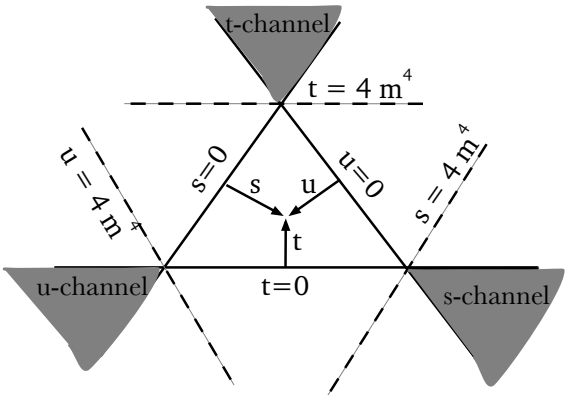


Fig. 2.2 Dalitz plot showing shaded region as the kinematically accessible region for $2 \to 2$ elastic scattering of particles of equal masses

where $p_1$, $p_2$ denote the 4-momenta of the incoming particles and $p_3$, $p_4$ denote the 4-momenta of outgoing particles. As discussed, the kinematics of $2 \to 2$ can be depicted in 2-dimensional space with the physically significant non-orthogonal Mandelstam variables as shown in Fig. 2.2. This type of representation of kinematic variables is called *Dalitz* plot, which helps in understanding the kinematically accessible region, and helps defining the threshold ( square of the sum of masses of the two incoming particles at rest) represented here by the dotted lines in each channel. The Mandelstam variables also carry another physical significance by describing the channel of scattering as depicted in Fig. 2.3. In our subsequent discussions we will consider $s$-channel elastic scattering.

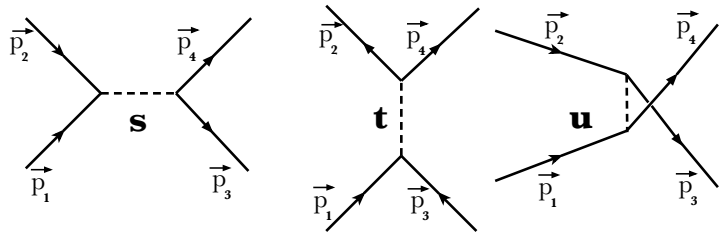


Fig. 2.3 Different physical channels corresponding to $s$, $t$ and $u$.

### Scattering cross-section

Noe we define a physical quantity which can be measured by experimentalists and is related to the scattering amplitude. The differential scattering cross-section (relevant for experimentalists, defined as transition rate per flux or solid angle $\Omega$) for a system of two incoming particles with equal masses and center of mass energy $\sqrt{s}$ in the center-of-mass frame is,

$$\left(\frac{d\sigma}{d\Omega}\right)_{CM} = \frac{1}{64\pi^2 s}|M_{2\to 2}(s,t)|^2. \tag{2.8}$$

In Eq. 2.8, the scattering amplitude as discussed in the previous section must be a function of only 2 kinematic variables, as such $s$ and $t$.
Cross-section for elementary particle scattering are usually measured in *milli-barns*, denoted by mb. A *barn* is $10^{-24}$ cm$^2$. The Fig. (2.1) is an example of one such result from experiments.

### Partial wave expansion

The elastic scattering amplitude can be conveniently represented in the basis of the free-particle states, in which all variables are discrete, except for the total momentum and energy. This is possible because the components of the momenta $\vec{p}_1, \vec{p}_2$ in a 2-particles state of the definite total momentum $\vec{P}_{CM} = 0$ and total center of mass energy $E^\star = \sqrt{s}$ form a 2 dimensional compact space, which is a $2-$sphere. Any function on such a compact space can be expanded in a series of generalized partial waves.

$$M_{2\to 2}(s,t) = \frac{1}{4\pi}\sum_l P_\ell(t,s)M_\ell(s) \tag{2.9}$$

where $P_\ell(t,s) \equiv P_\ell(\cos\theta)$ a Legendre function of the scattering angle $\theta$. $\theta$ is defined as,

$$\cos\theta = \frac{\vec{p}_1 \cdot \vec{p}_3}{|\vec{p}_1||\vec{p}_3|} = 1 + \frac{t}{2(s-4m^2)}$$

. Upon partial wave expansion, the $\theta$ dependence of the 2-sphere is absorbed in the Legendre function, therefore the scattering amplitude for each partial wave $\ell$, $M_\ell(s)$ is only a function of the $s$.

### Implications of Unitarity

The symmetries of the Lagrangian/Hamiltonian are preserved through the $S$-matrix, consequences of which are observed by measuring the invariant scattering amplitude $M(s,t)$ in experiments. Apart from symmetries, unitarity of the $S-$matrix enables us to put more restrictions on the scattering amplitude $M_{\alpha\beta}(s)$. Using the time reversal symmetry of the theory of strong interactions and unitarity of $S-$matrix, we can write

$$\mathrm{Im}\frac{1}{M_\ell(s)} = -\frac{1}{16\pi}\frac{\sqrt{s-4m^2}}{\sqrt{s}}\Theta(\sqrt{s}-2m). \tag{2.10}$$

This expression can be interpreted as $M_\ell(s)$ having a branch-cut at $s = 4m^2$, meaning it will have two Riemann sheets when $M_\ell(s)$ will be represented in the complex $s-$plane. The first sheet will have $\mathrm{Im}(\sqrt{s-4m^2}) > 0$, which is defined as the *physical* sheet and the second sheet will have $\mathrm{Im}(\sqrt{s-4m^2}) < 0$ which is defined as the *unphysical* sheet. These sheet can be visualized in Fig. 2.4.

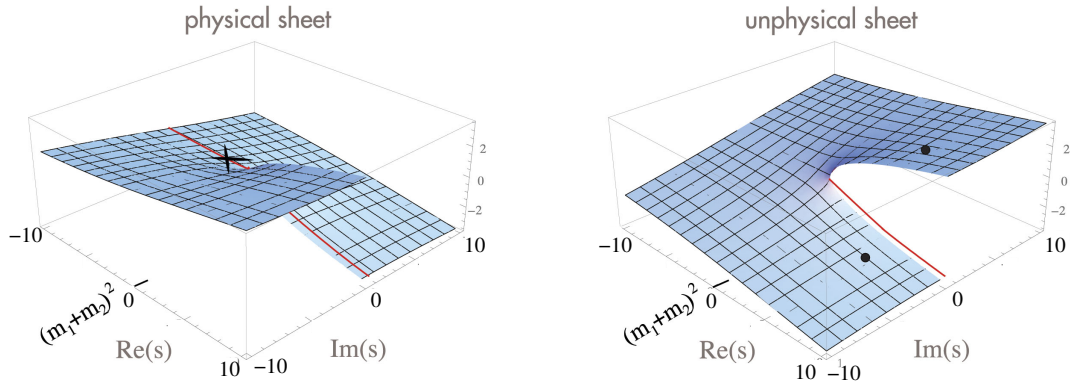


Fig. 2.4 Sketch of the imaginary part of a typical single–channel amplitude in the complex $s$-plane. The solid dots indicate allowed positions for resonance poles,the cross for a bound state. The solid line is the physical axis (shifted by $i\varepsilon$ into the physical sheet). The two sheets are connected smoothly along their discontinuities. (Assume $m_1 = m_2$ in our example) Fig credits [206]

If we only consider contribution from the $\ell$-th partial wave, then $S(s) = S_\ell(s) = \mathbb{I} + iT_\ell(s)$ where

$$\langle \{p_1, p_2, \ldots, p_{n'}\} | iT_\ell(s) | \{q_1, q_2, \ldots, q_n\} \rangle = \frac{1}{4\pi}(2\pi)^4 \delta^{(4)}(p_{out} - q_{in})\, iP_\ell(s,t) M_\ell(s). \tag{2.11}$$

Now upon applying the unitarity of $S$-matrix we can parametrize each partial wave $S_\ell(s)$ with real phase shift $\delta_\ell(s)$ as,

$$S_\ell(s) = e^{2i\delta_\ell(s)}. \tag{2.12}$$

We obtain the invariant scattering amplitude for each partial wave $l$ as,

$$M_\ell(s) = \frac{8\pi\sqrt{s}}{\sqrt{s-4m^2}} \left( \frac{1}{\cot\delta_\ell(s) - i} \right). \tag{2.13}$$

This equation can be understood as the *phase-shift* representation of the invariant scattering amplitude $M_\ell(s)$.

### 2.2.2 Pole structure

The invariant scattering amplitude contains information about intermediate states of angular momentum $l$ in the form of pole singularities. The $M_\ell(s)$ in the vicinity of a pole $s_0$ takes the form of $M_\ell \sim \frac{g^2}{s_0 - s}$ [49]. The pole singularities can be classified into the following classes as shown in Fig. (2.5):

- Poles on the real axis of the physical sheet below the threshold ($s = 4m^2$) are allowed and are identified as bound states. $M_\ell(s)$ takes the form $M_l \sim \frac{g^2}{s_0 - s}$, thus resulting in the mass of the bound-state as $\sqrt{s_0}$.
- Poles above the threshold on the real axis of the physical sheet are not allowed, as they violate unitarity.
- Poles off the real axis on the physical sheet are not allowed, as they violate causality.
- Poles on the real axis of the unphysical sheet below the threshold are allowed, and these particles are known as virtual bound-state ( or sometimes called anti-bound states). Virtual states can arise in case when interactions are attractive, but not attractive enough to form a bound state.
- Poles off the real axis of the unphysical sheet above the threshold are allowed, and give rise to resonant ($4^{th}$ quadrant) and anti-resonant ($1^{st}$ quadrant) states. These poles occur in complex conjugate pairs. The resonance poles are our area of interest.

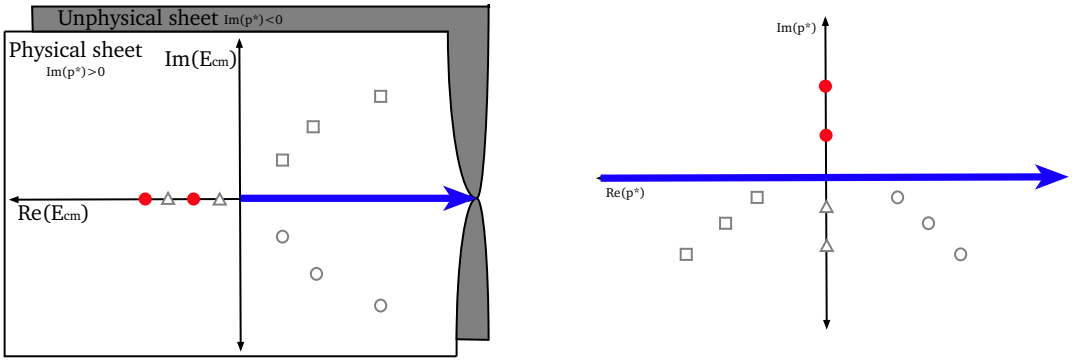


(a) (b)

Fig. 2.5 S-matrix poles in the (a) energy plane (b) momentum planes: the one in front is the physical sheet and one in back is the unphysical sheet. The blue solid arrows indicate the scattering states with a real momentum and a positive energy. The filled symbols represent poles on the physical sheet, and the open symbols (△, □, and ○) represent poles on the unphysical sheet. The △ points represent anti-bound or virtual bound states, □ represent anti-resonant states and ○ represent resonant states.

### 2.2.3 Remarks on Resonances and $S$-matrix formalism

In Eq. (2.13) if we use the definition $t_\ell(s) = \frac{1}{(\cot\delta_\ell(s) - i)}$, and focus only on narrow resonant contributions, $t_\ell(s)$[1] can be described with a Breit-Wigner form,

$$t_\ell(s) = \frac{\sqrt{s}\Gamma(s)}{m_R^2 - s - \mathrm{i}\sqrt{s}\Gamma(s)}, \tag{2.14}$$

where $m_R$ is the mass of the resonance and $\Gamma(s)$ is the decay width of the resonant particle. This resonant contribution corresponds to the phase shift

$$\delta_\ell(s) = \arctan\frac{\sqrt{s}\Gamma(s)}{m_R^2 - s}. \tag{2.15}$$

Quantitative estimation of the phase shift $\delta_\ell(s)$ can be obtained near the resonance, because of the sign change as $s$ varies from $s < m_R^2$ to $s > m_R^2$ which results in a jump in the phase shift by a value of $\pi$. We conclude that a phase shift of $\pi$ is a characteristic behavior of the presence of a narrow resonance in the scattering.
An important remark to emphasis is that unitarity is a necessary condition for obtaining resonances in the $S-$matrix formalism. This condition eliminates the possibility of perturbative treatment of the $S-$matrix, thus requiring the application of non-pertubative methods, to study resonances of which lattice QCD is the only known way, starting from the QCD action.

### 2.2.4 Resonant transition form factors

Since we have discussed the nature of scattering phase near a resonance, Watson's theorem, which states that the phase of an amplitude leading to a final state with two strongly interacting particles in a given partial wave is the same as the scattering phase of that pair, $\delta_\ell(E^{\star 2})$ [245], enables us to calculate amplitudes in systems which have the same final states. Therefore, the scattering phase $\delta(s)$ near resonance in a $2 \to 2$ system, can be utilized to extract the transition amplitude in systems with the same 2-particle final state. One such system with the same final state is the resonance photoproduction[2], where an incoming QCD-stable state interacts with a photon to produce the same resonance, and then decays into the same 2-particle QCD-stable final state as in the $2 \to 2$ case. This $1 \to 2$ photoproduction is described by the matrix element $\langle 2|J^\mu(0)|1\rangle$, which is constructed from the initial state $|1\rangle$, the insertion of the first order in perturbation theory QED current $J^\mu(0) = \frac{2}{3}\overline{u}\gamma^\mu u - \frac{1}{3}\overline{d}\gamma^\mu d$, with $u$ and

[1] Note that from Eq. (2.11) $T_\ell(s) = 2\frac{\sqrt{s}}{\sqrt{s-4m^2}}t_\ell(s)$

[2] Photoproduction is actually $2 \to 1$, but due to time reversal symmetry of strong interactions the physics is the same as $1 \to 2$

$d$ denoting the creation and annihilation up and down-quark fields [3] (defined without the factor of $e$), the final state $|2\rangle$ and four-momentum $P = (\sqrt{s+\vec{P}^2}, \vec{P})$. The 2-particle final state is projected to $l$-th partial wave which contains the resonance and the polarization of the system is described by $\varepsilon^{\nu}(P,m)$ [68]. As a consequence of Lorentz symmetry the transition amplitude $V_{1\to 2}$ of such system is connected to the matrix element $\langle 2|J^{\mu}(0)|1\rangle$ in the $\ell = 1$-th ($P$) partial wave in the following way,

$$\langle 2|J^{\mu}(0)|1\rangle = \frac{2iV_{1\to 2}(q^2,s)}{m}\varepsilon^{\nu\mu\alpha\beta}\varepsilon_{\nu}(P,m)(p_1)_{\alpha}P_{\beta}, \tag{2.16}$$

where $q = p_1 - P$ is the photon four-momentum transfer. The transition amplitude $V_{1\to 2}$ depends on both the photon four-momentum transfer $q^2$ and the invariant mass $s$.

Lets denote the resonance in the two systems $2 \to 2$ and $1 \to 2$ as $2 \to 1^{\star} \to 2$ and $1 \to 1^{\star} \to 2$ respectively. Then using insights from previous sections and Eqs. (2.11) we can write near resonance at $s = s_P \approx m_R^2 + im_r\Gamma$,

$$T_{2\to 2}(s) \sim \frac{G_{1^{\star}-2}}{s_P - s}. \tag{2.17}$$

where $G_{1^{\star}-2}$ denotes the coupling between the resonance $1^{\star}$ with the 2 particle final state. Since the scattering phase goes through a shift of $\pi$ resulting in a pole in $2 \to 2$ scattering amplitude, Watson's theorem ensures that the transition amplitude phase would also go through a similar phase shift resulting in a pole in the $1 \to 2$ transition amplitude. Thus,

$$V_{1\to 2}(0,s) \sim \frac{G_{1^{\star}-2}G_{1^{\star}-1}}{s_P - s} \tag{2.18}$$

where $G_{1^{\star}-1}$ denotes the coupling between the resonance $1^{\star}$ with the 1 particle initial state. From Eqs. (2.11) and (2.13), the $2 \to 2$ elastic scattering amplitude is related to the scattering phase-shift as,

$$T_{2\to 2}(s) = \frac{16\pi\sqrt{s}}{\sqrt{s-4m^2}}\left(\frac{1}{\cot\delta_{\ell}(s) - i}\right). \tag{2.19}$$

Motivated by Eqs.(2.17), (2.18) and the fact that the resonance decay width $\Gamma(s)$ introduced in Eq. (2.14) is often parametrized in terms of $G_{1^{\star}-2}$, we write the photoproduction amplitude

[3] The position space current is denoted as $J_{\mu}(t,\vec{x})$, and its Fourier transform will be labeled as $\tilde{J}_{\mu}(t,Q)$.

$V_{1\to 2}(q^2,s)$ as,

$$V_{1\to 2}(q^2,s) = \sqrt{\frac{16\pi}{\sqrt{s-4m^2}\Gamma(s)}}\frac{F(q^2,s)}{\cot\delta(s)-\mathrm{i}}$$
$$= \sqrt{\frac{16\pi}{\sqrt{s-4m^2}\Gamma(s)}}F(q^2,s)\sin\delta(s)\,e^{\mathrm{i}\delta(s)}, \tag{2.20}$$

where the form factor $F(q^2,s)$ no longer has a pole in $s$, and becomes equal to the photocoupling $G_{1^\star-1}$ for $s = m_R^2 + \mathrm{i}m_R\Gamma_R$ and $q^2 = 0$. More generally, we define the resonant form factor for arbitrary photon virtuality as

$$F_{1\to 1^\star}(q^2) = F(q^2, m_R^2 - \mathrm{i}m_R\Gamma_R). \tag{2.21}$$

Note that Eq. (2.20) explicitly satisfies Watson's theorem. Thus, now $F$ near the resonance is a regular function and can be Taylor expanded in $q^2$ and $s$ near resonance.

Therefore, for obtaining the transition amplitudes and resonance photocoupling, it is necessary to compute the transition matrix element $\langle 2|J^\mu(0)|1\rangle$ exactly in Eq. (2.16) which is then equated to the various model independent parametrizations of the resonant form factor with the photocoupling $G_{1^\star 2}$ being one of the fitted parameter. These fitted parameters are then used to compute the transition amplitude at different photon virtualities.

All in all, the necessary condition to compute the transition matrix element exactly projected onto the $\ell$-th partial wave which contains the resonance requires a non-perturbative treatment, thus making the application of lattice QCD methods essential.

# Chapter 3

# Lattice methods

In this chapter, the formulation of QCD on the lattice will be introduced. The need to study lattice techniques to probe non-perturbative phenomena of QCD from first principles at low energies has been motivated in Sec. 1.1.4 and Sec. 2.2.3. For the presentation on the lattice, we will proceed hereby introducing the following sub-topics:

- Application of Wick rotation (change of metric) and its consequences.
- Lattice Regularization and their artifacts.
- Overview of numerical simulations.

## 3.1 Wick rotation

Wick rotation is defined as the change of the metric from Minkowski to Euclidean as,

$$g_{\mu\nu} = \text{diag}(-1,+1,+1,+1) \rightarrow \delta_{\mu\nu} = \text{diag}(+1,+1,+1,+1) \tag{3.1}$$

which manifests itself in the QCD Lagrangian and action in the following way,

$$t_M = -it_E \tag{3.2}$$
$$d^4x_M = -id^4x_E \tag{3.3}$$
$$\mathscr{L}^M_{QCD} = -\mathscr{L}^E_{QCD} \tag{3.4}$$
$$S^M_{QCD} = iS^E_{QCD} \tag{3.5}$$
$$\left\langle \hat{O}^E \right\rangle = \frac{1}{\mathscr{Z}^E} \int \mathscr{D}A\mathscr{D}\psi\mathscr{D}\bar{\psi}\, O[\psi,\bar{\psi},A]\, e^{-S^E_{QCD}[\psi,\bar{\psi},A]} \tag{3.6}$$
$$\mathscr{Z}^E = \int \mathscr{D}A\mathscr{D}\psi\mathscr{D}\bar{\psi}\, e^{-S^E_{QCD}[\psi,\bar{\psi},A]}. \tag{3.7}$$

This change of metric, needs to preserve the physics of the quantum field theory of strong interactions. Osterwalder and Schrader [200] worked out the necessary and sufficient conditions for Green's functions (correlation functions) in Euclidean field theory to be analytically continued to a quantum field theory in Minkowski space. The validity of these conditions in the context of general gauge theories and QCD in the continuum specifically, is still an active area of research.

In Euclidean space-time, observables given in Eq. (3.7) take on a probabilistic interpretation namely, the probability $e^{-S^E_{QCD}[\psi,\bar{\psi},A]} \sim e^{-\beta\mathscr{H}}$, has an equivalence with the Boltzmann factor in statistical mechanics. This equivalence facilitates the application of analytical and computational tools from statistical mechanics in Euclidean field theory. One of the most powerful and widely used computational methods in statistical mechanics is the Monte Carlo simulation of equilibrium configurations on a discrete lattice, which is then used to measure correlation functions and relevant thermodynamic quantities. Lattice QCD uses a similar work-flow, as will be discussed in the next sections.

## 3.2 Lattice Regularization

QCD as a quantum field theory can be regularized in Euclidean space-time by means of a discrete space-time lattice. Discretization acts as a UV regulator which allows for low energy non-perturbative computations by means of Monte Carlo methods.
We define a hyper-cubic space-time (4-D) lattice with a lattice spacing "$a$", extending up to $aL$ $(aT)$ in the spatial directions (time direction). The boundary conditions chosen in this thesis are periodic boundary conditions, but in principle, there exist regularization schemes with different types of boundary conditions. This finite lattice spacing with periodic boundary conditions imposes an ultra-violet cutoff on the momenta. On the lattice, the allowed momentum values in any spatial direction are:

$$p_n = \pm\frac{2\pi n}{aL}, \quad n = 1, \cdots, L/2 \tag{3.8}$$

Having fixed the periodic boundary conditions for space-time, the next quantities are quark fields, for which the fermionic nature of quarks enforces the use of anti-periodic boundary conditions in the temporal extent of the lattice due to the spin-statistics theorem.
After the quark fields, we are left with 8 components of the gauge potential $A^b_\mu(x)$ in the continuum which needs to be defined on the lattice. We define,

$$A_\mu(x) = -gA^b_\mu(x)T_b \tag{3.9}$$

and using Eq. (1.4), we can write,

$$U_\mu(x) \equiv U(x,x+a\hat{\mu}) = \exp\left(i\int_x^{x+a\hat{\mu}} \mathrm{d}x_\mu A_\mu(x)\right) \simeq \exp\left(iaA_\mu(x+\frac{a}{2}\hat{\mu})\right). \quad (3.10)$$

This definition further satisfies the property

$$U_\mu^\dagger(x) = U_{-\mu}(x-\hat{\mu}), \quad (3.11)$$

and expanding Eq. (3.10) upto $\mathscr{O}(a^2)$,

$$U_\mu(x) = \mathbb{I} + iaA_\mu(x) + \mathscr{O}(a^2). \quad (3.12)$$

Thus, the *parallel transporter* function $U(x,y)$ introduced in Eq. (1.2) and Eq. (1.4), are unchanged and now $U(x,y)$ represents a function which transports a quark field at discrete space-time point $x$ to another discrete space-time point $y$ via a path linking them on the hyper-cubic lattice preserving probability and local gauge invariance. Thus, $U_\mu(x)$ are SU(3) matrices with elements that are bounded in the range $[0,1]$. In lattice terminology, $U_\mu(x)$ are called the *link variables*. The set of all parallel transporter functions on the lattice, $U \equiv \{U_\mu(x)\}$ for all $x$ on a lattice is defined as a *gauge configuration.*

We have defined a discrete space-time lattice with quark fields and link variables with appropriate boundary condition. The next objective is to define a gauge invariant measure on the lattice for integration over the gauge fields, to calculate any observable using Eq. (3.7). From Eq. (3.10), the mapping of $A_\mu(x)$ to $U_\mu(x)$ is continuous and regular, thus on the lattice,

$$\int \mathscr{D}A \equiv \int \prod_{x,\mu} \mathrm{d}U_\mu(x) = \int \mathscr{D}U, \quad (3.13)$$

where the product is over all lattice points $x$ and directions $\mu$. The gauge invariance of this measure, known as the *Haar* measure has been shown rigorously in Ref. [125].

Now we can divide the continuum action into two parts: *fermionic* part ($S_F^E$) and *gauge* part ($S_G^E$). We discuss different types of discretization schemes for the fermionic and gluonic(gauge) actions in the subsequent sections and dropping the superscript $E$ for Euclidean action.

### 3.2.1 Wilson Discretization

The gauge part can be written using Eq. (1.8) as,

$$S_{G,\text{Wilson}}[U] = \beta \sum_x \sum_{1\le\mu<\nu\le 4} \text{Re}\left[\text{Tr}(\mathbb{I} - \frac{1}{3}U_{\mu\nu}(x))\right], \tag{3.14}$$

where $U_{\mu\nu}(x) \equiv U_{\square}(x;\mu,\nu)$ and $\beta = 6/g^2$. $S_{G,\text{Wilson}}[U]$ is called the *Wilson plaquette* [251] gauge action. In principle, one can omit the $\mathbb{I}$ matrix in front, as it has no impact on the dynamics or the expectation values of the observable. For this discretization of gauge action, it has been shown that the physical states are positive and there exists a positive self-adjoint transfer matrix [169]. Also, in the infinite volume limit at strong coupling, the existence of a mass gap was shown in Ref. [201].

Now for the fermionic action, we use the definition in Eq. (1.3) as the forward *covariant* derivative, and similarly define a backward derivative to write the naive gauge invariant action as the central derivative,

$$S_{F,\,naive}[\psi,\bar{\psi},U] = a^4 \sum_{x,x'} \psi(x)\mathbb{M}(x,x')\psi(x'), \tag{3.15}$$

$$\text{where } \mathbb{M}(x) = \sum_{\mu=1}^{4} \gamma_\mu \frac{U_\mu(x)\delta_{x,x+\hat{\mu}} - U_{-\mu}(x)\delta_{x,x-\hat{\mu}}}{2a} + m.$$

It is useful to study some of the properties of this definition by taking the $U\mu(x) = 1$, i.e. for the case of free fermions. In this case we can perform the Fourier transform of $\mathbb{M}(x)$ to obtain $\tilde{\mathbb{M}}(p)$;

$$\tilde{\mathbb{M}}(p) = m + \frac{i}{a}\sum_{\mu=1}^{4} \gamma_\mu \sin(p_\mu a). \tag{3.16}$$

We can know invert to obtain the quark propagator and take the chiral and continuum limits($m = 0$ and $a \to 0$);

$$\tilde{\mathbb{M}}(p)^{-1}|_{m=0} = \frac{-ia^{-1}\sum_\mu \gamma_\mu \sin(p_\mu a)}{a^{-2}\sum_\mu \sin(p_\mu a)^2}. \tag{3.17}$$

We observe that this definition of the discrete fermion matrix yields 16 poles instead of 1. This lattice artifact is known as the *Fermionic doublers.* In order to solve this, Wilson [251, 252] proposed to add one additional term to Eq. (3.16) which doesn't contribute to the pole at $p = 0$, thus retaining the physical pole, but which induces a mass to the other 15 poles which goes to infinity as $a \to 0$, thus decoupling them in the continuum. In position space,

the Wilson action becomes,

$$S_{F,\,\text{Wilson}}[\psi,\bar{\psi},U] = a^4 \sum_{x,x'} \psi(x)\mathbb{M}(x,x')\psi(x') \tag{3.18}$$

$$\mathbb{M}(x,x') = -\frac{1}{2a}\sum_{\mu=\pm 1}^{\pm 4}(1-\gamma_\mu)U_\mu(x)\delta_{x+\hat{\mu},x'} + (m+\frac{4}{a})\delta_{x,x'}$$

where $\gamma_{-\mu} = -\gamma_\mu$,

$$\tilde{\mathbb{M}}(p)_{\text{Wilson}} = m + \frac{i}{a}\sum_{\mu=1}^{4}\gamma_\mu \sin(p_\mu a) + \frac{1}{a}\sum_{\mu=1}^{4}(1-\cos(p_\mu a)). \tag{3.19}$$

Now we have Wilson action for flavor $f$ as,

$$S_{\text{Wilson}} = S_{F,\text{Wilson}} + S_{G,\text{Wilson}}$$

### 3.2.2 Symanzik Improvement

The discretization artifacts in the Wilson action are, $\mathcal{O}(a)$ in $S_{F,\text{Wilson}}$ and $\mathcal{O}(a^2$ in $S_{G,\text{Wilson}}$. A systematic reduction of discretization errors by adding extra terms is called *Symanzik Improvement program* [233, 231, 230, 232]. Following the Symanzik improvement scheme, an irrelevant term, the so-called *clover term* is added to the Wilson action in such a way that discretization errors to $\mathcal{O}(a)$ cancel.

#### Wilson-clover

In order to have a $\mathcal{O}(a)$ improvement for the fermionic action, we add the following term,

$$S_{\text{Im},F} = S_{F,\,\text{Wilson}} + c_{SW}a^5\sum_x\sum_{\mu<\nu}\bar{\psi}(x)\frac{1}{2}\sigma_{\mu\nu}\hat{F}_{\mu\nu}(x)\psi(x) \tag{3.20}$$

where $c_{SW}$ is called the *Sheikholeslami–Wohlert coefficient* [220] where the improved action was obtained. Here $\hat{F}_{\mu\nu}$ is the gluon field strength tensor and $\sigma_{\mu\nu} = [\gamma_\mu,\gamma_\nu]/2i$. One possible definition of $\hat{F}_{\mu\nu}$ according to Ref. [110] is:

$$\hat{F}_{\mu\nu}(x) = -\frac{i}{8a^2}(Q_{\mu\nu}(x) - Q_{\nu\mu}(x)) \tag{3.21}$$

where $Q_{\mu\nu}(x)$ is,

$$Q_{\mu\nu}(x) = U_{\mu,\nu}(x) + U_{\nu,-\mu}(x) + U_{-\mu,-\nu}(x) + U_{-\nu,\mu}(x). \tag{3.22}$$

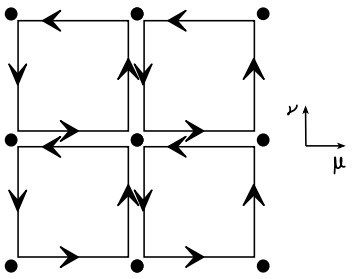


Fig. 3.1 Geometric representation of the clover term in terms of gauge links where the link variables are depicted by arrows, and the direction of arrows represent the direction of the link variables. Each dot represent the fermions on the lattice.

The geometric shape of this object resembles a *clover* leaf as shown in Fig. (3.1) so it is called *clover-improvement*. The value of $c_{SW}$ requires tuning to achieve $\mathscr{O}(a)$ improvement. A general scheme for constructing $\mathscr{O}(a^n)$ improvement without any doubling, based on the principles of dimensionality of the lattice operators was given by Lüscher and Weisz in Ref. [172] which is called *on-shell improvement*.

On-shell improvement $\mathscr{O}(a^2)$ for the gauge action can be achieved by including 6-link Wilson loops[1] along with the 4-link plaquette in Eq. (3.18).

$$S_{\mathrm{Im},G} = \beta \left[ \frac{c_0}{3} \sum_x \sum_{1\le\mu<\nu\le 4} \mathrm{Re\ Tr}(1 - U_{\mu\nu}(x)) + \frac{c_1}{3} \sum_x \sum_{1\le\mu<\nu<\delta<\gamma\le 6} \mathrm{Re\ Tr}(1 - U_{\mu\nu\delta\gamma}(x)) \right] \tag{3.23}$$

The values of $c_0$ and $c_1$ [172] are set to their tadpole-improved tree level values [157, 156].

$$c_1 = \frac{-1}{(12u_0^2)}, \qquad c_0 = \frac{5}{3}, \qquad c_{\mathrm{SW}} = \frac{1}{\tilde{u}_0^2}\,. \tag{3.24}$$

Here $u_0$ is the 4th root of the plaquette of the unsmeared gauge fields, and $\tilde{u}_0$ is the 4th root of the plaquette plaquette after stout smearing (discussed later in Sec. 4.5.2). It is found that $\tilde{u}_0$ is close to unity, which indicates that the tadpole-corrected tree-level value for $c_{\mathrm{SW}}$ is close to the non-perturbative value that gives full $\mathscr{O}(a)$ improvement. This has also been confirmed using preliminary non-perturbative determinations of $c_{\mathrm{SW}}$ using the Schrödinger functional method [224, 170].

### 3.2.3 Other discretization schemes

Apart from Wilson-clover, there are other discretization schemes namely,

[1] A closed loop $\mathscr{L}$, with $n-2$ spatial link variables and 2 temporal link variable, $W_n \equiv \mathrm{Tr}\left[\prod_{(x,\mu)\in\mathscr{L}} U_\mu(x)\right]$

- Overlap action [193–196]: This formulation is constructed to preserve chiral symmetry[2] on the lattice and by definition gauge covariant and without any fermionic doublers. It provides automatic $\mathcal{O}(a)$ improvement in the action. Since the definition of the operator is not ultra-local, there are many numerical challenges in simulating overlap fermions as discussed in Refs. [148, 143].

- Domain Wall action [146, 217, 109, 218]: This formulation constructs fermions on the 4-D interface of a 5-D lattice which becomes chiral in the limit of infinite 5-th dimension. Numerical simulations using Domain Wall fermions have been implemented in Ref. [15].

- Twisted mass action [101–103, 225, 221]: This formulation is defined with two mass-degenerate quark flavors of Wilson fermions and an additional mass term which breaks the isospin symmetry between $u$ and $d$ quarks which importantly serves as an infrared regulator to remove exceptional configurations. The definition also provides automatic $\mathcal{O}(a)$ improvement on its operators. Numerical simulations using twisted mass fermions at the physical point have been achieved for two flavors of degenerate light quarks ($N_f = 2$) in Ref. [3] and using in addition strange and charm quarks ($N_f = 2+1+1$) in Ref. [10, 98].

**Symmetries on the lattice**

After discussing different discretization schemes, we need to evaluate which symmetries are preserved from the continuum and their consequences. Symmetries determine the universality class of the discretized actions, and observables calculated using different actions but within the same universality are expected to yield similar results when $a \to 0$. The discretized action in all schemes except for twisted mass discretization satisfies all these discrete symmetries: charge conjugation ($\mathscr{C}$), parity ($\mathscr{P}$), time-reversal ($\mathscr{T}$), isospin symmetry ($m_u = m_d$) and also local gauge symmetry by definition. In the twisted mass action, all symmetries except parity and isospin symmetry are conserved, but these symmetries are restored in the continuum limit. Apart from these symmetries, chiral symmetry which is an approximate symmetry in the continuum at finite quark mass is satisfied by certain discretization schemes.
An essential symmetry that is not preserved upon discretization is the angular momentum symmetry SU(2) (double cover of SO(3)) which includes half-integer spin representations). This complicates the definition of spin on the lattice. The consequence of this broken symmetry has been discussed in detail in the next chapter.

[2]Chiral symmetry is an approximate symmetry of the QCD Lagrangian, in which quarks are taken to be massless.

### 3.2.4 Observables on the lattice

The expression for the observables $\hat{O}$ as defined in Eq.(3.7), on the lattice can be written as,

$$\langle \hat{O} \rangle = \frac{1}{\mathscr{Z}} \int \mathscr{D}U \mathscr{D}\psi \mathscr{D}\bar{\psi}\, O[\psi, \bar{\psi}, U]\, e^{-S_{QCD}[\psi,\bar{\psi},U]} \tag{3.25}$$

in which the integral over the fermionic fields can be performed using Grassmann calculus.

#### Grassmann calculus

Grassmann variables ($\bar{\psi}$, $\psi$) are defined by the following algebra,

$$\{\psi_i, \psi_j\} = 0, \tag{3.26}$$

which is appropriate for representing the anti-commuting fermionic fields. In Grassmann calculus, using the *Mathews-Salam* formula [176, 175] we can perform Gaussian integrals over Grassmann variables, such as:

$$\int \mathrm{d}\psi \mathrm{d}\bar{\psi}\, e^{i\int d^4x\, \bar{\psi}\mathbb{M}\psi} = \det(\mathbb{M}), \tag{3.27}$$

which we use to write the expectation value of a physical observable $\hat{O}[U]$ (which is only a function of gauge fields), as,

$$\langle \hat{O} \rangle = \frac{1}{\mathscr{Z}} \int \mathscr{D}U\, O[U]\, e^{\ln[\det(\mathbb{M}(U))] - S_{\mathrm{Im},G}}. \tag{3.28}$$

If the observable is a function of fermionic fields (Grassmann variables), it can written as a product of equal number of fermionic ($\psi_{i_1}\psi_{i_2}\cdots\psi_{i_n}$) and anti-fermionic fields ($\bar{\psi}_{j_1}\bar{\psi}_{j_2}\cdots\bar{\psi}_{j_n}$), then using Wick's theorem we can write,

$$\begin{aligned}\left\langle \psi_{i_1}\overline{\psi}_{j_1}\ldots\psi_{i_n}\overline{\psi}_{j_n}\right\rangle_F &= \frac{1}{Z_F}\int \prod_{k=1}^{N} \mathrm{d}\psi_k \mathrm{d}\overline{\psi}_k\, \psi_{i_1}\overline{\psi}_{j_1}\ldots\psi_{i_n}\overline{\psi}_{j_n} \exp\left(\sum_{l,m=1}^{N}\overline{\psi}_l \mathbb{M}_{lm}\psi_m\right) \\ &= (-1)^n \sum_{P(1,2,\ldots,n)} \mathrm{sign}(P)\left(\mathbb{M}^{-1}\right)_{i_1 j_{P_1}}\left(\mathbb{M}^{-1}\right)_{i_2 j_{P_2}}\cdots\left(\mathbb{M}^{-1}\right)_{i_n j_{P_n}}\end{aligned} \tag{3.29}$$

where the sum in the second line runs over all permutations $P(1,2,3,\cdots,n)$ of the numbers $1,2,3,\cdots,n$, and $\mathrm{sign}(P)$ is the sign of the permutation $P$. This combination of fermionic fields is defined as the contraction of fermionic fields, thus, one can substitute the time-ordered product of fermionic fields in the operator $\hat{O}$ with suitable factors of $\mathbb{M}^{-1}$ which no

longer depend on $\psi$, $\bar{\psi}$. In the subsequent chapters, we will be using $S_{\mathrm{Im}} = S_{\mathrm{Im},F} + S_{\mathrm{Im},G}$, and denote it with just $S$.

## 3.3 Lattice Simulations

In this section, we briefly discuss the general principles of developing algorithms used in lattice simulations.

### 3.3.1 Monte Carlo

The integral over link variables defined in Eq. (3.28), whose measure is defined in Eq. (3.13), is a high dimensional integral, which can be approximated by a Monte Carlo integration weighted by *importance sampling*:

$$\langle O \rangle = \lim_{N\to\infty} \frac{1}{N} \sum_{n=1}^{N} O[U_n], \tag{3.30}$$

with each $U_n \equiv \{U_\mu^n(x) \,|\, \forall x \in \Lambda, \text{and } 1 \leq \mu \leq 4\}$ being a gauge configuration (which is a set of all parallel transporters defined on the lattice $\Lambda$) sampled according to the probability distribution density,

$$\mathrm{dP}(U) = \frac{e^{-S[U]}\mathscr{D}U}{\int \mathscr{D}[U] e^{-S[U]}}, \tag{3.31}$$

the so-called *Gibbs measure*. The gauge field configurations $U_n$ are our random variables. In order to generate gauge configuration with the probability density defined in Eq. (3.31), we use the idea of Markov chains.

#### Markov Chain

A Markov Chain Monte Carlo is a stochastic process in which a finite set of configurations $U_{\tau_1}, U_{\tau_2}, \cdots$ is generated sequentially according to some transition probability $P_{ij} = P(U_i \to U_j)$. The state of the system at any given simulation time $\tau_i$ will be a multi-dimensional random variable, whose distribution depends only on the preceding state, i.e $P_{ij}$ depends only on the state $U_i$. A set of configurations generated in this way is called a Markov chain. Monte Carlo integration with importance sampling preferentially chooses configurations that have a strong weight. At the same time, it is assured that the sample average estimates the ensemble average. This means that the sample is representative of the ensemble.

One important restriction on transition probability in Markov chain Monte Carlo is, that it must satisfy the so-called *detailed balance* condition,

$$e^{-S(U)}P(U \to U') = e^{-S(U')}P(U' \to U). \tag{3.32}$$

There are many algorithms which satisfy this condition, one of which is the *Metropolis* algorithm, which is given by,

1. Choose an arbitrary test configuration $U$.

2. Accept the configuration $U'$ as a successor of configuration $U$ with probability,

$$P(U \to U') = \begin{cases} \frac{e^{-S(U')}}{e^{-S(U)}} & \text{if } e^{-S(U')} < e^{-S(U)} \\ 1 & \text{else} \end{cases} \tag{3.33}$$

   This step is called the Metropolis accept/reject step. Since the probability of transition to a configuration $U'$ is not 0, it ensures *ergodicity*.

Furthermore, there are advanced algorithms like Hybrid Monte Carlo [84], Langevin, Multi-Boson, Over-relaxation and Microcanonical which optimize the step 1, by choosing a new $U'$ such that it improves computation of step size of the Markov chain and reduce auto-correlation. These algorithms require the next Metropolis step to satisfy Eq. (3.32). Apart from Metropolis, there are algorithms like the Heat Bath which combines steps 1 and 2 to improve the acceptance rate by redefining $U'$ in a way which already satisfies Eq. (3.32).

### 3.3.2 Solvers

As discussed in Sec. 3.2.4, $\mathbb{M}^{-1}$ i.e. the quark propagator, is required to calculate the contractions of the fermionic fields in the observable $O$. In Eq. (3.20), we can define Wilson Dirac operator $D$ [3], such that $D = a^4\mathbb{M}$. Thus, we need to solve:

$$D(U)x \;=\; b \tag{3.34}$$

The solution $x$ is desired for an appropriately defined $b$ and gauge configurations $U$. Given the sparsity and dimensions of $D$, it is only feasible to consider iterative solvers for the problem.

Typically iterative Krylov solvers such as Conjugate Gradient (CG), Bi-conjugate gradient (BiCGstab), Generalized Conjugate residual (GCR) are used to solve Eq. (3.34) to reach to a

[3] This is the most commonly used notation in the community

solution upto a predefined tolerance. The solution after $n$th iteration belongs to $n$-dimensional Krylov subspace $\mathscr{K}_n$ spanned by

$$b, Db, D^2b, \cdots, D^{n-1}b.$$

It has been proven that the solution of a typical non-singular $N \times N$ matrix $D$, belongs to $\mathscr{K}_N$. A generic iterative Krylov solver builds up this space explicitly or implicitly in order to reach to a solution of desired tolerance defined by the ratio of the norms of its residual $r_n = b - Dx_n$ calculated after $n$ iterations and the right-hand side $b$. In each step $x_n$ is chosen such that it minimizes the norm of the residual. Different methods vary by different definitions of the norm. Furthermore, these iterative methods for Dirac propagator are implemented on the normal equations which is, $(DD^T)y = b$ with $x = y^T b$ or normal residuals $(D^T D)x = \tilde{b}$ with $\tilde{b} = D^T b$.

But all these methods suffer from the condition of *critical slowing down*. Critical slowing down can be explained as: the condition number $\kappa(D) \equiv ||D|| \cdot ||D^{-1}||$ is proportional to $(am)^{-1}$, thus, making the operator ill-conditioned as $a \to 0$ (continuum limit) and $m \to 0$ (chiral limit), which jeopardizes application of any iterative method directly to invert $D$ close to or at the physical point as shown in Fig. 3.2. Furthermore, one of the most computationally expensive steps is the calculation of the *matrix-vector product* for a large matrix such as the Dirac operator, Krylov solvers also suffer from the repeated computation of this matrix-vector product as shown in Fig. 3.3.

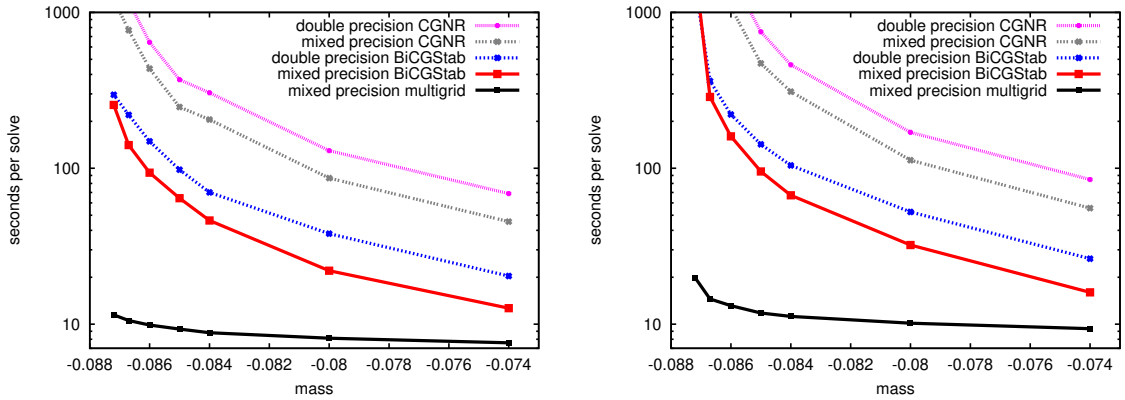


Fig. 3.2 Time to solution (in seconds) for a single solve versus quark mass for various Krylov solvers and multigrid. The left plot is for the $24^3 \times 128$ lattice and the right is for $32^3 \times 256$. *Fig credits* [199]

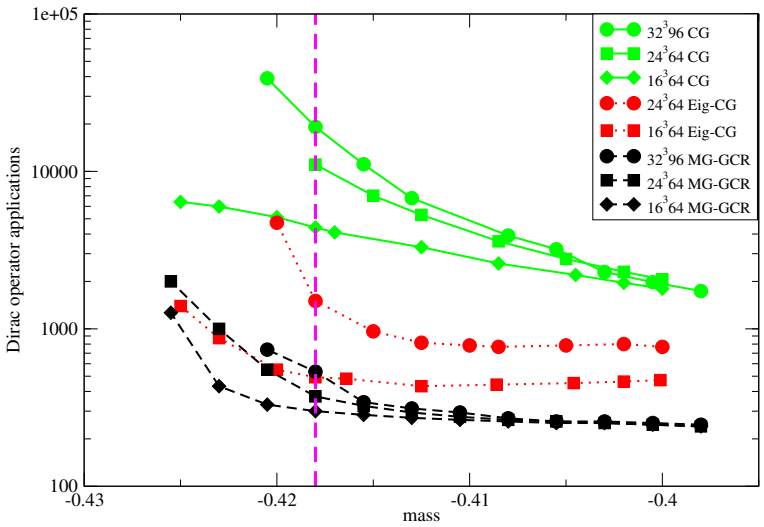


Fig. 3.3 Comparison of the total number of Wilson matrix-vector operations until convergence for CG, Eig-CG [226] and MG-GCR *Fig credits* [24]

.

In order to overcome these problems of the direct application of Krylov solvers on a lattice, multigrid preconditioners [199][4] are used which involve application of different Krylov subspace solvers with low tolerances to different coarse-grain sizes of the same lattice, thus obtaining an approximate solution which is then used to define the preconditioner of the Wilson-Dirac operator. In a nutshell, it can be understood as solving for low frequency (slowly converging) eigen modes of the Wilson-Dirac operator on a coarse grid with high tolerance (such that it converges relatively faster) and this solution is then relaxed onto the actual fine grid which is used to define a preconditioner for solving for high frequency (fast converging) eigen modes using a different Krylov subspace solver with a low tolerance; this process is repeated over and over again till convergence [24]. Figures 3.2, 3.3 and 3.4 illustrate the advantage of using this multigrid preconditioner over conventional Krylov subspace methods.

[4] A preconditioner $P$, for a system $Ax = b$ is defined as $AP^{-1}Px = b$,where $AP^{-1}$ is the preconditioner operator, and we solve for $Px$ instead of $x$.

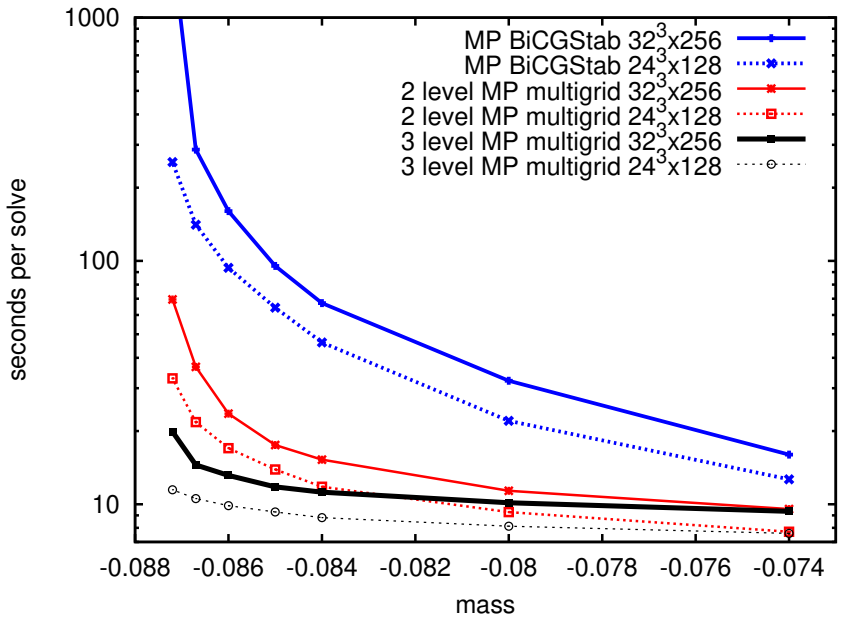


Fig. 3.4 Comparison of 2 and 3-level Multigrid over standard Krylov solvers for 2 lattice sizes. *Fig credits* [199]

### 3.3.3 Error estimates

In lattice Monte Carlo simulations, the sources of errors can be primarily divided into two categories:

- Systematic error: In general can't be computed, but can be estimated. The origin of these errors can be attributed to the following:
  - Chiral Extrapolation: This arises due to unphysical quark masses in the simulation, the results from which need to be chirally extrapolated to physical quark masses. Simulating at larger than physical quark masses is computationally cheaper, which is why in the past chiral extrapolations have been a source of systematic error. This has been eliminated in recent simulations directly at the physical point.
  - Lattice Discretization: To estimate the effect of lattice discretization, one needs to calculate the observable using configurations generated from simulations with different lattice spacings. Nowadays with the advent of exact algorithms and Symanzik improvement programs, there is a methodical way to estimate these effects.

- Finite volume: This effect could be attributed to the interaction of a particle with its neighboring images(due to periodic boundary conditions). For large $L$ and $T$, this interaction is mediated by pion exchange, therefore it is reasonable to compare the correlation length of the pion, $1/m_\pi$ to the spatial ($L$) and temporal ($T$) extent of the lattice. For $T/m_\pi \sim L/m_\pi >> 1$, it has been shown in Ref. [172] that the finite volume effects are exponentially suppressed. Thus, this source of error can be estimated by calculating the observable in simulations with different volumes of the box. One interesting remark would be, the idea of estimating the volume dependence of correlation functions on the lattice, led to the formulation of theory for studying resonances on the lattice [172, 171, 173].
- Excited state effects: In the subsequent chapter, the methodology for extracting ground states from correlation functions have been discussed using exponential fits to functions at $t \to \infty$. If the ground state has excited state contamination then the single exponential fits will result in high $\chi^2$ values. It will be observed that we need multi-exponential fits and variational method with different smeared interpolators for the same particle to extract its ground state with negligible excited state effects.

- Statistical errors: Statistical errors arise from the variance in the value of the observable over the Markov Chain, due to the statistical nature of Monte Carlo. These errors depend on the number of gauge ensemble used and can be calculated exactly. In a Markov Chain Monte-Carlo simulations, since the gauge configuration at a particular Monte Carlo time $t$ is generated by modifying the gauge configuration at a previous Monte Carlo time $t_0$, there is an autocorrelation between these two configurations. Monte Carlo time-dependent autocorrelation for an observable $O$ is computed by,

$$C_O(t) = \frac{\langle O(t_0)\, O(t_0+t)\rangle - \langle O(t_0)\rangle \langle O(t_0+t)\rangle}{\langle O^2(t_0)\rangle - \langle O(t_0)\rangle^2} \tag{3.35}$$

  For practical purposes, we need the integrated autocorrelation time, to calculate the degree of correlation between the configurations generated in the lattice simulations, which is given by,

$$\tau^{\text{int}}_{\text{auto}} = \frac{\sum_{t=1}^{\infty} \left(\langle O(t_0)\, O(t_0+t)\rangle - \langle O\rangle^2\right)}{\langle O^2\rangle - \langle O\rangle^2} \tag{3.36}$$

  Now, we describe a method of data analysis which takes into account these autocorrelation effects while computing an observable $O$.

**Jack-knife error estimation**

Given an observable $O$ with $N$ gauge configurations, the most common and effective way which takes into account autocorrelation, to estimate its error is through *jackknife* resampling. In this method, *binning* is used to construct blocks of data in direction of evolution of Monte-Carlo time, with bin-size $B$. The $N$ samples are divided into $N_B$ blocks of bin-size $B$. The block estimators are

$$o_k = \frac{1}{B}\sum_{i=1}^{B} O_{(k-1)B+i} \;\; (k = 1, \cdots, N_B) \tag{3.37}$$

The bin-width should exceed the autocorrelation time of the observable to ensure that the $N_B$ can be treated as uncorrelated. The jackknife-based variance of the mean is given by,

$$\sigma^2_{jack} = \frac{N_B - 1}{N_B}\sum_{k=1}^{N_B} [\tilde{o}_k - \bar{O}]^2, \tag{3.38}$$

where $\bar{O} = \frac{1}{N}\sum_{i=1}^{N} O_i$ is the mean of $O$ over $N$ measurements, and $\tilde{o}_k = \frac{1}{N-B}\left(\sum_{i=1}^{N} O_i - B\, o_k\right)$.

In recent years, there have been a few developments towards the application of machine learning algorithms in lattice QCD aiming to reduce the computational cost and minimize the sources of error in calculating observables on the lattice [255, 219, 7]. In the first attempt towards this direction, we have implemented a machine learning model to study the physics of an Ising spin system. As Ising is a simple statistical physics system, it serves an ideal testing ground for the development of new lattice techniques, which can later be extended to lattice QCD. In the next section, we briefly summarize our effort in this direction.

## 3.4 Machine Learning techniques for the study of statistical systems

### 3.4.1 Introduction

Machine learning (ML) has been recently used as a very effective tool for the study and prediction of data in various fields of physics, from statistical physics to theoretical high energy physics. Numerical data from Lattice Field Theory can be studied using all three types of ML models: Supervised [57, 256, 189], Unsupervised and Self-Learning. Examples in supervised ML are classification tasks with Support Vector Machines (SVMs) or (convolutional) Neural Networks applied to the discovery of phase transitions. For unsupervised

learning, examples such as Principal Component Analysis (PCA) [244, 238, 137, 246, 99], Restricted Boltzmann Machines (RBMs) [75, 108] and Autoencoders are used to gain insights on the phase diagram of lattice models and discover parameters of fundamental Hamiltonians. Self-learning policies are also applied to Monte Carlo methods to improve statistical sampling for physics formulated on lattices. Very recently, similar studies have been applied for simulations of quantum fields on the lattice, such as the $SU(2)$ gauge theory [247] with increased complexity in the data due to the structure of the $SU(2)$ gauge group. Within the broader effort for the investigation of forward looking applications for the study of statistical systems, such as Lattice Field Theories, using machine learning, part of this thesis was devoted to the application of unsupervised learning for the study of phase transitions, with specific application in the Ising model. The study is presented in what follows, and is based on the following publication:

- C. Alexandrou, C. Chrysostomou, A. Athenodorou, **S. Paul** "Unsupervised identification of the phase transition on the 2D-Ising model," [arXiv:1903.03506v1][8]

### 3.4.2 The Ferromagnetic 2-Dimensional Ising Model

The general Hamiltonian of 2-D Ising model on the spin configurations is given by,

$$H = -J \sum_{i,j=nn(i)}^{N} s_i s_j - \mu h \sum_{i=1}^{N} s_i \,, \tag{3.39}$$

where $J$ is the self-interaction between neighbouring spins, $h$ the external magnetic field and $\mu$ is the atomic magnetic moment. Note that in the first sum, the notation $nn(i)$ represents nearest-neighbour pairs; the sum is taken over all nearest-neighbouring pairs.

#### Swendsen-Wang algorithm

The MC simulation for the 2D-Ising model is conventionally performed using the Metropolis algorithm. Since this algorithm is based on local updates, near the critical temperature where the correlation length diverges, it faces the problem of critical slowing down. In order to tackle this problem, we have implemented the Swendsen-Wang cluster algorithm [229, 243], which is based on global updates of the spin configurations. This algorithm relies on the formation of bonds between every pair of nearest neighbours$(ij)$ that are aligned at a given temperature $T$, with a probability $p_{ij} = 1 - \exp(-2\beta J)$, where $\beta = \frac{1}{k_B T}$ ($k_B \equiv$ Boltzmann constant). A single cluster is defined as all the spins, which are connected via bonds. The global update is defined as the collective flipping with a probability of $1/2$, on all the spins in

each cluster [147, 100]. This step works because of the so-called Fortuin-Kasteleyn mapping of the Ising model on the random-cluster model. Thus, global updates enable us to produce equilibrium configurations close to the $T_c$ with a few thermalization steps.

### Monte-Carlo simulation setup

In this study, we chose to investigate the case of zero external magnetic field ($h = 0$) and for simplicity, we have set $J = 1$ and $k_B = 1$. In this case, the theoretically calculated value of the critical temperature is

$$T_c = \frac{2}{\ln\left(1+\sqrt{2}\right)} = 2.269185\,. \tag{3.40}$$

To extract experimentally this quantity one has to investigate the order parameter of theory, namely the magnetization. The first question that we address is whether we can get an approximate estimate of this temperature by using unsupervised learning. To this purpose, we choose a sequence of different values of temperature, and for each one, we start from a frozen configuration of spins, perform a large enough number of thermalization sweeps and then save the configuration. For every single temperature, we repeat the procedure 200 times.

### Phase structure, observables and order parameters

The phase structure of the 2D-Ising model can be reduced to the study of the magnetic order of the system [62]. If we suppose that there are $N_\uparrow$ spins pointing upwards and $N_\downarrow$ spins pointing downwards, then the total magnetic moment would be $N_\uparrow - N_\downarrow$ ($\mu = 1$). The largest possible magnetic moment would, therefore, be $N$. Thus, we can define the magnetic order parameter or magnetization per spin configuration naturally as:

$$m = (N_\uparrow - N_\downarrow)/N\,, \tag{3.41}$$

while the average magnetization $M = \langle m \rangle$. $M$ can get values between $-1$ and 1, and the average of the absolute magnetization $\tilde{m} = \langle |m| \rangle$ is just the magnetic order. Hence, if $\tilde{m}$ is close to 0, then the system is highly disordered and, thus, not magnetised, with approximately half of the spins pointing up and the other half pointing down. On the other hand, if $\tilde{m}$ is approximately 1, the system is ordered and, thus, magnetised with nearly all the spins pointing in the same direction.

The point $T = T_c$ is called the *critical point* and separates the ordered $T < T_c$ phase and disordered $T > T_c$ phase. At $T = T_c$ the system is described by a second order phase transition, i.e. *à la* Ehrenfest [141] the first derivative of the free energy with respect to the external field which is the order parameter is continuous while the second derivative of the free energy is discontinuous.

### 3.4.3 Deep Learning Autoencoders

Autoencoders are a variety of artificial neural networks utilized for learning data codings in an unsupervised manner, efficiently [240, 241]. An autoencoder aims to define a representation (encoding) for an assemblage of data, usually performing dimensionality reduction. An autoencoder encodes the input data ($\{X\}$) from the input layer into a latent dimension ($\{z\}$), and then uncompresses that latent dimension into an approximation of the original data ($\{X\}$). This drives the autoencoder to engage in dimensionality reduction, by learning how to ignore the noise and recognise significant characteristics of the input data. The first layer of an autoencoder might learn to encode simple, identifiable and local features, and the second layer by using the output of the first layer learns to encode more complex and less local features, until the final layer of the encoder learns to identify and encode the most complex and global characteristics of the input data. As Fig. 3.5 shows, an autoencoder consists of two components, the encoder function $g_\phi$ and a decoder function $f_\theta$ and the reconstructed input is $X = f_\theta(g_\phi(x))$.

In the training phase, the autoencoder learns the parameters $\phi$ and $\theta$ together, where $f_\theta(g_\phi(x))$ can approximate an identity function. Various metrics can be used to measure the error between the original input $X$ and the reconstruction $\tilde{X}$, but the most simple and most commonly used is the Mean Square Error (MSE) as this is provided in Eq. 3.42, where $n_{\text{data}}$ is the number of data points:

$$MSE(\theta,\phi) = \frac{1}{n_{\text{data}}} \sum_{i=1}^{n_{\text{data}}} (X_i - f_\theta(g_\phi(X_i)))^2 . \tag{3.42}$$

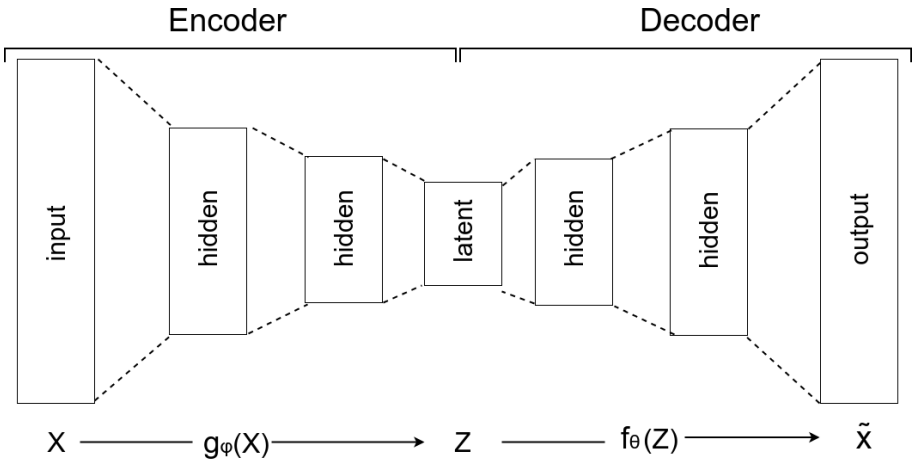


Fig. 3.5 Basic structure of an autoencoder

**Proposed Autoencoder Model**

For the analysis of the proposed method, an eight-layer, fully connected (Dense), autoencoder is proposed, as Fig. 3.6 shows, where the encoder compresses the configurations into a single latent dimension. Through experimentation, we determine that the best model to detect the transition consists of the encoder with the input layer, first, second and third hidden layers having 625, 256, 64 and 1 neurons, respectively. The activation function used is relu, as shown in Eq. 3.43, for all layers except the third hidden layer, where tanh was used, as shown in Eq. 3.44. For the decoder, the first, second and third hidden layers use 64, 256, and 625 neurons, respectively. For the output layers, the number of neurons is set to be equal to the number of values in the configuration under investigation. The activation function used is relu, as given in Eq. 3.43, for all hidden layers, and for the output layer, tanh is used, as per Eq. 3.44.

$$\text{relu} : y = max(0,x) = \left\{ \begin{array}{ll} x, & \text{if } x > 0 \\ 0 & \text{if } x \leq 0 \end{array} \right\}. \tag{3.43}$$

$$\tanh : y = \frac{1-e^{-2x}}{1+e^{-2x}}. \tag{3.44}$$

For the proposed autoencoder model we use the so-called dropout realization technique [132]. The dropout regularization technique refers to dropping out neurons from each layer, randomly, when training. Dropout is successfully used for reducing over-fitting in neural networks by preventing complex co-adaptations on training data. For the training of the proposed autoencoder model the data are split into training (66.66...%) and testing (33.33...%) sets, and the training is performed for 2000 iterations. The implementation was performed using Keras [65] and Tensorflow [2].

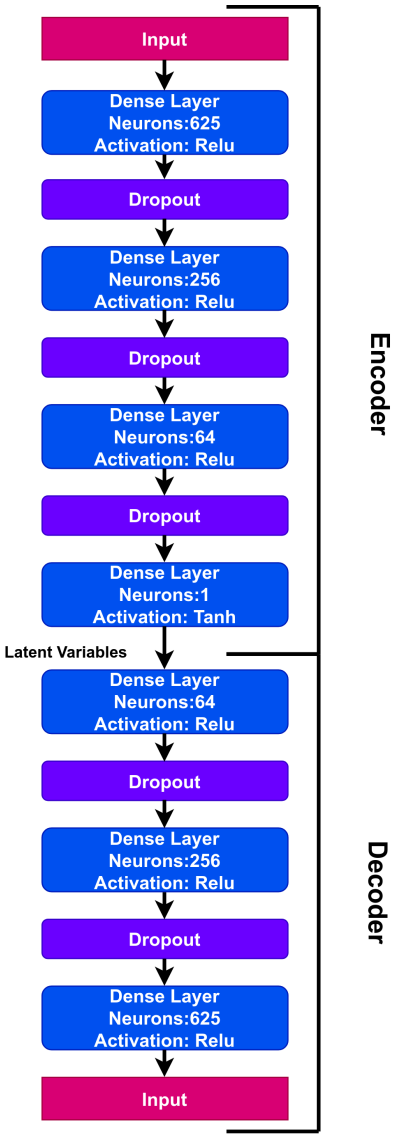


Fig. 3.6 Proposed autoencoder model in the standard Machine Learning nomenclature.

### 3.4.4 Results

### 3.4.5 The latent dimension per configuration

Each configuration is re-expressed in the form of a vector, and then it is read as an input by the autoencoder. One can think of the input as a column with entries of 1 and -1, placed in some lexicographic order and having a length equal to $L^2$. More precisely, for each different lattice size $L = N_x = N_y$ we feed to the network all the configurations produced for all different temperatures, and we extract the latent dimension $z_{i_{\text{conf}}}$. In other words, each

configuration is assigned a number, the latent dimension, which includes all the physically necessary information so that the decoder re-creates the actual configuration. It should be made clear that configurations for different lattice volumes have been fed separately into the autoencoder, i.e. the autoencoder receives information for only one lattice volume, and thus, it "knows" nothing about configurations produced for other volume sizes.

In order to identify signals of the phase structure of the 2D-Ising model, as a first step, we investigate how the latent dimension $z_{i_{\text{conf}}}$ behaves as a function of the temperature $T$ for each configuration. We produce 40000 configurations, namely 200 configurations for every single temperature. The produced configurations are for 200 different values of temperatures within the range $T = 1 - 4.5$ and separated by $\delta T = 0.0175$. We make sure that we cover the whole range of temperatures between the two extreme cases of the Ising behaviour, the nearly "frozen" at $T \simeq 1$, and the complete disordered $T \simeq 4.5$. Furthermore, we assume that we have no prior knowledge of what is happening in between these two extremes. We note that we could choose different temperature ranges that cover all possible phase regions; for instance, we could choose instead $T = 0.01 - 1000$ with $\delta T = 0.01$, but of course, the computational effort would be much more significant.

In Fig. 3.7 we show the latent dimension for each different configuration, as a function of the temperature $T$, for four different lattice sizes, $L = 25, 35, 50, 150$.

### 3.4.6 The absolute average latent dimension

Since the latent dimension per configuration is symmetric with respect to the $T$ axis, it would be reasonable to define the average absolute latent dimension as a parameter indicating the phase as

$$\tilde{z} = \frac{1}{N_{\text{conf}}} \sum_{i=1}^{N_{\text{conf}}} |z_{i_{\text{conf}}}| \, . \tag{3.45}$$

Fig. 3.7 shows that the latent dimension resembles the behaviour of the magnetization per spin configuration as a function of the temperature. The absolute average magnetization defines the order parameter of the system distinguishing the two different phases. For the case of the autoencoder we can define an additional quasi-order parameter as the absolute average latent dimension.

In the left-hand-side of Fig. 3.8 we provide the magnetisation as a function of the temperature while on the right-hand side we provide the absolute latent dimension. Indeed the absolute latent dimension looks similar to the magnetisation, albeit becoming steeper as the lattice size increases. Clearly, the magnetization behaves as an order parameter with

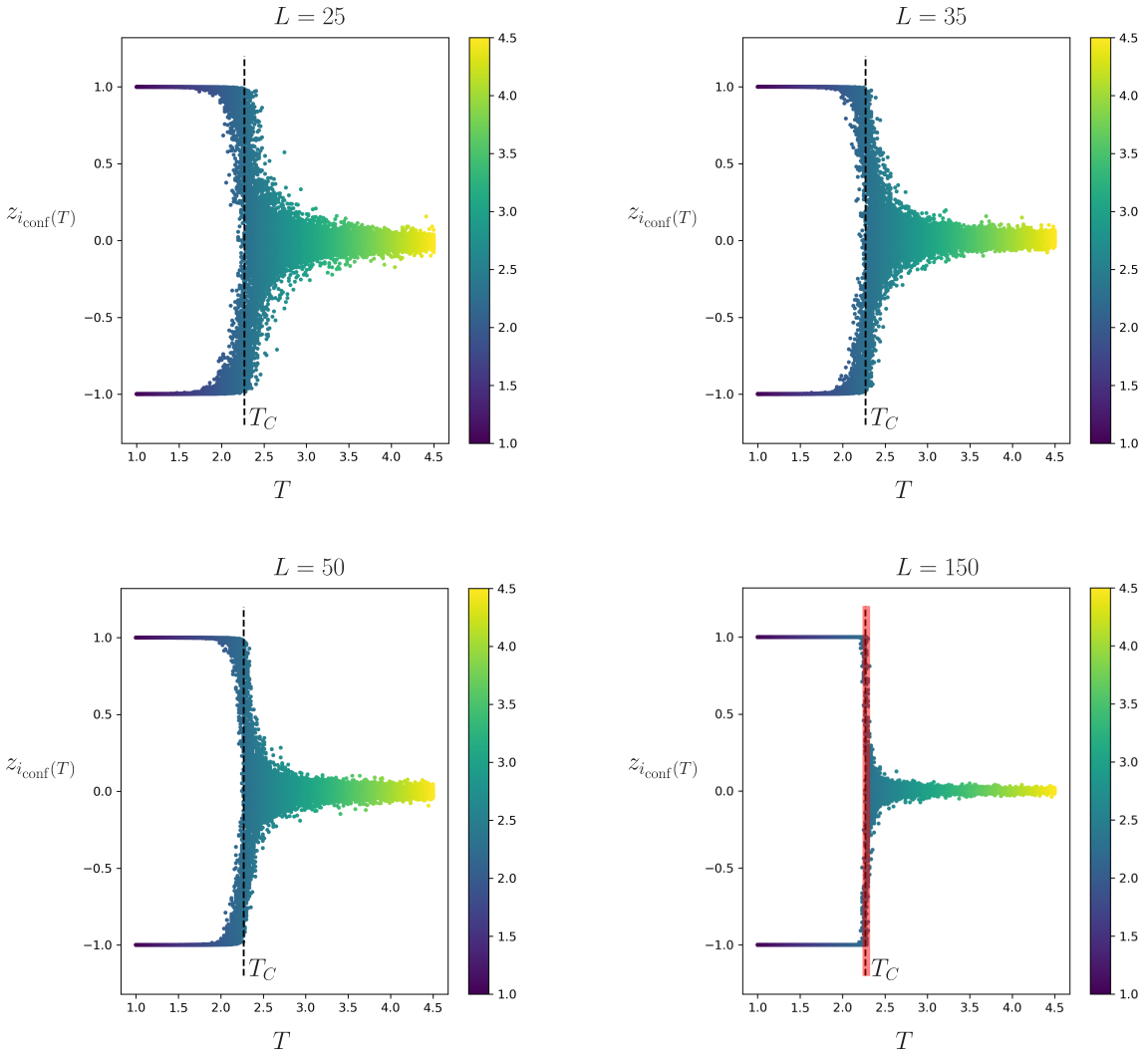


Fig. 3.7 The latent dimension for each configuration as a function of the temperature for four different lattice volumes. The dashed line represents the analytically extracted value of the critical temperature (Eq. 3.40). The red shaded area in the plot for $L = 150$ is the region where (by fitting to a constant) we expect to find the $T_c(L = 150)$. The color on the gradient illustrator on the right denotes the temperature $T$.

the characteristics of a second order phase transition while the absolute latent dimension is consistent with a first order phase transition. We can, therefore, conclude that the absolute average latent dimension can be used as an order parameter to identify the critical temperature, but cannot capture the right order of the phase transition. The fact that $\tilde{z}$ as a function of the temperature becomes steeper as the lattice size increases suggests that the critical temperature $T_c(L)$ as a function of the lattice size $L$ extracted from the autoencoder data will suffer less from finite-size scaling effects. Traditionally, $T_c(L)$ can be extracted by probing the peak of

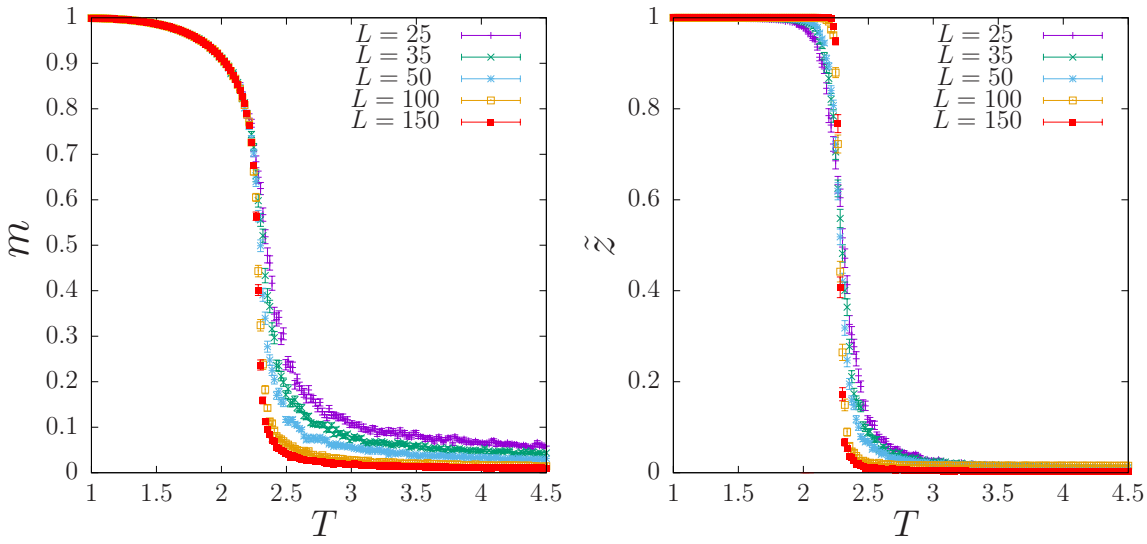


Fig. 3.8 The average magnetisation ($m$) and latent dimension ($\tilde{z}$) as a function of the temperature for five different lattice volumes.

the magnetic susceptibility $\chi$ at zero magnetic field $h$, where

$$\chi = \frac{L^2}{T}\left(\langle m^2\rangle - \langle m\rangle^2\right). \tag{3.46}$$

According to finite size scaling theory, close enough to $T_c$, magnetic susceptibility $\chi$ scales as

$$\chi \propto (t)^{-\gamma}, \tag{3.47}$$

where $t = (T - T_c)/T_c$ is the reduced temperature and $\gamma = 7/4$ a critical exponent [62]. The magnetic susceptibility measures the ability of a spin to respond due to a change in the external magnetic field. In the same manner we define the *latent susceptibility* as

$$\chi_{\tilde{z}} = \frac{L^2}{T}\left(\langle \tilde{z}^2\rangle - \langle \tilde{z}\rangle^2\right). \tag{3.48}$$

### 3.4.7 The Latent Susceptibility and the Critical Temperature

In Fig. 3.9 we present $T_c(L)$ extracted from fitting the latent susceptibility and the magnetic susceptibility as a function of $1/L$. Results obtained using the latent susceptibility suffer less from finite-size scaling effects as compared to those when using the magnetic susceptibility. Adopting, the usual finite-size scaling behaviour

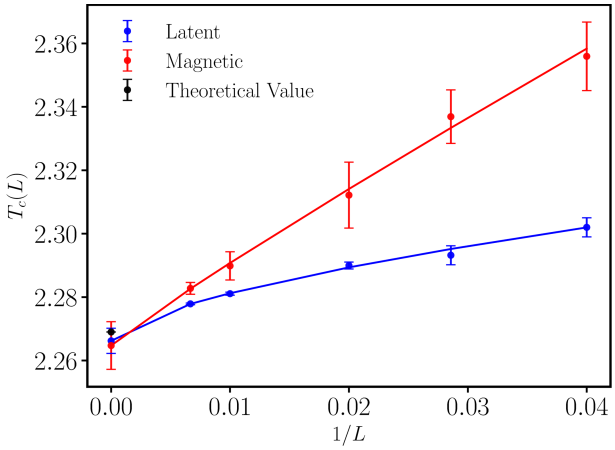


Fig. 3.9 The critical temperature $T_c(L)$ extracted from fitting the magnetic (red) and the latent (blue) susceptibilities as a function of $1/L$ to Eq. 3.49.

$$T_c(L) - T_c(L=\infty) \propto L^{-1/\nu}, \tag{3.49}$$

we fit both susceptibilities to the ansatz $T_c(L) = T_c(L=\infty) + \alpha L^{-1/\nu}$. Our findings are listed in Table 3.1.

Table 3.1 The results for $T_c(L=\infty)$ and $\nu$ extracted by fitting the magnetic as well as the latent susceptibilities to the ansatz $T_c(L) = T_c(L=\infty) + \alpha L^{-1/\nu}$.

| Susceptibility | $T_c(L=\infty)$ | $\nu$ | $\chi^2$/dof |
|---|---|---|---|
| Magnetic | 2.265(8) | 1.08(20) | 0.15 |
| Latent | 2.266(4) | 1.60(14) | 0.41 |

As expected, fitting the data for $T_c(L)$ resulting from the magnetic susceptibility yields values of $T_c(L=\infty)$ and $\nu$ which are consistent with the analytically extracted values $T_c = 2.269184$ and $\nu = 1$. Turning now to the case of the latent dimension, it appears that the results of $T_c(L)$ when fitted with a form of the known scaling behaviour of Eq. 3.49, yield a value for $T_c(L=\infty)$, which is in accordance with the theoretical expectation. This provides

a good piece of evidence that the deep learning autoencoder does not only predict the phase regimes of the 2D-Ising model as well as give an estimate for the critical temperature but can also lead to a precise evaluation of the critical temperature.

### 3.4.8 Conclusion

We can conclude that the proposed deep learning (fully-connected) autoencoder can not only identify, in an unsupervised manner, the phase structure of the 2D-Ising model but can also lead to a precise extraction of the critical temperature at the limit of the infinite volume. As shown in Fig. 3.9 the values of $T_c(L)$ suffer from less finite size effects compared to those usually extracted by using the peak of the magnetic susceptibility, and one would thus expect that the autoencoder could give a more precise prediction for $T_c$. There are other several related directions in which this study can be extended. Since our proposed autoencoder has been tested just in one system, it would be important to investigate its generalisation to other physical systems with non-trivial phase structure. Finally, our future plans involve the testing of the autoencoder as a tool for the unsupervised extraction of the phase structure of physical systems with continuous symmetries. These involve quantum field theories formulated on the lattice such as the 3D $\phi^4$ with $O(2)$ symmetry [22] where the phase transition is of second order and belongs to the same universality class as the 2D-Ising model, the 3D $U(1)$ gauge theory [23] for which the phase transition is of infinite order and belongs to the same universality class as the 2D $XY$ model, as well as the 3D $SU(N)$ gauge theory [164] which has a second-order phase transition for $N \leq 3$, a weakly first order for $N = 4$ and first order for $N \geq 5$.

In the context of this thesis, we observe that the machine learning algorithms have the potential to be used as novel computational methods to calculate observables in the finite volume. Therefore, another promising avenue of the extension of this research is towards calculating observables in lattice QCD.

# Chapter 4

# Hadron spectroscopy on the lattice

In this chapter, the methods of calculating finite volume spectra from lattice QCD will be discussed concisely. In quantum field theory, we have field operators for every state characterized by its quantum numbers which when operated on vacuum creates that state with the desired quantum numbers. These quantum numbers respect the symmetries of the Lagrangian. Similarly, on the lattice for creating a state with the desired quantum numbers, we need to identify the symmetries which the lattice operator has to satisfy to be well-defined on the lattice. Symmetries on the lattice were discussed in the previous chapter where all symmetries except the explicit breaking of Poincare symmetry on the lattice was discussed. In the first section of this chapter, we define the angular momentum on the lattice and the connection with the continuum. Then we define the interpolating operators of single meson and baryon, and two particle meson-meson and meson-baryon systems that respect the symmetries of the lattice. Once we have the basic building blocks to define a correlation function with these interpolating operators, we summarize various components and techniques necessary to compute correlation functions. After this, we give a concise overview of smearing, which is a lattice method used to make lattice calculations of ground state spectra more robust and decrease its statistical errors. In the subsequent sections, we describe different methodologies to extract discrete energies from these correlation functions and use them to compute resonance parameters implementing the Lüscher formalism. Along the same lines, if the final states of scattering are the same, one can proceed towards calculating resonance transition form factors from the lattice, which will be briefly discussed in the final section.

## 4.1 Angular momentum on the lattice

In the continuum, states are classified according to their angular momentum $J$, corresponding to the irreducible representations (irreps) of SU(2), and parity $P$. SU(2) can be decomposed into infinite irreducible representations, single-valued representations labelled by integer angular momenta $j = 0, 1, 2, \cdots$ plus the double-valued representations labelled by $j = 1/2, 3/2, 5/2, \cdots$. In order to include parity, we construct the irreps of SU(2)$\otimes\{\mathbb{I}, -\mathbb{I}\}$. The irreps are: single-valued integer spin irreps with parity $+1$, parity $-1$, double-valued half-integer spin irreps with parity $+1$ and $-1$. Thus, all quantum mechanical spinors (fermions and bosons) can be well represented by an element in any of the irreps of SU(2)$\otimes\{\mathbb{I}, -\mathbb{I}\}$. The 3-D shape of the spatial extent of the lattice determines the symmetry group of the lattice, which is also called as the *Little Group*.

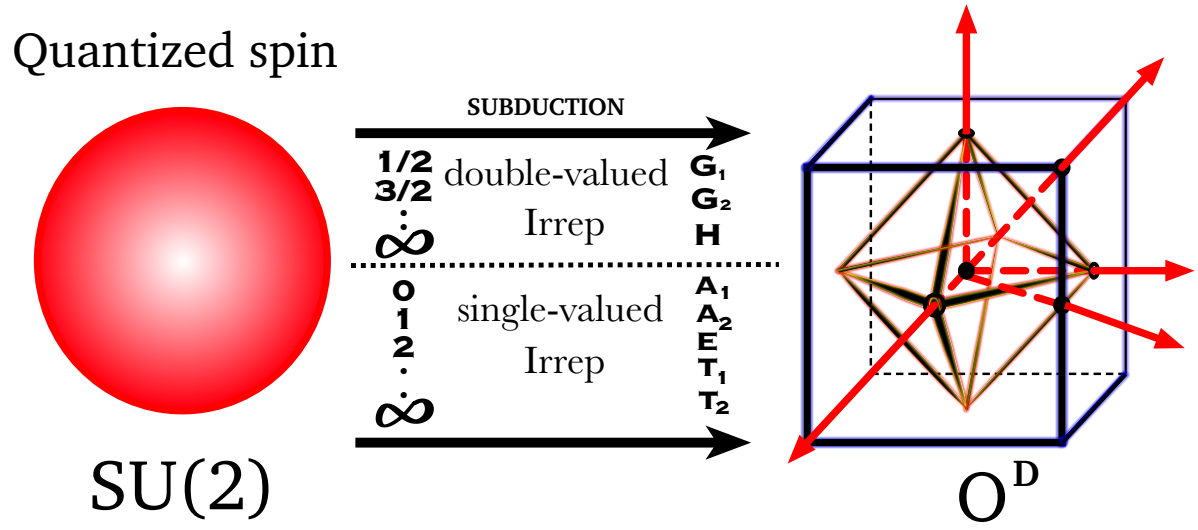


Fig. 4.1 Finite discrete rotational symmetry group (right, $O^D$) of the lattice compared with infinite continuous rotational symmetry group (left, SU(2)) of the continuum. The red arrows indicate the axes of rotations. The subduction mapping is shown diagrammatically in the middle.

In order to construct an operator on the lattice, corresponding to a boson or fermion in the continuum, we need to map the infinite irreps of the continuous symmetry group in the continuum to the finite irreps of the discrete Little Group of the lattice. This mapping is a many-to-one mapping, as depicted in Fig. 4.1. Therefore, we are interested in *subducing* the irreps of the continuum onto the lattice irreps. The formula to compute the multiplicity $m_J^\Lambda$

of an irrep $\Lambda$ of the finite Little Group in spin $J$ is given by,

$$m_J^\Lambda = \frac{1}{g}\sum_k n_k \chi_k^\Lambda \chi_k^J, \tag{4.1}$$

where there are $n_k$ elements in the conjugacy class $k$ with irreducible character $\chi_k^\Lambda$ and $g = \sum_k n_k$ [188, 76]. The $\chi_k^J$ (defined as the character in Representation theory) is the trace of the SU(2) matrices for spin $J$ of irrep and rotation $\theta$ which is fixed for a given conjugacy class $k$. Using Eq. (4.1), we list the subduction of the SU(2) irreps to irreps of $O^D$ in Table. 4.1. In

Table 4.1 Subduction of SU(2) into $O^D$

| spin $J$ | Subduction into $\Lambda$ of $O^D$ |
|---|---|
| 0 | $A_1$ |
| $1/2$ | $G_1$ |
| 1 | $T_1$ |
| $3/2$ | $H$ |
| 2 | $E \oplus T_2$ |
| $5/2$ | $G_2 \oplus H$ |
| 3 | $A_2 \oplus T_1 \oplus T_2$ |
| $7/2$ | $G_1 \oplus G_2 \oplus H$ |
| 4 | $A_1 \oplus E \oplus T_1 \oplus T_2$ |
| $9/2$ | $G_1 \oplus 2H$ |
| 5 | $E \oplus 2T_1 \oplus T_2$ |
| $11/2$ | $G_1 \oplus G_2 \oplus 2H$ |
| 6 | $A_1 \oplus A_2 \oplus E \oplus T_1 \oplus 2T_2$ |

order to sample various kinematic regimes (different values of center of mass energies) to study scattering, it is necessary to define operators in frames with different center of mass energies. Therefore, it is paramount to identify the symmetries in these moving frames, as discussed in the next section.

### 4.1.1 Center of Mass frame

In the center of mass frame of the scattering particle(s), the spatial extent of the lattice is a cube. Therefore, on the lattice, the continuous rotational symmetry is broken and the symmetry group (Little group) is reduced to the discrete cubic group ($O$) [144, 30] called the Octahedral group of all the 24 rotations of a cube. This group can be decomposed into 5 single-valued irreps.

#### Bosons

The point group $O_h$ is defined as: $O \otimes \{\mathbb{I}, -\mathbb{I}\}$ (Inversions), therefore it has 48 elements and 10 single-valued irreps. Thus, we need to define a many-to-one mapping from single-valued irreps of the continuum group SU(2)$\otimes\{\mathbb{I}, -\mathbb{I}\}$ to the single-valued irreps of $O_h$. The character table for the $O_h$ group in-terms of its conjugacy classes and irreps can be found in Ref. [73, 74, 185].

#### Fermions

The double cover of the point group $O_h^D$ is constructed by introducing a new generator in $O_h$, denoted by $\bar{E}$ which represents a rotation by $2\pi$ about any axis, thus it has 96 elements. Since it is a generator, it adds another irrep containing just itself, in addition to 2 irreps created by acting on two conjugacy classes of $O$. Thus, $O^D$ has 8 irreps and with the inclusion of parity (space inversions), $O_h^D$ has 16 irreps. The parity doublets are denoted by *gerade* and *ungerade*. It is worth noting that inclusion of $\bar{E}$ makes the extra 3 (6, with parity) irreps as double-valued representation. Therefore, we need to define a many-to-one mapping from double-valued irreps of the continuum group SU(2)$\otimes\{\mathbb{I}, -\mathbb{I}\}$ to the 3 (6) double-valued irreps of $O_h^D$. The character table for the $O_h^D$ group in-terms of its conjugacy classes and irreps can be found in Ref. [73, 74, 185].

### 4.1.2 Moving frames

When the frame of reference is defined for a non-zero center of mass momentum (denoted by $\vec{P}$), the spatial extent of the lattice is an irregular tetrahedron as shown in Fig. (4.2). The discrete symmetry group of that irregular tetrahedron is a subgroup of $O_h^D$. The various symmetry groups for different moving frame momenta are listed in Table. (4.2). The change in the shape of the lattice due to a Lorentz boost is depicted in Fig. (4.2).

Table 4.2 The reference frames (i.e., total momenta $\vec{P}$) and the associated Little Groups.

| $\vec{P}\,[\frac{2\pi}{L}]$ | Little Group (Bosons) | Little Group (Fermions) |
|---|---|---|
| $(0,0,0)$ | $O_h$ | $O_h^D$ |
| $(0,0,1)$ | $D_{4h}$ | $C_{4v}^D$ |
| $(0,1,1)$ | $D_{2h}$ | $C_{2v}^D$ |
| $(1,1,1)$ | $D_{3d}$ | $C_{3v}^D$ |

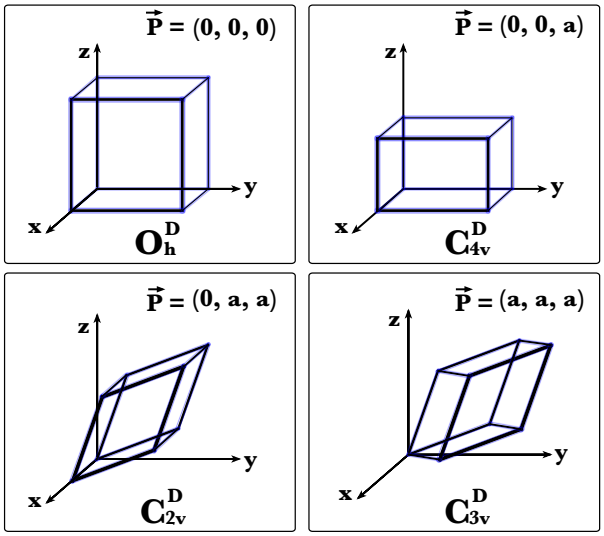


Fig. 4.2 The 3-D shape of the spatial extent of the lattice in different moving frames is depicted,

On the lattice, the inverse of the subduction identifies the spin content of a lattice energy eigen-state transforming as an irrep $\Lambda$ of $O_h^D$ ( or $O_h$). In the center of mass frame, the spin content of the irreps of $O^D$ is shown in Table (4.3).

Table 4.3 Inverse Subduction of $O^D$ for identifying SU(2) Irreps in spectra

| $\Lambda$ of $O^D$ | Spin $J$ |
|---|---|
| $G_1$ | $1/2, 7/2, 9/2, 11/2, \cdots$ |
| $G_2$ | $5/2, 7/2, 11/2, 13/2, \cdots$ |
| $H$ | $3/2, 5/2, 7/2, 9/2, \cdots$ |
| $A_1$ | $0, 4, 6, 8, \cdots$ |
| $A_2$ | $3, 6, 7, 9, \cdots$ |
| $E$ | $2, 4, 5, 6, \cdots$ |
| $T_1$ | $1, 3, 4, 5, \cdots$ |
| $T_2$ | $2, 3, 4, 5, \cdots$ |

Therefore, in order to extract such a lattice energy eigen-state, one needs to construct interpolating fields projected into the irrep $\Lambda$. In the next section, we discuss the construction of hadron interpolating fields.

## 4.2 Interpolating field operators

In this section, we discuss the construction of hadron interpolating field operators, necessary to compute relevant correlation functions for any observable on the lattice. The field operator which creates a hadronic state when it operates on the vacuum is called an *interpolating field operator* (also called interpolator). The quark sources are combined with elements of the Clifford algebra to construct gauge invariant interpolators with definite quantum numbers. Interpolators can be constructed to represent a single hadron or multiple hadrons. A general overview on the construction of these interpolators is given in the subsequent section.

### 4.2.1 Single Hadron Interpolators

We start our discussion by constructing the interpolators for the hadrons of the quark contents of mesons ($\bar{\psi}_1$, $\psi_2$)[1] and baryons($\bar{\psi}_1$, $\psi_2$, $\psi_3$). To construct a general single hadron interpolator $O_{\mathrm{M/B}}$ in a particular lattice irrep $\Lambda$ (with $n^{\mathrm{th}}$ multiplicity in the continuum irrep $J$) of the Little Group $LG(\vec{P})$ for a momentum $\vec{P}$, to represent a continuum state with spin J and spin-component m, using the group *projection* method, we can write,

$$O^{\Lambda,r,n,\vec{P}}_{\mathrm{M/B}}(t) = \frac{\dim(\Lambda)}{N_{LG(\vec{P})}} \sum_{R\in LG(\vec{P})} \Gamma^{\Lambda}_{r,r}(R)\, U_R\, O^{\mathrm{Jm}}_{\mathrm{M/B}}(t,\vec{P})\, U^{\dagger}_R \quad r \in \{1,\ldots,\dim(\Lambda)\}, \tag{4.2}$$

where $\dim(\Lambda)$ is the dimension of the irrep, $N_{LG(\vec{P})}$ is the order of the Little Group, and $\Gamma^{\Lambda}$ are the representation matrices of the elements (including rotations and reflections) $R \in LG(\vec{P})$ [185] and $U_R$ is the unitary operator in the continuum which applies the transformation $R$. This projection generates $\dim(\Lambda)$ lattice operators for a particle in the continuum with spin J.

#### Meson Interpolators

Thus, now we define a general meson interpolator of the form $O_{\mathrm{M}}$ as,

$$O_{\mathrm{M}}(\vec{P},t) = \sum_{\vec{x}} \bar{\psi}_1(\vec{x},t)\,\Gamma\,\psi_2(\vec{x},t)\; e^{-i\vec{P}\cdot\vec{x}}. \tag{4.3}$$

where $\psi_1(\vec{x},t)$ and $\psi_2(\vec{x},t)$ represents two quark fields with appropriate flavors needed to define the meson $M$. The $\mathscr{C}$, $\mathscr{P}$ and $\mathscr{T}$ symmetries are preserved by the bilinear form of the meson interpolator and choice of the Dirac structure (element of Clifford algebra). The list of different choices of Dirac structures ($\Gamma$) for different mesons is given in Table. 4.4.

[1] Mesons not in the quark model like the exotic mesons, tetra-quarks, hybrid mesons and gluons are an active field of research

Table 4.4 Meson Interpolators

| State | J (spin) | Charge Conjugation $\mathscr{C}$ | Parity ($\mathscr{P}$) | $\Gamma$ | Particles |
|---|---|---|---|---|---|
| Scalar | 0 | + | + | i, $\gamma_0$ | $f_0$, $a_0$ |
| Pseudoscalar | 0 | + | - | $\gamma_5$, $\gamma_0\gamma_5$ | $\pi^{\pm}$, $\pi^0$, $\eta$ |
| Vector | 1 | - | - | $\gamma_i$, $\gamma_0\gamma_i$ | $\rho^{\pm}$, $\rho^0$, $\omega$ |
| Axial vector | 1 | + | + | $\gamma_i\gamma_5$ | $a_1$, $f_1$ |
| Tensor | 1 | - | + | $\gamma_i\gamma_j$ | $h_1$, $b_1$ |

### Baryon Interpolators

And now for a definition of a general baryon interpolator of the form $O_{\mathrm{B}}$, we refer to Ref. [28, 30, 29]. In the scope of this thesis, we discuss only the construction of nucleon and delta interpolators.

**Nucleon Interpolating Operators:** The most general form of a nucleon interpolating operator can be expressed as:

$$O_B(\vec{x},t,\Gamma_1,\Gamma_2) = \varepsilon_{abc} \left[ \psi_1^{aT}(\vec{x},t)\,\Gamma_1\,\psi_2^b(\vec{x},t) \right] \Gamma_2\,\psi_3^c(\vec{x},t).$$

Here $a,b$ and $c$ are color indices, $T$ denotes transposition. The $\Gamma_1$ and $\Gamma_2$ are the different combinations of Dirac structures (combinations of Gamma matrices). $q_1$, $q_2$ ansd $q_3$ are quarks of different flavours. The quantity inside [ ] is defined as a *diquark* structure.

In order to construct 3-quark current interpolating fields, we can follow a prescription as first described by [138]. In Ref. [138], the author introduces as an ansatz,

$$\begin{aligned} O_{B_1}(\vec{x},t) &= \varepsilon_{abc} \left[ u_a^T(\vec{x},t) C\gamma_5 d_b(\vec{x},t) \right] u_c(\vec{x},t)\,, \\ O_{B_2}(\vec{x},t) &= \varepsilon_{abc} \left[ u_a^T(\vec{x},t) C d_b(\vec{x},t) \right] \gamma_5 u_c(\vec{x},t) \end{aligned}$$

where $C$ is the charge conjugation matrix and $T$ denotes transposition in spinor space. The form of the nucleon interpolating operator ensures all quarks are in a $s$(or $d$) angular momentum state( which implies the relative momenta between the quarks are 0).

Another much more formal way of constructing the 3-quark operators was described in Ref [70]. We want to construct a spin-1/2 operator consisting of 3 of the $d(=4)$-dimensional Dirac spinors(quarks). So we are looking at a space of $E = d \times d \times d$, where $d$ is the 4-dimensional space of Dirac spinors. Vectors of $E$ are Lorentz-transformed by operators

which are generated by that part of the total angular momentum of the nucleon representing the spin angular momentum of that particle. $E$ is reducible into direct sums of the irreducible representations of the restricted Lorentz group $SO^{+}(1,3;\mathbb{R})$. So for a given spin $n$, we look into the irrep $D(j_1,j_2)$ (where $n = j_1 \pm j_2$) of the restricted Lorentz group. The decomposition of $E$ in terms of irreps of the restricted Lorentz group is given as:

$$E = 5\,\{D(0,\tfrac{1}{2}) \oplus D(\tfrac{1}{2},0)\} \,\oplus\, 3\,\{D(\tfrac{1}{2},1) \oplus D(1,\tfrac{1}{2})\} \,\oplus\, \{D(\tfrac{3}{2}.0) \oplus D(0,\tfrac{3}{2})\} \tag{4.4}$$

Following the calculation in Ref. [70], for spin $\frac{1}{2}$ operator we look into the 5 basis operators belonging to $D(0,\frac{1}{2}) \oplus D(\frac{1}{2},0)$ and 3 basis operators belonging to $D(\frac{1}{2},1) \oplus D(1,\frac{1}{2})$.
As in Ref. [70], we proceed to decompose these two irreps into irreps of the SU(3) group, and isolate the ones corresponding to the non-strange baryon. We find,

$$\begin{aligned}
O_{B_1}(\vec{x},t) &= \varepsilon_{abc}\,\left[u_a^T(\vec{x},t)\,C\gamma_5\,d_b(\vec{x},t)\right]\,u_c(\vec{x},t)\,,\\
O_{B_2}(\vec{x},t) &= \varepsilon_{abc}\,\left[u_a^T(\vec{x},t)\,C\,d_b(\vec{x},t)\right]\,\gamma_5 u_c(\vec{x},t)\,,\\
O_{B_3}(\vec{x},t) &= \varepsilon_{abc}\,\left[u_a^T(\vec{x},t)\,C\gamma_5\,\gamma^\nu\,d_b(\vec{x},t)\right]\,\left(g_{\mu\nu} - \frac{1}{4}\gamma_\mu\gamma_\nu\right)u_c(\vec{x},t).
\end{aligned}$$

As noticed, $O_{B_3}$ belongs to $D(\frac{1}{2},1) \oplus D(1,\frac{1}{2})$, so it has contributions from spin $\frac{3}{2}$ and spin $\frac{1}{2}$. For ease of calculations, as pointed out in Ref. [154] we take the leading term $g_{\mu\nu}$, then we are reduced to

$$\begin{aligned}
O_{B_1}(\vec{x},t) &= \varepsilon_{abc}\,\left[u_a^T(\vec{x},t)\,C\gamma_5\,d_b(\vec{x},t)\right]\,u_c(\vec{x},t)\,,\\
O_{B_2}(\vec{x},t) &= \varepsilon_{abc}\,\left[u_a^T(\vec{x},t)\,C\,d_b(\vec{x},t)\right]\,\gamma_5 u_c(\vec{x},t)\,,\\
O_{B_3}(\vec{x},t) &= \varepsilon_{abc}\,\left[u_a^T(\vec{x},t)\,C\gamma_5\,\gamma_\mu\,d_b(\vec{x},t)\right]\,u_c(\vec{x},t)
\end{aligned}$$

In order to project $O_{B_3}$ to spin $\frac{1}{2}$, we follow the prescription in Ref. [153], which independently confirms the choice of $O_{B_3}$ made in Ref. [58]. In Ref. [58], they have concluded,

$$O_{N1}(\vec{x},t) = \varepsilon_{abc}\,\left[u_a^T(\vec{x},t)\,C\gamma_5\,d_b(\vec{x},t)\right]\,u_c(\vec{x},t)\,, \tag{4.5}$$

$$O_{N2}(\vec{x},t) = \varepsilon_{abc}\,\left[u_a^T(\vec{x},t)\,C\,d_b(\vec{x},t)\right]\,\gamma_5 u_c(\vec{x},t)\,, \tag{4.6}$$

$$O_{N3}(\vec{x},t) = \varepsilon_{abc}\,\left[u_a^T(\vec{x},t)\,C\gamma_5\,\gamma_t\,d_b(\vec{x},t)\right]\,u_c(\vec{x},t) \tag{4.7}$$

In Ref. [58], there is an interesting discussion on the diquark structure, and also they have concluded that all the operators belong to distinct irreps of the parity-chiral group. The comprehensive procedure of obtaining baryonic currents has been also discussed in Ref. [71].

**$\Delta$ Interpolating Operators:** In order to construct the lowest lying baryon octet Delta interpolating operator, we look at the Irrep $D(\frac{1}{2},1) \oplus D(1,\frac{1}{2})$, and we follow [70] to get the following,

$$O_{\Delta 1}(\vec{x},t) = \varepsilon_{abc} \left[ u_a^T(\vec{x},t) C\gamma_\mu u_b(\vec{x},t) \right] u_c(\vec{x},t)$$

where $\mu = 1,2$ and 3.
We also look at Irrep $D(\frac{3}{2},0) \oplus D(0,\frac{3}{2})$ from [70]. Using Fierz transformations, we construct a few other interpolating operators of the following form, which have the same quantum numbers,

$$O_{\Delta 1}(\vec{x},t) = \varepsilon_{abc} \left[ u_a^T(\vec{x},t) C\gamma_\mu u_b(\vec{x},t) \right] u_c(\vec{x},t) \tag{4.8}$$
$$O_{\Delta 2}(\vec{x},t) = \varepsilon_{abc} \left[ u_a^T(\vec{x},t) C\gamma_\mu \gamma_t u_b(\vec{x},t) \right] u_c(\vec{x},t)\,, \tag{4.9}$$
$$O_{\Delta 3}(\vec{x},t) = \varepsilon_{abc} \left[ u_a^T(\vec{x},t) C\gamma_\mu \gamma_t \gamma_5 u_b(\vec{x},t) \right] \gamma_5 u_c(\vec{x},t) \tag{4.10}$$

Though all are valid $\Delta$-baryon interpolators, we find that in practice only the first one has been used by lattice groups in the literature.

### 4.2.2 Two-Hadron Interpolators

In studying of scattering of two hadrons, we need to construct two-hadron interpolators to understand the shift in energies when there is an existence of a resonance in the spectrum. We can construct two hadron interpolators via the an outer product of two single hadron interpolators. Thus an two hadron interpolator can be defined as,

$$O_{h_1 h_2}(\vec{p}_1,\vec{p}_2,t) = O_{h_1}(\vec{p}_1,t) O_{h_2}(\vec{p}_2,t), \tag{4.11}$$

where $h_1$, $h_2$ are either $M$ for meson or $B$ for baryon.

## 4.3 Correlation functions

We have constructed the relevant interpolators needed to study mesons and baryons (nucleons and delta). By Wightman axioms [228] for quantum field theory and the Ostrader-Schrader theorem [201, 200], we need to construct correlation functions through which we can describe all the features (observables) of the quantum field theory. In Euclidean formulation, a time

correlator of operators $O(\vec{x},t), \bar{O}(\vec{0},0)$ is given by,

$$C(\vec{p},t) = \sum_{\vec{x}} \left\langle O(\vec{x},t)\, \bar{O}(\vec{0},0) \right\rangle e^{-i\vec{p}\cdot\vec{x}} \tag{4.12}$$

The time correlator when written in energy basis is given by,

$$C(\vec{p},t) = \sum_{n} \langle \Omega \,|\, O \,|\, n \rangle \left\langle n \,\middle|\, \bar{O} \,\middle|\, \Omega \right\rangle e^{-t\,E_n(\vec{p})} = |Z_0|^2\, e^{-t\,E_0(\vec{p})}(1 + \mathscr{O}(e^{-t\Delta E(\vec{p})})) \tag{4.13}$$

where $Z_0 = \langle \Omega \,|\, O \,|\, n \rangle$ represents the overlap of the state defined by $O$ with the ground state, $E_0(\vec{p})$ is the ground state energy and $\Delta E$ is the energy difference between the ground state and first excited state. We extract the ground state energy by taking $t$ large enough so that $t\Delta E \gg 1$. The ground state energy $E_0(\vec{p})$ is related to the mass of the hadron by the relativistic dispersion relation,

$$E(\vec{p}) = \sqrt{m_H^2 + \vec{p}^2}(1 + \mathscr{O}(a|\vec{p}|)), \tag{4.14}$$

where $a$ is the lattice spacing. We can calculate the energy of a moving hadron on the lattice using the two-point correlation function of that hadron. From Sec. 3.2.4, using Grassmann algebra and Wick's theorem we can write the correlation function in terms of the propagator $\mathbb{M}^{-1}$. In the next sections, we describe different propagators we need to calculate correlation functions.

### 4.3.1 Building blocks for the correlation functions

Correlation functions on the lattice can be constructed with these fundamental blocks:

**a. Point-to-all propagator:** Writing the quark and anti-quark fields as $\psi(t_f,\vec{x})^a_\alpha$ and $\bar{\psi}(t_i,\vec{x}_i)^b_\beta$, where $\alpha,\beta$ are spin indices and $a,b$ are color indices, the point-to-all propagator $S_f$ from the fixed initial point $x_i = (t_i,\vec{x}_i)$ to any final point $x_f = (t_f,\vec{x}_f)$ on the lattice is the matrix element of the inverse of the lattice Dirac operator $\mathbb{M}$:

$$
\begin{aligned}
S_f(t_f,\vec{x};t_i,\vec{x}_i)^{ab}_{\alpha\beta} &= \langle \psi(t_f,\vec{x}_f)^a_\alpha \, \bar{\psi}(t_i,\vec{x}_i)^b_\beta \rangle_f \\
&= \sum_{t_f,\vec{x}_f} \mathbb{M}^{-1}(t_f,\vec{x}_f;t_i,\vec{x}_i)^{ac}_{\alpha\gamma} \, \eta^b_{t_i,\vec{x}_i,\beta}(t_f,\vec{x}_f)^c_\gamma . \qquad (4.15)
\end{aligned}
$$

$$
\eta^b_{t_i,\vec{x}_i,\beta}(t_f,\vec{x}_f)^a_\alpha = \delta_{t_f,t_i}\delta_{\vec{x}_f,\vec{x}_i}\,\delta^{ab}\,\delta_{\alpha\beta}\,, \quad a,b=0,1,2,\ \alpha,\beta=0,1,2,3\,.
$$

where $\eta^b_{t_i,\vec{x}_i,\beta}(t_f,\vec{x}_f)^c_\gamma$ is the point source.

**b. Sequential propagator:** The sequential propagator describes the quark flow through a vertex of a given flavor and Lorentz structure. It is obtained from a point-to-all propagator by a second (sequential) inversion on a source built from the point-to-all propagator $S_f(t_{seq},\vec{x}_{seq};t_i,\vec{x}_i)$ with an inserted vertex at timeslice $t_{seq}$ with spin structure $\Gamma$ and momentum insertion $\vec{p}$:

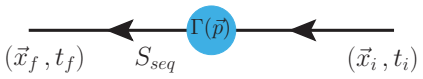


$$
\begin{aligned}
&S_{seq}(t_f,\vec{x}_f;t_{seq},\vec{p},\Gamma;t_i,\vec{x}_i) \\
&= \sum_{\vec{x}_{seq}} \mathbb{M}^{-1}(t_f,\vec{x}_f;t_{seq},\vec{x}_{seq}) \times \Gamma\, \mathrm{e}^{i\vec{p}\cdot\vec{x}_{seq}}\, S_f(t_{seq},\vec{x}_{seq};t_i,\vec{x}_i)\,. \qquad (4.16)
\end{aligned}
$$

**c. Stochastic timeslice-to-all propagator:** The stochastic timeslice-to-all propagator is defined as the inversion of the Dirac matrix with a stochastic timeslice momentum source:


$$
\begin{aligned}
&S_{st}(t_f,\vec{x}_f;t_i,\vec{x}_i) = \\
&\frac{1}{N_{\text{sample}}} \sum_{r=1}^{N_{\text{sample}}} \phi^r_{t_i,\vec{p}_i}(t_f,\vec{x}_f)\, \xi^r_{t_i,\vec{0}}(t_i,\vec{x}_i)^\dagger\,, \qquad (4.17)
\end{aligned}
$$

where

$$
\phi^r_{t_i,\vec{p}_i} = \mathbb{M}^{-1}\,\xi^r_{t_i,\vec{p}_i} \text{ and } \xi^r_{t_i,\vec{p}_i}(t,\vec{x}) = \delta_{t,t_i}\,\mathrm{e}^{i\vec{p}_i\cdot\vec{x}}\,\xi^r_{t_i}(\vec{x})\,.
$$

For each $r=1,\ldots,N_{\text{sample}}$, $\xi^r_{t_i}$ is a spin-color timeslice vector with independently distributed entries for real and imaginary part, $\xi^r_{t_i}(t,\vec{x})^a_\alpha \sim \mathbb{Z}_2 \times i\mathbb{Z}_2$, so that the expectation values with

respect to the stochastic noise, denoted as $\mathrm{E}[\ \ ]$, satisfy

$$\mathrm{E}\left[\xi^r_{t_i}(t,\vec{x})^a_\alpha\right] = 0, \tag{4.18}$$

$$\mathrm{E}\left[\xi^{r_1}_{t_{i_1}}(\vec{x}_1)^{a_1}_{\alpha_1}\left(\xi^{r_2}_{t_{i_2}}(\vec{x}_2)^{a_2}_{\alpha_2}\right)^*\right] = \delta^{r_1,r_2}\,\delta_{t_{i_1},t_{i_2}}\,\delta_{\vec{x}_1,\vec{x}_2}\,,\delta_{\alpha_1,\alpha_2}\,\delta^{a_1,a_2}\,. \tag{4.19}$$

This technique provides a good way to efficiently evaluate all-to-all propagators with reasonable cost. We apply spin-dilution to make use of the efficient one-end-trick [178] in our contractions. In this case, the stochastic sources read

$$\xi^r_{t_i,\vec{p}_i,\alpha}(t,\vec{x})^b_\beta = \delta_{t,t_i}\,\delta_{\alpha,\beta}\,\mathrm{e}^{i\vec{p}_i\cdot\vec{x}}\,\xi^r_{t_i}(\vec{x})^b, \tag{4.20}$$

and the color timeslice vectors $\xi^r_{t_i}$ have expectation values analogous to those in Eqs. (4.18) and (4.19). The one-end-trick then allows for the representation of a product of quark propagators by two stochastic propagators through a vertex is given again by $\Gamma$ and $\vec{p}$ as

$$\begin{aligned}\mathrm{E}\left[\phi^r_{t_i,\vec{p}_i,\kappa}(x)^a_\alpha\,(\Gamma\gamma_5)_{\kappa\lambda}\,\phi^r_{t_i,0,\lambda}(z)^{b*}_{\beta'}\,(\gamma_5)_{\beta'\beta}\right] \\ = S(t_x,x;t_i,\vec{x}_i)^{ac}_{\alpha\kappa}\,\mathrm{e}^{i\vec{p}_i\cdot\vec{x}_i}\,(\Gamma\gamma_5)_{\kappa\lambda}\,S(t_z,\vec{z};t_i,\vec{x}_i)^{bc*}_{\beta'\lambda}\,(\gamma_5)_{\beta'\beta} \\ = \left(S(t_x,\vec{x};t_i,\vec{x}_i)\,\mathrm{e}^{i\vec{p}_i\cdot\vec{x}_i}\,\Gamma\,S(t_i,\vec{x}_i;t_z,\vec{z})\right)^{ab}_{\alpha\beta}.\end{aligned} \tag{4.21}$$

Equation (4.21) used in addition $\gamma_5$-hermiticity for the Dirac propagator, $S(t_x,\vec{x};t_y,\vec{y})^\dagger = \gamma_5\,S(t_y,\vec{y};t_x,\vec{x})\,\gamma_5$.

## 4.4 Signal enhancement methods

In practical applications several techniques are used to increase the overlap of the single hadron interpolator with the ground state of the hadron of interest. From Eq. (4.13), if we define $Z = C(\vec{p},0)$, then the overlap function is $|Z_0|/|Z|$, which we want to maximize through these techniques. These will be presented in the following sections.

### 4.4.1 Extended source

A very common method to increase the overlap of the ground state is called *Gaussian/Wuppertal smearing* where the quark fields in the interpolator are enveloped by a gauge invariant func-

tion of the spatial coordinates and link variables.

$$\psi^{sm}(\vec{x},t) = \sum_{\vec{y}} W(\vec{x},\vec{y};U(t))\psi(\vec{y},t), \tag{4.22}$$

where

$$W(\vec{x},\vec{y};U(t)) \equiv (\mathscr{I} + \alpha H(\vec{x},\vec{y};U(t)))^n, \tag{4.23}$$

with

$$H(\vec{x},\vec{y};U(t)) = \sum_{k=1}^{3} \left( U_k(\vec{x},t)\delta_{\vec{x},\vec{y}-\hat{k}} + U_k^{\dagger}(\vec{x}-\hat{k},t)\delta_{\vec{x},\vec{y}+\hat{k}} \right). \tag{4.24}$$

The parameters $\alpha$ and $n$ are tuned to increase the overlap with the ground state. The operator $W(\vec{x},\vec{y};U(t))$ depends on the gauge links.

## 4.5 Link Smearing

The calculation of propagators for correlation functions needs inversion of the Dirac operator. The Dirac operator is riddled with violent short distance (Ultraviolet) fluctuations of the gauge field, which makes inversions computationally expensive. The idea from statistics that average of random variates fluctuate less than the variates themselves, can help ameliorate this problem. In this case, the random variates are the neighbouring gauge link variables, and this idea of averaging them is called smearing. Below are the sections, where we will discuss different methodologies based on this common idea.

### 4.5.1 APE smearing

As motivated in the previous section, an envelop function can be designed for the link variables which visually corresponds to averaging the gauge links locally over its neighbours (”fattening“ of the links). In APE smearing, one takes the average over the given original link and the six staples connecting its endpoints,

$$U_{\mu}^{APE}(x) = \mathrm{Proj}_{SU(3)} \left( (1-\alpha)U_{\mu}(x) + \frac{1}{\alpha} \sum_{\nu \neq \mu} S_{\mu\nu}(x) \right), \tag{4.25}$$

where

$$S_{\mu\nu}(x) = U_{\nu}(x)U_{\mu}(x+\hat{\nu})U_{\nu}^{\dagger}(x+\hat{\mu}) + U_{\nu}^{\dagger}(x-\hat{\nu}), U_{\mu}(x-\hat{\nu})U_{\nu}(x-\hat{\nu}+\hat{\mu}) \tag{4.26}$$

and the real parameter $\alpha$ can be adjusted to optimize the reduction in the noise. In every iteration we perform in the smoothing procedure it is important to project $U_\mu^{APE}(x)$ onto the SU(3) group. A visual description is depicted in Fig. 4.3.

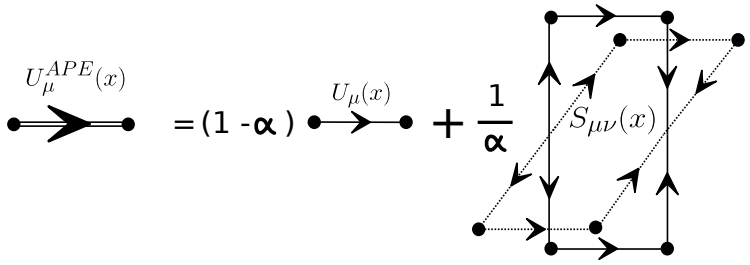


Fig. 4.3 $U_\mu^{APE}(x)$ defined as the weighted sum of $U_\mu(x)$ and its neighbouring staples $S_{\mu\nu}$.

### 4.5.2 Stout Smearing

This method involved redefinition of the each link variables as,

$$U'_\mu(x) = e^{iQ_\mu(x)} U_\mu(x) \tag{4.27}$$

where $Q_\mu(x)$ is a traceless hermitian matrix constructed from staples

$$Q_\mu(x) = \frac{i}{2}\left(\Omega_\mu^\dagger(x) - \Omega_\mu(x) - \frac{1}{3}\,\mathrm{Tr}\left[\Omega_\mu^\dagger(x) - \Omega_\mu(x)\right]\right), \tag{4.28}$$

with

$$\Omega_\mu(x) = \left(\sum_{\nu\neq\mu} \rho_{\mu\nu} S_{\mu\nu}(x)\right) U_\mu^\dagger(x),$$

where $S_{\mu\nu}$ is defined in Eq. (4.26). The tunable parameters are $\rho_{\mu\nu}$.
All the smearing techniques we showed are iterative, thus they affect not just the neighbouring sites, and as a result the asymptotic behaviour of the quark propagator needs to be checked to ensure that no long-range effects remain.

## 4.6 Variational method

In a lattice calculation, we can have several interpolators for the same particle of interest, and all of the interpolators can have overlap with the ground state of the hadron. This motivates a variational technique for finding an optimal linear combination of interpolators. Assuming

our choice of interpolators form a complete basis, we can define a correlation matrix as

$$C_{ij}\left(t-t'\right)=\left\langle O_j(t)O_j\left(t'\right)^{\dagger}\right\rangle=\sum_n\langle O_i(0)|n\rangle\,\mathrm{e}^{-E_n(t-t')}\left\langle n|O_j(0)^{\dagger}\right\rangle, \tag{4.29}$$

where $E_n$ is the finite volume energy of the $n^{\text{th}}$ state and $\langle O_i(0)|n\rangle$ the overlaps of the $n^{\text{th}}$ state with the state created by the interpolator $O_i$ from vacuum. To obtain these finite volume energies $E_n$ for a choice of the set of $N$ interpolators, we need to solve the *Generalized EigenValue Problem* (GEVP) [184, 173, 43, 198] defined as,

$$C(t)u_n(t)=\lambda_n(t)C\left(t_0\right)u_n(t)\qquad 1\leq n\leq N \tag{4.30}$$

where $t_0$ is fixed and small, $u_n(t)$ are generalized eigenvectors and $t>t_0$. The normalization of the generalized eigenvectors is fixed by

$$u_iC(t_0)(u)_j=\delta_{ij}. \tag{4.31}$$

At large $t$, the eigenvalues $\lambda_n(t,t_0)$, which are also referred to as principal correlators, behave as

$$\lambda_n(t,t_0)=\mathrm{e}^{-E_n(t-t_0)}. \tag{4.32}$$

$$E_n^{eff}\left(t,t_0\right)=-\ln\left(\frac{\lambda_n\left(t,t_0\right)}{\lambda_n\left(t+1,t_0\right)}\right). \tag{4.33}$$

To determine the energies $E_n$, we fit the eigenvalues either with the single-exponential form of Eq. 4.32 or with the two-exponential form

$$\lambda^n(t,t_0)=(1-B)\mathrm{e}^{-E_n(t-t_0)}+B\mathrm{e}^{-E_n(t-t_0)}, \tag{4.34}$$

which includes a small contribution from higher-lying excited states with energies $E_n^{'\Lambda,\vec{P}}$ [173, 43]. In order to extract energies reliably from the fit, one can perform stability analysis, whereby given a fit range $(t_{min},t_{max})$, we fix the $t_{max}$ and vary $t_{min}$ and study the variation of $\chi^2$ of the fit. A good stable fit would correspond to almost constant values of $\chi^2$ upon varying $t_{min}$.

Alternatively, due to charge conjugation symmetry, the entire $C(t)$ is real-valued (in the infinite statistics limit). Consequently, the overlap factors $\langle O_i(0)|n\rangle$ are also real-valued. Thus, one can perform fits to each element of the correlation matrix for $t_{min}\leq t\leq t_{max}$ using

the model described as,

$$C_{ij}(t) \approx \sum_{n=1}^{N_{\text{states}}} Z_{i,n} Z_{j,n} \mathrm{e}^{-E_n t}, \tag{4.35}$$

and this method is called *Matrix fit analysis*, where $t_{min}$ has to be chosen large enough such that contributions from $n > N_{states}$ become negligible. For an $m \times m$ correlation matrix, this model has $N_{states} \times (m+1)$ parameters. To ensure that the energies returned from the fit are ordered, we used the logarithms of the energy differences, $l_n = \ln(aE_n - aE_{n-1})$, instead of $aE_n$ (for $n > 1$) as parameters in the fit. To simplify the task of finding suitable start values for the iterative $\chi^2$-minimization process, we also rewrote the overlap parameters as $Z_{i,n} = B_{i,n} Z_i$ with $B_{i,n} = 1$ for $n$ equal to the state with which $O_i$ has the largest overlap. Good initial guesses for $Z_i$ can then be obtained from single-exponential fits of the form $Z_i Z_i \mathrm{e}^{-E_n t}$ to the diagonal elements $C_{ii}(t)$ in an intermediate time window in which the $n$-th state dominates, and the start values of $B_{i,n}$ can be set to zero.

The spectrum is the energy eigenvalues of the Hamiltonian, of the states with the quantum numbers of the hadron described by the correlation matrix, which we obtain from the fits. The spectrum will consist both of energies corresponding to levels with predominant overlap to single hadron operators as well as energy levels with dominant overlap to multi-hadron operators. However, not all energy levels can be clearly separated into these two categories, thus labeling the levels as a single hadron state or a multi-hadron state is not unique. Sometimes there are energy levels that couple both to single hadron operators and multi hadron operators equally. Therefore, in order to interpret the spectrum, we need to take into account the finite volume effects.

In the subsequent sections, we develop the formalism of taking into account the finite volume effects. Only then we will be in a position to interpret the finite volume spectrum in terms of hadrons in the continuum.

## 4.7 Elastic scattering of two particles in a finite volume

In this section, we review the Lüscher formalism which relates finite volume spectra with infinite volume scattering phase shifts. We start with developing the kinematics needed to introduce the formalism.

### 4.7.1 Kinematics

We consider interaction between two particles of masses $m_1$ and $m_2$ in a lattice box of volume $L^3$, with total 3-momentum $\vec{P}$. Since the interacting particles are in a box, they are

constrained by the periodic boundary conditions, thus the total momentum is quantized.[2]

$$\vec{P} = \vec{p}_1 + \vec{p}_2 = \frac{2\pi}{L}\vec{d}, \tag{4.36}$$

$$\vec{d} \in \mathbb{Z}^3$$

where $\vec{p}_1$ and $\vec{p}_2$ are momenta of the two particles in the laboratory frame (LF) i.e. the rest frame of the box. In the centre of mass (CM) frame, the energy of the system can be written as,

$$E^* = \sqrt{p^{*2} + m_1^2} + \sqrt{p^{*2} + m_2^2} \tag{4.37}$$

where $\vec{p}^*$ is the momentum of the particles in the CM frame. The CM frame energy is related to the LF energy by,

$$E_L = \sqrt{P^2 + E^{*2}}. \tag{4.38}$$

In the LF the CM is moving at $\vec{v}$, where

$$\vec{v} = \vec{P}/E_L \tag{4.39}$$

Thus, CM frame is connected to the LF by a standard Lorentz Transformation,

$$\vec{p}^{\,*} = \vec{\gamma}(\vec{p}_1 - \vec{v}\sqrt{p_1^2 + m_1^2}) = -\vec{\gamma}(\vec{p}_2 - \vec{v}\sqrt{p_2^2 + m_2^2}) \tag{4.40}$$

where

$$\vec{\gamma} = \frac{1}{\sqrt{1-v^2}}\frac{\vec{v}}{|v|} = \gamma\frac{\vec{v}}{|v|}$$

and we have used the shorthand notation,

$$\vec{\gamma}\vec{p} = \gamma\vec{p}_{\parallel} + \vec{p}_{\perp}$$

where $\vec{p}_{\parallel}$ and $\vec{p}_{\perp}$ are components of $\vec{p}$, parallel and perpendicular to the center of mass velocity: $\vec{p}_{\parallel} = (\vec{p}\cdot\vec{v})\vec{v}/v^2$ and $\vec{p}_{\perp} = \vec{p} - \vec{p}_{\parallel}$.

In a special case, where we have two pions $m = m_1 = m_2$, thus,

$$p^{*2} = \frac{1}{4}(E_L^2 - P^2) - m^2 \tag{4.41}$$

[2] As opposed to, in the non interacting case, where the individual momenta are quantized.

In the non-interacting case, since $\vec{p}_1$ and $\vec{p}_2$ are quantized, we can write

$$\vec{\bar{p}}^{*} = (2\pi/L)\vec{n}\,, \quad \vec{n} \in P_{\vec{d}} = \left\{ \vec{n} \,\middle|\, \vec{n} = \vec{\gamma}^{-1}(\vec{m} + \vec{d}/2)\,, \text{ for } \vec{m} \in \mathbb{Z}^3 \right\}\,. \tag{4.42}$$

From the energy shift in the interacting and the non interacting case, we extract the scattering phase shifts. The formalism for relating this shift in energy with scattering phase shift, is discussed in the next section.

### 4.7.2 Lüscher formalism

The Lüscher quantization condition for elastic scattering is,

$$\det\left(\mathbb{I} + \mathrm{i}t_\ell(s)\left(\mathbb{I} + \mathrm{i}\mathscr{M}^{\vec{P}}\right)\right) = 0 \tag{4.43}$$

where $t_\ell(s)$ is the infinite-volume scattering amplitude, which is parametrised by the infinite-volume scattering phase shift $\delta_\ell(s)$ given by,

$$t_\ell(s) = \frac{1}{\cot\delta_\ell(s) - \mathrm{i}} \tag{4.44}$$

with $s$ being the squared CM energy. The $\mathscr{M}^{\vec{P}}$ is a matrix-valued function that depends on the finite-volume spectrum and volume. The quantization condition can be simplified for each momentum frame according to the symmetries in that frame. Note that this is an exact condition with no additional corrections due to finite volume, thus, the Lüscher quantization condition eliminates all the finite volume effects in $\mathscr{M}^{\vec{P}}$ systematically to connect the $\mathscr{M}^{\vec{P}}$ to the infinite volume $t$-matrix. The condition is identical for mesons and baryons, but only the basis of representing the $\mathscr{M}^{\vec{P}}$ is different in both the cases.

#### Mesons

The $\mathscr{M}^{\vec{P}}$ for integer spin particles is related to its counterpart for spin-zero particles by a basis transformation [171, 33]. Thus, it is worthwhile to discuss the scattering of spin zero mesons. The matrix $\mathscr{M}^{\vec{P}}$ has the indices $\mathscr{M}^{\vec{P}}_{lm,l'm'}$, where $l, l'$ label the irreducible representations of $SO(3)$ and $m, m'$ are the corresponding row indices, with $\vec{P} = \frac{2\pi}{L}\vec{d}$. The explicit expression of $\mathscr{M}^{\vec{d}}$ is,

$$\mathscr{M}^{\mathrm{d}}_{lm,l'm'}\left(q^2\right) \equiv \frac{(-1)^l}{\gamma\pi^{3/2}} \sum_{j=|l-l'|}^{l+l'} \sum_{s=-j}^{j} \frac{i^j}{q^{j+1}} Z^{\vec{d}}_{js}\left(1; q^2\right) C_{lm,js,l'm'} \tag{4.45}$$

$$C_{lm,js,l'm'} \equiv (-1)^{m'} i^{l-j+l'} \sqrt{(2l+1)(2j+1)(2l'+1)} \begin{pmatrix} l & j & l' \\ m & s & -m' \end{pmatrix} \begin{pmatrix} l & j & l' \\ 0 & 0 & 0 \end{pmatrix} \tag{4.46}$$

where $\gamma = E/\sqrt{s}$ the Lorentz boost factor, $C_{lm,js,l'm'}$ is expresses in terms of $3j$-Wigner symbols related to the Clebsch-Gordon coefficients, and $\vec{q} = \frac{L\vec{p}^*}{2\pi}$. The modified zeta function $Z_{lm}^{\vec{d}}$ is defined as,

$$Z_{lm}^{\vec{d}}\left(s;q^2\right) \equiv \sum_{\mathbf{r}\in P_{\vec{d}}} \frac{\mathscr{Y}_{lm}(\mathbf{r})}{(\mathbf{r}^2-q^2)^s} \tag{4.47}$$

The $Z_{lm}^{\vec{d}}\left(s;q^2\right)$ is finite for $l \neq 0$, but the sum Eq. (4.47) converges slowly for practical evaluation. A derivation of a suitable expression for numerical evaluation is given in the Ref. [162]. It reproduces the known result in the special case $m_1 = m_2$ [216]. Assuming $\delta_{l>1} = 0$, the matrix $M$ is $4\times 4$ in the basis $lm = 00, 10, 11, 1-1$ and the expression $\mathscr{M}^{\mathbf{d}}_{lm,l'm'}$ (4.45) leads to the following form for general $\vec{d}$,

$$\mathscr{M}^{\vec{d}}_{lm,l'm'} = \begin{array}{c} \\ 00 \\ 10 \\ 11 \\ 1-1 \end{array} \begin{array}{c} \begin{array}{cccc} 00 & 10 & 11 & 1-1 \end{array} \\ \begin{pmatrix} w_{00} & i\sqrt{3}w_{10} & i\sqrt{3}w_{11} & i\sqrt{3}w_{1-1} \\ -i\sqrt{3}w_{10} & w_{00}+2w_{20} & \sqrt{3}w_{21} & \sqrt{3}w_{2-1} \\ i\sqrt{3}w_{1-1} & -\sqrt{3}w_{2-1} & w_{00}-w_{20} & -\sqrt{6}w_{2-2} \\ i\sqrt{3}w_{11} & -\sqrt{3}w_{21} & -\sqrt{6}w_{22} & w_{00}-w_{20} \end{pmatrix} \end{array}, \tag{4.48}$$

The $Y_{lm}$ by the side denote the SO(3) basis in which the $\mathscr{M}$ matrix is written down. Here we defined $w_{lm}$ to simplify the notation as,

$$w_{lm} = \frac{Z_{lm}^{\vec{d}}}{\pi^{3/2}\sqrt{2l+1}\,\gamma\, q^{l+1}} \tag{4.49}$$

The matrix $\mathscr{M}^{\vec{P}}$ can be further simplified by taking into account the symmetries for a given Little Group ($\vec{P}$) and its irrep $\Lambda$. An example calculation of the quantization condition for $\vec{P} = (0,0,0)$ in the irrep $A_1^+$, using the properties of $Z_{lm}^{\mathrm{d}}\left(s;q^2\right)$, results in,

$$\tan\delta_0\left(p^{*2}\right) = \frac{\pi^{3/2}q}{Z_{00}\left(1;q^2\right)}, \quad l=0 \tag{4.50}$$

In another example, for $A_1$ in $C_{2v}$ in a moving frame[3] $\vec{P} = (1,1,0)$ is given by,

$$\mathbf{d} = e_x + e_y, A_1 \text{ of } C_{2v}: \quad \tan\delta_0\left(p^*\right) = \frac{\pi^{3/2}\gamma q}{Z_{00}^{\mathrm{d}}\left(1;q^2\right)} \quad \text{if } \delta_1\left(p^*\right) \ll \delta_0\left(p^*\right). \tag{4.51}$$

[3] In moving frames, parity is not a good quantum number, which is why $A_1$ doesn't have the $+/-$ notation as in CM frame.

### Baryons

For baryons, using the $t$-matrix parametrization and the total angular-momentum basis of the interacting particles, we obtain

$$\det[\mathscr{M}^{\vec{P}}_{Jlm,J'l'm'} - \delta_{JJ'}\delta_{ll'}\delta_{mm'}\cot\delta_{Jl}] = 0, \tag{4.52}$$

where $M^{\vec{P}}_{Jlm,J'l'm'}$ contains the finite-volume spectra for the scattering of two particles with spins $\vec{s_1}$ and $\vec{s_2}$ and total linear momentum $\vec{P}$. The angular momentum $\vec{l}$ is the contribution from the $l$th partial wave such that the total angular momentum $\vec{J}$ is equal to $\vec{l}+\vec{s_1}+\vec{s_2}$. For fixed $J$ and $l$, we have $-J \leq m \leq J$. Thus, the $\mathscr{M}$ matrix represents the mixing of the different angular momenta in finite volume. In the $t$-matrix, $\delta_{Jl}$ denotes the infinite-volume phase shift for a given $J$ and $l$. It becomes quite evident from the addition of angular momenta that $\mathscr{M}$ is an infinite-dimensional matrix, because of the infinitely many possible values of $l$. To enable a lattice calculation, we need to select a cut-off $l_{max}$, and ignore higher partial waves. This can be justified for small center-of-mass momenta $p^*$, because $\delta(p^*) \propto (p^*)^{2l+1}$.

After imposing a cutoff $l_{max}$, the finite-dimensional matrix $\mathscr{M}$ can be further simplified into a block diagonal form through a basis transformation of the irreps of the symmetry groups of the lattice. Given a lattice symmetry group $G$ with irrep $\Lambda$ (from Table. 6.2), the matrix element in the new basis can be written as

$$\langle \Lambda r J l n | \mathscr{M}^{\vec{P}} | \Lambda' r' J' l' n' \rangle = \sum_{m,m'} c^{\Lambda r n}_{Jlm}\, c^{\Lambda' r' n'}_{J'l'm'}\, \mathscr{M}^{\vec{P}}_{Jlm,J'l'm'}, \tag{4.53}$$

where the row $r$ runs from 1 to the dimension of $\Lambda$, $n$ labels the multiplicity of the irrep, and $c^{\Lambda r n}_{Jlm}$ and $c^{\Lambda' r' n'}_{J'l'm'}$ are the relevant Clebsch-Gordan coefficients as calculated in [112].
From Schur's lemma, we know that $\mathscr{M}^{\vec{P}}$ is block-diagonalized in the new basis,

$$\langle \Lambda r J l n | \mathscr{M}^{\vec{P}} | \Lambda' r' J' l' n' \rangle = \delta_{\Lambda\Lambda'}\delta_{rr'}\mathscr{M}^{\Lambda}_{Jln,J'l'n'}. \tag{4.54}$$

where $\mathscr{M}^{\Lambda}_{Jln,J'l'n'}$ is the matrix which forms the block diagonal for the matrix $\mathscr{M}^{\vec{P}}$. For an example of moving frame with $\vec{P} = (0,0,1)$ for which the Little Group is $C_{2v}$, this block diagonal decomposition in terms of its irreps $G_1$ and $G_2$ is depicted in Fig. 4.4.

Once we have the $\mathscr{M}^{\vec{P}}$, after this we can proceed as we did for mesons to write the full matrix element in terms of zeta functions and calculate the quantization conditions.

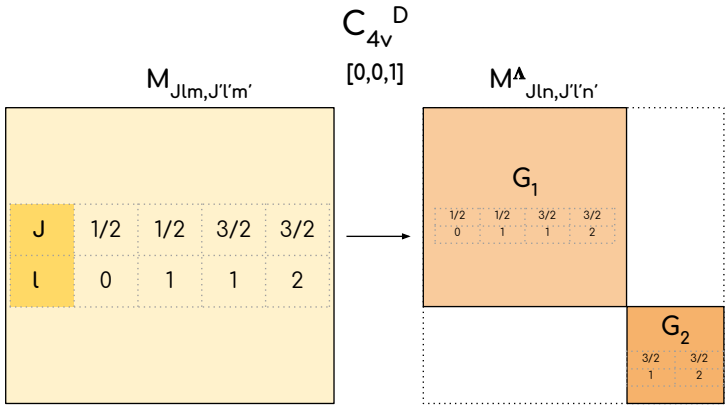


Fig. 4.4 Block diagonalization of the $M$ matrix in the irrep basis. The case shown is for the $C_{4v}^{D}$ group.

**Resonance parameters from lattice**

As discussed in Sec. 2.2.3, a narrow resonant contribution to $t_\ell(s = E^{*2})$ can be described[4] by a Breit-Wigner (BW) form,

$$t_\ell(s) = \frac{\sqrt{s}\Gamma(s)}{m_R^2 - s - \mathrm{i}\sqrt{s}\Gamma(s)}, \tag{4.55}$$

which corresponds to the phase shift

$$\delta_\ell(s) = \arctan \frac{\sqrt{s}\Gamma(s)}{m_R^2 - s}. \tag{4.56}$$

The form of the decay width $\Gamma(s)$ is chosen according to the decay channel of the scattering resonance.

## 4.8 Spectrum interpretation: After taking FV effects

Now that we have discussed the finite volume effects through the Lüscher quantization condition, we are in a position to resolve the finite volume spectra and understand all energy levels. As as example, we will discuss a non-trivial case of finite volume spectra from Ref. [49], in which we have elastic scattering of spin-zero mesons with a S-wave Breit

[4]Note that a typical Breit-Wigner model does not work for very broad resonance such as the $\sigma$ and $\kappa$ scalar resonances [210].

Wigner resonant contribution to the scattering amplitude. Thus we can write,

$$\tan\delta_0\left(E^\star\right) = \frac{E^\star\Gamma\left(E^\star\right)}{m_R^2 - E^{\star 2}} \quad \text{with} \quad \Gamma\left(E^\star\right) = \frac{g^2}{6\pi}\frac{m_R^2}{E^{\star 2}}q^\star \tag{4.57}$$

where $E^\star$ is the center of mass energy, and $q^\star$ is the center of mass momentum. We choose $m_R$ to be 1182 MeV and three increasing values of the coupling, $g = \{1.0, 2.0, 3.0\}$. For a given lattice size $L$, equating Eqs. (4.50) and (4.57) for $A_1^+$ irrep in the center of mass frame, we can obtain $E^\star$ in terms of $L$ for a fixed $g$. The values of $E^\star$ are plotted against $L$ in Fig. (4.5).

In lattice calculations, when we obtain finite volume spectra, it is ambiguous to associate energy level to a specific particle in the continuum. The behaviour of the spectra can be summarized as follows:

- *Extra energy level*: One can notice that at lower coupling, for all $L$, in the vicinity of resonant energy, there is always an extra energy level (beyond those expected in the non-interacting case), which quite often is misinterpreted as the resonance (and a fake plateau is fitted to it and reported as the resonance mass). But as $g$ increases, that extra energy moves further away from the resonant energy level, thus resulting in spurious values.

- *Avoided level-crossing*: This feature is quite evident at points where the non-interacting levels intersect the resonant energy level. If we have a particular lattice simulation at a lattice size $L$ such that at that $L$, the non-interacting levels intersect the resonant energy level, the finite volume spectra drift away from the resonant energy level, and higher the coupling more is the difference from the resonant energy level. Thus, in this case, assigning the continuum resonance to the extra energy level, would be incorrect. Another important observation is that the phase shift changes from 0 to $\pi$ gradually with an increase in the coupling.

This behaviour shows that we always need to perform the Lüscher analysis to extract infinite volume resonance parameters from finite volume spectra, in order to avoid erroneously associating lattice energy levels to the resonance.

Another interesting scenario is that of finite volume spectra near a weakly attractive or repulsive potential. Taking the same example from Ref. [49] in Fig. 4.6, the phase-shift equation is $\tan\delta_0(q^\star) = a_0\, q^\star$ where $a_0$ is the scattering length.

In Ref. [172] it was shown that the energy shift of the lowest two-particle state is proportional to $\frac{-a_0}{mL^3}$ where $a_0$ is the $s$-wave scattering length.

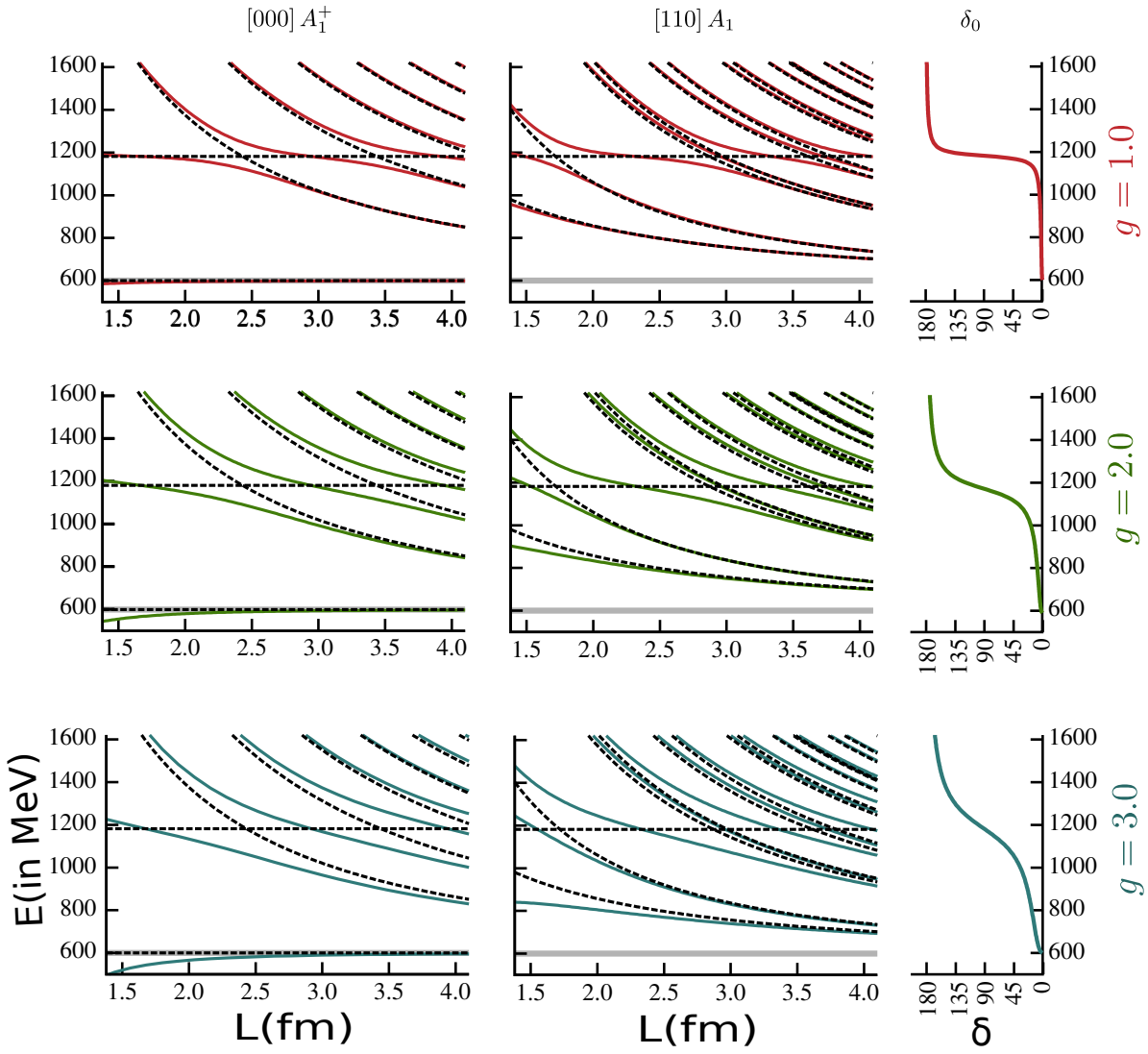


Fig. 4.5 Finite volume energy spectrum in two irreps $A_1^+$ and $A_1$ for a Breit-Wigner resonance with three values of decay couplings. Plotted is the CM frame energy, $E^\star$ in MeV, against $L$ in $fm$. Scattering particles have mass 300 MeV and Breit-Wigner resonant mass is $m_R = 1182$ MeV. Dashed black curves show non-interacting energy levels, and the gray band at 600 MeV indicates the kinematic threshold. Rightmost panel shows the elastic phase-shift in degrees. *Figure credits [49]*

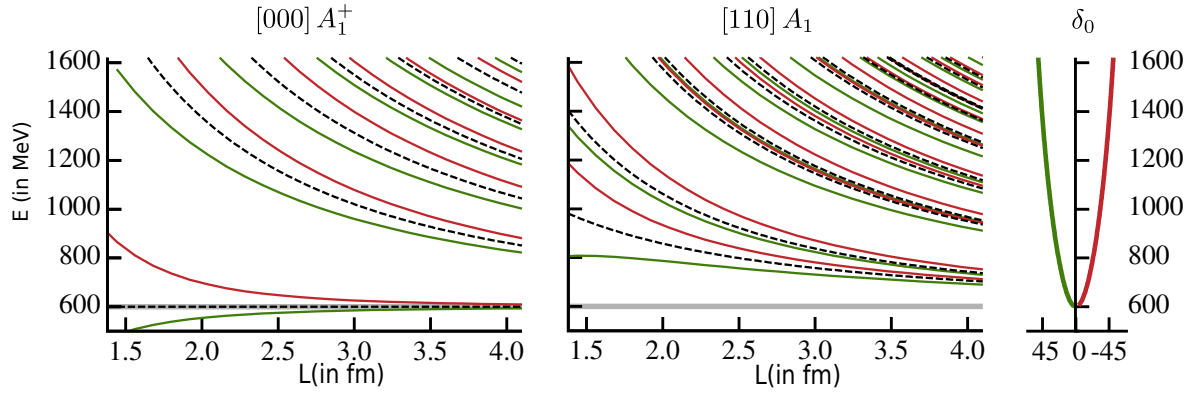


Fig. 4.6 Finite volume spectrum in a rest-frame irrep and a moving-frame irrep for weak attractive (green) and repulsive (red) elastic scattering. Non-interacting energy levels are indicated by the dashed black lines and the gray band shows the kinematic threshold ($2m_\pi$). Plotted is CM-frame energy, $E^\star$ in MeV, against $L$ in $fm$. Scattering particles have mass 300 MeV and the scattering length is $|a| = 0.32\ fm$. Rightmost panel shows the corresponding elastic phase-shift in degrees. *Figure credits [49]*

The distinguishing feature of the finite volume spectra for a weakly attractive potential is the existence of an energy level below the threshold ($E_{\text{thres.}} = 2\sqrt{p^2 + m_\pi^2}$) with the phase shift transitioning from 0 to $\pi/4$ very gradually. On the other hand, for the weakly repulsive potential the phase shift transitioning from 0 to $-\pi/4$ very gradually. We can conclude that qualitatively this behaviour is consistent with the results in Ref. [172].

## 4.9 Resonance photoproduction

Using the phase shifts computed from the Lüscher formalism, the Lellouch-Lüscher formalism for $1 \to 2$ in Ref. [51, 155] can be utilized to calculate the electromagnetic transition form factors. There have been studies on the lattice of transition form factors by calculating 3-point correlation functions with the electromagnetic current insertion in finite volume, but the intermediate state was always considered on lattices with pion mass in which it was a stable hadron [202, 223, 203]. Also another drawback of these calculations is the Maiani-Testa no-go theorem, according to which there is no simple relation between Euclidean-space time correlators and the desired Minkowski-spacetime transition matrix elements, whenever the initial or final states contain multiple hadrons [174]. Going beyond spectroscopy, Lellouch and Lüscher also found the relation between finite-volume and infinite-volume $1 \to 2$ transition matrix elements for the case of the nonleptonic weak decay $K \to \pi\pi$ [155]. The formalism was later extended to include all elastic states below the inelastic threshold [165] and to moving frames [67], and more recently to multiple coupled two-body channels [129],

matrix elements of arbitrary external currents with four-momentum transfer [50, 54], and $2 \to 2$ matrix elements [55] (see also Refs. [183, 32, 66, 4, 80, 5] for related work). This generalization of the Lellouch Lüscher formula in Ref. [50] came to be known as the Briceno Walker Loud formalism, which has been conveniently tailored for lattice calculations, as will be discussed in Sec. 5.2.1.

### 4.9.1 Transition form factor

Following [50], we can write the relation between the generic finite-volume matrix element $|\langle \mathbf{1};L|J^{\mu}(0)|\mathbf{2};L\rangle|$, and the infinite-volume matrix element $\mathscr{H}^{\mu}_{2,1} = \langle \mathbf{1}|J^{\mu}(0)|\mathbf{2}\rangle$

$$|\langle \mathbf{1};L|J^{\mu}(0)|\mathbf{2};L\rangle| = \frac{\sqrt{\left(\mathscr{H}^{\mu}_{1,2}\right)\mathscr{R}\left(\mathscr{H}^{\mu}_{2,1}\right)}}{L^3\sqrt{2E_1}} \tag{4.58}$$

where $\mathscr{R}$ is the finite volume residue of the fully-dressed two-hadron propagator defined as,

$$\mathscr{R}\left(E_2,\vec{P}\right) \equiv \lim_{P_0 \to E_2}\left[\frac{(P_0 - E_2)}{\left(\mathbb{I} + \mathrm{i}t_{\ell}(s)\left(\mathbb{I} + \mathrm{i}\mathscr{M}^{\vec{P}}\right)\right)}\right]. \tag{4.59}$$

It can be observed that the denominator is the Lüscher quantization condition inside the determinant. Thus, we can carry over the Lüscher formalism results developed in the previous sections. The infinite-volume matrix element $\mathscr{H}^{\mu}_{1,2}$ can be decomposed in terms of the infinite volume transition amplitude.

The relation Eq. (4.58) takes into account in a relativistic and model-independent way, for strong interactions between hadrons in QCD upto corrections which scale like $\mathscr{O}\left(e^{-m_{\pi}L}\right)$. The use of a single insertion of the vector current is accurate upto first order of pertubation theory in QED. In the next chapter, we discuss the application of this formalism.

# Chapter 5

# Meson resonances & photoproduction

In the last decade, there have been extensive studies of low-lying meson resonances on the lattice, starting with the $\rho$ meson [11, 113, 177, 19, 123, 142, 94, 105, 151, 21, 211, 87, 249, 26, 61, 136, 118, 107, 17] that served as the first evidence for the practical applicability of the Lüscher methodology for extracting resonance parameters. In this chapter we discuss the implementation of the Lüscher formalism to study $\rho$ resonance in $\pi\pi$ scattering. Furthermore, the $\rho$ resonance parameters obtained are taken as input in the Briceno, Walker, Loud formalism to extract resonance photoproduction transition form factor and coupling. This chapter is based on the following two publications:

- C. Alexandrou, L. Leskovec, S. Meinel, J. W. Negele, **S. Paul**, M. Petschlies, A. Pochinsky, G. Rendon, S. Syritsyn, "*P*-wave $\pi\pi$ scattering and the $\rho$ resonance from lattice QCD," Phys.Rev. D96 (2017) no.3, 034525 [11].

- C. Alexandrou, L. Leskovec, S. Meinel, J. W. Negele, **S. Paul**, M. Petschlies, A. Pochinsky, G. Rendon, S. Syritsyn, "$\pi\gamma \to \pi\pi$ transition and the $\rho$ radiative decay width from lattice QCD," Phys.Rev. D98 (2018) no.7, 074502 [12].

## 5.1 $\rho$ resonance

The simplest QCD-unstable hadron[1] is the $\rho$ resonance, which decays into two pions with a branching ratio of 99.9%. As such, it is considered a benchmark for hadron spectroscopy on the lattice.

[1] In the scattering of $n$ QCD-stable hadrons, unstable hadrons correspond to the poles off the real axis as discussed in Sec. 2.2.2.

### 5.1.1 Motivation

The $\rho$ resonance appears as a pole in the $I = 1$ elastic $P$-wave $\pi\pi$ scattering amplitude. This scattering amplitude plays an important role in many Standard Model processes, and its energy dependence must be determined accurately as part of lattice calculations of matrix elements involving the $\rho$ [50], such as $\pi\gamma \to \rho(\to \pi\pi)$ [52, 53] and $B \to \rho(\to \pi\pi)\ell\bar{\nu}_\ell$. Because the scattering is elastic, the energy dependence of the scattering amplitude can be expressed in terms of a single real number, the phase shift. For a simple resonance, such as the $\rho$, the phase shift starts near 0 at the threshold, then goes through $\pi/2$ when the invariant mass is near the mass of the resonance and continues toward $\pi$ as the invariant mass leaves the resonance region.

While the Maiani-Testa theorem [174] prohibits the extraction of scattering amplitudes directly from Euclidean correlation functions in infinite volume (except at the threshold), Lüscher's method [171] circumvents the basic assumptions of this theorem and takes advantage of the finite lattice volume. The energy levels of a two-hadron system in a finite volume are shifted by the interactions between the hadrons. These energy shifts are related to the infinite-volume scattering matrix via the Lüscher quantization condition [171] as briefly summarized in the previous chapter. The Lüscher quantization condition provides a (many-to-one) mapping between the discrete finite-volume multi-hadron spectrum and the elastic scattering amplitude.

The relation was initially derived in the rest frame, and was extended to moving frames and coupled-channels in Refs. [216, 149, 67, 129, 122, 51]. Further generalizations to particles of unequal mass, arbitrary spin, and three-particle systems were given in Refs. [163, 56, 41]. Other methods that have been used to study resonances are the Hamiltonian effective field theory approach [126], which is similar to the Lüscher method, the HALQCD approach [139], where the Nambu-Bethe-Salpeter wave function is calculated and used to determine a potential between two hadrons, and the method of Refs. [179, 14, 13], which relies on a perturbative interpretation of the mixing of nearby states.

### 5.1.2 About $\pi\pi$ scattering

In this section we briefly describe the input parameters for elastic $\pi\pi$ $P$-wave scattering in the $I(J^{PC}) = 1(1^{--})$ channel in the continuum [69].

From Eq. (2.15), a resonant contribution to the phase shift $\delta_\ell$ which depends on the invariant mass ($s$) of the system and the partial wave $\ell$ of the scattering channel, is given by,

$$\delta_\ell(s) = \arctan \frac{\sqrt{s}\Gamma(s)}{m_R^2 - s}. \tag{5.1}$$

In this work, we consider two different Breit Wigner forms (**BW I** and **BW II**) for the $\ell = 1$ decay width $\Gamma(s)$:

- **BW I:** $P$-wave decay width:

$$\Gamma_I(s) = \frac{g_{\rho\pi\pi}^2}{6\pi}\frac{k^3}{s}, \tag{5.2}$$

  where $g_{\rho\pi\pi}$ is the coupling between the $\pi\pi$ scattering channel and the $\rho$ resonance, and $k$ is the scattering momentum defined via $\sqrt{s} = 2\sqrt{m_\pi^2 + k^2}$. This form was used in most previous lattice QCD studies.

- **BW II:** $P$-wave decay width modified with Blatt-Weisskopf barrier factors [242]:

$$\Gamma_{II}(s) = \frac{g_{\rho\pi\pi}^2}{6\pi}\frac{k^3}{s}\frac{1 + (k_R r_0)^2}{1 + (k r_0)^2}, \tag{5.3}$$

  where $k_R$ is the scattering momentum at the resonance position and $r_0$ is the radius of the centrifugal barrier.

In certain cases, for example in $P$-wave $N\pi$ scattering, the phase shift is known to receive both resonant and nonresonant (NR) contributions [168]. We also allow for this possibility in our analysis of $\pi\pi$ scattering and write the full $P$-wave phase shift as

$$\delta_1(s) = \delta_1^{BW}(s) + \delta_1^{NR}(s). \tag{5.4}$$

We investigate three different models for a nonresonant background contribution $\delta_1^{NR}$:

- **NR I:** a constant nonresonant phase $A$:

$$\delta_1^{NR}(s) = A. \tag{5.5}$$

- **NR II:** a nonresonant phase depending linearly on $s$:

$$\delta_1^{NR}(s) = A + Bs, \tag{5.6}$$

where $A$ and $B$ are free parameters.

- **NR III:** zeroth order nonresonant effective-range expansion (ERE):

$$\delta_1^{NR}(s) = \text{arccot}\frac{2a_1^{-1}}{\sqrt{s - s^{thres}}}, \tag{5.7}$$

where $a_1^{-1}$ is the inverse scattering length and $s^{thres} = 4m_\pi^2$ is the $\pi\pi$ threshold invariant mass.

### 5.1.3 Lattice parameters

#### Gauge Ensemble

Table 5.1 Details of the gauge-field ensemble. $N_L$ and $N_T$ denote the number of lattice points in the spatial and time directions. The lattice spacing, $a$, was determined using the $\Upsilon(2S) - \Upsilon(1S)$ splitting. The ensemble was generated with $N_f = 2+1$ flavors of sea quarks with bare masses $am_{u,d}$ and $am_s$, which lead to the given values of $am_\pi$, $am_N$, and $am_{\eta_s}$. The $\eta_s$ is an artificial pseudoscalar $s\bar{s}$ meson that can be used to tune the strange-quark mass [78, 83]. The uncertainties given here are statistical only.

| | C13 | MeV |
|---|---|---|
| $N_L^3 \times N_T$ | $32^3 \times 96$ | |
| $\beta$ | 6.1 | |
| $N_f$ | $2+1$ | |
| $c_{sw}$ | 1.2493097 | |
| $am_{u,d}$ | $-0.285$ | |
| $am_s$ | $-0.245$ | |
| $N_{config}$ | 1041 | |
| $a$ [fm] | 0.11403(77) | |
| $L$ [fm] | 3.649(25) | |
| $am_\pi$ | 0.18295(36) | 316.59(62) |
| $am_N$ | 0.6165(23) | 1066.84(40) |
| $am_{\eta_s}$ | 0.3882(19) | 671.77(3.29) |
| $m_\pi L$ | 5.865(32) | |
| $Z_V$ | 0.7903(2) | |

The parameters of the lattice gauge-field ensemble are given in Table 5.1. The gluon action is a tadpole-improved tree-level Symanzik action [233, 231, 232, 172]. We use the same

clover-improved Wilson action [251, 220] for the sea and valence quarks. The gauge links in the fermion action are smeared using one level of stout smearing [191] with staple weight $\rho = 0.125$. The lattice scale reported in Table 5.1 was determined from the $\Upsilon(2S) - \Upsilon(1S)$ splitting [78, 180] calculated with NRQCD [158] at the physical $b$-quark mass. The strange-quark mass is consistent with its physical value as indicated by the ''$\eta_s$" mass [78, 83].

**The pion mass and dispersion relation**

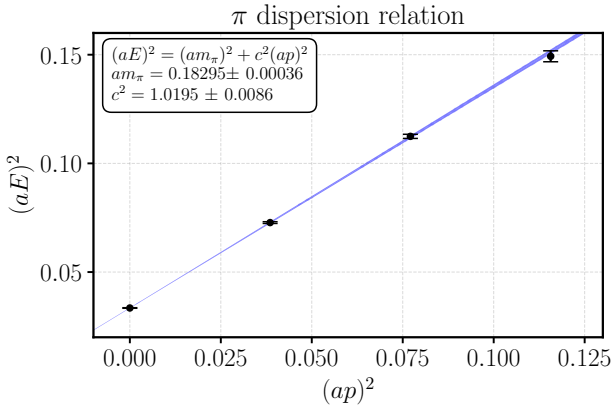


Fig. 5.1 Pion dispersion relation. The pion mass and speed of light determined from the dispersion relation are consistent with a relativistic dispersion relation with the rest frame pion energy.

To determine the $\rho$ resonance parameters with the Lüscher method we need to know the pion dispersion relation. We performed a fit of the pion energies using the form $(aE)^2 = (am_\pi)^2 + c^2(ap)^2$ in the range $0 \leq p^2 \leq 3(2\pi/L)^2$, which yields $am_\pi = 0.18295(36)$ and $c^2 = 1.0195(86)$. Given that $c^2$ is consistent with 1 within 2%, we use the relativistic dispersion relation $(aE)^2 = (am_\pi)^2 + (ap)^2$ in the subsequent analysis.

### 5.1.4 Interpolating fields and two-point functions

We aim to determine the values of the scattering phase shift $\delta_1(s)$ for many values of $s$ near the $\rho$ resonance mass. The lattice volume we use ($L \approx 3.6$ fm) allows us to obtain a sufficient number of energy levels in the region of interest from only the single volume combined with multiple moving frames, $\vec{P}$. In this work, we use the moving frames and irreducible representations ($\Lambda$) listed in Table 5.2.

Table 5.2 The reference frames (i.e., total momenta $\vec{P}$), associated Little Groups, and irreducible representations used to determine the multi-hadron spectrum in the $I(J^{PC}) = 1(1^{--})$ channel. For the Little Groups and irreps with give both the Schönflies notation and the subduction notation in parenthesis. Due to a reduction in symmetry, the Little Group irreps $\Lambda$ contain not only $J^P = 1^-$ states, but also higher $J$, starting with $J = 3$. In the channel we investigate, the $J = 3$ contributions have been shown to be negligible [93, 87].

| $\vec{P}\,[\frac{2\pi}{L}]$ | Little Group | Irrep $\Lambda$ | $J$ |
|---|---|---|---|
| $(0,0,0)$ | $O_h$ | $T_1^-$ | $1^-, 3^-, \ldots$ |
| $(0,0,1)$ | $D_{4h}$ ($\mathrm{Dic}_4$) | $A_2^-$ ($A_1$) | $1^-, 3^-, \ldots$ |
| $(0,0,1)$ | $D_{4h}$ ($\mathrm{Dic}_4$) | $E^-$ ($E$) | $1^-, 3^-, \ldots$ |
| $(0,1,1)$ | $D_{2h}$ ($\mathrm{Dic}_2$) | $B_1^-$ ($A_1$) | $1^-, 3^-, \ldots$ |
| $(0,1,1)$ | $D_{2h}$ ($\mathrm{Dic}_2$) | $B_2^-$ ($B_1$) | $1^-, 3^-, \ldots$ |
| $(0,1,1)$ | $D_{2h}$ ($\mathrm{Dic}_2$) | $B_3^-$ ($B_2$) | $1^-, 3^-, \ldots$ |
| $(1,1,1)$ | $D_{3d}$ ($\mathrm{Dic}_3$) | $A_2^-$ ($A_1$) | $1^-, 3^-, \ldots$ |
| $(1,1,1)$ | $D_{3d}$ ($\mathrm{Dic}_3$) | $E^-$ ($E$) | $1^-, 3^-, \ldots$ |

**Interpolating fields**

The spectra in the frames and irreps listed in Table 5.2 are obtained from two-point correlation functions constructed using two different types of interpolating fields: local single-hadron quark-antiquark interpolating fields $\{O_{\bar{q}q}\}$, and two-hadron interpolating fields $\{O_{\pi\pi}\}$. We choose the quantum numbers $J^{PC} = 1^{--}$ and $I = 1, I_3 = 1$ (corresponding to the $\rho^+$ resonance[2]), and write

$$O_{\bar{q}q}(t,\vec{P}) = \sum_{\vec{x}} \bar{d}(t,\vec{x})\,\Gamma\,u(t,\vec{x})\,\mathrm{e}^{\mathrm{i}\vec{P}\cdot\vec{x}}, \tag{5.8}$$

$$O_{\pi\pi}(t,\vec{p}_1,\vec{p}_2) = \frac{1}{\sqrt{2}}\left(\pi^+(t,\vec{p}_1)\,\pi^0(t,\vec{p}_2) - \pi^0(t,\vec{p}_1)\,\pi^+(t,\vec{p}_2)\right), \tag{5.9}$$

where $\vec{P} = \vec{p}_1 + \vec{p}_2$, and the single-pion interpolators are given by

$$\pi^+(t,\vec{p}) = \sum_{\vec{x}} \bar{d}(t,\vec{x})\,\gamma_5\,u(t,\vec{x})\,\mathrm{e}^{i\vec{p}\cdot\vec{x}}$$

$$\pi^0(t,\vec{p}) = \sum_{\vec{x}} \frac{1}{\sqrt{2}}\left(\bar{u}(t,\vec{x})\,\gamma_5\,u(t,\vec{x}) - \bar{d}(t,\vec{x})\,\gamma_5\,d(t,\vec{x})\right)\mathrm{e}^{i\vec{p}\cdot\vec{x}}.$$

We do not include quark-antiquark interpolators with derivatives, as past calculations have shown that such interpolators do not improve the determination of the spectrum near the $\rho$ resonance mass region [151].

[2]Due to the exact isospin symmetry in our lattice QCD calculation all three isospin components $\rho^+, \rho^-$, and $\rho^0$ are degenerate.

In Eq. (5.8), we use two different $\Gamma$ matrices, namely $\gamma_i$ and $\gamma_0\gamma_i$, which all overlap with the $I(J^{PC}) = 1(1^{--})$ quantum numbers. The single-hadron interpolators are projected to the finite-volume irreps $\Lambda$ of the Little Group $LG(\vec{P})$ for the momentum $\vec{P}$ using

$$O^{\Lambda,\vec{P}}_{\bar{q}q}(t) = \frac{\dim(\Lambda)}{N_{LG(\vec{P})}} \sum_{\hat{R}\in LG(\vec{P})} \chi_\Lambda(\hat{R}) \hat{R}\, O_{\bar{q}q}(t,\vec{P}), \tag{5.10}$$

where $\dim(\Lambda)$ is the dimension of the irrep, $N_{LG(\vec{P})}$ is the order of the Little Group, and $\chi_\Lambda(\hat{R})$ is the character of $\hat{R} \in LG(\vec{P})$ [185].

The second interpolator type, Eq. (5.9), is built from products of two single-pion interpolators as discussed in Sec. 4.2.2, and projected to the irrep $\Lambda$ of the Little Group. In this case, the projection proceeds through the formula given in Ref. [94]:

$$O^{\Lambda,\vec{P}}_{\pi\pi}(t) = \frac{\dim(\Lambda)}{N_{LG(\vec{P})}} \sum_{\hat{R}\in LG(\vec{P})} \chi_\Lambda(\hat{R}) \Big( \pi^+(t,\vec{P}/2+\hat{R}\vec{p})\, \pi^0(t,\vec{P}/2-\hat{R}\vec{p}) - \pi^0(t,\vec{P}/2+\hat{R}\vec{p})\, \pi^+(t,\vec{P}/2-\hat{R}\vec{p}) \Big), \tag{5.11}$$

where

$$\vec{p} = \frac{\vec{P}}{2} + \frac{2\pi}{L}\vec{m}, \;\; \vec{m} \in \mathbb{Z}^3. \tag{5.12}$$

An alternative method to construct the interpolators is the subduction method [187, 86, 214], which gives the same types of interpolators as we find with the projection method.s

We use the schematic notation $O_1$ for quark-antiquark interpolators with $\gamma_i$, $O_2$ for quark-antiquark interpolators with $\gamma_0\gamma_i$, and $O_3$, $O_4$ for two-pion interpolators with the $\vec{m} = (0,0,\pm 1)$ and $\vec{m} = (0,\pm 1,\pm 1)$ possible $\vec{p}$ in the given irrep.

### Wick contractions

The correlation matrix $C^{\Lambda,\vec{P}}_{ij}(t)$ is obtained from the interpolators defined above as

$$C^{\Lambda,\vec{P}}_{ij}(t_f - t_i) = \langle O^{\Lambda,\vec{P}}_i(t_f)\, O^{\Lambda,\vec{P}}_j(t_i)^\dagger \rangle\,, \tag{5.13}$$

where $t_i$ is the source time and $t_f$ is the sink time. The correlation matrix elements are expressed in terms of quark propagators by performing the Wick contractions (i.e., by performing the path integral over the quark fields in a given gauge-field configuration). The resulting quark-flow diagrams are shown in Fig. 5.2 (for the case $I = 1$ considered here,

further disconnected diagrams[3] cancel due to exact isospin symmetry). In this section, we use the generic notation $\bar{q}q$ for the $i = 1,2$ interpolators and $\pi\pi$ for the $i = 3,4$ interpolators to describe our method.

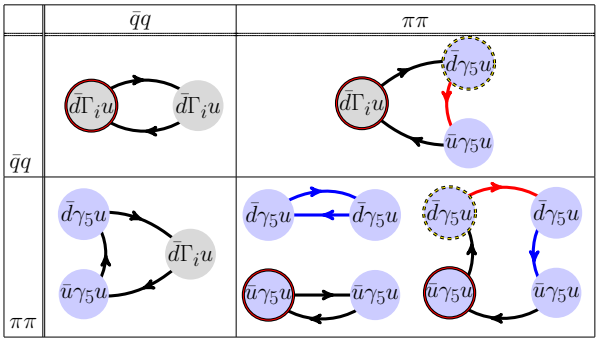


Fig. 5.2 The Wick contractions corresponding to the correlation matrix elements of type $C_{\bar{q}q-\bar{q}q}$ (upper-left corner), $C_{\pi\pi-\bar{q}q}$ (lower-left corner), $C^{\text{direct}}_{\pi\pi-\pi\pi}$ and $C^{\text{box}}_{\pi\pi-\pi\pi}$ (lower-right corner). The source location for the forward propagator is shown with a black circle around the interpolating field, while a dotted circle indicates a sequential source. The red lines indicate sequential propagators and the blue lines indicate stochastic all-to-all propagators. The lower left diagram is not computed directly, and is instead obtained as the conjugate of the upper right diagram.

The diagrams in Fig. 5.2 are obtained from point-to-all propagators, sequential propagators and stochastic timeslice-to-all propagators as discussed in Sec. 4.3.1. The signal enhancement methods implemented are:

**a. Smearing:** To enhance the dominance of the lowest lying states contributing to a correlator we apply source and sink smearing to the propagator types listed above: for all inversions of the Dirac matrix we replace $D^{-1} \to W\left[U_{\text{APE}}\right] D^{-1} W\left[U_{\text{APE}}\right]^{\dagger}$, where $W\left[U_{\text{APE}}\right]$ denotes the Wuppertal-smearing operator [124] using an APE-smeared gauge field [6] with the parameters $n = 25$, $\alpha_{APE} = 2.5$. Since the source and sink smearing is always applied, we will not denote it explicitly.

**b. Coherent sequential sources:** In order to increase the available statistics for a fixed number of gauge configurations we calculate all correlators for 8 equidistant source locations separated in time by $T/8$ and with spatial source coordinates independently and uniformly sampled over the spatial lattice. We then take results from all source locations and average over them.

[3] These refer to the type of Wick contractions where a contraction line originating from a source goes back to the same source i.e. sink is the source.

To reduce the computational cost for the sequential propagators, we insert 2 point-to-all propagators into a single sequential source before inverting the Dirac matrix on the latter:

$$\begin{aligned} S_{seq} &= D^{-1}\,\xi_{seq}, \\ \xi_{seq}(t,\vec{x}) &= \Gamma\,\mathrm{e}^{i\vec{p}\cdot\vec{x}}\left(\delta_{t,t_i^{(0)}}\,S_f\big(t_i^{(0)},\vec{x};t_i^{(0)},\vec{x}_i\big)+\delta_{t,t_i^{(1)}}\,S_f\big(t_i^{(1)},\vec{x};t_i^{(1)},\vec{x}_i\big)\right), \end{aligned} \tag{5.14}$$

where $t_i^{(1)} = t_i^{(0)} + T/2 \bmod T$.

The correlation matrix is then built from these propagators as follows:

**a.** $\bar{q}q - \bar{q}q$ **correlators:** The typical 2-point correlator with a single-hadron interpolator at source and sink is constructed using point-to-all propagators:

$$\begin{aligned} C_{\bar{q}q-\bar{q}q}(t_f-t_i;\vec{p}_f,\Gamma_f;\vec{p}_i,\Gamma_i) = -\sum_{\vec{x}_f}\mathrm{Tr}\big(&(\gamma_5 S_f(t_f,\vec{x}_f;t_i,\vec{x}_i)\,\gamma_5)^{\tilde{\dagger}} \\ &\times\Gamma_f\,S_f(t_f,\vec{x}_f;t_i,\vec{x}_i)\,\Gamma_i\big)\mathrm{e}^{i\vec{p}_f\cdot\vec{x}_f+i\vec{p}_i\cdot\vec{x}_i}. \end{aligned} \tag{5.15}$$

Above, $(\quad)^{\tilde{\dagger}}$ denotes the Hermitian adjoint with respect to only spin-color indices. We use the convention $\vec{p}_f = -\vec{p}_i$.

The direct diagram of the $C_{\pi\pi-\pi\pi}$ correlation function is the product of two of the previous correlators with $\Gamma_i = \gamma_5 = \Gamma_f$. However, translational invariance allows only one of the $\vec{x}_i$ to be fixed. To perform the sum over $\vec{x}_i$, we use the one-end-trick and define

$$\begin{aligned} C_{\bar{q}q-\bar{q}q,oet}(t_f-t_i;\Gamma_f,\vec{p}_f;\Gamma_i,\vec{p}_i) = -\sum_{\alpha,\beta}\sum_{\vec{x}_f}&(\Gamma_i\gamma_5)_{\alpha\beta}\,\phi_{t_i,0,\beta}(t_f,\vec{x}_f)^{\tilde{\dagger}}\,\gamma_5\Gamma_f \\ &\times\phi_{t_i,\vec{p}_i,\alpha}(t_f,\vec{x}_f)\,\mathrm{e}^{i\vec{p}_f\cdot\vec{x}_f}, \end{aligned} \tag{5.16}$$

where $\phi_{t_i,0,\beta}$ and $\phi_{t_i,\vec{p}_i,\alpha}$ are the spin-diluted stochastic timeslice-to-all propagators from Eqs. (4.17) and (4.20). The stochastic-sample index $r$ is suppressed for brevity.

**b.** $\pi\pi - \bar{q}q$ **correlators:** The only contribution to the $I = 1$ correlators with a two-pion interpolator at the source and a single-hadron interpolator at the sink reads

$$\begin{aligned} C_{\bar{q}q-\pi\pi}(t_f-t_i;\Gamma_f,\vec{p}_f;\vec{p}_{i_1},\vec{p}_{i_2}) = -\sum_{\vec{x}_f}\mathrm{Tr}\big(&S_f(t_f,\vec{x}_f;t_i,\vec{x}_{i_1})^{\tilde{\dagger}}\,\gamma_5\Gamma_f \\ &\times S_{seq}(t_f,\vec{x}_f;t_i,\vec{p}_{i_2};t_i,\vec{x}_{i_1})\big)\,\mathrm{e}^{i\vec{p}_f\cdot\vec{x}_f+i\vec{p}_{i_1}\cdot\vec{x}_{i_1}}, \end{aligned} \tag{5.17}$$

where $S_{seq}$ is the sequential propagator from Eq.(5.14).

**c. $\pi\pi-\pi\pi$ correlators:** The direct diagram in the lower right panel of Fig. 5.2 is obtained as the product of two $\bar{q}q-\bar{q}q$ correlators as

$$C^{\text{direct}}_{\pi\pi-\pi\pi}(t_f-t_i;\vec{p}_{f_1},\vec{p}_{f_2},\vec{p}_{i_1},\vec{p}_{i_2}) = C_{\bar{q}q-\bar{q}q}(t_f-t_i;\gamma_5,\vec{p}_{f_1};\gamma_5,\vec{p}_{i_1}) \times C_{\bar{q}q-\bar{q}q,oet}(t_f-t_i;\gamma_5,\vec{p}_{f_2};\gamma_5,\vec{p}_{i_2})\,. \tag{5.18}$$

The box-type diagram in the lower right panel of Fig. 5.2 requires point-to-all, sequential, and stochastic propagators and is calculated in two steps:

$$C^{\text{box}}_{\pi\pi-\pi\pi}(t_f-t_i,\vec{p}_{f_1},\vec{p}_{f_2},\vec{p}_{i_1},\vec{p}_{i_2}) = -\frac{1}{N_{\text{sample}}}\sum_{r=1}^{N_{\text{sample}}}\sum_{\alpha,a}\eta^r_\phi\left(t_f,t_i;\vec{p}_{f_1};\vec{x}_{i_1}\right)^a_\alpha \times \eta^r_\xi\left(t_f,t_i;\vec{p}_{f_2},\vec{p}_{i_2};\vec{x}_{i_1}\right)^a_\alpha \mathrm{e}^{i\vec{p}_{i_1}\cdot\vec{x}_{i_1}}\,, \tag{5.19}$$

where

$$\eta^r_\xi\left(t_f,t_i;\vec{p}_{f_2},\vec{p}_{i_2};\vec{x}_{i_1}\right) = \sum_{\vec{x}_{f_2}}\xi^r_{t_f}(t_f,\vec{x}_{f_2})^{\tilde{\dagger}}\,\gamma_5 \times S_{seq}\left(t_f,\vec{x}_{f_2};t_i,\vec{p}_{i_2};t_i,\vec{x}_{i_1}\right)\mathrm{e}^{i\vec{p}_{f_2}\cdot\vec{x}_{f_2}} \tag{5.20}$$

and

$$\eta^r_\phi\left(t_f,t_i;\vec{p}_{f_1};\vec{x}_{i_1}\right) = \sum_{\vec{x}_{f_1}} S_f(t_f,\vec{x}_{f_1};t_i,\vec{x}_{i_1})^{\tilde{\dagger}} \times \phi^r_{t_f,0}(t_f,\vec{x}_{f_1})\,\mathrm{e}^{i\vec{p}_{f_1}\cdot\vec{x}_{f_1}}\,. \tag{5.21}$$

In Eqs. (5.19), (5.20) and (5.21) we used $\gamma_5$-Hermiticity of the quark propagator as well as $\Gamma_{i_j}=\gamma_5=\Gamma_{f_j}\,, j=1,2$.

The $\pi\pi$-$\pi\pi$ elements of the correlation matrix are constructed as

$$C_{\pi\pi-\pi\pi}(t_f-t_i;\vec{p}_{f_1},\vec{p}_{f_2},\vec{p}_{i_1},\vec{p}_{i_2}) = \frac{1}{2}C^{\text{direct}}_{\pi\pi-\pi\pi}(t_f-t_i;\vec{p}_{f_1},\vec{p}_{f_2},\vec{p}_{i_1},\vec{p}_{i_2}) - C^{\text{box}}_{\pi\pi-\pi\pi}(t_f-t_i;\vec{p}_{f_1},\vec{p}_{f_2},\vec{p}_{i_1},\vec{p}_{i_2}). \tag{5.22}$$

### 5.1.5 Spectrum results

We extract the energy levels $E_n^{\Lambda,\vec{P}}$ from the correlation matrices using two alternative methods. The first method, discussed in Sec. 5.1.5, is the variational analysis, also known as the generalized eigenvalue problem (GEVP). The second method, discussed in Sec. 5.1.5, employs multi-exponential fits directly to the correlation matrix.

### Variational analysis

We checked the GEVP spectrum for $t_0/a \in [2,9]$ and found that the central values are independent of $t_0$ within statistical uncertainties. We set $t_0/a = 3$ for our main analysis, which minimizes the overall statistical noise. The chosen fit types, fit ranges, corresponding $\chi^2$ values, the energies, and other derived quantities are presented in Table 5.3. The operator basis used is $O_{1234}$ in all irreps except $E$, where we only use $O_{123}$ because the energy level dominantly overlapping with $O_4$ is too far above the region of interest.

For each quantity $y$, the first uncertainty given is the statistical uncertainty, obtained from single-elimination jackknife. The second uncertainty is the systematic uncertainty, estimated using the prescription

$$\sigma_y^{sys} = max\left(|y'_{avg} - y_{avg}|, \sqrt{|\sigma_y'^2 - \sigma_y^2|}\right), \tag{5.23}$$

where $y_{avg}$ and $\sigma_y$ are the central value and statistical uncertainty for the chosen fit range specificed in Table 5.3, and $y'_{avg}$, $\sigma'_y$ are the central value and statistical uncertainty obtained with $t_{min}/a$ increased by 1.

Table 5.3 GEVP results for the energy levels. We set $t_0/a = 3$ and use the one-exponential form in Eq. (4.32) to fit the principal correlators. $O_{1234}$ represents $O_1$, $O_2$, $O_3$ and $O_4$ interpolators have been utilized to construct the correlation matrix. The Fit Range column denotes $[\frac{t_{min}}{a}, \frac{t_{max}}{a}]$. Also shown are the corresponding center-of-mass energy $\sqrt{s_n^{\Lambda,\vec{P}}}$ and extracted phase shift $\delta_1\left(\sqrt{s_n^{\Lambda,\vec{P}}}\right)$ where $n$ denotes the label on the energy levels from lowest to the highest. The last column indicates whether the energy level is used our global analysis of $\pi\pi$ scattering (see Sec. 5.1.7).

| $\frac{L}{2\pi}\lvert\vec{P}\rvert$ | $\Lambda$ | Basis | $n$ | Fit range | $\frac{\chi^2}{\text{dof}}$ | $aE_n^{\Lambda,\vec{P}}$ | $a\sqrt{s_n^{\Lambda,\vec{P}}}$ | $\delta_1$ [°] | Included |
|---|---|---|---|---|---|---|---|---|---|
| 0 | $T_1$ | $O_{1234}$ | 1 | 8-18 | 0.82 | 0.4588(16)(12) | 0.4588(16)(12) | 86.0(1.6)(1.2) | Yes |
| 0 | $T_1$ | $O_{1234}$ | 2 | 8-18 | 0.66 | 0.5467(16)(9) | 0.5467(16)(9) | 166.5(2.1)(1.3) | Yes |
| 0 | $T_1$ | $O_{1234}$ | 3 | 7-15 | 1.54 | 0.6713(41)(104) | 0.6713(41)(104) | 172.9(4.7)(168.1) | No |
| 1 | $A_2$ | $O_{1234}$ | 1 | 8-18 | 0.61 | 0.44536(73)(23) | 0.39974(82)(25) | 2.81(25)(9) | Yes |
| 1 | $A_2$ | $O_{1234}$ | 2 | 8-18 | 1.04 | 0.5124(20)(17) | 0.4732(22)(18) | 131.3(1.9)(1.6) | Yes |
| 1 | $A_2$ | $O_{1234}$ | 3 | 9-16 | 0.69 | 0.5983(31)(37) | 0.5652(33)(39) | 6.1(7.1)(8.3) | No |
| 1 | $E$ | $O_{123}$ | 1 | 8-18 | 1.43 | 0.5004(18)(14) | 0.4603(20)(16) | 93.7(1.7)(1.3) | Yes |
| 1 | $E$ | $O_{123}$ | 2 | 8-17 | 1.37 | 0.6136(25)(24) | 0.58134(27)(26) | 166.3(2.8)(2.7) | Yes |
| $\sqrt{2}$ | $B1$ | $O_{1234}$ | 1 | 8-18 | 1.23 | 0.5041(13)(10) | 0.4207(16)(12) | 8.84(89)(68) | Yes |
| $\sqrt{2}$ | $B1$ | $O_{1234}$ | 2 | 8-17 | 1.09 | 0.5557(26)(27) | 0.4814(30)(31) | 144.9(2.3)(2.4) | Yes |
| $\sqrt{2}$ | $B2$ | $O_{1234}$ | 1 | 8-18 | 0.56 | 0.5189(15)(11) | 0.4384(18)(13) | 19.9(1.7)(1.2) | Yes |
| $\sqrt{2}$ | $B2$ | $O_{1234}$ | 2 | 8-18 | 1.18 | 0.5634(26)(23) | 0.4902(30)(27) | 152.0(2.6)(2.4) | Yes |
| $\sqrt{2}$ | $B2$ | $O_{1234}$ | 3 | 8-16 | 1.28 | 0.6717(40)(49) | 0.6116(44)(54) | 158(14)(17) | No |
| $\sqrt{2}$ | $B3$ | $O_{1234}$ | 1 | 9-18 | 0.97 | 0.5376(38)(34) | 0.4603(45)(39) | 99.1(3.5)(3.1) | Yes |
| $\sqrt{2}$ | $B3$ | $O_{1234}$ | 2 | 9-18 | 1.15 | 0.6573(43)(49) | 0.5958(48)(54) | 174(15)(172) | No |
| $\sqrt{2}$ | $B3$ | $O_{1234}$ | 3 | 8-14 | 0.82 | 0.6780(67)(88) | 0.6185(74)(96) | 167.0(5.6)(6.9) | No |
| $\sqrt{3}$ | $A2$ | $O_{1234}$ | 1 | 8-18 | 0.68 | 0.5538(35)(49) | 0.4371(44)(62) | 15.5(3.4)(4.8) | Yes |
| $\sqrt{3}$ | $A2$ | $O_{1234}$ | 2 | 8-16 | 1.41 | 0.5905(35)(39) | 0.4827(43)(48) | 149(11)(13) | Yes |
| $\sqrt{3}$ | $A2$ | $O_{1234}$ | 3 | 8-16 | 1.10 | 0.6093(49)(50) | 0.5055(59)(60) | 156.5(7.5)(14.4) | No |
| $\sqrt{3}$ | $E$ | $O_{123}$ | 1 | 8-16 | 0.71 | 0.5641(37)(41) | 0.4501(47)(50) | 44.4(5.0)(5.3) | Yes |
| $\sqrt{3}$ | $E$ | $O_{123}$ | 2 | 7-16 | 0.72 | 0.6195(33)(54) | 0.5178(39)(64) | 160.6(3.3)(5.4) | Yes |

### Matrix fit analysis

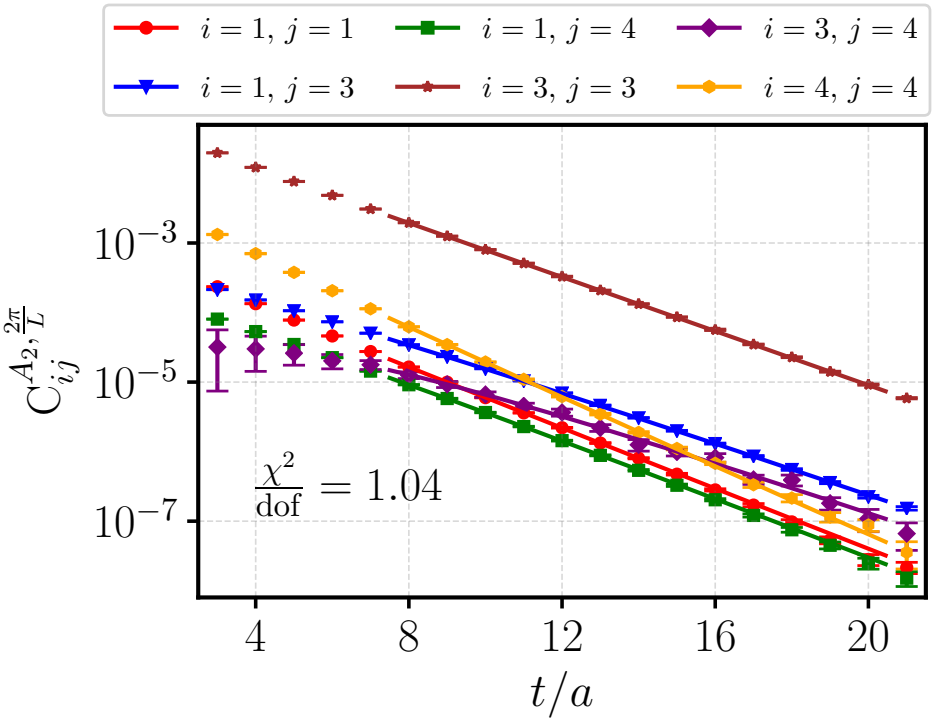


Fig. 5.3 Sample matrix fit with $N_{states} = 3$ for $|\vec{P}| = \frac{2\pi}{L}, \Lambda = A_2$ in the range between $t_{min}/a = 8$ and $t_{min}/a = 20$.

An example matrix fit is shown in Fig. 5.3. In the matrix fits, we excluded the interpolating fields $O_2$, which are very similar to $O_1$ and did not provide useful additional information. For each $(\Lambda, \vec{P})$, we performed either $3 \times 3$ matrix fits (including $O_1$, $O_3$, $O_4$) with $N_{states} = 3$ or $2 \times 2$ matrix fits (including $O_1$ and $O_3$) with $N_{states} = 2$. We set $t_{max} = 20$ and varied $t_{min}$. The matrix fit results for $aE_n^{\Lambda,\vec{P}}$ are shown as the black diamonds in the right panels of Figs. 5.4 and 5.5. We observe that the results for all extracted energy levels stabilize for $t_{min} \gtrsim 8$.

### Comparison between GEVP and MFA

The results obtained from the GEVP and the MFA are compared in Figs. 5.4 and 5.5. The left panels show the effective energy

$$aE_{eff}^n(t) = \ln \frac{\lambda_n(t,t_0)}{\lambda_n(t+a,t_0)} \tag{5.24}$$

of the GEVP principal correlators, while the right panes show the fit results $aE^n_{fit}$ from both the GEVP and the MFA as a function of $t_{min}$ (we did not find any significant dependence on $t_{max}$). For the GEVP, we show both one- and two-exponential fits using Eqs. (4.32) and (4.34). We find that the one-exponential GEVP fit results are very similar (both in central value and uncertainty) to the MFA results, except for the $n = 3$ energy level of the $|\vec{P}| = \sqrt{2}\frac{2\pi}{L}, \Lambda = B_1$ correlation matrix where the principal correlator obtained from the GEVP with the basis $O_{1234}$ does not show a plateau and we do not extract this energy level. Surprisingly, we found that removing the second quark-antiquark operator $O_2$ from the basis yields a stable plateau and stable fit results for the $n = 3$ energy level, as shown in Fig. 5.6. Note that $O_2 \sim \bar{q}\gamma_0\gamma_i q$ has a very similar structure as $O_1 \sim \bar{q}\gamma_i q$. For $n = 1$ and $n = 2$, the one-exponential fit results for the chosen $t_{\mathrm{min}}/a = 8$ change by less than $0.5\sigma$ when removing $O_2$. We also performed additional GEVP fits with a reduced basis in all other irreps, and found that none of the fitted energies changed significantly (in fact, the reduced basis gives slightly larger uncertainties in most cases). Given that the $n = 3$ energy in the $B_1$ irrep is above the $4\pi$ and $K\bar{K}$ thresholds, we do not use this energy level in our further analysis.

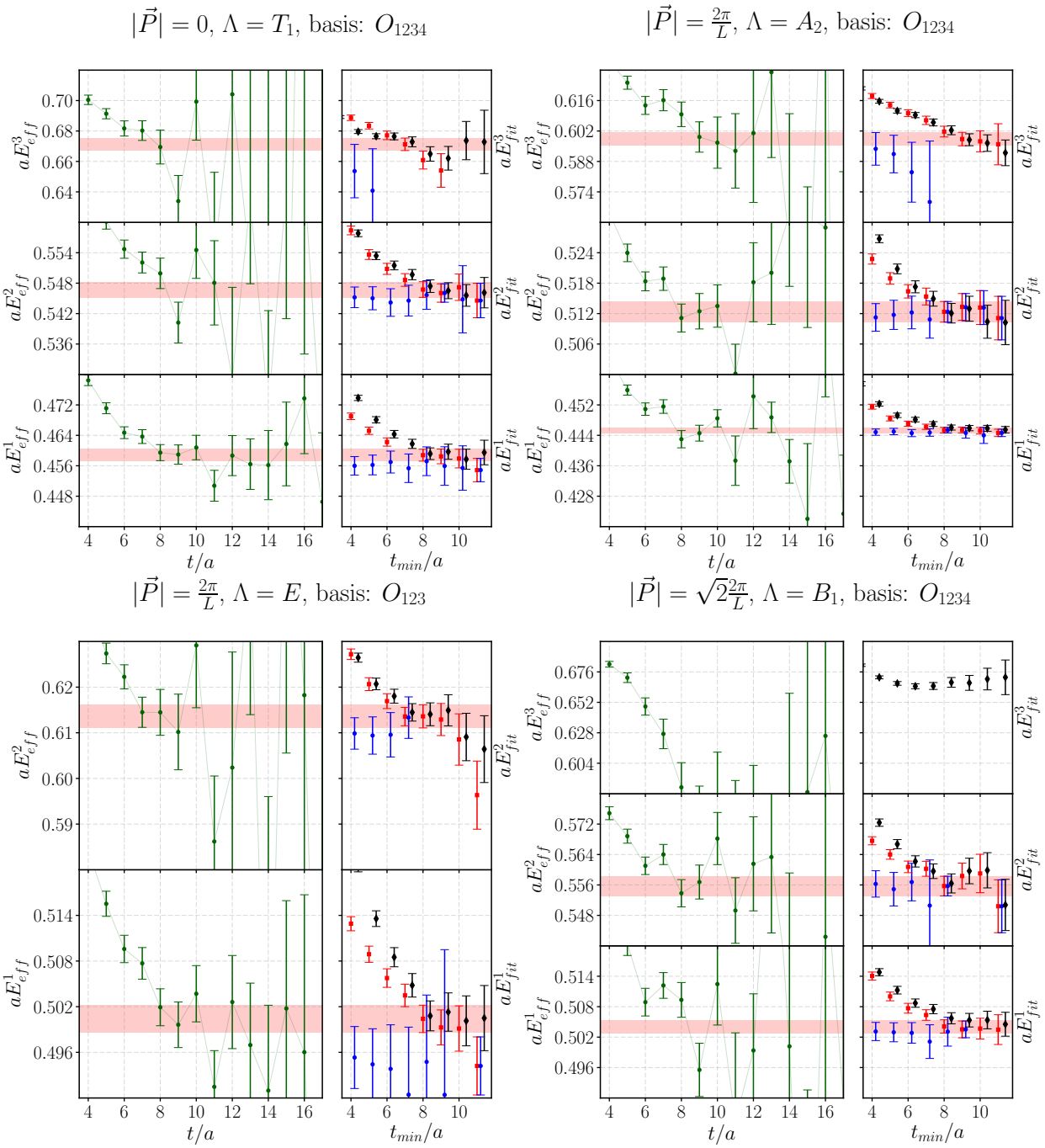


Fig. 5.4 Comparison between MFA and GEVP for the momentum frames and irreps $\frac{L}{2\pi}|\vec{P}| = 0, 1, \sqrt{2}$ and $\Lambda = T_1, A_2, E, B_1$, respectively. The green circles on the left panel show the effective energies $E^n_{eff}$ determined from the principal correlators. In the right panel we present the fitted energies as they depend on the choice of $t_{min}$. Black diamonds are obtained from MFA, red squares are obtained from the single exponential fits to the principal correlator [see Eq. (4.32)], and blue circles are from two-exponential fits to the principal correlator [see Eq. (4.34)]. Note that not all two-exponential fits are shown, as they can become unstable. The red horizontal bands give the $1\sigma$ statistical-uncertainty ranges of the selected one-exponential GEVP fits listed in Table 5.3.

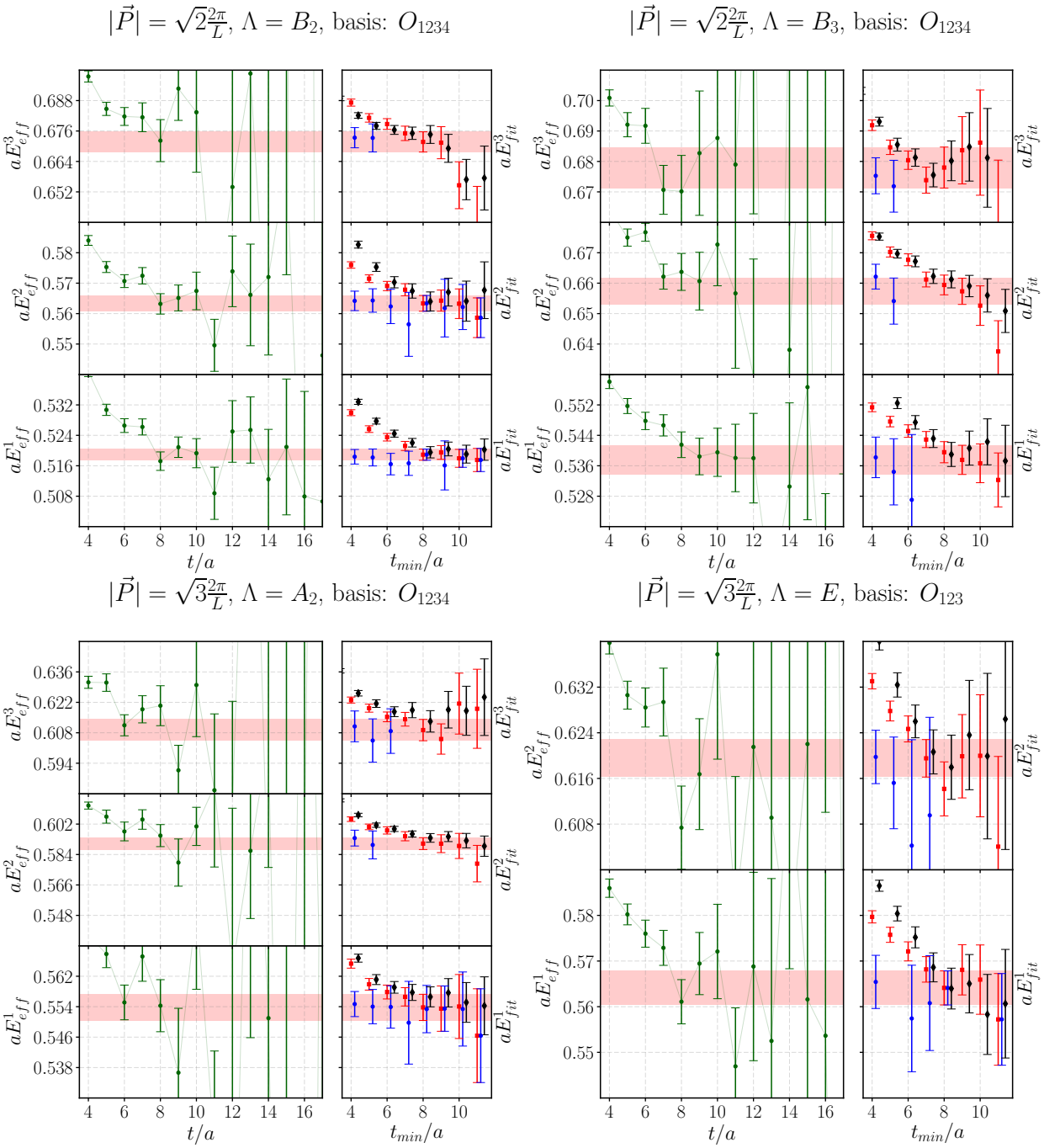


Fig. 5.5 As in Fig. 5.4, but for $\frac{L}{2\pi}|\vec{P}| = \sqrt{2}, \sqrt{3}$ and $\Lambda = B_2, B_3, A_2, E$.

Finally, we note that the two-exponential fits to the GEVP principal correlators find plateaus at much smaller $t_{min}$ but are significantly noisier compared to the MFA and one-exponential GEVP fits. Overall, we have shown that the MFA and GEVP methods are equivalent, and we use the one-exponential GEVP fit results given in Table 5.3 in our further analysis. These results are also indicated with the red bands in Figs. 5.4 and 5.5.

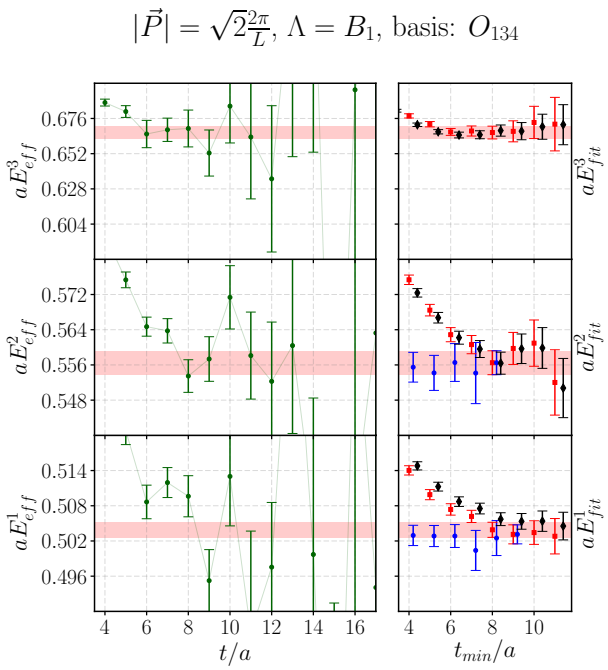


Fig. 5.6 Comparison between MFA and GEVP for the $B_1$ irrep with $|\vec{P}| = \sqrt{2}\frac{2\pi}{L}$ as in Fig. 5.4, but with $O_2$ removed from the basis for the GEVP.

### 5.1.6 The Lüscher analysis: formalism

Even though we have some energy levels with quite large invariant mass (see Table 5.3), we limit our energy region of interest below $0.55a^{-1}$ where we are safely away from the $4\pi$ ($\approx 0.73$) and $K\bar{K}$ ($\approx 0.6$) thresholds [64] and can safely perform the elastic scattering analysis of the Lüscher method.

The quantization condition for elastic $\pi\pi$ scattering is

$$\det\left(\mathbb{1} + \mathrm{i}t_\ell(s)(\mathbb{1} + \mathrm{i}\mathscr{M}^{\vec{P}})\right) = 0, \tag{5.25}$$

where $t_\ell(s)$ is the infinite-volume scattering amplitude, which is related to the infinite-volume scattering phase shift $\delta_\ell(s)$ via Eq. (4.44). The quantization condition (5.25) then reduces to the following equations for each $\vec{P}$ and $\Lambda$:

$$
\begin{aligned}
&\vec{P} = 0, \quad \Lambda = T_1\text{:} \\
&\cot\delta_1(s_n^{\Lambda,\vec{P}}) = w_{0,0}\left(k_n^{\Lambda,\vec{P}}, L\right) \\
&\vec{P} = \frac{2\pi}{L}(0,0,1),\ \Lambda = A_2\text{:} \\
&\cot\delta_1(s_n^{\Lambda,\vec{P}}) = w_{0,0}\left(k_n^{\Lambda,\vec{P}}, L\right) + 2w_{2,0}\left(k_n^{\Lambda,\vec{P}}, L\right) \\
&\vec{P} = \frac{2\pi}{L}(0,0,1),\ \Lambda = E\text{:} \\
&\cot\delta_1(s_n^{\Lambda,\vec{P}}) = w_{0,0}\left(k_n^{\Lambda,\vec{P}}, L\right) - w_{2,0}\left(k_n^{\Lambda,\vec{P}}, L\right) \\
&\vec{P} = \frac{2\pi}{L}(0,1,1),\ \Lambda = B_1\text{:} \\
&\cot\delta_1(s_n^{\Lambda,\vec{P}}) = w_{0,0}\left(k_n^{\Lambda,\vec{P}}, L\right) + \frac{1}{2}w_{2,0}\left(k_n^{\Lambda,\vec{P}}, L\right) + \mathrm{i}\sqrt{6}w_{2,1}\left(k_n^{\Lambda,\vec{P}}, L\right) - \sqrt{\frac{3}{2}}w_{2,2}\left(k_n^{\Lambda,\vec{P}}, L\right) \\
&\vec{P} = \frac{2\pi}{L}(0,1,1),\ \Lambda = B_2\text{:} \\
&\cot\delta_1(s_n^{\Lambda,\vec{P}}) = w_{0,0}\left(k_n^{\Lambda,\vec{P}}, L\right) + \frac{1}{2}w_{2,0}\left(k_n^{\Lambda,\vec{P}}, L\right) - \mathrm{i}\sqrt{6}w_{2,1}\left(k_n^{\Lambda,\vec{P}}, L\right) - \sqrt{\frac{3}{2}}w_{2,2}\left(k_n^{\Lambda,\vec{P}}, L\right) \\
&\vec{P} = \frac{2\pi}{L}(0,1,1),\ \Lambda = B_3\text{:} \\
&\cot\delta_1(s_n^{\Lambda,\vec{P}}) = w_{0,0}\left(k_n^{\Lambda,\vec{P}}, L\right) - w_{2,0}\left(k_n^{\Lambda,\vec{P}}, L\right) + \sqrt{6}w_{2,2}\left(k_n^{\Lambda,\vec{P}}, L\right) \\
&\vec{P} = \frac{2\pi}{L}(1,1,1),\ \Lambda = A_2\text{:} \\
&\cot\delta_1(s_n^{\Lambda,\vec{P}}) = w_{0,0}\left(k_n^{\Lambda,\vec{P}}, L\right) - \mathrm{i}\sqrt{\frac{8}{3}}w_{2,2}\left(k_n^{\Lambda,\vec{P}}, L\right) - \sqrt{\frac{8}{3}}\left(\mathrm{Re}\left[w_{2,1}\left(k_n^{\Lambda,\vec{P}}, L\right)\right] + \mathrm{Im}\left[w_{2,1}\left(k_n^{\Lambda,\vec{P}}, L\right)\right]\right) \\
&\vec{P} = \frac{2\pi}{L}(1,1,1),\ \Lambda = E\text{:} \\
&\cot\delta_1(s_n^{\Lambda,\vec{P}}) = w_{0,0}\left(k_n^{\Lambda,\vec{P}}, L\right) + \mathrm{i}\sqrt{6}w_{2,2}\left(k_n^{\Lambda,\vec{P}}, L\right). \qquad (5.26)
\end{aligned}
$$

The scattering analysis can be performed in two different ways, and in this work we present a comparison between the methods:

- In the first approach, Eqs. (5.26) are used to map each individual energy level $(s_n^{\Lambda,\vec{P}})$ to the corresponding value of the scattering phase shift $\delta_1(s_n^{\Lambda,\vec{P}})$. One then fits a phase-shift model to the extracted values of $\delta_1(s_n^{\Lambda,\vec{P}})$.

- In the second approach, a model for the $t$-matrix is fitted directly to the spectrum via the quantization condition [119]. This method has proven to be quite successful in recent years [86–88, 250, 249, 89, 48]. Unlike the first approach, the $t$-matrix fit method is also well-suited for more complicated coupled-channel analyses.

### 5.1.7 The Lüscher analysis: results

**Direct fits to the phases**

The discrete $P$-wave phase shifts determined for several $\vec{P},\Lambda$ are listed in Table 5.3 with to the invariant masses.

We then fit the models described in Sec. 5.1.2 to the phase shift points.

To correctly estimate the uncertainties of the model parameters, we include the uncertainties in both $\sqrt{s}$ and $\delta_1$ in the construction of the $\chi^2$ function. To this end, we define

$$\chi^2 = \sum_{\vec{P},\Lambda,n} \sum_{\vec{P}',\Lambda',n'} \sum_{i\in\left\{\sqrt{s_n^{\Lambda,\vec{P}}},\, \delta_1(s_n^{\Lambda,\vec{P}})\right\}} \sum_{j\in\left\{\sqrt{s_{n'}^{\Lambda',\vec{P}'}},\, \delta_1(s_{n'}^{\Lambda',\vec{P}'})\right\}} (y_i^{avg} - f_i)[C^{-1}]_{ij}(y_j^{avg} - f_j), \quad (5.27)$$

where $i$ and $j$ are generalized indices labeling both the data points for $\sqrt{s}$ and $\delta_1$. The covariance matrix $C$ is therefore a $2N \times 2N$ matrix, where $N = 15$ is the total number of energy levels included in the fit (see the last column of Table 5.3). For $i$ corresponding to a $\sqrt{s}$ data point, the function $f_i$ is equal to a nuisance parameter $\sqrt{s_n^{\Lambda,\vec{P}}}$; for $i$ corresponding to a $\delta_1$ data point, the function $f_i$ is equal to the phase shift model evaluated at the corresponding $\sqrt{s_n^{\Lambda,\vec{P}}}$. The total number of parameters in the fit is thus equal to $N$ plus the number of parameters in the phase shift model.

When constructing the covariance matrix, we included the correlations between all invariant-mass values and the correlations between all phase-shift values. We found that the covariance matrix becomes ill-conditioned when including also the cross-correlations between $\sqrt{s}$ and $\delta_1$ as expected when dealing with fully correlated data. We therefore, neglect these contributions in the evaluation of $\chi^2$. The cross-correlations are nevertheless accounted for in our estimates of the parameter uncertainties, which are obtained by jackknife resampling.

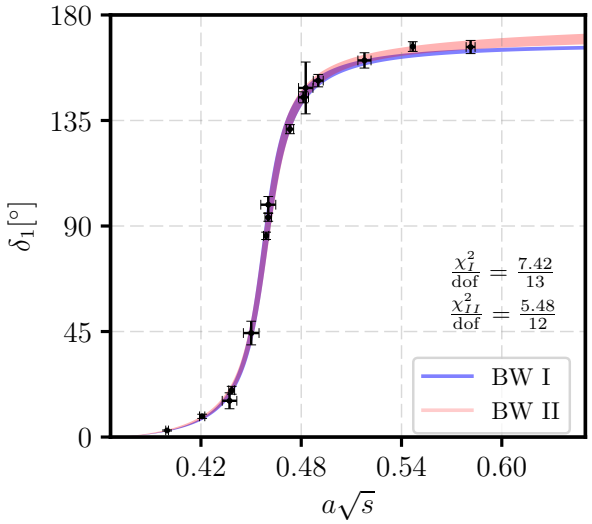


Fig. 5.7 Comparison of fitting **BW I** versus fitting **BW II** to the phase shift data. The bands indicate the $1\sigma$ statistical uncertainty.

Table 5.4 Comparison of the parameters for the resonant **BW I** and **BW II**.

| Model | $\frac{\chi^2}{\mathrm{dof}}$ | $am_\rho$ | $g_{\rho\pi\pi}$ | $(ar_0)^2$ |
|---|---|---|---|---|
| **BW I** | 0.571 | 0.4599(19)(13) | 5.76(16)(12) | |
| **BW II** | 0.457 | 0.4600(18)(13) | 5.79(16)(12) | 8.6(8.0)(1.2) |

The fit of the simplest possible model, **BW I**, is shown as the blue curve in Fig. 5.7 and the resulting parameters $m_\rho$ and $g_{\rho\pi\pi}$ are given in the first row of Table 5.4. As before, the first uncertainty given is statistical, and the second uncertainty is the systematic uncertainty arising from the choice of $t_{min}$. To obtain the latter, we repeated the Breit-Wigner fit for the phase shifts extracted with $t_{min} + a$ for all energy levels, and then applied Eq. (5.23) to $m_\rho$ and $g_{\rho\pi\pi}$. We follow the same procedure for all other models.

We then investigate the effect of adding the Blatt-Weisskopf barrier factors [242] to the decay width appearing in the Breit-Wigner parametrization of $\delta_1(s)$, which leads to model **BW II**. The resulting fit is shown as the red curve in Fig. 5.7 (alongside the blue **BW I** curve) and the resulting parameters are given in the second row of Table 5.4. The **BW II** model appears to give a slightly better description of the data at high invariant mass, but the parameters $m_\rho$ and $g_{\rho\pi\pi}$ are essentially unchanged. Furthermore, the centrifugal barrier radius $r_0$ is consistent with zero at the $1.1\sigma$ level, indicating that it is not a very significant degree of freedom. We note that this could be related to the high pion mass used in our calculation, which limits the phase space available for the decay and suppresses the centrifugal barrier effect.

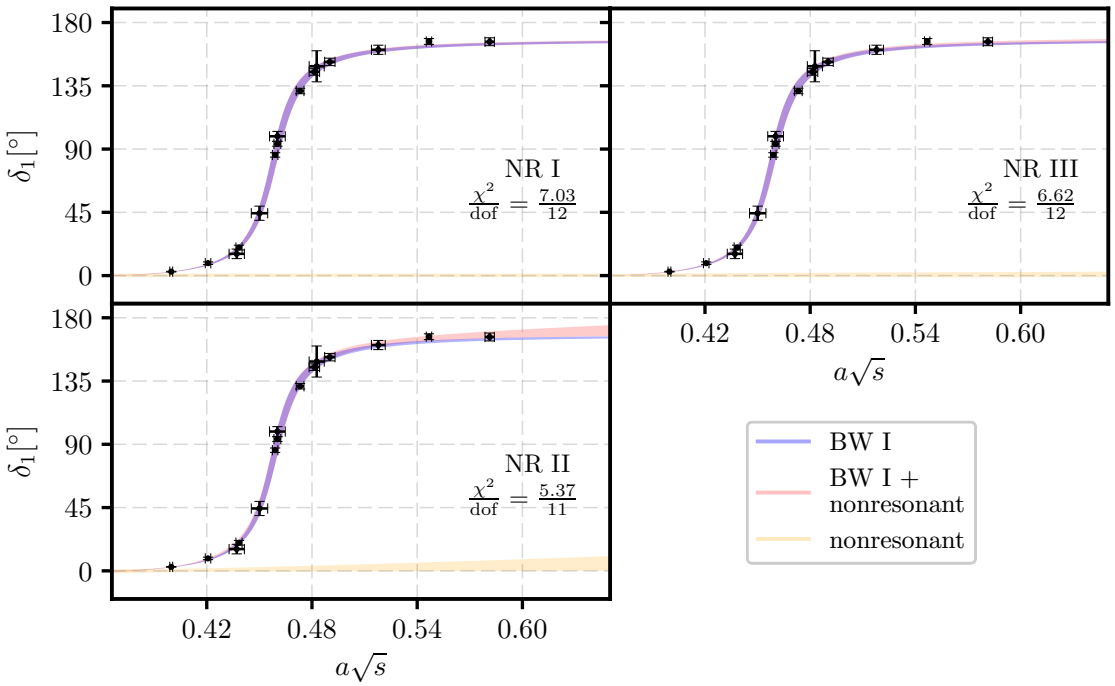


Fig. 5.8 Contribution of nonresonant background models as described in Sec. 5.1.2 to the resonant Breit-Wigner **BW I**.

Table 5.5 Parameters of the phase shift model combining the resonant Breit-Wigner model **BW I** and various nonresonant models.

| Model | $\frac{\chi^2}{\mathrm{dof}}$ | $am_\rho$ | $g_{\rho\pi\pi}$ | | |
|---|---|---|---|---|---|
| **NR I** | 0.586 | 0.4600(19)(13) | 5.74(17)(14) | $A = 0.16(31)(18)°$ | |
| **NR II** | 0.488 | 0.4602(19)(13) | 5.84(21)(20) | $A = -2.9(2.7)(3.4)°$ | $a^{-2}B = 19.2(16.6)(20.1)°$ |
| **NR III** | 0.552 | 0.4601(19)(13) | 5.74(16)(13) | $aa_1^{-1} = -19.8(27.4)(98.1)$ | |

We continue by investigating whether there is a nonresonant contribution to the scattering phase shift. We first add a nonresonant contribution to the resonant model **BW I**. In Fig. 5.8 we compare the resonant-only fit (blue curve) with the full fits for three different forms of the nonresonant contributions (red curves). For clarity, we also show the nonresonant contributions obtained from the full fits separately (orange curves). The fit results are given in Table 5.5. We find that the parameters of each of the three parametrizations **NR I** (constant phase), **NR II** (a nonresonant phase depending linearly on $s$), and **NR III** (zeroth-order Effective Range Expansion[4] are consistent with zero, and the results for $m_\rho$ and $g_{\rho\pi\pi}$ also do not change significantly.

[4]Defined as $\delta_1^{NR} = \cot^{-1}\left(\frac{-2a}{\sqrt{s-s^{\mathrm{thres}}}}\right)$ where $a$ is the inverse scattering length

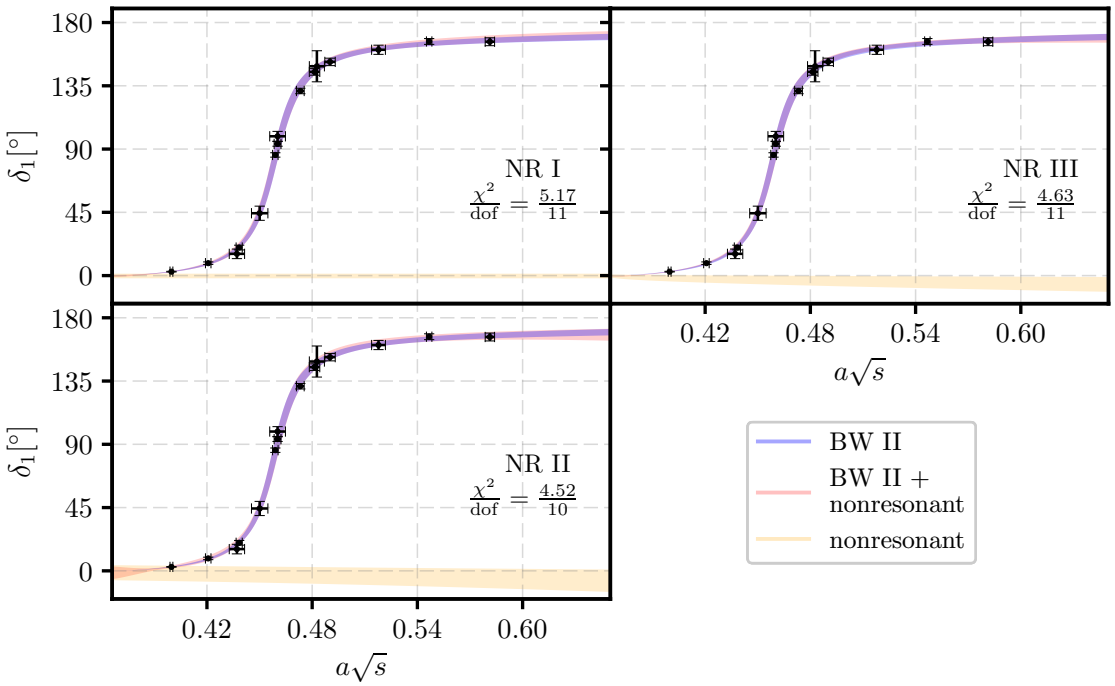


Fig. 5.9 Contribution of nonresonant background models as described in Sec. 5.1.2 to the resonant Breit-Wigner model **BW II**. None of the background phase shift models shows a strong sign of deviation away from 0.

Table 5.6 Parameters of the phase shift model combining the resonant Breit-Wigner model **BW II** and various nonresonant models.

| Model | $\frac{\chi^2}{\mathrm{dof}}$ | $am_\rho$ | $g_{\rho\pi\pi}$ | $(ar_0)^2$ | | |
|---|---|---|---|---|---|---|
| **NR I** | 0.470 | 0.4599(19)(26) | 5.83(20)(21) | 15.8(23.5)(1825.8) | $A = -0.28(0.73)(12.56)°$ | |
| **NR II** | 0.452 | 0.4596(20)(14) | 5.77(21)(20) | 107.0(440.9)(631.0) | $A = 1.3(4.5)(5.3)°$ | $a^{-2}B = -19.8(16.0)(17.0)°$ |
| **NR III** | 0.421 | 0.4595(18)(8) | 5.78(20)(9) | 109.7(128.7)(117.6) | $aa_1^{-1} = 2.4(1.7)(2.4)$ | |

Performing the analogous analysis for the resonant model **BW II** gives the phase shift curves shown in Fig. 5.9 and fit parameters in Table 5.6. Again, the parameters of the nonresonant contribution are consistent with zero, and $m_\rho$ and $g_{\rho\pi\pi}$ do not change significantly. When adding the nonresonant contributions to the **BW II** model, the uncertainty of the centrifugal barrier parameter $r_0$ increases substantially.

Overall, we find that the minimal resonant model **BW I** is sufficient for a good description of our results for the elastic $I = 1$ $\pi\pi$ $P$-wave scattering.

### Fitting a $t$-matrix to the spectrum

For the $t$-matrix fit to the spectrum, we define the $\chi^2$ function as

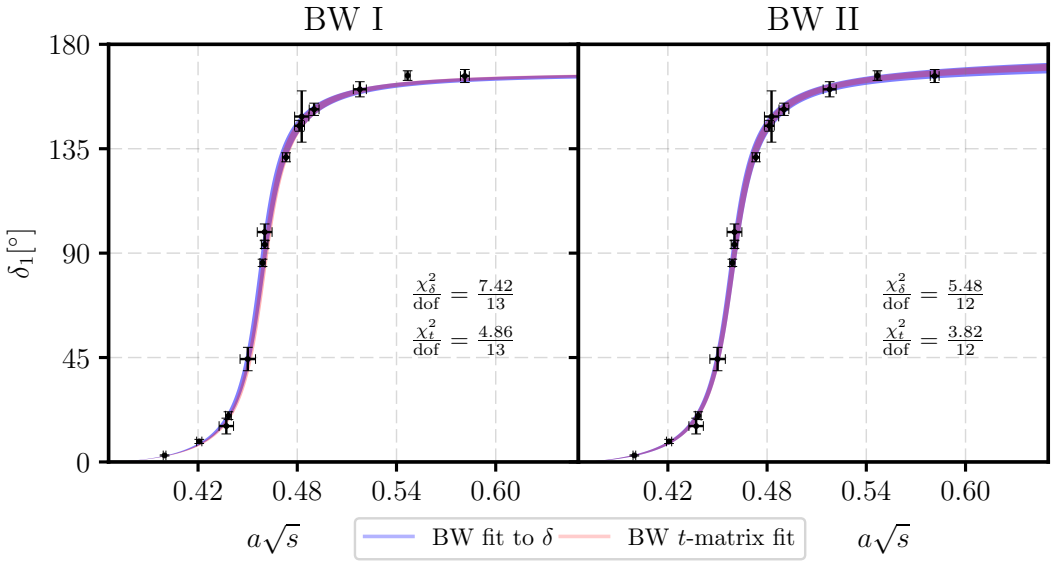


Fig. 5.10 Comparison of $t$-matrix fit and fit to the phase shifts for Breit-Wigner models I and II.

Table 5.7 Comparison of $t$-matrix fits with direct fits to the phase shifts.

| Fit type | $\frac{\chi^2}{\mathrm{dof}}$ | $am_\rho$ | $g_{\rho\pi\pi}$ | $(ar_0)^2$ |
|---|---|---|---|---|
| **BW I** Fit to $\delta_1$ | 0.571 | 0.4599(19)(13) | 5.76(16)(12) | |
| **BW I** $t$-matrix fit | 0.374 | 0.4609(16)(14) | 5.69(13)(16) | |
| **BW II** Fit to $\delta_1$ | 0.457 | 0.4600(18)(13) | 5.79(16)(12) | 8.6(8.0)(1.2) |
| **BW II** $t$-matrix fit | 0.318 | 0.4603(16)(14) | 5.77(13)(13) | 9.6(5.9)(3.7) |

$$\chi^2 = \sum_{\vec{P},\Lambda,n} \sum_{\vec{P}',\Lambda',n'} \left( \sqrt{s_n^{\Lambda,\vec{P}}}^{[avg]} - \sqrt{s_n^{\Lambda,\vec{P}}}^{[model]} \right) [C^{-1}]_{\vec{P},\Lambda,n;\vec{P}',\Lambda',n'} \left( \sqrt{s_{n'}^{\Lambda',\vec{P}'}}^{[avg]} - \sqrt{s_{n'}^{\Lambda',\vec{P}'}}^{[model]} \right), \tag{5.28}$$

where the invariant-mass values $\sqrt{s_{n'}^{\Lambda',\vec{P}'}}^{[model]}$ are obtained by solving the inverse Lüscher problem, i.e. determining the finite-volume spectrum from a given $t$-matrix model [119, 87]. Above, $C$ is the matrix of covariances between all invariant-mass values labeled by $\vec{P},\Lambda,n$ (in our case, this is a $15 \times 15$ matrix). The only fit parameters in this approach are the parameters of the $t$ matrix (for example, $am_\rho$ and $g_{\rho\pi\pi}$ for the **BW I** model).

When fitting the $t$-matrix directly to the spectrum we consider only the two resonant models, as results from Sec. 5.1.7 show no indication of a nonresonant phase contribution. The parameters obtained from the $t$-matrix fits are compared to the parameters of the direct fits to the phase shifts in Table 5.7. The plots of the models with parameters from the two different fit approaches are compared in Fig. 5.10. The central values and uncertainties obtained with the two methods are consistent, which confirms previous findings [119, 87] that the two approaches are equivalent not only theoretically but also in practice. We note that the values of $\chi^2/\text{dof}$ are generally quite small. We have tested for the presence of autocorrelations in the data using binning but found no significant effect.

### Final result for the $\rho$ resonance parameters

Given the discussion in the previous sections, we choose to quote the results of the $t$-matrix fit with the resonant Breit-Wigner model **BWI** as our final values of $am_\rho$ and $g_{\rho\pi\pi}$ for the ensemble of gauge configurations used here [with $am_\pi = 0.18295(36)$ and $am_N = 0.6165(23)$]:

$$\begin{matrix} am_\rho = 0.4609(16)(14) \\ g_{\rho\pi\pi} = 5.69(13)(16) \end{matrix} \begin{pmatrix} 1.0 & 0.326 \\ & 1.0 \end{pmatrix}. \tag{5.29}$$

The phase shift curve of our chosen fit is shown in Fig. 5.11. Above, the first uncertainties given are statistical, and the second uncertainties are the systematic uncertainties related to the choice of $t_{min}$ in the spectrum analysis. Also given in Eq. (5.29) is the statistical correlation matrix for $am_\rho$ and $g_{\rho\pi\pi}$. The exponentially suppressed finite-volume errors in $m_\rho$ and $g_{\rho\pi\pi}$ are expected to be of order $\mathcal{O}(\mathrm{e}^{-m_\pi L}) \approx 0.3\%$. Given that we have only one

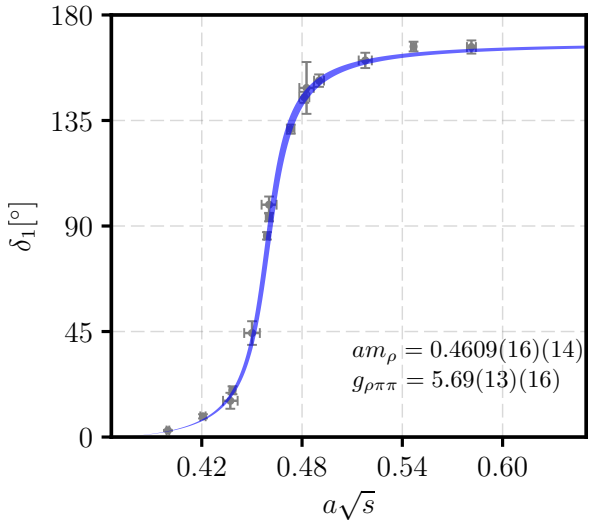


Fig. 5.11 Final result of fitting the resonant model **BW I** to the spectrum via the $t$-matrix fit. The gray data points are the results of the individual phase shift extractions for each energy level, and are not used in the $t$-matrix fit.

lattice spacing, we are unable to quantify discretization errors (except in the pion dispersion relation, Sec. 5.1.3, where we find $c^2$ to be consistent with 1 within 2%). Using the lattice spacing determined from the $\Upsilon(2S) - \Upsilon(1S)$ splitting (see Table 5.1), we obtain

$$\begin{aligned} m_\pi &= 316.6(0.6)_{stat}(2.1)_a \text{ MeV}, \\ m_\rho &= 797.6(2.8)_{stat}(2.4)_{sys}(5.4)_a \text{ MeV}, \\ g_{\rho\pi\pi} &= 5.69(13)_{stat}(16)_{sys}. \end{aligned} \tag{5.30}$$

It is important to note that the lattice spacing uncertainty given here is statistical only. As a consequence of the heavier-than-physical pion mass and lattice artifacts, different quantities used to set the scale of an individual ensemble yield different results for $a$ and hence for $m_\pi$ and $m_\rho$ in units of MeV. We therefore prefer to report the dimensionless ratios

$$\begin{aligned} \frac{am_\pi}{am_N} &= 0.2968(13)_{stat}, \\ \frac{am_\rho}{am_N} &= 0.7476(38)_{stat}(23)_{sys}, \end{aligned} \tag{5.31}$$

in which the lattice scale cancels.

In Fig. 5.12 we compare our results for the $\rho$ coupling and mass with the results of previous studies performed by the CP-PACS collaboration (CP-PACS '07) [19], the ETMC collaboration (ETMC '10) [94], the PACS-CS collaboration (PACS-CS '11) [21], Lang et al.

(Lang et al. '11) [151], the Hadron Spectrum collaboration (HadSpec '12 and HadSpec '15) [87, 249], Pellisier et al. (Pellisier et al. '12) [211], the RQCD collaboration (RQCD '15) [26], Guo et al. (Guo et al. '16) [118], Bulava et al. (Bulava et al. '16) [61], and Fu et al. (Fu et al. '16) [107]. In the right half of the figure, we use the values of $m_\pi$ and $m_\rho$ in MeV as reported in each reference. In the left half of the figure, we instead use the dimensionless ratios $am_\pi/am_N$ and $am_\rho/am_N$, where $am_\pi$ and $am_N$ are the pion and nucleon masses in lattice units computed on the same ensemble as $am_\rho$. The nucleon masses were obtained from Refs. [192, 9, 166, 82, 152, 20, 27, 236].

We find that our value for the coupling $g_{\rho\pi\pi}$ is in good agreement with previous studies both as a function of $m_\pi$ and $am_\pi/am_N$. Furthermore, it is consistent with the general finding that $g_{\rho\pi\pi}$ has no discernible pion-mass dependence in the region between $m_{\pi,phys}$ and approximately $3m_{\pi,phys}$.

Concerning the results for the $\rho$ mass, the left and right panels Fig. 5.12 show very different behavior. This discrepancy arises from the different methods used to set the lattice scale on a single ensemble, which can lead to misleading conclusions. To avoid the substantial ambiguities associated with the scale setting, we only consider the dimensionless ratio $am_\rho/am_N$ in the following discussion.

The $N_f = 2+1$ results for $am_\rho/am_N$ obtained with Wilson-Clover-based fermion actions all approximately lie on a straight line leading to the experimental value (shown as the filled green circle in Fig. 5.12). The $N_f = 2+1$ data points using staggered fermions (Fu et al. '16) are consistent with that line except for one outlier.

The $N_f = 2$ results are dispersed around the $N_f = 2+1$ values in both directions. The discrepancies between the different results could arise from any of several systematic effects, such as excited-state contamination in the determination of the $\pi\pi$ spectrum or the nucleon mass, various potential issues in fitting the data, and discretization errors which manifest themselves for example in deviations from the relativistic continuum dispersion relation for the single-pion energies. Additionally, the Lüscher method only addresses power-law finite volume effects and does not take into account the exponentially suppressed finite-volume effects which are estimated to scale asymptotically as $O(e^{-m_\pi L})$. Note that for some of the studies, these can be as high as $O(10\%)$ and it is thus not clear whether the asymptotic regime is reached. An example for systematics associated with the pion dispersion relation can be seen in the CP-PACS '07 study, where the two different results for $am_\rho$ at the same pion mass were obtained using either the relativistic continuum dispersion relation or a free-boson lattice dispersion relation. An example of systematic effects that might be associated with the data analysis can be seen when comparing the Pellisier et al. '12 results with the Guo

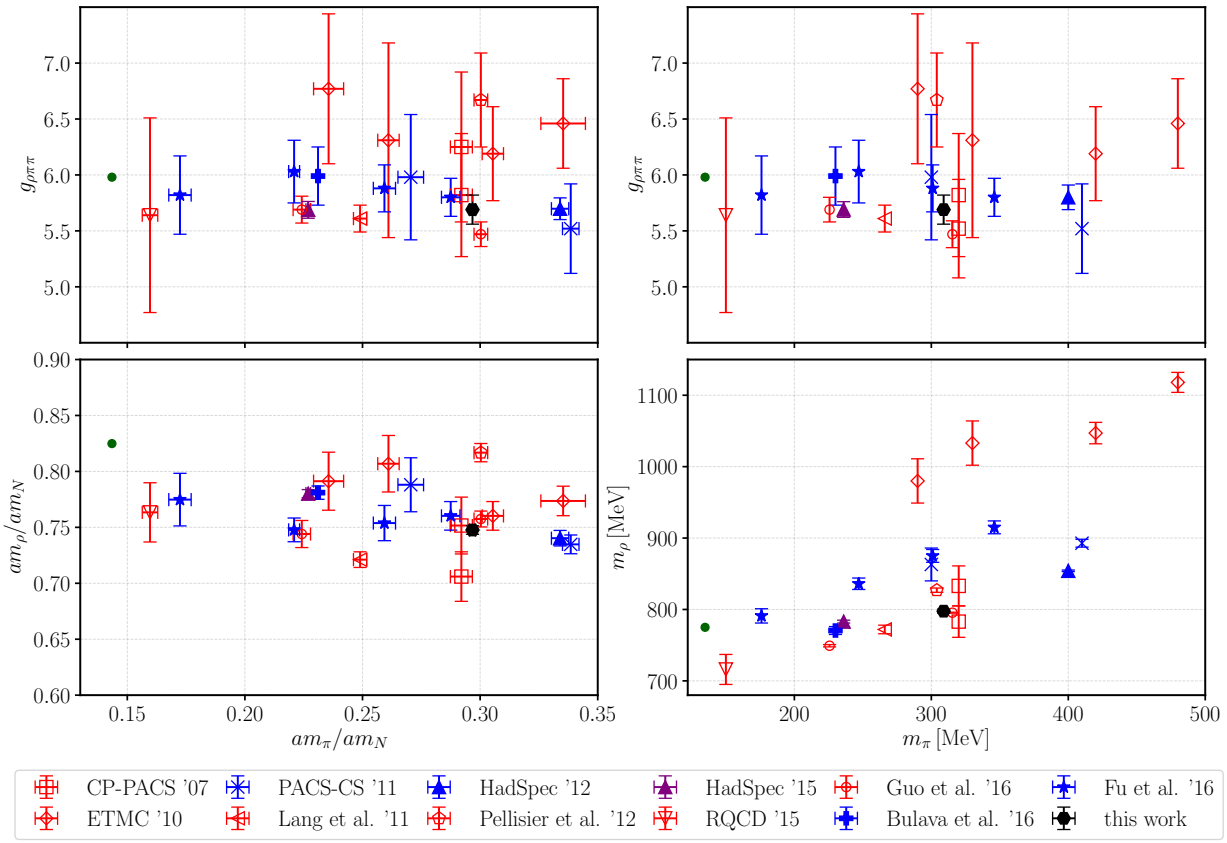


Fig. 5.12 Comparison of our results for the $\rho$ mass and coupling with previous lattice QCD calculations. In the two left panels, we use the dimensionless ratios $am_\rho/am_N$ and $am_\pi/am_N$, while in the two right panels we use $m_\pi$ and $m_\rho$ in MeV as reported by each collaboration (with different scale setting methods; the error bars do not include the scale-setting ambiguities). The open red symbols mark calculations with $N_f = 2$ gauge ensembles, while the filled blue symbols denote calculations with $N_f = 2+1$ sea quarks; the only study so far that explicitly included the $K\bar{K}$ channel, HadSpec '15, is presented as a purple upward facing triangle. The results of our present work are shown with filled black hexagons. In the left-hand plots, the HadSpec '15 results are offset horizontally by $-1.8\%$ so that they do not overlap with the result of Bulava et al. '16. In the right-hand plots, we offset our results by $-8$ MeV to avoid overlap with Guo et al. '16. The experimental values [207], where $g_{\rho\pi\pi}$ was calculated from $\Gamma$ using Eq. (5.2), are shown with filled green circles.

et al. '16 results at $am_\pi/am_N \approx 0.3$. Both studies used the same ensemble, but arrive at significantly different values for the $\rho$ resonance parameters.

Keeping these caveats in mind, it is nevertheless interesting to note that our $N_f = 2+1$ results for both $am_\rho/am_N$ and $g_{\rho\pi\pi}$ agree well with the recent $N_f = 2$ results from Guo et al. '16 at almost the same pion mass. This suggests that the effects of the dynamical strange quark are small at $m_\pi \approx 320$ MeV. The HadSpec '15 study, which explicitly included the $K\bar{K}$ channel in their valence sector, provides further evidence that the strange quark does not play a major role in the $\rho$ resonance mass.

## 5.2 $\pi\pi \to \pi\gamma$ transition & $\rho$ radiative decay

The $\rho$ resonance parameters determined on the lattice can be extended using the Briceno, Hansen, Walker-Loud formalism to calculate the transition form factors for photoproduction and the $\rho$ resonant photocoupling as discussed in Sec. 4.9,

### 5.2.1 Introduction

A concise introduction to resonance photoproduction in lattice QCD has been discussed in Sec. 4.9. The first numerical calculations involving the Lellouch-Lüscher formalism were performed for $K \to \pi\pi$, providing an ab-initio Standard-Model prediction of direct CP violation in this process [44, 140, 25]. More recently, the generalization of the formalism by Briceño, Hansen, and Walker-Loud (BHWL) [50] was applied by the Hadron Spectrum Collaboration to compute the $\pi\gamma \to \pi\pi$ amplitude, with the $\pi\pi$ system in a $P$-wave, as a function of photon virtuality and $\pi\pi$ invariant mass [52, 53]. This amplitude describes $\rho$ photoproduction and radiative decay [197, 150], and also plays an important role in dispersion relations used to calculate the hadronic contributions to the anomalous magnetic moment of the muon [134, 133, 72, 121]. Various theoretical aspects of the $\pi\gamma \to \pi\pi$ process have also been discussed in Refs. [235, 37, 16, 237, 128, 145, 135]. As far as the finite-volume formalism is concerned, the $\pi\gamma \to \pi\pi$ amplitude in the $\rho$ resonance region is one of the simplest $1 \to 2$ processes to study on the lattice, because the $\pi\pi$ scattering is almost completely elastic in the relevant energy region.

In this section, we perform a lattice QCD calculation of the $\pi\gamma \to \pi\pi$ transition building upon Sec. 5.1 on $\pi\pi$ scattering. In contrast to the original Lellouch-Lüscher approach to the nonleptonic $K \to \pi\pi$ decay, where the lattice parameters need to be tuned such that the final and initial hadronic states have equal energy, the BHWL formalism enables us to obtain the $\pi\gamma \to \pi\pi$ amplitude for all $\pi\pi$ energy levels and arbitrary momentum transfer.

### 5.2.2 The $\pi\gamma \to \pi\pi$ process

The resonance photoproduction process $\pi\gamma \to \rho$ is obtained from the more general process $\pi\gamma \to \pi\pi$, where the final $\pi\pi$ state is in $P$-wave and couples strongly to the $\rho$ resonance with isospin $I = 1, I_3 = 1$ and $J^{PC} = 1^{--}$. Throughout this section (except where stated otherwise), we allow the photon to be virtual, but continue to denote it as just $\gamma$. The $\pi\pi$ photoproduction is described by the continuum infinite-volume matrix element $\langle \pi\pi | J^\mu(0) | \pi \rangle$, which is constructed from the initial state $|\pi\rangle$, the insertion of the QED current $J^\mu$ (defined without the factor of $e$) and the final state $|\pi\pi\rangle$ with $I = 1$ and four-momentum $P = (\sqrt{s + \vec{P}^2}, \vec{P})$. The latter is projected to the $P$-wave, so that it couples to the $\rho$ resonance, where the polarization of the system is described by $\varepsilon^\nu(P,m)$ [68]. Due to Lorentz symmetry, the matrix element decomposes like

$$\langle \pi\pi | J^\mu(0) | \pi \rangle = \frac{2\mathrm{i}\mathscr{V}_{\pi\gamma\to\pi\pi}(q^2, s)}{m_\pi} \varepsilon^{\nu\mu\alpha\beta} \varepsilon_\nu(P,m)(p_\pi)_\alpha P_\beta, \tag{5.32}$$

where $q = p_\pi - P$ is the photon four-momentum transfer. Above, the current is taken in position space, and the single-pion state is normalized as

$$\langle \pi, \vec{p}\,'_\pi | \pi, \vec{p}_\pi \rangle = 2E_\pi^{\vec{p}_\pi} (2\pi)^3 \delta^3(\vec{p}_\pi - \vec{p}\,'_\pi). \tag{5.33}$$

The $P$-wave two-pion states with polarization $m$ are given by

$$\begin{aligned} &|\pi\pi, \sqrt{s}, \vec{P}, 1, m\rangle \\ &= \frac{1}{\sqrt{4\pi}} \int \mathrm{d}\hat{\vec{k}}_{\mathrm{cm}}\, Y^*_{1m}(\hat{\vec{k}}_{\mathrm{cm}}) |\pi\pi, \sqrt{s}, \vec{P}, \hat{\vec{k}}_{\mathrm{cm}}\rangle, \end{aligned} \tag{5.34}$$

where $|\pi\pi, \sqrt{s}, \vec{P}, \hat{\vec{k}}_{\mathrm{cm}}\rangle$ is a two-pion state with total momentum $\vec{P}$, relative momentum direction unit vector $\hat{\vec{k}}_{\mathrm{cm}}$ in the center-of-momentum frame, and invariant mass $\sqrt{s}$. These states are normalized according to

$$\begin{aligned} &\langle \pi\pi, \sqrt{s'}, \vec{P}', \hat{\vec{k}}'_{\mathrm{cm}} | \pi\pi, \sqrt{s}, \vec{P}, \hat{\vec{k}}_{\mathrm{cm}} \rangle \\ &= 2E_1\,(2\pi)^3\, 2E_2\,(2\pi)^3\, \delta^3(\vec{k} - \vec{k}\,')\delta^3(\vec{P} - \vec{k} - \vec{P}' + \vec{k}\,'), \end{aligned} \tag{5.35}$$

where $E_1$ and $E_2$ are the individual pion energies,

$$E_1 = \sqrt{m_\pi^2 + \vec{k}^2}, \tag{5.36}$$

$$E_2 = \sqrt{m_\pi^2 + (\vec{P} - \vec{k})^2}. \tag{5.37}$$

These normalizations of states imply that the matrix element Eq. (5.32) is dimensionless and that $\mathscr{V}_{\pi\gamma\to\pi\pi}$ has units of $\mathrm{MeV}^{-1}$. Notice that there is no explicit $\rho$ label in the amplitude; this is because the $\rho$ is not a QCD asymptotic state, but rather a resonance in $P$-wave $\pi\pi$ scattering with $I = 1$ associated with the pole in the scattering amplitude $\mathscr{T}_{\pi\pi\to\pi\pi}$ at $s_P \approx m_R^2 - i m_R \Gamma_R$. The transition amplitude $\mathscr{V}_{\pi\gamma\to\pi\pi}$ depends on both the photon four-momentum transfer $q^2$ and the $\pi\pi$ invariant mass $s$. As discussed in Sec. 2.2.4, we write the photoproduction amplitude $\mathscr{V}_{\pi\gamma\to\pi\pi}(q^2, s)$ as

$$\begin{aligned}\mathscr{V}_{\pi\gamma\to\pi\pi}(q^2, s) &= \sqrt{\frac{16\pi}{k\Gamma(s)}} \frac{F(q^2, s)}{\cot\delta(s) - \mathrm{i}} \\ &= \sqrt{\frac{16\pi}{k\Gamma(s)}} F(q^2, s) \sin\delta(s)\, e^{\mathrm{i}\delta(s)},\end{aligned} \tag{5.38}$$

where the form factor $F(q^2, s)$ no longer has a pole in $s$, and becomes equal to the photocoupling $g_{\rho\pi\gamma}$ for $s = m_R^2 + \mathrm{i} m_R \Gamma_R$ and $q^2 = 0$. More generally, we define the resonant form factor for arbitrary photon virtuality as

$$F_{\pi\gamma\to\rho}(q^2) = F(q^2, m_R^2 - \mathrm{i} m_R \Gamma_R). \tag{5.39}$$

We consider two physically observable quantities we can determine from $|\langle\pi\pi|J_\mu(0)|\pi\rangle|$. The first is the $\pi\gamma \to \pi\pi$ cross section as a function of $\pi\pi$ invariant mass, which in the center-of-momentum frame is given by [52]

$$\sigma(\pi\gamma \to \pi\pi; s, q^2) = \frac{e^2}{16\pi} k\, |\vec{p}_\pi| \frac{4|\mathscr{V}_{\pi\gamma\to\pi\pi}(q^2, s)|^2}{m_\pi^2}. \tag{5.40}$$

This cross section can be measured at $q^2 = 0$, i.e., with a real photon. A second physically observable quantity is related to the $\rho$ resonance, which appears in the $\pi\pi$ system. The $\rho$ radiative decay width $\Gamma(\rho \to \pi\gamma)$ is determined by the photocoupling $g_{\rho\pi\gamma} = F(0, m_R^2 -$

i$m_R\Gamma_R$) as [206]

$$\Gamma(\rho \to \pi\gamma) = \frac{2}{3}\alpha \left(\frac{(m_\rho^2 - m_\pi^2)}{2m_\rho}\right)^3 \frac{|g_{\rho\pi\gamma}|^2}{m_\pi^2}. \tag{5.41}$$

### 5.2.3 Correlation functions

To determine the finite-volume matrix elements we are interested in, we need to compute two-point functions for the single-pion system ($J^{PC} = 0^{-+}$, $I = 1$, $I_3 = 1$) and for the two-pion system ($J^{PC} = 1^{--}$, $I = 1$, $I_3 = 1$), as well as three-point functions with an insertion of the electromagnetic current. The generalized eigenvectors obtained in the spectroscopic analysis of the two-point functions are then used to construct optimized three-point functions. The construction of two-point functions has already been discussed in Sec. 5.1.4.

The current insertion that represents the interactions between the photon and the hadrons depends on the photon momentum $\vec{q}$, which combined with the initial and final state momenta satisfies momentum conservation: $\vec{P} + \vec{q} - \vec{p}_\pi = 0$. For the current insertion operator we use

$$J_\mu(t_J, \vec{q}) = \sum_{\vec{x}} e^{i\vec{q}\cdot\vec{x}} J_\mu(t_J, \vec{x}), \tag{5.42}$$

with the local current

$$J_\mu(t_J, \vec{x}) = Z_V \left(\frac{2}{3}\bar{u}(t_J, \vec{x})\gamma_\mu u(t_J, \vec{x}) - \frac{1}{3}\bar{d}(t_J, \vec{x})\gamma_\mu d(t_J, \vec{x})\right). \tag{5.43}$$

The renormalization coefficient $Z_V$ was determined in Ref. [114] and is listed in Table 5.1.

The three-point correlation functions are then obtained from the sink/source interpolators and current insertion as

$$C_{3,\,\mu,i}^{\vec{p}_\pi,\vec{P},\Lambda,r}(t_\pi, t_J, t_{\pi\pi}) = \langle O_\pi^{\vec{p}_\pi}(t_\pi)\, J_\mu(t_J, \vec{q})\, O_i^{\vec{P},\Lambda,r\,\dagger}(t_{\pi\pi})\rangle, \tag{5.44}$$

where $t_{\pi\pi}$ is the source time, $t_J$ is the current insertion time and $t_\pi$ is the sink time. The three-point function is expressed in terms of quark propagators by evaluating Wick contractions. Fig. 5.13 shows the quark-flow diagrams needed to calculate the $C_{3,\,\mu,i}^{\vec{p}_\pi,\vec{P},\Lambda,r}$ three-point functions. The current-disconnected diagrams labeled (a) and (b), i.e. the diagrams where the quarks flow go from the current $J_\mu$ directly back to the current $J_\mu$, are omitted in this study. For the case of nucleon electromagnetic form factors, such current-disconnected contributions are known to be of order 1% for the quark masses used here [115].

The Wick contractions depicted in Fig. 5.13 are constructed from point-to-all, sequential and stochastic time-slice propagators defined in Sec. 4.3.1. In this section, we will use short

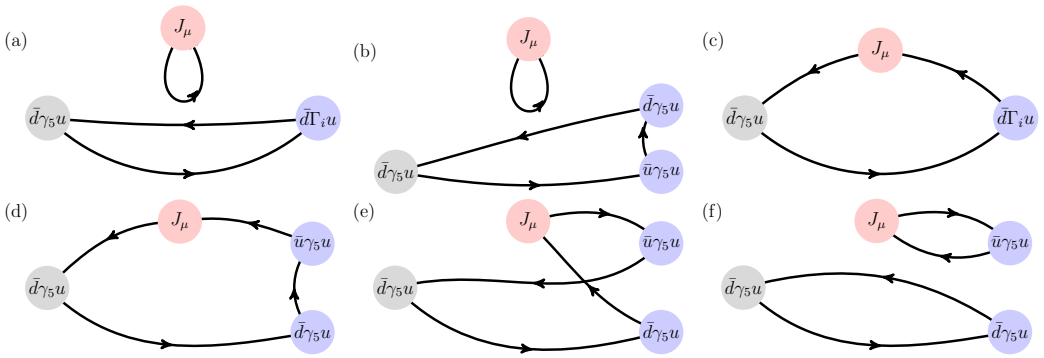


Fig. 5.13 The different topologies of Wick contractions that make up the three-point function $C^{\vec{p}_\pi,\vec{P},\Lambda,r}_{3,\,\mu,i}(t_\pi,t_J,t_{\pi\pi})$.

hand four-vector notation $(x)$ instead of explicit spatial and temporal indices $(t,\vec{x})$. The technique builds upon and extends the scheme used in Sec. 5.1.4 for the construction of two-point correlation functions. This combination of propagator types is optimized considering flexibility to construct all required diagrams, minimal input of stochastic noise into correlation functions and economy in the cost of producing quark propagators and contractions.

The quark propagator loops of the connected diagrams (c) and (d) in Fig. 5.13 are closed using the stochastic time-slice propagator from current vertex $J_\mu$ to pion vertex $\bar{d}\,\gamma_5\,u$ at sink. Based on the application of point-to-all and stochastic propagator these diagrams are factorized into elementary contractions. For diagram (c), we have

$$\begin{aligned}\mathrm{Tr}\big(S_f(x_i;x_J)\,\gamma_\mu\,S(x_J;x_f)\,\gamma_5\,S(x_f;x_i)\,\Gamma_i\big) &= \mathrm{E}\left[\eta_\phi(x_J)^a_\alpha\,\eta_\xi(x_f)^b_\beta\right]\,\delta^{ab}\,(\Gamma_i\,\gamma_5)_{\beta\alpha}\,, \qquad (5.45)\\ \eta_\phi(x_J) &= S_f(x_J;x_i)^\dagger\,\gamma_5\gamma_\mu\,\phi_{t_\pi}(x_J)\,,\\ \eta_\xi(x_f) &= \xi^r_{t_\pi}(x_f)^\dagger\,\gamma_5\,S_f(x_f;x_i),\end{aligned}$$

where in our implementation, $\eta_{\phi,\xi}$ are contracted, Fourier transformed and stored separately as $\eta_\phi(t_J,\vec{q})$ and $\eta_\xi(t_\pi,\vec{p}_\pi)$ for each stochastic sample. Subsequently they are used to recombine the diagram for all required momenta $\vec{q}$, $\vec{p}_\pi$ as well as any vertex $\Gamma_i$ and $\vec{P}$ at the source. Diagram (d) follows analogously by promoting the point-to-all propagator $S_f(x_f;x_i)$ in Eq.

(5.45) to a sequential propagator,

$$\begin{aligned}
&\mathrm{Tr}\big(S_f(x_{i_1};x_J)\,\gamma_\mu\,S(x_J;x_f)\,\gamma_5\,S(x_f;x_{i_2})\times\\
&\gamma_5\,\mathrm{e}^{i\vec{p}_{i_2}\vec{x}_{i_2}}\,S_f(x_{i_2};x_{i_1})\,\Gamma_i\big) \qquad (5.46)\\
&\quad=\mathrm{E}\left[\eta_\phi(x_J)^a_\alpha\,\eta_\xi(x_f)^b_\beta\right]\,\delta^{ab}\,(\Gamma_i\,\gamma_5)_{\beta\alpha}\,,\\
&\eta_\phi(x_J)=S_f(x_J;x_{i_1})^\dagger\,\gamma_5\gamma_\mu\,\phi_{t_\pi}(x_J)\,,\\
&\eta_\xi(x_f)=\xi^r_{t_\pi}(x_f)^\dagger\,\gamma_5\,S_{seq}(x_f;t_{\pi\pi},\gamma_5,\vec{p}_{i_2};x_{i_1})\,.
\end{aligned}$$

For diagram (e) in Fig. 5.13, the one-end-trick setup in Eq. (4.21) leads to the factorization of the diagram,

$$\begin{aligned}
&\mathrm{Tr}\big(S_f(x_{i_1};x_J)\,\gamma_\mu\,S(x_J;x_{i_2})\,\mathrm{e}^{i\vec{p}_{i_2}\vec{x}_{i_2}}\\
&\times\gamma_5\,S(x_{i_2};x_f)\,\gamma_5\,S_f(x_f;x_{i_1})\,\Gamma_i\big) \qquad (5.47)\\
&\quad=\mathrm{E}\left[\eta^{(\lambda)}_\phi(x_J)_\alpha\,\eta^{(\lambda)}_{\bar\phi}(x_f)_\beta\right]\,(\Gamma_i\,\gamma_5)_{\beta\alpha}\,,\\
&\eta^{(\lambda)}_\phi(x_J)=S_f(x_J;x_{i_1})^\dagger\,\gamma_5\gamma_\mu\,\phi_{t_{\pi\pi},\vec{p}_{i_2},\lambda}(x_J)\,,\\
&\eta^{(\lambda)}_{\bar\phi}(x_f)=\phi_{t_{\pi\pi},0,\lambda}(x_f)^\dagger\,S_f(x_f;x_{i_1})\,.
\end{aligned}$$

Finally, diagram (f) is calculated as the product of propagator loop traces using again the one-end-trick,

$$\begin{aligned}
&\mathrm{Tr}\big(S(x_{i_2};x_J)\,\gamma_\mu\,S(x_J;x_{i_2})\,\gamma_5\big)\,\mathrm{e}^{i\vec{p}_{i_2}\vec{x}_{i_2}}\\
&\qquad\times\mathrm{Tr}\big(S_f(x_{i_1};x_f)\,\gamma_5\,S_f(x_f;x_{i_1})\,\Gamma_i\big) \qquad (5.48)\\
&\quad=\mathrm{E}\left[\phi_{t_{\pi\pi},0,\lambda}(x_J)^\dagger\,\gamma_5\gamma_\mu\,\phi_{t_{\pi\pi},\vec{p}_{i_2},\lambda}\right]\\
&\qquad\times\mathrm{Tr}\big(S_f(x_f;x_{i_1})^\dagger\,S_f(x_f;x_{i_1})\,\Gamma_i\,\gamma_5\big)
\end{aligned}$$

All quark propagators are smeared at their source and sink side in the same way as in Sec. 5.1.4.

### 5.2.4 Optimized three-point functions

The spectral decomposition of the three-point function $C^{\vec{p}_\pi,\vec{P},\Lambda,r}_{3,\,\mu,i}(t_\pi,t_J,t_{\pi\pi})$, keeping as before only the ground-state contribution for the pion (for large $t_\pi - t_J$), is

$$\begin{aligned} &C^{\vec{p}_\pi,\vec{P},\Lambda,r}_{3,\,\mu,i}(t_\pi,t_J,t_{\pi\pi}) \\ &= \sum_n Z^{\vec{p}_\pi}_\pi \, Z^{n,\vec{P},\Lambda\,\dagger}_i \, \langle \pi,\vec{p}_\pi|J_\mu(0,\vec{q})|n,\vec{P},\,\Lambda,\,r\rangle_{FV} \\ &\qquad \times \frac{e^{-E^{\vec{p}_\pi}_\pi (t_\pi - t_J)} e^{-E^{\vec{P},\Lambda}_n (t_J - t_{\pi\pi})}}{2E^{\vec{P},\Lambda}_n 2E^{\vec{p}_\pi}_\pi}. \end{aligned} \tag{5.49}$$

For the $\pi\pi$ system we want to project to the $n$-th state. This will allow us to have a definite invariant mass, $\sqrt{s^{\vec{P},\Lambda}_n}$, and momentum transfer, $(q^2)^{\vec{p}_\pi}_{n,\vec{P},\Lambda} = (E^{\vec{P},\Lambda}_n - E^{\vec{p}_\pi}_\pi)^2 - \vec{q}^{\,2}$, in our matrix element. To achieve this we utilize the orthogonality between the generalized eigenvectors and overlap factors from Sec. 5.1.5[5],

$$v^{n\,\vec{P},\Lambda}_i(t_0)\, Z^{m\,\vec{P},\Lambda\,\dagger}_i = \sqrt{2E^{\vec{P},\Lambda}_n}\, e^{E^{\vec{P},\Lambda}_n t_0/2} \delta_{nm}, \tag{5.50}$$

and construct the optimized three-point function [85, 34, 223]

$$\begin{aligned} &\Omega^{\vec{p}_\pi,\vec{P},\Lambda,r}_{3,\,\mu,n}(t_\pi,t_J,t_{\pi\pi},t_0) \\ &= v^{n\,\vec{P},\Lambda}_i(t_0)\, C^{\vec{p}_\pi,\vec{P},\Lambda,r}_{3,\,\mu,i}(t_\pi,t_J,t_{\pi\pi}) \\ &= \langle O^{\vec{p}_\pi}_\pi(t_\pi)\, J_\mu(t_J,\vec{q})\, \mathscr{O}^{n,\vec{P},\Lambda,r}(t_{\pi\pi},t_0)\rangle. \end{aligned} \tag{5.51}$$

This gives

$$\begin{aligned} &\Omega^{\vec{p}_\pi,\vec{P},\Lambda,r}_{3,\,\mu,n}(t_\pi,t_J,t_{\pi\pi},t_0) \\ &= \sqrt{2E^{\vec{P},\Lambda}_n}\, e^{E^{\vec{P},\Lambda}_n t_0/2}\, Z^{\vec{p}_\pi}_\pi \, \langle \pi,\vec{p}_\pi|J_\mu(0,\vec{q})|n,\vec{P},\Lambda,r\rangle_{FV} \\ &\qquad \times \frac{e^{-E^{\vec{p}_\pi}_\pi (t_\pi - t_J)} e^{-E^{\vec{P},\Lambda}_n (t_J - t_{\pi\pi})}}{2E^{\vec{P},\Lambda}_n 2E^{\vec{p}_\pi}_\pi}, \end{aligned} \tag{5.52}$$

and we see that the optimized three-point function overlaps only to the single definite state $|n;\vec{P},\Lambda,r\rangle$.

[5] Note that this choice depends on the normalization of the generalized vectors [cf. Eq. (4.31)].

### 5.2.5 Determining the finite volume matrix elements

To extract the finite-volume matrix elements $\langle \pi, \vec{p}_\pi | J_\mu(0,\vec{q}) | n, \vec{P}, \Lambda, r \rangle_{FV}$ from the correlation functions, we construct the ratio

$$R_{\mu,n}^{\vec{p}_\pi,\vec{P},\Lambda,r}(t_\pi,t_J,t_{\pi\pi}) = \frac{\Omega_{3,\,\mu,n}^{\vec{p}_\pi,\vec{P},\Lambda,r}(t_\pi,t_J,t_{\pi\pi},t_0)\,\Omega_{3,\,\mu,n}^{\vec{p}_\pi,\vec{P},\Lambda,r\,\dagger}(t_\pi,t',t_{\pi\pi},t_0)}{C_\pi^{\vec{p}_\pi}(\Delta t)\,\lambda_n^{\vec{P},\Lambda}(\Delta t,t_0)}, \tag{5.53}$$

where $C_\pi^{\vec{p}_\pi}$ is the pion correlator, $\lambda_n^{\vec{P},\Lambda}$ is the principal correlator of the variational analysis, $\Delta t = t_\pi - t_{\pi\pi}$ is the source-sink separation, and $t' = t_{\pi\pi} + t_\pi - t_J$. The $t_0$ dependence of the optimized three-point function cancels with the $t_0$ dependence of the principal correlator. Inserting Eq. (5.52) into Eq. (5.53) gives (for large time separations)

$$R_{\mu,n}^{\vec{p}_\pi,\vec{P},\Lambda,r}(t_\pi,t_J,t_{\pi\pi}) = \frac{|\langle \pi, \vec{p}_\pi | J_\mu(0,\vec{q}) | n, \vec{P}, \Lambda, r \rangle_{FV}|^2}{4E_n^{\vec{P},\Lambda}E_\pi^{\vec{p}_\pi}}. \tag{5.54}$$

The matrix elements determined from Eq. (5.53) still contain residual excited-state contamination that decays exponentially for large $\Delta t$, $t_J - t_{\pi\pi}$, and $t_\pi - t_J$. We have data for $\Delta t/a = 8, 10, 12$. There are several ways to proceed from this point on:

1) Set $t_J - t_{\pi\pi} = \Delta t/2$ and fit only the $\Delta t$ dependence of the matrix element with an excited-state model, as for example in Ref. [81],

2) Fit both the $\Delta t$ and $t_J - t_{\pi\pi}$ dependence with an excited-state model,

3) Fit constants to the ratios (assuming that only the desired initial and final states contribute), varying the time ranges to assess residual contamination.

We found that options 1) and 2) did not yield stable fits, because we have too few source-sink separations and the statistical uncertainties are too large. We therefore use option 3), where we investigate whether the various fits are statistically compatible, and estimate a systematic uncertainty associated with the fit choice. In Fig. 5.14 we present results for the matrix elements $|\langle \pi, \vec{p}_\pi | J_\mu(0,\vec{q}) | n, \vec{P}, \Lambda, r \rangle_{FV}|$ at representative kinematic points (plots for the other kinematic points are shown in the Appendix of Ref. [12]. As explained in the caption of the figure, we perform fits for many different time ranges and then choose one that appears to have plateaued for further analysis. To estimate the systematic uncertainty associated with the fit range for the ratio, we compute the change in the central value when going from the chosen fit to $\Delta t/a = 10$, as marked with an $X$ in Fig. 5.14. As a cross-check, we also tested an alternative method for extracting the matrix elements, in which we did not use

ratios, but fitted the three-point functions of Eq.(5.52) after dividing out the time dependence and overlap factors. That method gives results consistent with the ratio method. Because the ratio of Eq.(5.54) also depends on the energies $E_n^{\vec{P},\Lambda}$, we additionally include a second systematic uncertainty associated with the choice of the fit range used in the spectrum analysis of Sec. 5.1.5. The numerical results for all kinematic points are listed in the Appendix of Ref. [12]. There, both systematic uncertainties have been added in quadrature to the statistical uncertainties.

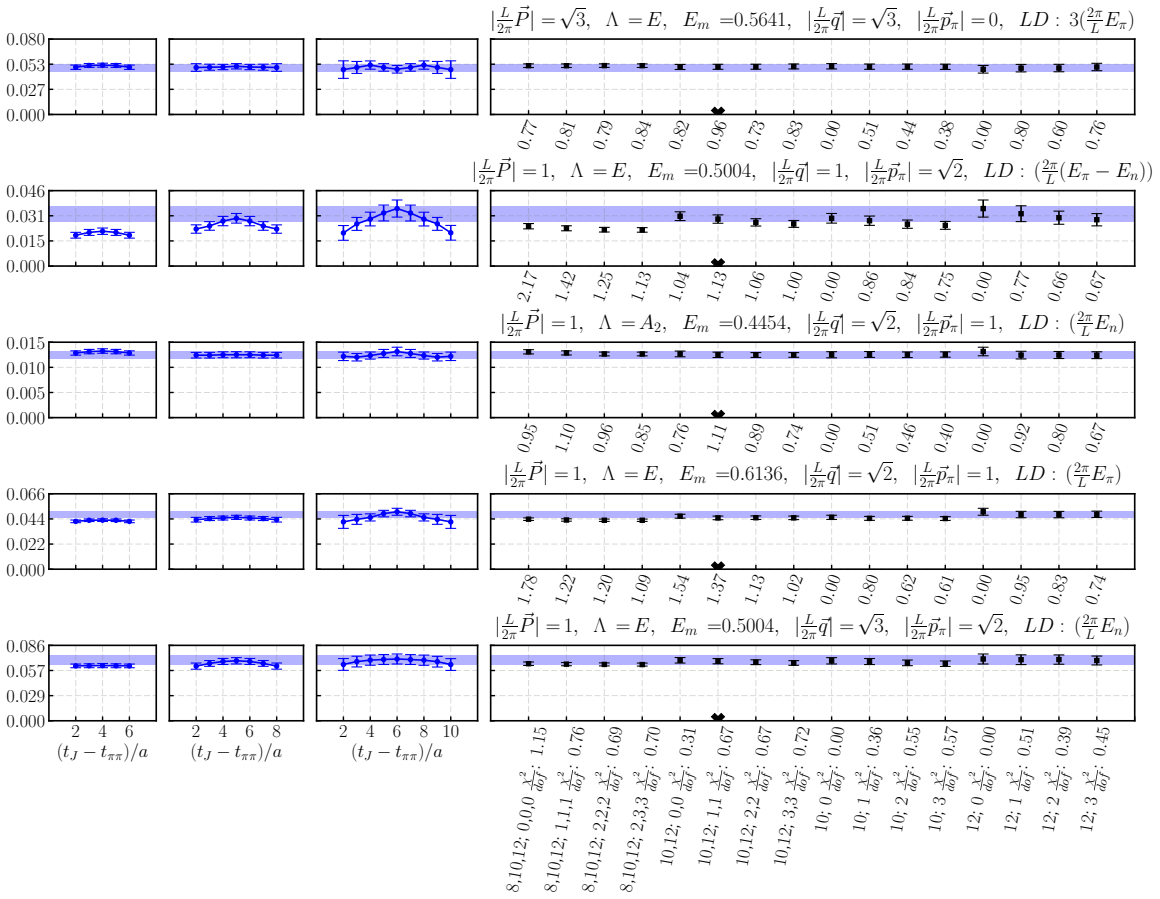


Fig. 5.14 Examples of results for the finite-volume matrix elements $|\langle \pi, \vec{p}_\pi | J_\mu(0,\vec{q}) | n, \vec{P}, \Lambda, r \rangle_{FV}|$. The left three panels show the data as a function of $t_J - t_{\pi\pi}$ for the three different source-sink separations. The right panels show the fitted values for multiple different fit ranges, which are indicated at the bottom. There, the first set of numbers are the included source-sink separations, and the second set of numbers are the distances from the mid-point that are included for each of these source-sink separations. The blue bands show the chosen fit result, and the half-crosses mark the fits that are used to estimate systematic uncertainties. The values of $\chi^2/\text{dof}$ are also given. The quantity denoted as *LD* is the kinematic factor appearing next to $2i\mathcal{V}_{\pi\gamma\to\pi\pi}/m_\pi$ in Eq. (5.32).

.

### 5.2.6 Mapping from finite volume to infinite volume

**Lellouch-Lüscher factors**

The mapping between a finite-volume matrix element $|\langle \pi, \vec{p}_\pi | J_\mu(0,\vec{q}) | n, \vec{P}, \Lambda, r \rangle_{FV}|$ calculated on the lattice and the corresponding infinite-volume matrix element $|\langle \pi, \vec{p}_\pi | J_\mu(0) | s, q^2; \vec{P}, \Lambda, r \rangle_{IV}|$, for our normalization of states, is [155, 50, 54, 66]

$$\begin{aligned} &\frac{|\langle \pi, \vec{p}_\pi | J_\mu(0) | s, q^2; \vec{P}, \Lambda, r \rangle_{IV}|^2}{|\langle \pi, \vec{p}_\pi | J_\mu(0,\vec{q}) | n, \vec{P}, \Lambda, r \rangle_{FV}|^2} \\ &= \frac{1}{2E_n^{\vec{P},\Lambda}} \frac{16\pi\sqrt{s_n^{\vec{P},\Lambda}}}{k_n^{\vec{P},\Lambda}} \left( \frac{\partial \delta}{\partial E} + \frac{\partial \phi^{\vec{P},\Lambda}}{\partial E} \right) \Bigg|_{E=E_n^{\vec{P},\Lambda}}. \end{aligned} \tag{5.55}$$

Note that the current in the infinite-volume matrix element is evaluated in position space at $\vec{x} = 0$, while the current in the finite-volume matrix element is projected to momentum $\vec{q}$. The energy-dependence of the $\pi\pi$ $P$-wave scattering phase shift $\delta$ has to be determined from the Lüscher analysis on the same lattice. We use our Breit-Wigner fits from Sec. 5.1.7, as already discussed in Sec. 5.2.2. The function $\phi^{\vec{P},\Lambda}$ in Eq. (5.55) appears in the Lüscher quantization condition as

$$\cot\delta = \cot\phi^{\vec{P},\Lambda} = \sum_{l,m} c_{lm}^{\vec{P},\Lambda} w_{lm}(k^2_{\vec{P},\Lambda}), \tag{5.56}$$

where $w_{lm}$ is defined as

$$w_{lm}(k^2) = \frac{Z_{lm}^{\vec{P}}\left(1; (kL/(2\pi))^2\right)}{\pi^{3/2}\sqrt{2l+1}\gamma(\frac{kL}{2\pi})^{l+1}}, \tag{5.57}$$

with the generalized zeta function $Z_{lm}^{\vec{P}}$ and the Lorentz gamma factor $\gamma$. The quantization conditions for $\cot\phi^{\vec{P},\Lambda}$ used are discussed in Sec. 5.1.6; the nonzero factors $c_{lm}^{\vec{P},\Lambda}$ appearing in elastic $P$-wave $\pi\pi$ scattering are also listed in Table 5.8. The right-hand side of Eq. (5.55), known as the Lellouch-Lüscher factor, depends on the $\pi\pi$ system's momentum $\vec{P}$, irreducible representation $\Lambda$, invariant mass $\sqrt{s_n^{\vec{P},\Lambda}}$, and scattering momentum $k_n^{\vec{P},\Lambda}$. In Fig. 5.15 we show the Lellouch-Lüscher factors as a function of invariant mass. Calculating the derivative

| $\frac{L}{2\pi}\vec{P}$ | $\Lambda$ | $(l,m)$ | $c_{lm}^{\vec{P},\Lambda}$ |
|---|---|---|---|
| $(0,0,0)$ | $T_1$ | $(0,0)$ | $1$ |
| $(0,0,1)$ | $A_2$ | $(0,0)$ | $1$ |
| | | $(2,0)$ | $2$ |
| | $E$ | $(0,0)$ | $1$ |
| | | $(2,0)$ | $-1$ |
| $(0,1,1)$ | $B_1$ | $(0,0)$ | $1$ |
| | | $(2,0)$ | $\frac{1}{2}$ |
| | | $(2,1)$ | $\mathrm{i}\sqrt{6}$ |
| | | $(2,2)$ | $-\sqrt{\frac{3}{2}}$ |
| | $B_2$ | $(0,0)$ | $1$ |
| | | $(2,0)$ | $\frac{1}{2}$ |
| | | $(2,1)$ | $-\mathrm{i}\sqrt{6}$ |
| | | $(2,2)$ | $-\sqrt{\frac{3}{2}}$ |
| | $B_3$ | $(0,0)$ | $1$ |
| | | $(2,0)$ | $-1$ |
| | | $(2,2)$ | $\sqrt{6}$ |
| $(1,1,1)$ | $A_2$ | $(0,0)$ | $1$ |
| | | $(2,1)$ | $-\mathrm{i}\sqrt{\frac{8}{3}}$ |
| | | $(2,2)$ | $-\sqrt{\frac{8}{3}}(\mathrm{Re}+\mathrm{Im})$ |
| | $E$ | $(0,0)$ | $1$ |
| | | $(2,0)$ | $\mathrm{i}\sqrt{6}$ |

Table 5.8 Nonzero values of $c_{lm}$ appearing in the quantization condition for elastic $P$-wave $\pi\pi$ scattering. Above, the term with Re and Im means $-\sqrt{\frac{8}{3}}(\mathrm{Re}[w_{22}]+\mathrm{Im}[w_{22}])$.

$\frac{\partial\phi^{\vec{P},\Lambda}}{\partial E}$ in practice means that we must calculate the derivative of $w_{lm}(k^2)$:

$$\frac{\partial\phi^{\vec{P},\Lambda}}{\partial E} = \frac{s^2-(m_1^2-m_2^2)^2}{2\sqrt{s}^3}\frac{1}{1+\cot^2\phi^{\vec{P},\Lambda}} \times\sum_{l,m} c_{lm}\frac{\partial w_{lm}(k^2)}{\partial k^2}, \tag{5.58}$$

where $m_1$, $m_2$ are the two hadron masses; in the case of $\pi\pi$ scattering $m_1=m_2=m_\pi$. In the rest frame, the derivative of $Z_{lm}$ is again a zeta function:

$$\frac{\partial}{\partial\hat{k}^2}Z_{lm}^{\vec{P}=\vec{0}}(s;\hat{k}^2) = sZ_{lm}^{\vec{P}=\vec{0}}(s+1;\hat{k}^2). \tag{5.59}$$

Since this does not hold in moving frames, we compute the derivative numerically.

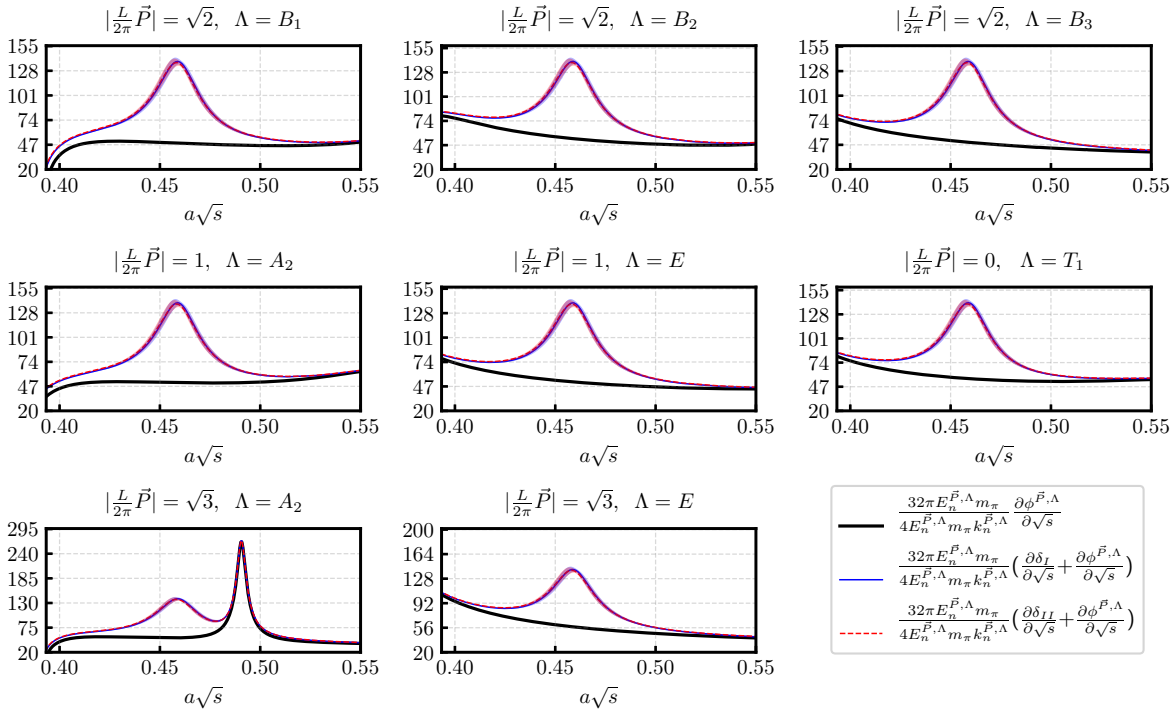


Fig. 5.15 The Lellouch-Lüscher factors as a function of invariant mass, for the momentum frames and irreps used here. The thick black lines show the non interacting Lellouch-Lüscher factors (without the phase-shift derivative). The thin blue lines and dashed red lines show the full Lellouch-Lüscher factors, using the **BW I** and **BW II** models Sec. 5.1.2 for the scattering phase shift. The bands indicate the statistical uncertainties.

In Fig. 5.15 we can see that the two different models for the phase shift $\delta$, **BW I** and **BW II**, are statistically compatible. Nevertheless, we use both Breit-Wigner models in our analysis to quantitatively assess this.

The fitting systematic uncertainties in $E_n^{\vec{P},\Lambda}$ enter in the Lellouch-Lüscher factors not only via the explicit factor of $E_n^{\vec{P},\Lambda}$ in Eq. (5.55), but also through the phase-shift parametrization fitted to these energies via the Lüscher quantization condition. In Sec. 5.1.5, we estimated the systematic uncertainties in $E_n^{\vec{P},\Lambda}$ by comparing the results of exponential fits with start times $t_{\text{min}}$ and $t_{\text{min}} + a$. To correctly propagate these uncertainties to the Breit-Wigner parameters, we then performed the Lüscher analysis and the Breit-Wigner fits for both sets of energies. In the present work, we therefore also repeat the mappings of the $\pi\gamma \to \pi\pi$ matrix elements (and the subsequent analysis) for both sets of Breit-Wigner parameters.

**Lorentz decomposition of the infinite-volume matrix elements**

The infinite-volume matrix elements $\langle s, q^2; \vec{P}, \Lambda, r | J_\mu(0, \vec{q}) | \pi, \vec{p}_\pi \rangle_{IV}$ obtained from Eq. (5.55) still carry the finite-volume irrep indices $\vec{P}$, $\Lambda$, $r$. The infinite-volume states $\langle s, q^2; \vec{P}, \Lambda, r|$ are linear combinations of the states labeled by the continuum polarization index $m$ in Eq. (5.34). The coefficients of these linear combinations are given by the irrep projection formula Eq. (4.2). We form the same linear combinations of the polarization vectors on the right-hand side of Eq. (5.32) to obtain the irrep-projected form-factor decompositions. Taking this into account, we can determine the values of the infinite-volume transition amplitude $\mathscr{V}_{\pi\gamma\to\pi\pi}$.

### 5.2.7 Fitting the amplitude $\mathscr{V}_{\pi\gamma\to\pi\pi}$

**Parametrization of the infinite-volume transition amplitude**

To allow the calculation of observables, the transition amplitude $\mathscr{V}_{\pi\gamma\to\pi\pi}(q^2, s)$ determined with lattice QCD at 48 discrete values of $q^2$ and $s$ needs to be fitted to an analytic parametrization. In Sec. 5.2.2, we factored out the $\rho$ pole in $s$ according to Watson's theorem,

$$\mathscr{V}_{\pi\gamma\to\pi\pi}(q^2, s) = \frac{F(q^2, s)}{m_R^2 - s - \mathrm{i}\sqrt{s}\Gamma_i(s)} \sqrt{\frac{16\pi s \Gamma_i(s)}{k}}. \tag{5.60}$$

What remains is the transition form factor $F(q^2, s)$, which should not have any additional poles in $s$ in our region of interest. To obtain a model-independent parametrization of $F(q^2, s)$, we perform a two-dimensional Taylor expansion in the variables

$$\mathscr{S} = \frac{s - m_R^2}{m_R^2} \tag{5.61}$$

and

$$z = \frac{\sqrt{t_+ - q^2} - \sqrt{t_+ - t_0}}{\sqrt{t_+ - q^2} + \sqrt{t_+ - t_0}}, \tag{5.62}$$

after dividing out the lowest expected pole in $q^2$:

$$F(q^2, s) = \frac{1}{1 - \frac{q^2}{m_P^2}} \sum_{n,m} A_{nm} z^n \mathscr{S}^m. \tag{5.63}$$

The variable $\mathscr{S}$ was chosen to be dimensionless and small near the resonance. The definition of $z$ maps the complex $q^2$ plane, cut along the real axis for $q^2 > t_+$, to the interior of the unit

circle [46, 47, 45, 35, 36, 182]. The constant $t_0$ determines which value of $q^2$ is mapped to $z = 0$; we choose $t_0 = 0$. The constant $t_+$ should be set to the lowest branch point. For the QED current, the branch cut starts at $(3m_\pi)^2$ and the lowest pole is located at $m_\omega^2$. However, because we neglect the disconnected contributions, we use $t_+ = (2m_\pi)^2$ and $m_P = m_\rho$.[6] $A_{nm}$ are the parameters to be filled.

In practice, the series in Eq. (5.63) needs to be truncated. We organize these truncations into three different families:

**F1)** Combined order $K$:

$$F(q^2,s) = \frac{1}{1-\frac{q^2}{m_P^2}} \sum_{n+m\le K} A_{nm} z^n \mathscr{S}^m, \tag{5.64}$$

**F2)** Order $N$ in $z$, combined order $K$:

$$F(q^2,s) = \frac{1}{1-\frac{q^2}{m_P^2}} \sum_{n=0}^{N} \sum_{m=0}^{K-n} A_{nm} z^n \mathscr{S}^m, \tag{5.65}$$

**F3)** Order $N$ in $z$, order $M$ in $\mathscr{S}$:

$$F(q^2,s) = \frac{1}{1-\frac{q^2}{m_P^2}} \sum_{n=0}^{N} \sum_{m=0}^{M} A_{nm} z^n \mathscr{S}^m. \tag{5.66}$$

The first two families, **F1** and **F2**, cut the series at the combined $z$ and $\mathscr{S}$ order, while the third family **F3** separately specifies the orders in $z$ and $\mathscr{S}$. In the limit of large $K$, $N$, $M$, all parametrizations become equal.

In the construction of $\chi^2$, we take into account the uncertainties in all $z$ and $s$ values by promoting these values to nuisance parameters, like we did (for the $s$ values) in Sec. 5.1.7. The covariance matrix, which we estimate using single-elimination jackknife, is therefore a $3N_{\text{data}} \times 3N_{\text{data}}$ matrix, where $N_{\text{data}} = 48$ is the number of kinematic points. We added the systematic uncertainties associated with the choices of fit ranges in the matrix element fits and spectrum fits in quadrature to the diagonal elements of the covariance matrix. The uncertainties of the best-fit parameters are obtained from the Hessian of $\chi^2$ at the minimum.

[6] Because $m_P^2 > t_+$, it is not actually necessary to factor out the pole, but there is no harm in doing so.

### The fit results

For each of the different families of parametrizations **F1**-**F3** we investigate several fits while keeping the power of $z$ below 3, and power of $\mathscr{S}$ below 4. We find that when the $z$-expansion goes to order $n = 3$ or higher, the additional parameters are consistent with zero and no longer contribute to the description of the data; similarly, for the $\mathscr{S}$ expansion, at order $m = 4$ the parameters become statistically consistent with zero. We drop all parametrizations yielding fit parameters with uncertainties larger than 100 times their central values. We also remove parametrizations that lead to $\frac{\chi^2}{\text{dof}} > 1.1$, which includes those that are of 0-th order in the $z$-expansion.

We name the parametrizations according to the type of Breit-Wigner, family of truncation, and truncation limits. The parametrizations that survive the cuts are consistent with each other within the uncertainties, and we choose "BWII F1 K2" as our nominal parametrization.

In Fig. 5.16 we present the fitted $\mathscr{V}_{\pi\gamma\to\pi\pi}$ combined with the data points in a three-dimensional plot as a function of $\sqrt{s}$ and $q^2$. Fig. 5.17 instead shows a top-down view as a density plot, where the discrete values of $\sqrt{s}$ allowed by the finite volume for which we have results appear as vertically aligned points.

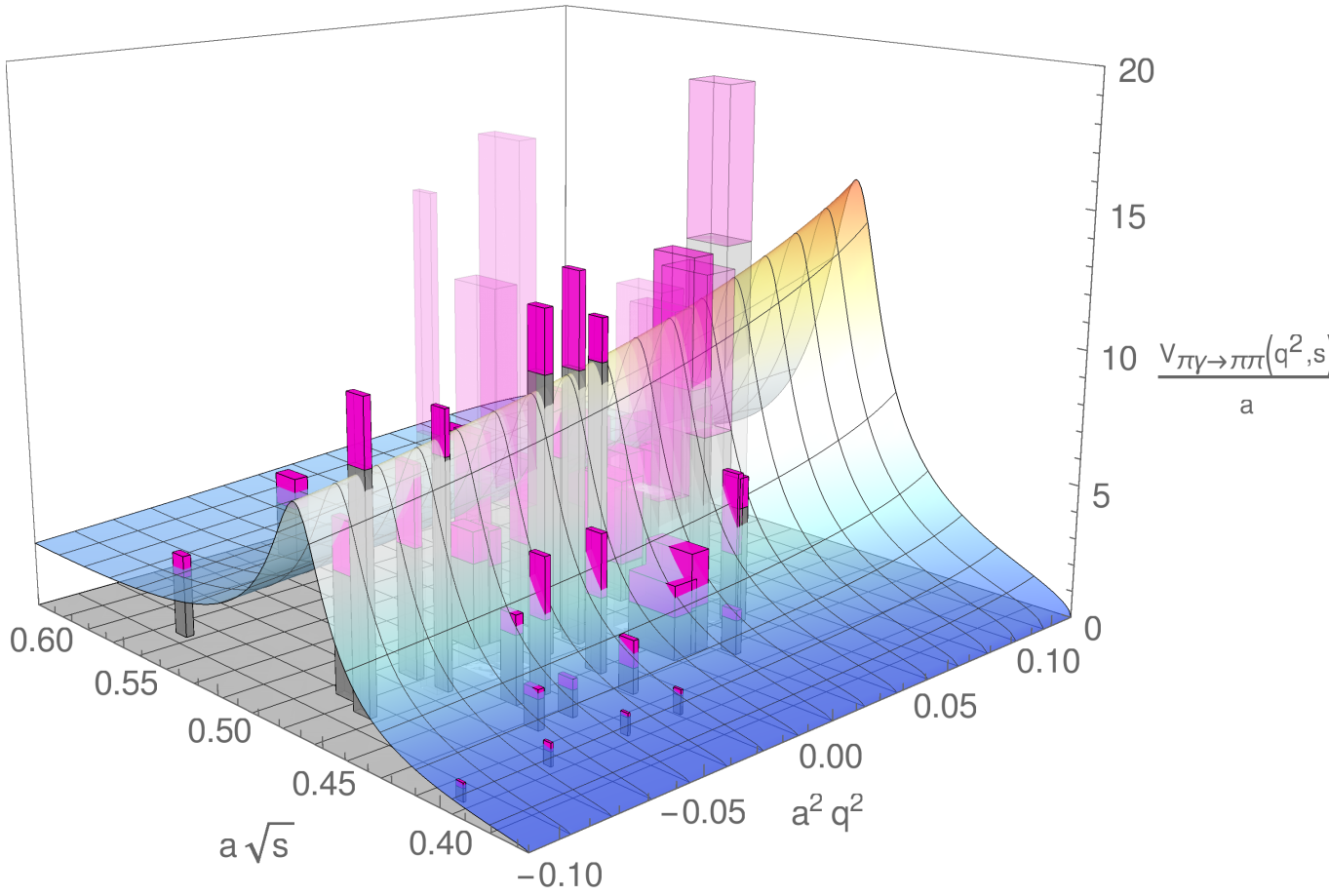


Fig. 5.16 Three-dimensional plot of the transition amplitude $\mathcal{V}_{\pi\gamma\to\pi\pi}$ (in lattice units) as a function of $\sqrt{s}$ and $q^2$. The lattice QCD results are shown as the vertical bars, where the widths and depths correspond to the uncertainties in $a\sqrt{s}$ and $a^2q^2$, and the magenta sections at the tops cover the range from $\mathcal{V}_{\pi\gamma\to\pi\pi} - \sigma_{\mathcal{V}_{\pi\gamma\to\pi\pi}}$ to $\mathcal{V}_{\pi\gamma\to\pi\pi} + \sigma_{\mathcal{V}_{\pi\gamma\to\pi\pi}}$. Data points with larger uncertainty are plotted with reduced opacity. The surface shows the central value of the nominal fit function ("BWII F1 K2").

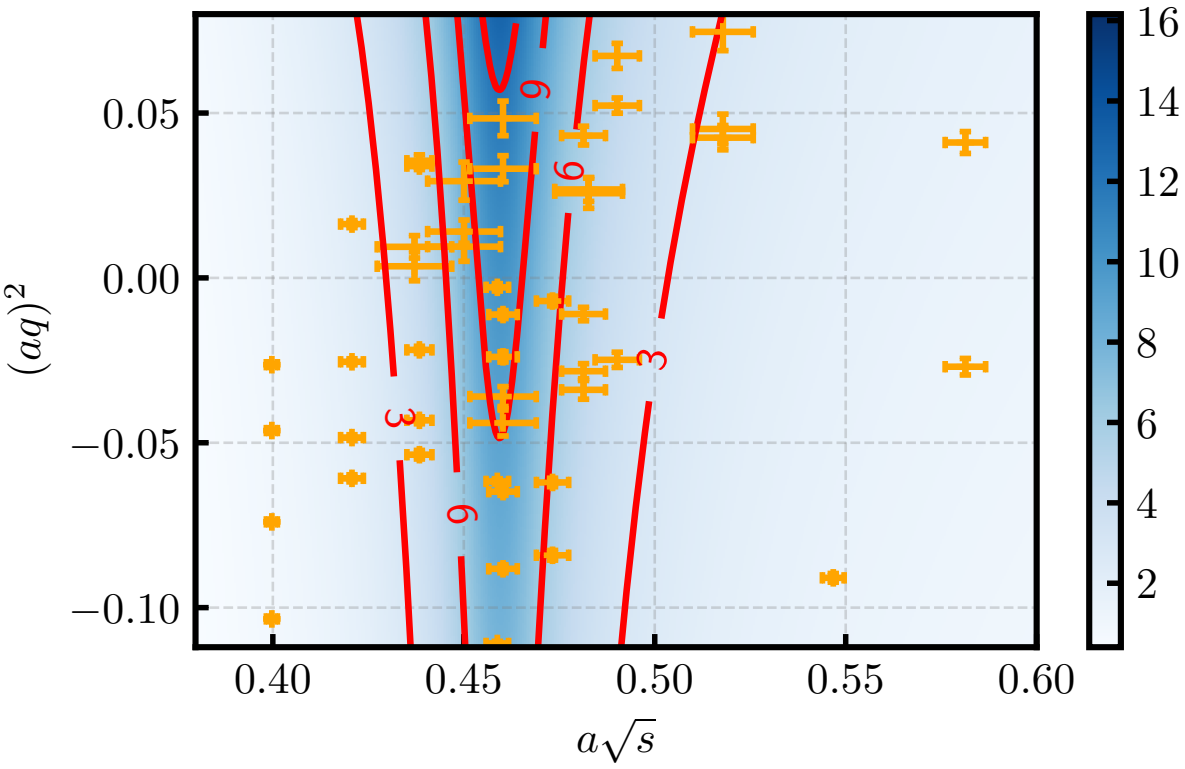


Fig. 5.17 Density plot of the fitted transition amplitude $\mathscr{V}_{\pi\gamma\to\pi\pi}$ (in lattice units, nominal parametrization "BWII F1 K2") in the $a\sqrt{s}$ and $(aq)^2$ plane. The locations of the discrete lattice QCD data points are indicated by the orange points with error bars.

The slices of the fitted amplitude at these discrete values of $\sqrt{s}$ are plotted as a function of $q^2$ in Fig. 5.18, where the upper panel shows the slices with $\sqrt{s} \geq m_R$ while the lower panel shows the slices with $\sqrt{s} < m_R$. We can see that the parametrization describes both the $\sqrt{s}$ and $q^2$ dependence of the data well.

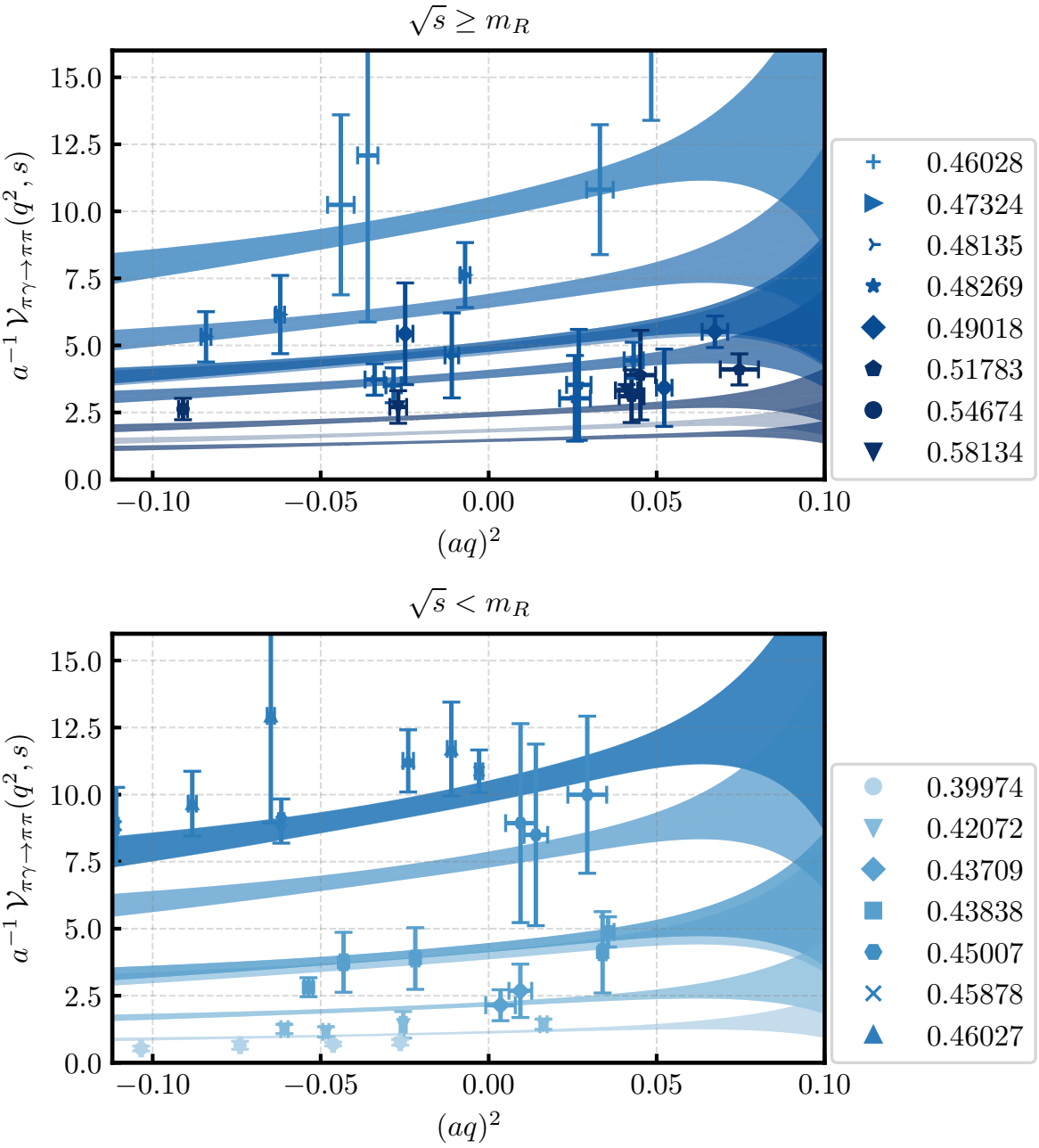


Fig. 5.18 The transition amplitude $\mathcal{V}_{\pi\gamma\to\pi\pi}$ (in lattice units, nominal parametrization "BWII F1 K2"), sliced by value of invariant mass $\sqrt{s}$, as a function of $q^2$. The shaded bands correspond to the $1\sigma$ regions of the fitted parametrizations; their colors and brightness match the data points at the same $a\sqrt{s}$, as indicated by the symbols in the legend.

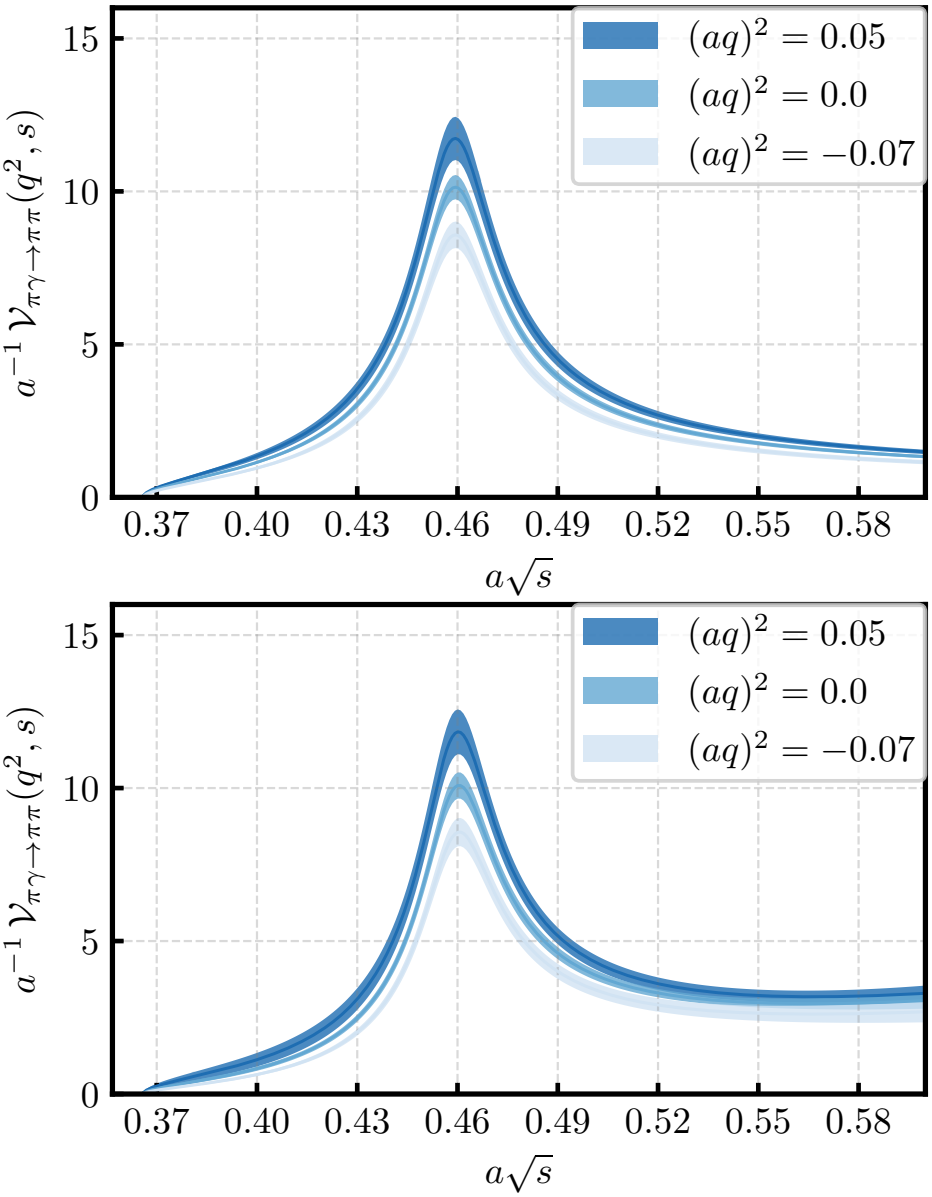


Fig. 5.19 The transition amplitude $\mathcal{V}_{\pi\gamma\to\pi\pi}$ as a function of the $\pi\pi$ invariant mass, for three different values of $q^2$. The top panel corresponds to the nominal parametrization "BWII F1 K2", and the bottom panel corresponds to the parametrization "BWI F1 K2".

Qualitatively, we can see two main features in $\mathcal{V}_{\pi\gamma\to\pi\pi}$: the amplitude is falling off as $q^2$ decreases, and shows the expected enhancement in $\sqrt{s}$ attributed to the $\rho$ resonance. The amplitude vanishes at the threshold $2m_\pi$, then rises and falls steeply as the resonance region is crossed. This can also be seen in Fig. 5.19, where we plot $\mathcal{V}_{\pi\gamma\to\pi\pi}$ as a function of the invariant mass for three different values of $q^2$. In this figure, we show plots for both the

nominal parametrization "BWII F1 K2" and for the parametrization "BWI F1 K2" that does not include the Blatt-Weisskopf barrier factor. At large $\sqrt{s}$, these parametrizations show some deviation. Nevertheless, for both parametrizations, the falloff of the amplitude at large $\sqrt{s}$ is slower than what would be expected for purely resonant behavior, indicating that the $\pi\gamma \to \pi\pi$ transition probability remains sizable even when the invariant mass is far above the resonance position. This is also reflected in Figs. 5.20 and 5.21, where we plot the function $F(q^2,s)$ that does not contain the Breit-Wigner factor. The slow falloff of $\mathcal{V}_{\pi\gamma\to\pi\pi}$ as a function of $\sqrt{s}$ corresponds to growing $F$. The other parametrizations show the same behavior, confirming a nontrivial $s$-dependence of the function $F(q^2,s)$.

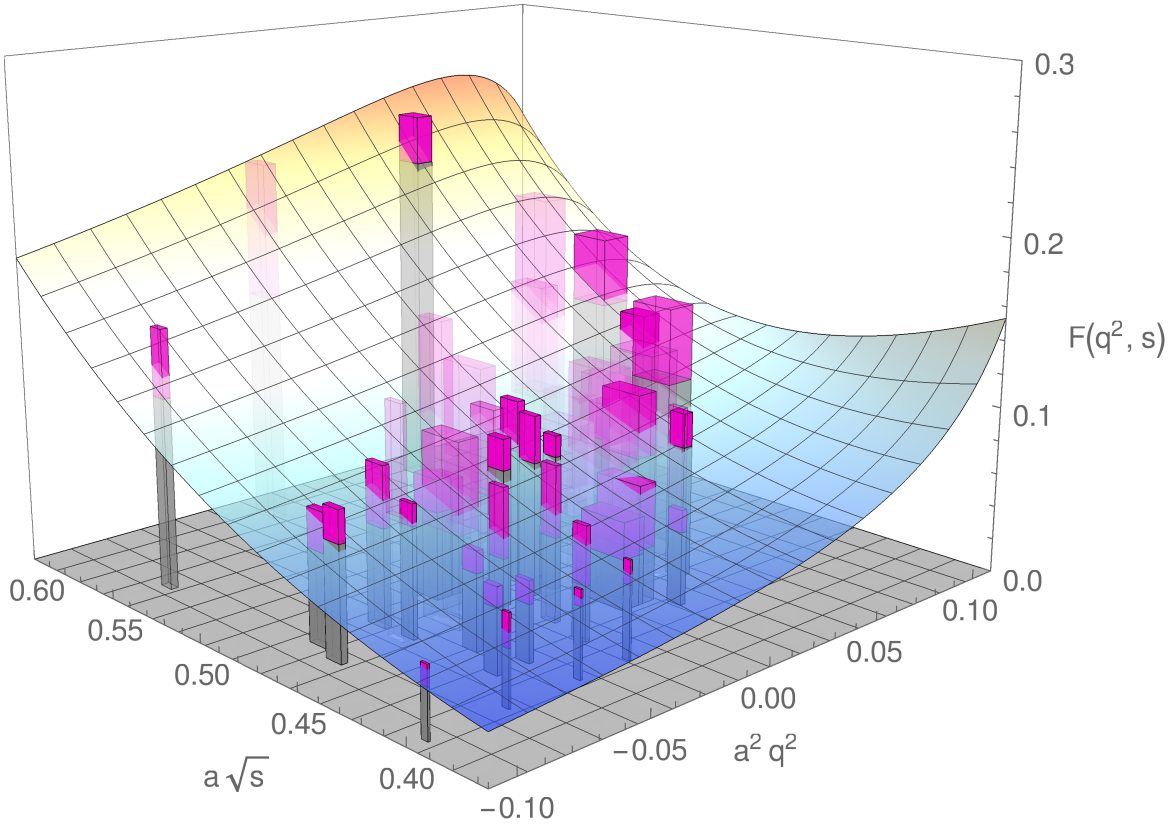


Fig. 5.20 Like Fig. 5.16, but for the function $F(q^2,s)$. The data points are divided by the central value of the Breit-Wigner factor (cf. Eq. ((2.18))) to represent the same quantity.

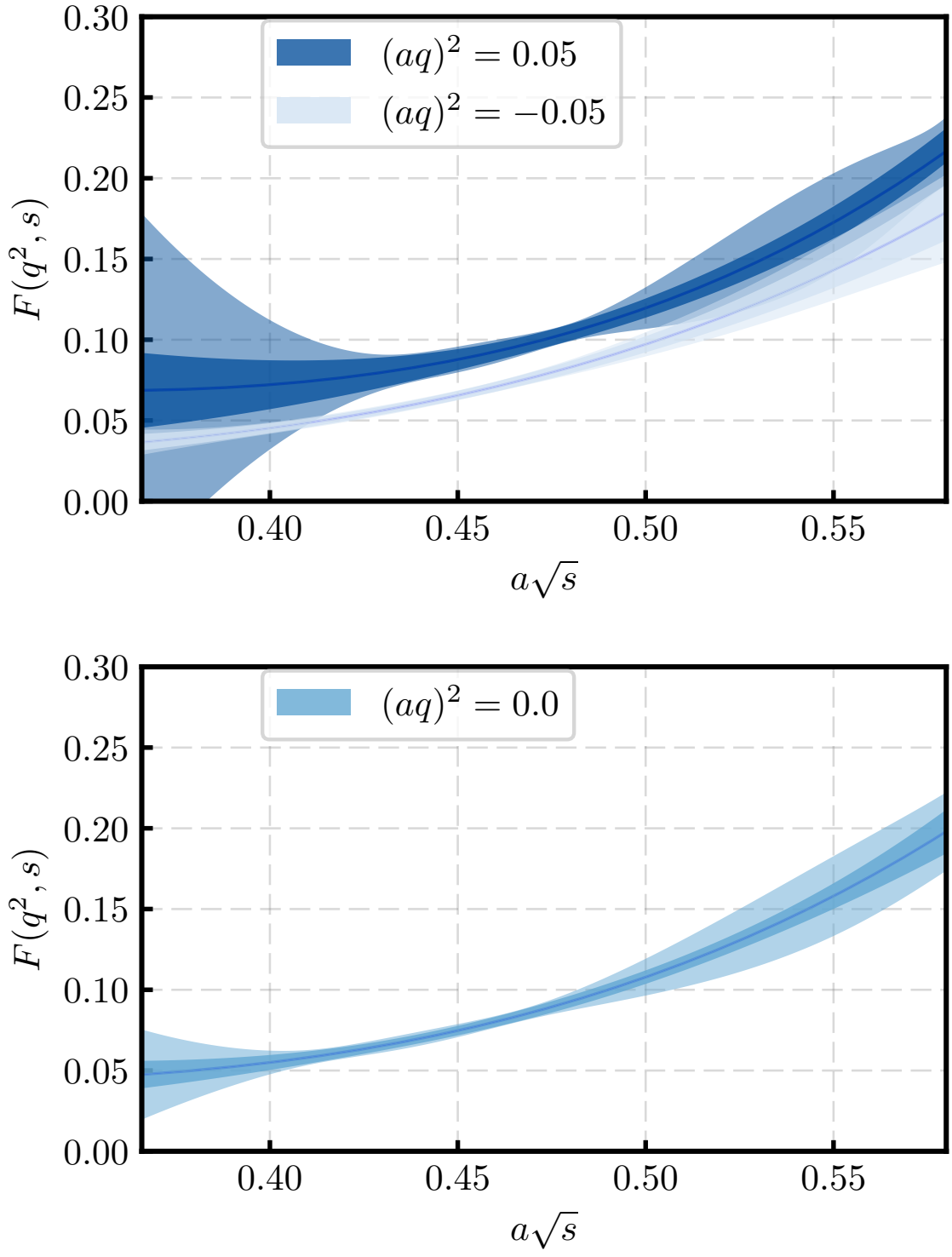


Fig. 5.21 The form factor $F(q^2, s)$, as a function of the $\pi\pi$ invariant mass, for two different nonzero values of $q^2$ (top) and for $q^2 = 0$ (bottom). Plotted is the central value of the nominal parametrization "BWII F1 K2" along with the two uncertainties: the inner (darker) shaded region represents the statistical and systematical uncertainties, and the outer (lighter) region includes also the parametrization uncertainty, estimated as the root-mean-square deviation of the central values obtained from the different parametrizations with respect to the nominal one.

### 5.2.8 Observables

As discussed in Sec. 5.2.2 we consider two main observable quantities, both with a real photon ($q^2 = 0$): the $\pi\gamma \to \pi\pi$ cross section and the $\rho$ radiative decay width. The $\pi\gamma \to \pi\pi$ cross section of Eq. (5.40) evaluated with our nominal parametrization "BWII F1 K2" of $\mathscr{V}_{\pi\gamma\to\pi\pi}(s, q^2 = 0)$ is shown in Fig. 5.22. Note that we evaluated Eq. (5.40) using the heavier-than-physical pion mass of this ensemble, $m_\pi \approx 320$ MeV. Because the $\rho$ resonance is narrower than in nature, the peak value of the cross section is higher [53].

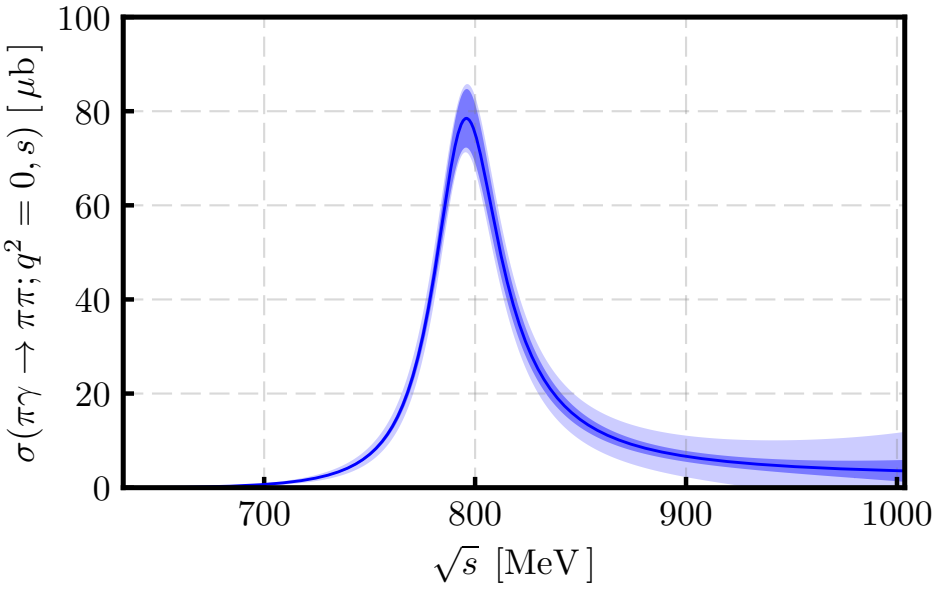


Fig. 5.22 The two-pion photoproduction cross section as a function of the $\pi\pi$ invariant mass, computed with the nominal parametrization "BWII F1 K2" of the amplitude, for our pion mass of $m_\pi \approx 320$ MeV. The inner (darker) shaded region indicates the statistical and systematic uncertainties, and the outer (lighter) shaded region also includes the parametrization uncertainty, estimated as explained in the caption of Fig. 5.21.

To determine the $\rho$ radiative decay width, $\Gamma(\rho \to \pi\gamma)$, we must first determine the photocoupling $g_{\rho\pi\gamma}$, which requires us to analytically continue the transition amplitude $\mathscr{V}_{\pi\gamma\to\pi\pi}$ to the pole position. The resulting resonant form factor $F_{\pi\gamma\to\rho}(q^2)$, defined in Eq. (5.39), is presented in Fig. 5.23. We find that the imaginary part of the resonant form factor is consistent with zero, and the real part slowly rises as a function of $q^2$. The resonant form factor at $q^2 = 0$ is equal to the photocoupling, $g_{\rho\pi\gamma} = F_{\pi\gamma\to\rho}(0)$. Our results for $g_{\rho\pi\gamma}$, now for all fourteen amplitude parametrizations that gave good fits, are shown in Fig. 5.24.

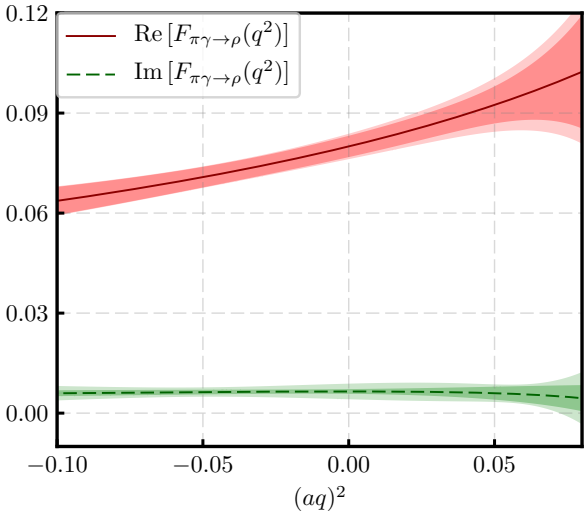


Fig. 5.23 The real and imaginary parts of the resonant form factor $F_{\pi\gamma\to\rho}(q^2)$ obtained by analytically continuing the nominal parametrization "BWII F1 K2" of the $\pi\gamma \to \pi\pi$ amplitude to the $\rho$ resonance pole. The inner (darker) shaded region indicates the statistical and systematic uncertainties, and the outer (lighter) shaded region also includes the parametrization uncertainty, estimated as explained in the caption of Fig. 5.21.

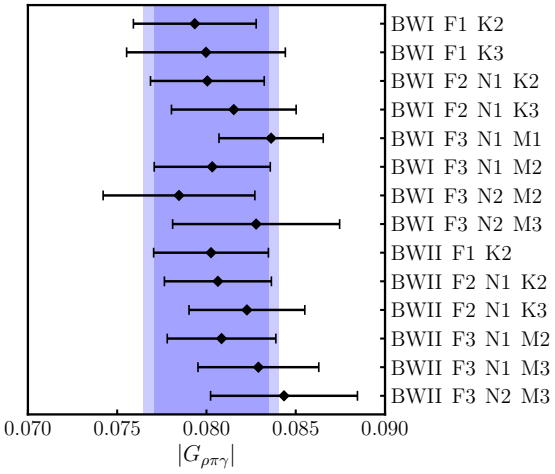


Fig. 5.24 The $\rho$ meson photocoupling determined from the fourteen different parametrizations of the $\pi\gamma \to \pi\pi$ amplitudes. The bands indicate the value and uncertainties obtained from the nominal parametrization "BWII F1 K2", where the outer (lighter) band includes (added in quadrature) the root-mean-square deviation between all parametrizations and the chosen one.

We find that the photocouplings extracted from the different parametrizations are consistent with each other. Nevertheless, we estimate a systematic uncertainty associated with the

choice of parametrization as

$$\sqrt{\sum_{i=1}^{N} \frac{(x_i - x_{\text{chosen}})^2}{N-1}}, \tag{5.67}$$

where $x_i$ is the photocoupling determined from the $i$-th parametrizations, $N = 14$ is the number of different parametrizations, and $x_{\text{chosen}}$ is the value obtained from the nominal parametrization, "BWII F1 K2". Our final result for the photocoupling is

$$|g_{\rho\pi\gamma}| = 0.0802(32)(20), \tag{5.68}$$

where the first uncertainty includes the statistical uncertainty and the systematic uncertainty from the two-point and three-point function fits, while the second uncertainty is our estimate from Eq. (5.67) of the parametrization dependence.

The kinematic factors in Eq. (5.41) lead to a strong pion-mass dependence of the $\rho$ radiative decay width. We can calculate the decay width for the physical pion mass under the assumption that the pion-mass dependence of the photocoupling is negligible. This gives

$$\Gamma(\rho \to \pi\gamma) = 84.2(6.7)(4.3)\,\text{keV}, \tag{5.69}$$

where we used $m_\rho = 775$ MeV and $m_\pi = 140$ MeV. For comparison, the experimental value of the $\rho^\pm$ radiative decay width is $68(7)$ keV [206].

### 5.2.9 Conclusion

All in all, we have determined the transition amplitude $\mathscr{V}_{\pi\gamma\to\pi\pi}(q^2, s)$ with few-percent uncertainty in a broad kinematic region around the $\rho$ pole in invariant mass $s$ and around zero momentum transfer $q^2$, using model-independent parametrizations based on a series expansion in the variables $z$ and $\mathscr{S}$, defined in Eqs. (5.62) and (5.61). The results obtained from several different truncations of the series are consistent with each other. One important remark on our results is that although we have observed the expected enhancement of the amplitude associated with the $\rho$ resonance, but we find that for large $\sqrt{s}$ the amplitude falls off slower than the expected for a purely resonant behavior. In our analysis, we compared two different Breit-Wigner parametrizations of the $\pi\pi$ scattering phase shift (with and without a Blatt-Weisskopf barrier factor). These parametrizations yield consistent results for $\mathscr{V}_{\pi\gamma\to\pi\pi}(q^2, s)$ in most of the kinematic range, but differ for large $\sqrt{s}$.

By analytically continuing $\mathscr{V}_{\pi\gamma\to\pi\pi}(q^2, s)$ to the $\rho$ pole, we have also determined the $\pi\gamma \to \rho$ resonant form factor and the $\rho$ photocoupling. All truncations of the series used for

$\mathscr{V}_{\pi\gamma\to\pi\pi}(q^2,s)$, and both Breit-Wigner functions, lead to consistent results for the photocoupling, as can be seen in Fig. 5.24. Our final result for this coupling is $|g_{\rho\pi\gamma}| = 0.0802(32)(20)$, which is $1.6\sigma$ above the value extracted from the measured $\rho^{\pm}$ radiative decay width [206] using Eq. (5.41), $|g_{\rho\pi\gamma}|_{\text{exp}} = 0.0719(37)$. Most of the past lattice studies of this quantity [253, 77, 203, 223] were performed in the single-hadron approach, in which the coupling of the $\rho$ to the $\pi\pi$ system is not taken into account. In literature, till now the only other calculation of transition form factor and photocoupling of Refs. [52, 53] used the multi-hadron approach at a pion mass of approximately 400 MeV and obtained a value of $|g_{\rho\pi\gamma}|$ around 0.12, as can be seen in Fig. 12 of [53].

# Chapter 6

# Towards $\Delta$ Resonance & photoproduction

The study of the $\rho$-meson presented in Chapter 5 has allowed us, beyond providing an up-to-date estimate of the $\rho$-meson transition form-factor and decay-width, to develop the formalism and methodology for the study of resonances using lattice QCD. With this as a stepping stone, we will explore more complex $2 \to 2$ scattering systems. In this chapter, we build the two and three-point correlation functions with projected interpolators needed to study the lowest lying baryon resonance, the $\Delta$ and present some preliminary results for the GEVP spectra, as part of an on-going program for the study of resonance properties in the meson-baryon system.

## 6.1 $\Delta$ resonance

Here we explore nucleon-pion scattering in the $I = 3/2$ and $J^P = 3/2^+$ channel where the lowest-lying baryon resonance, the $\Delta(1232)$, is located. This resonance has a mass of $\approx 1210$ MeV and a decay width of $\Gamma_{\Delta \to N\pi} \approx 117$ MeV [207]. The $I = 3/2$ $P$-wave $N\pi$ channel is the dominant decay mode, with a branching fraction of 99.4%. The PDG only lists one other decay mode - $N\gamma$ with a branching fraction 0.6%. The process is almost completely elastic [222], but nearby inelastic resonances with similar quantum numbers could have a small contribution on the phase shift that needs to be taken into account in the analysis.

Previous studies of the $\Delta$ coupling to the $N\pi$ channel have used the Michael-McNeile method to determine the coupling [14] as well as the Lüscher method [181, 239, 18]. With either method, compared to the $\rho$-meson study of Chapter 5, the main challenge is the more complex quark contractions involved. A main component of this thesis has been to develop

an efficient methodology for computing the quark correlation functions for the $N\pi/\Delta$ system, which we will highlight in this Chapter.

### Gauge Ensemble

The parameters of the lattice gauge-field ensemble used in our study of the Δ-resonance are given in Table 6.1. The gluon action is a tadpole-improved tree-level Symanzik action [233, 231, 232, 172] and the fermionic action is $2+1$ flavors of tree-level improved Wilson-clover action [251, 220]. The gauge links in the fermion action are smeared using two levels of HEX smearing [90]. The lattice scale reported in Table 6.1 was determined mass-independently from the physical values of the ratios $m_\pi/m_\Omega$ and $m_K/m_\Omega$. The $s$ quark masses are tuned to have a mass close to physical. This ensemble was chosen because the $m_\Delta^{\text{stable}} > m_\pi + m_N$ (when Δ is treated as a QCD-stable hadron as in Ref. [90]), and from Eq. (3.8), the $m_\Delta^{\text{stable}}$ lies within the lowest and the highest energies of a $\pi N$ state accessible on the lattice, i.e. $E_{\pi N}^{\text{lowest}} < m_\Delta < E_{\pi N}^{\text{highest}}$ .

Table 6.1 Details of the gauge-field ensemble. $N_L$ and $N_T$ denote the number of lattice points in the spatial and time directions. The lattice spacing was obtained by the physical values of the ratios $m_\pi/m_\Omega$ and $m_K/m_\Omega$. The ensemble was generated with $N_f = 2+1$ flavors of sea quarks with bare masses $am_{u,d}$ and $am_s$, which lead to the given values of $am_\pi$, $am_N$, and $am_{\eta_s}$. The $\eta_s$ is an artificial pseudoscalar $s\bar{s}$ meson that can be used to tune the strange-quark mass [78, 83]. The uncertainties given here are statistical only.

| | A7 | MeV |
|---|---|---|
| $N_L^3 \times N_T$ | $24^3 \times 48$ | |
| $\beta$ | 3.31 | |
| $N_f$ | $2+1$ | |
| $c_{sw}$ | 1.0 | |
| $am_{u,d}$ | $-0.0953$ | |
| $am_s$ | $-0.040$ | |
| $N_{config}$ | 600 | |
| $a$ [fm] | 0.116 | |
| $L$ [fm] | 2.8 | |
| $am_\pi$ | 0.1493(6) | 254(1) |
| $am_N$ | 0.6302(41) | 1072(7) |
| $m_\pi L$ | 3.6 | |

### 6.1.1 Interpolators and correlation functions

To extract the lattice spectrum in the nucleon and Δ channel, we construct correlation matrices from two-point functions of one and two-hadron interpolating fields with quantum numbers of the Nucleon ($N$), Delta ($\Delta$) and Pion-Nucleon ($\pi N$) respectively. As building blocks, we use the familiar single-hadron interpolating fields for the pion, nucleon and Δ discussed in Sec. 4.2. Our choices of total momenta for the $\pi N$ system are listed in the first column of Table 6.2.

Table 6.2 Choices of total momenta (and numbers of equivalent directions), along with the relevant symmetry groups, irreducible representations Λ, and in parenthesis their angular momentum content.

| $\frac{L}{2\pi}\vec{P}_{ref}[N_{dir}]$ | Group | $N_{elem}$ | $\Lambda(J):\pi(0^-)$ | $\Lambda(J):N(\frac{1}{2}^+)$ | $\Lambda(J):\Delta(\frac{3}{2}^+)$ |
|---|---|---|---|---|---|
| (0,0,0) [1] | $O_h^D$ | 96 | $A_{1u}(0,4,...)$ | $G_{1g}(\frac{1}{2},\frac{7}{2},...)\oplus G_{1u}(\frac{1}{2},\frac{7}{2},...)$ | $H_g(\frac{3}{2},\frac{5}{2},...)\oplus H_u(\frac{3}{2},\frac{5}{2},...)$ |
| (0,0,1) [6] | $C_{4v}^D$ | 16 | $A_2(0,1,...)$ | $G_1(\frac{1}{2},\frac{3}{2},...)$ | $G_1(\frac{1}{2},\frac{3}{2},...)\oplus G_2(\frac{3}{2},\frac{5}{2},...)$ |
| (0,1,1) [12] | $C_{2v}^D$ | 8 | $A_2(0,1,...)$ | $G(\frac{1}{2},\frac{3}{2},...)$ | $G(\frac{1}{2},\frac{3}{2},...)$ |
| (1,1,1) [8] | $C_{3v}^D$ | 12 | $A_2(0,1,...)$ | $G(\frac{1}{2},\frac{3}{2},...)$ | $G(\frac{1}{2},\frac{3}{2},...)\oplus F_1(\frac{3}{2},\frac{5}{2},...)\oplus F_2(\frac{3}{2},\frac{5}{2},...)$ |

We apply group-theoretical subduction/projection to obtain operators that transform irreducibly under rotations and reflections of the proper symmetry group as discussed in Sec. 4.2 with Eq. (4.2). The single-hadron operators transform under rotations as

$$\begin{aligned} R\pi(t,\vec{x})R^{-1} &= \pi(t,R^{-1}\vec{x}),\\ RN(t,\vec{x})R^{-1} &= S(R)N(t,R^{-1}\vec{x}),\\ R\Delta(t,\vec{x})^{\alpha}_{k}R^{-1} &= A(R)_{kk'}S(R)\Delta^{\alpha}_{k'}(t,R^{-1}\vec{x}), \end{aligned} \tag{6.1}$$

where $A(R)=U^1(\omega,\Theta,\Psi)$ denotes the 3-dimensional irrep of SU(2) with the variables $\omega$, $\Theta$ and $\Psi$ representing the parameters of the basis[1], and $S(R)$ is the 2-dimensional spinor representation of $SU(2)$,

$$S(R)=\begin{bmatrix} U^{1/2}(R) & 0\\ 0 & U^{1/2}(R)\end{bmatrix}. \tag{6.2}$$

[1] If the basis is chosen as Euler angles basis, then these three are the Euler angles $\alpha$, $\beta$ and $\gamma$.

Table 6.3 Multiplicities of irreps of the group $O_h^D$ (rest frame) in the subduction of half-integer-$J$ irreps of $SU(2)$. The subscripts $g/u$ indicate the parity *gerade/ungerade* (even/odd).

| $Irr\backslash J$ | $J=1/2$ | $J=3/2$ | $J=5/2$ | $J=7/2$ | $J=9/2$ |
|---|---|---|---|---|---|
| $G_{1g/u}$ | 1 | 0 | 0 | 1 | 1 |
| $G_{2g/u}$ | 0 | 0 | 1 | 1 | 0 |
| $H_{g/u}$ | 0 | 1 | 1 | 1 | 2 |

The inversions are given by

$$\begin{aligned} I\pi(t,\vec{x})I^{-1} &= -\pi(t,-\vec{x}), \\ IN(t,\vec{x})I^{-1} &= \gamma_t N(t,-\vec{x}), \\ I\Delta(t,\vec{x})I^{-1} &= \gamma_t \Delta(t,-\vec{x}). \end{aligned} \tag{6.3}$$

Our choice of the Euclidean $\gamma$-matrices is the DeGrand-Rossi basis.
In moving frames, the choice of center of mass momentum $\vec{P}$ determines the relevant symmetry group. Looking at Table 6.3, the $J$ value of the hadron tells us in which irrep (of the rest frame) it should be contained. It is possible to find the multiplicity $m$ of the irrep $\Gamma^{\Lambda}$ in the matrix $M(R)$ realizing the transformation (e.g. $S(R)$ for the single nucleon) using the Eq. (4.1). The multiplicities $m$ give us the numbers of multiplicities of the irreps for the specific operator we want to project (see Table 6.3). This corresponds to the number of independent projected operators we can extract for a specific irrep $\Lambda$ and row $r$. In Figs. 6.1 and 6.2, we show schematically the decomposition of the transformation matrices $S(R)$ for the nucleon and $A(R)\otimes S(R)$ for the Delta in all frames relevant for this study.

Once we correctly identified the tensor decomposition in each irrep, we used our code to project the $N$, $\Delta$ and $N\pi$ interpolators (the single $\pi$ does not need projection). Most of the projections lead to linearly dependent operators [190]. We made use of the Gram-Schmidt procedure to construct linear combinations of operators orthogonal to each other. As an example for the nucleon-pion system, we show one projected operator in the rest frame in irrep $H_g$ and row $r=1$:

$$\frac{1}{2}\pi(1,0,0)N_2(-1,0,0)+\frac{1}{2}i\pi(0,1,0)N_2(0,-1,0)-\frac{1}{2}i\pi(0,-1,0)N_2(0,1,0)-\frac{1}{2}\pi(-1,0,0).N_2(1,0,0).$$

The momentum directions are given in brackets and the subscript of the nucleon operator labels the Dirac index. Taking into account all linearly independent operators, rows and momentum directions in the 8 irreps of the 4 frames considered, we reach a total of 1720

projected operators for Delta and the nucleon-pion system. In order to maximize the statistics, we use all of them when building the correlation functions.

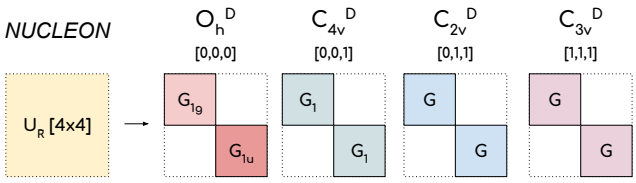


Fig. 6.1 Tensor decomposition of the nucleon transformation matrices. Applying Eq. (4.1) to the nucleon transformation matrices $S(R)$ tells us the multiplicity of the irreps containing $J = 1/2$ in each frame. This information guides us in the projection of the single-nucleon interpolator. It shows that in the rest frame we can have one projected interpolator for each of the irreps $G_{1g}$ and $G_{1u}$. On the other hand, in each moving frame, we can build two linearly independent nucleon interpolators since the same irrep has a double multiplicity.

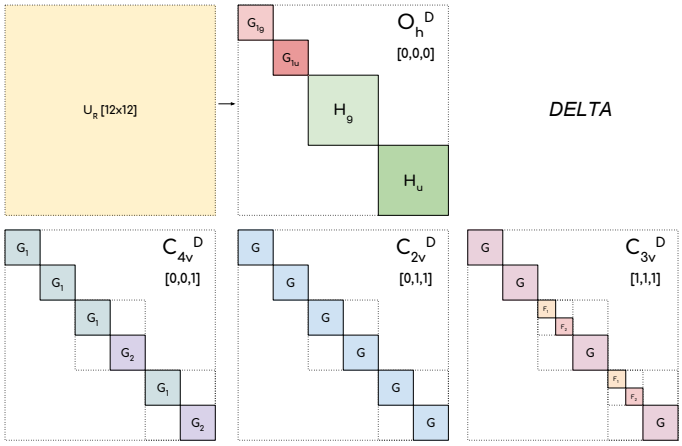


Fig. 6.2 Tensor decomposition of the Delta transformation matrices. The transformation matrix for the Delta comes from the tensor product $A(R) \otimes S(R)$ in Eq. (6.1) (with inversion from Eq. (6.3)). Applying Eq. (4.1) shows the multiplicity of irreps containing $J = 3/2$. In the rest frame, there are only single multiplicities, while in moving frames there are several multiplicities. For example, for the group $C_{2v}^D$ the same irrep $G$ appears 6 times. In fact, we can build 6 independent projected operators for a single $\Delta$ in this irrep.

The two-point functions obtained from the interpolators above are evaluated by Wick contraction and factorization into products of diagram building blocks. The latter are calculated numerically from point-to-all, sequential and stochastic propagators. Figure 6.3

shows the topology types for the diagrams obtained from the $\Delta - \Delta$ and $\Delta - \pi N$ two-point correlation functions in the left panel. The right panel shows the same for the $\pi N - \pi N$ correlator. In both panels, each topology represents 2 to 4 actual diagrams.

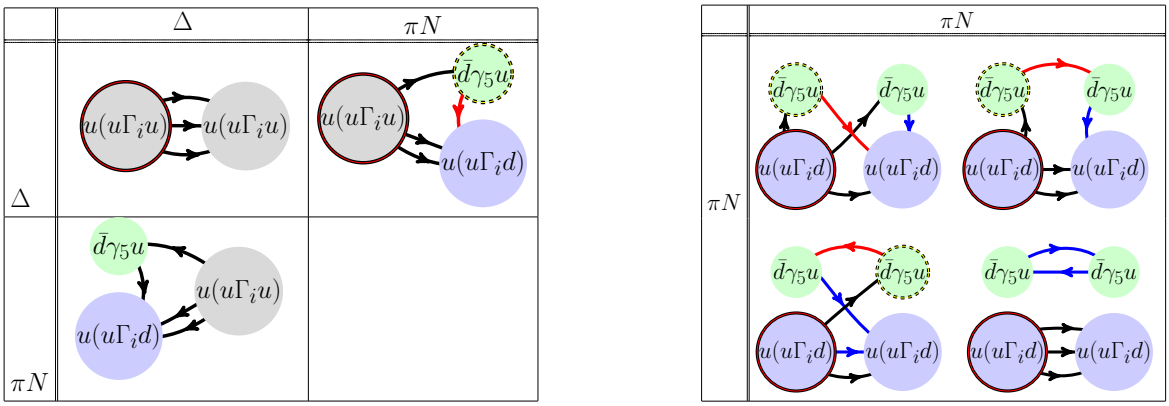


Fig. 6.3 Left panel: Two-point function contractions involving the Δ interpolator. Grey circles represent the Δ, green circles represent the $\pi$, and blue circles represent the $N$. A circle with a solid outline represents a point source, while the dotted outline represents a sequential source. The black arrow lines represent point-to-all propagators, and the red arrow lines represent sequential propagators. Right panel: Two-point function contractions for $\pi N - \pi N$, otherwise analogous to the left panel. The blue arrow lines represent stochastic propagators.

The computation of the $\pi N \to \pi N$ correlation functions is a computationally demanding task. We developed a state-of-the-art method for segregating the stochastic source and stochastic propagator part in all the $\pi N \to \pi N$ diagrams, which can be later recombined to form the diagrams in Fig. 6.3. This procedure can be visually illustrated in Fig. 6.4.

Another major advantage of using this factorization scheme is the re-occurrence of these factors in three-point functions ($\pi N \to \mathrm{J} \to N$) with a current insertion J, as in Fig. 6.5. We observe that the factors highlighted by green in two and three point functions in Fig. 6.4 and Fig. 6.5 are exactly the same. Therefore, computing these factors once for the two-point functions can be reused to compute the three-point functions, thus saving approximately $\mathscr{O}(10) \times N_{\text{configurations}}$ of computational resources.

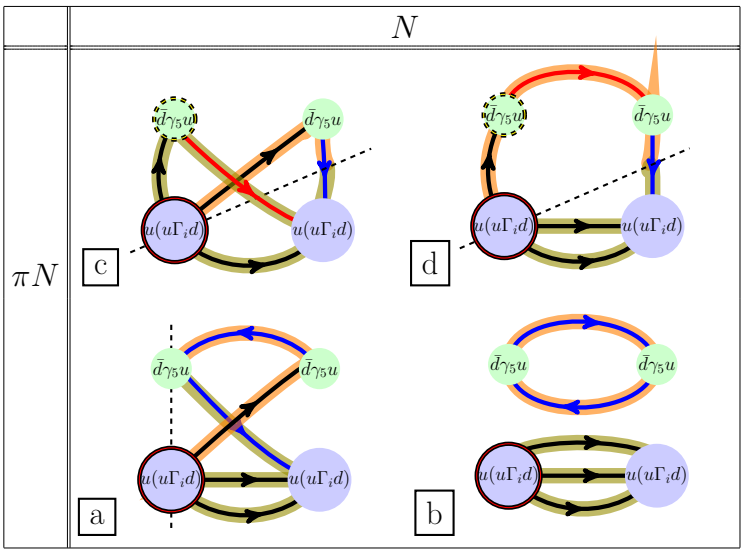


Fig. 6.4 The two factors of the two-point functions are represented by the green and the orange highlights. For diagrams (b.), (c.) and (d.), the dotted line separates the two factors along the point source and the product of stochastic source and propagators. In diagram (a.), the dotted line separates the two factors along the point source and the product of two stochastic one-end-trick propagators.

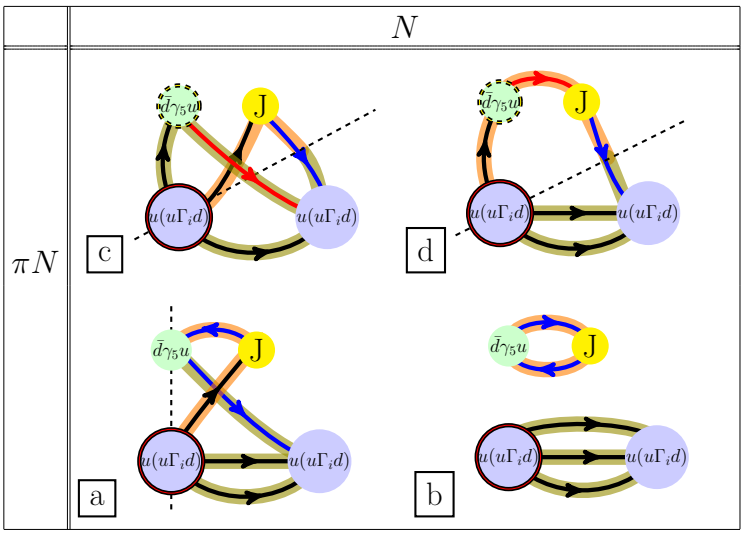


Fig. 6.5 The two factors of the three-point functions with a current insertion $J$, are represented by the olive and the orange parts. The current insertion is represented by the yellow circle containing J. The dotted line separates the two factors along the point source the product of the stochastic source and propagators in the diagrams (b.), (c.) and (d.). In diagram (a.) the dotted line separates the two factors along the point source and the product of two stochastic one-end-trick propagators.

### 6.1.2 Spectrum results

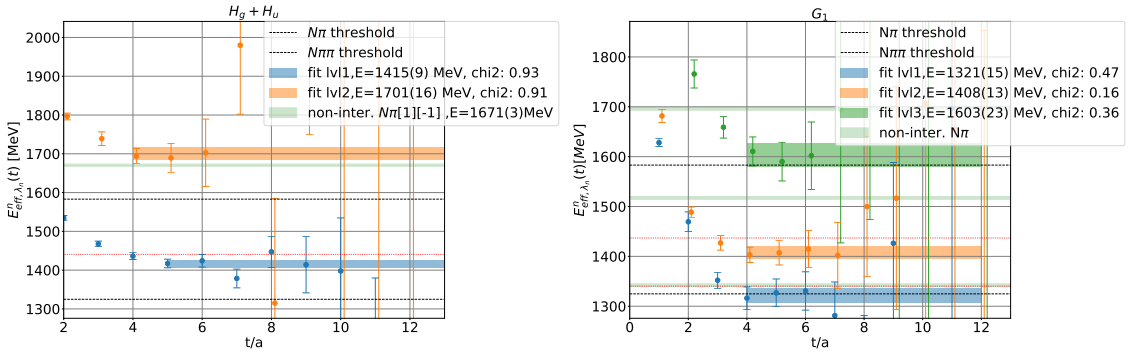


Fig. 6.6 Effective-energy plots. Left panel: Rest frame $\vec{P} = \frac{2\pi}{L}(0,0,0)$: group $O_h^D$, irreps $H_g$ (forward-propagating) and $H_u$ (backward-propagating). The ground state has maximum overlap with the single-hadron Δ-like interpolator, while the first excited level shows an expected shift in energy with respect to the first non-interacting nucleon-pion energy. Right panel: Moving frame $\vec{P} = \frac{2\pi}{L}(0,0,1)$: group $C_{4v}^D$, irrep $G_1$. The ground state has a dominant overlap to the $N\pi$ two-hadron interpolator, while the second energy level overlaps dominantly with the Δ operator. The other two levels display a shift in energy with respect to their non-interacting counterparts, in the direction away from the resonance.

With a basis of projected interpolators we construct correlation matrices $C_{ij}^{\Lambda,r,m}$ and make use of the variational method (Generalized EigenValue Problem) [43] to determine the energy spectrum in each irrep, as defined in Sec. 4.6. Fig. 6.6 shows the effective energies and the fit results for the chosen time ranges, in two irreps, one from the center of mass frame and one from $\vec{P} = (0,0,1)$ moving frame. We perform single-exponential fits directly on the principal correlators. To ensure that early-time excited-state contamination is negligible, we perform stability tests by looking for a plateau while varying $t_{min}$ in the fit time interval $[t_{min}, t_{max}]$ which is the same procedure implemented in Sec. 5.1.5.

### 6.1.3 Lüscher Analysis: Phase shift fit results

We implement the Lüscher analysis as discussed in Sec. 4.7.2 for baryons on the obtained spectrum. The block-diagonalization of the matrix $\mathscr{M}^{\vec{P}}$ into its irreps Λ, was emphasized in Sec. 4.7.2 with an example in the moving frame $\vec{P} = \frac{2\pi}{L}(0,0,1)$ with symmetry group $C_{4v}^D$. We revisit that example by depicting the decomposition in Fig. 6.7 and further simplify the quantization condition. With two irreps $G_1$ and $G_2$, Eq. (5.25) simplifies to one quantization condition per irrep,

$$\det(M^{G_1}_{Jln,J'l'n'} - \delta_{JJ'}\delta_{ll'}\delta_{nn'}\cot\delta^{G_1}_{Jl}) = 0, \tag{6.4}$$

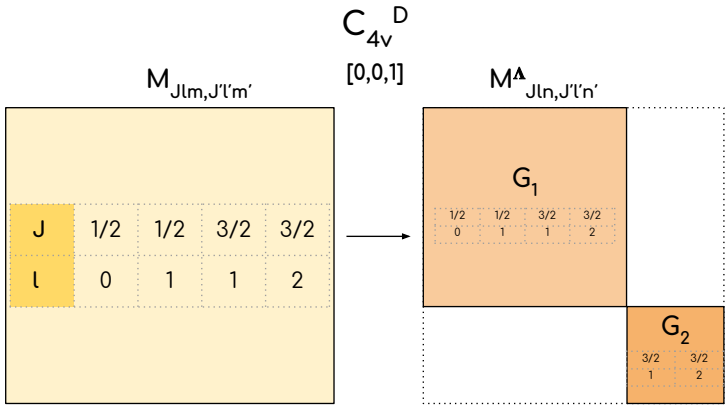


Fig. 6.7 Block diagonalization of the $M$ matrix in the irrep basis. The case shown is for the $C_{4v}^{D}$ group.

$$\det(M^{G_2}_{Jln,J'l'n'} - \delta_{JJ'}\delta_{ll'}\delta_{nn'}\cot\delta^{G_2}_{Jl}) = 0. \tag{6.5}$$

This basis transformation, along with the angular-momentum content, is also shown schematically in Fig. 6.7. The angular-momentum content depicts the mixing of various partial waves that contribute to the $J = 3/2$ channel.

The quantization conditions can be written in terms of $w_{js}$ functions (where $|l-l'| \leq j \leq l+l'$ and $-j \leq s \leq j$) that include the generalized Zeta functions. For the case of $G_2$, considering all relevant $J,l$ values of the phase shift $\delta_{J,l}$ present in the energy region of interest, the quantization condition can be written as

$$9\left(w_{1,0} - w_{3,0}\right)^2 - 25\left(-\cot\delta^{G_2}_{\frac{3}{2},1} + w_{0,0} - w_{2,0}\right)\left(-\cot\delta^{G_2}_{\frac{3}{2},2} + w_{0,0} - w_{2,0}\right) = 0. \tag{6.6}$$

The mixing between $l = 1$ and $l = 2$, is shown in Eq. (6.6). If we neglect contributions from $l = 2$, we arrive at the quantization condition as used in Ref. [112].

Due to the existence of eigenstates with the same total angular momentum $J$, but different orbital angular momenta $l$, we have mixtures in scattering amplitudes originating from nearby Δ resonances. In this preliminary study, we are only interested in the phase shift $\delta_{J=\frac{3}{2},l=1}$. Having fixed $l_{max}$, we neglect the contributions from higher partial waves. To extract the resonance parameters, we directly fit the phase shift values obtained from the quantization conditions in different irreps, to a phase shift model as already discussed as the first approach in Sec. 5.1.6. From the fitted energy levels obtained from the GEVP, we use irreps $H_g + H_u$

in $O_h^D$ (CM frame), $G_2$ in $C_{2v}^D$ (moving frame with $\vec{P} = (0,0,1)$) and $G$ in $C_{4v}^D$ (moving frame with $\vec{P} = (0,1,1)$)[2].

For the Δ resonance, the decay width can be expressed in effective field theory [205] to lowest order as

$$\Gamma_{EFT}^{LO}(s) = \frac{g_{\Delta-\pi N}^2}{48\pi} \frac{E_N + m_N}{E_N + E_\pi} \frac{p^{*3}}{m_N^2}, \tag{6.7}$$

with the dimensionless coupling $g_{\Delta-\pi N}$ and center-of-mass momentum $p^*$.

We also take the general $P$-wave decay width formed used in all lattice calculations, given by,

$$\Gamma(s) = \frac{g_{\Delta\pi N}^2}{6\pi} \frac{p^{*3}}{s} \tag{6.8}$$

Thus, the fit results of fitting the phase shift values obtained to these two models of decay width are shown in Figs. 6.8 and 6.9.

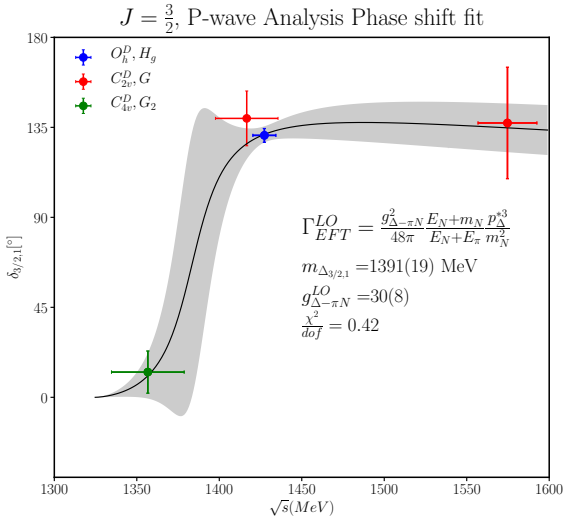


Fig. 6.8 The $J = 3/2$, $P$-wave, $N$-$\pi$ scattering phase shift with the decay width written in effective field theory to lowest order.

Table 6.4 Parameters for the resonant P-wave decay width and Lowest order EFT expansion of decay width, along with the experimental value

| Model | $\frac{\chi^2}{\text{dof}}$ | $m_\Delta$ | $g_{\Delta\pi N}$ |
|---|---|---|---|
| $\Gamma_{P-\text{wave}}$ | 0.42 | 1386(21) | 18(5) |
| $\Gamma_{EFT}^{LO}$ | 0.457 | 1391(19) | 30(8) |
| Experimental | | 1232(1) | 29.4(3) |

[2]It should be noted that from Table. 6.2, $G$ contains mixing from lower partial waves $J = 1/2$, $\ell = 0$ But for the current analysis, we neglect the $J = 1/2$, $\ell = 0$ contributions.

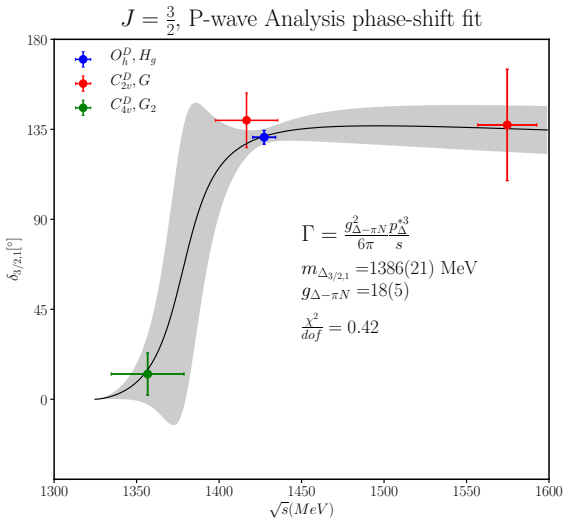


Fig. 6.9 The $J = 3/2$, $P$-wave, $N$-$\pi$ scattering phase shift with general $P$-wave decay width.

In Table. 6.4, we provide the results for $m_\Delta$ and $g_\Delta \pi N$ after analyzing 200 configurations. Qualitative comparison with the experiment shows that the factorization scheme enables an affordable calculation of the $\Delta$-$\pi N$ system at the full statistics of 600 configurations.

## 6.2 Conclusion

In this Chapter, we have computed the two-point functions with the state-of-the-art factorization method which saves computational resources of the $\mathcal{O}(10) \cdot N_{configurations}$. The factors computed for two-point functions can be reused to compute three-point functions with an electromagnetic current insertion. We construct the correlation matrices using these two-point functions for each relevant irrep of the symmetry group of the lattice. Using the spectra extracted from the GEVP analysis of these correlation matrices in the Lüscher formalism, we have computed phase-shift values in the CM frame and two moving frames. With the analysis of 200 configurations at hand, we are restricted to few irreps for the analysis. Qualitative comparison with the experiment yields reasonable agreement allowing us to proceed to the full-statistics calculation employing this factorization method.

.

# Chapter 7

# Conclusion

In this thesis, we have presented a study of meson and baryon resonances in $2 \to 2$ scattering via direct simulation of the theory of strong interactions using lattice techniques. We have developed state-of-the-art methods to compute the correlation functions, utilized the recently developed Multigrid preconditioned Krylov-subspace solver to compute the quark propagators and successfully implemented the Lüscher formalism for studying meson and baryon resonances. Furthermore, we built upon our computation of resonance parameters to extract the transition form factors and coupling in resonance photoproduction using the recently developed Briceno, Hansen, Walker-Loud formalism. In addition, we performed an exploratory study of machine learning on the 2-D Ising model.

## 7.1 Summary of results

In the meson scattering sector, we have calculated the parameters for the narrow lowest lying $\rho$ meson resonance describing the elastic $I = 1$, $P$-wave $\pi\pi$ scattering using lattice QCD with $2+1$ flavors of clover fermions. Our calculation is performed with a pion mass of $m_\pi \approx 320$ MeV and a lattice size of $L \approx 3.6$ fm. We find that at a pion mass of $am_\pi = 0.18295(36)_{stat}$ we obtain $g_{\rho\pi\pi} = 5.69(13)_{stat}(16)_{sys}$, $am_\rho = 0.4609(16)_{stat}(14)_{sys}$, and $am_\rho/am_N = 0.7476(38)_{stat}(23)_{sys}$, where the first uncertainty is statistical and the second is the systematic uncertainty due to the choice of fit ranges. Our results for the $\rho$ resonance parameters, when compared in a scale invariant way i.e. by taking the ratio of the resonance mass with the nucleon mass, are in agreement with other $N_f = 2+1$ and $N_f = 2$ results in the literature. Moreover, the coupling $g_{\rho\pi\pi}$ shows no pion mass dependence which is compatible with the general findings. For the $\rho$ resonance photoproduction $\pi\pi \to \pi\gamma$, we implemented the extension of the Lüscher formalism, Briceño, Hansen, Walker-Loud formalism to compute the transition form factor and the photocoupling $|G_{\rho\pi\gamma}| = 0.0802(32)(20)$. The model-

independent parametrization of the transition form factor $\mathscr{V}_{\pi\gamma\to\pi\pi}(s,q^2)$ shows no discernible changes when the series is truncated at different values. It is worth noting that, for large $\sqrt{s}$ the amplitude falls off slower than the expected for a purely resonant behavior. Nevertheless, the value of photocoupling obtained in $1.6\sigma$ away from the experimental value, which is highly encouraging. Apart from $\pi\pi$ scattering, in the meson sector, on the same ensemble there is an ongoing investigation for $K^*$ resonance in the $P$ wave $\pi K$ channel [215].

Our study of baryon scattering resonances includes the $P$-wave $\pi N$ scattering analysis where we have developed a state-of-the-art factorization method for evaluating the two-point correlation functions which led to the reduction in computational cost by $\mathscr{O}(10) \times N_{\text{configurations}}$. Moreover, we can reuse these factors, to evaluate three-point functions with an electromagnetic current insertion. Our proof-of-concept analysis for obtaining scattering phase-shifts, yield results which match qualitatively the experiment, paving the way for a full-fledged analysis.

## 7.2 Outlook

In the case of the meson scattering study, future calculations at lower pion masses, larger volumes, and additional values of the lattice spacing are needed to extrapolate to the physical point and to obtain a better estimate of the systematic errors. One source of systematic errors is the residual contamination from higher excited states in the analysis of the correlation functions. Better control over this contamination can be achieved by using more than three source-sink separations for three-point functions and employing more advanced analysis methods [60] for analyzing two-point functions.

For the $P$-wave $\pi N$ scattering, computations for the correlation functions for the full set of statistics are still ongoing. In order to get the complete picture we would like to obtain the GEVP spectra for all the irreps and perform the Lüscher analysis for the $2 \to 2$ $\pi N$ system to extract the $\Delta$ resonance parameters. These resonance parameters can then be utilized to study the $\Delta$ photoproduction in the $\pi N$ channel.

# References


[1] Aad, G. et al. (2012). Observation of a new particle in the search for the Standard Model Higgs boson with the ATLAS detector at the LHC. *Phys. Lett.*, B716:1–29.

[2] Abadi, M., Barham, P., Chen, J., Chen, Z., Davis, A., Dean, J., Devin, M., Ghemawat, S., Irving, G., Isard, M., et al. (2016). Tensorflow: a system for large-scale machine learning. In *OSDI*, volume 16, pages 265–283.

[3] Abdel-Rehim, A. et al. (2017). First physics results at the physical pion mass from $N_f = 2$ Wilson twisted mass fermions at maximal twist. *Phys. Rev.*, D95(9):094515.

[4] Agadjanov, A., Bernard, V., Meißner, U. G., and Rusetsky, A. (2014). A framework for the calculation of the $\Delta N \gamma^*$ transition form factors on the lattice. *Nucl. Phys.*, B886:1199–1222.

[5] Agadjanov, A., Bernard, V., Meißner, U.-G., and Rusetsky, A. (2016). The $B \to K^*$ form factors on the lattice. *Nucl. Phys.*, B910:387–409.

[6] Albanese, M. et al. (1987). Glueball Masses and String Tension in Lattice QCD. *Phys. Lett.*, B192:163–169.

[7] Albergo, M. S., Kanwar, G., and Shanahan, P. E. (2019). Flow-based generative models for Markov chain Monte Carlo in lattice field theory.

[8] Alexandrou, C., Athenodorou, A., Chrysostomou, C., and Paul, S. (2019). Unsupervised identification of the phase transition on the 2D-Ising model.

[9] Alexandrou, C., Brinet, M., Carbonell, J., Constantinou, M., Harraud, P. A., Guichon, P., Jansen, K., Korzec, T., and Papinutto, M. (2011). Axial Nucleon form factors from lattice QCD. *Phys. Rev.*, D83:045010.

[10] Alexandrou, C. et al. (2018a). Simulating twisted mass fermions at physical light, strange and charm quark masses. *Phys. Rev.*, D98(5):054518.

[11] Alexandrou, C., Leskovec, L., Meinel, S., Negele, J., Paul, S., Petschlies, M., Pochinsky, A., Rendon, G., and Syritsyn, S. (2017). $P$-wave $\pi\pi$ scattering and the $\rho$ resonance from lattice QCD. *Phys. Rev.*, D96(3):034525.

[12] Alexandrou, C., Leskovec, L., Meinel, S., Negele, J., Paul, S., Petschlies, M., Pochinsky, A., Rendon, G., and Syritsyn, S. (2018b). $\pi\gamma \to \pi\pi$ transition and the $\rho$ radiative decay width from lattice QCD. *Phys. Rev.*, D98(7):074502.

[13] Alexandrou, C., Negele, J. W., Petschlies, M., Pochinsky, A. V., and Syritsyn, S. N. (2016). Study of decuplet baryon resonances from lattice QCD. *Phys. Rev.*, D93(11):114515.

[14] Alexandrou, C., Negele, J. W., Petschlies, M., Strelchenko, A., and Tsapalis, A. (2013). Determination of $\Delta$ resonance parameters from lattice QCD. *Phys. Rev.*, D88(3):031501.

[15] Allton, C. et al. (2008). Physical Results from 2+1 Flavor Domain Wall QCD and SU(2) Chiral Perturbation Theory. *Phys. Rev.*, D78:114509.

[16] Ametller, L., Knecht, M., and Talavera, P. (2001). Electromagnetic corrections to gamma pi+- —> pi0 pi+-. *Phys. Rev.*, D64:094009.

[17] Andersen, C., Bulava, J., Hörz, B., and Morningstar, C. (2018a). The $I = 1$ pion-pion scattering amplitude and timelike pion form factor from $N_{\mathrm{f}} = 2 + 1$ lattice QCD.

[18] Andersen, C. W., Bulava, J., Hörz, B., and Morningstar, C. (2018b). Elastic $I = 3/2p$-wave nucleon-pion scattering amplitude and the $\Delta(1232)$ resonance from $\mathrm{N}_f$=2+1 lattice QCD. *Phys. Rev.*, D97(1):014506.

[19] Aoki, S. et al. (2007). Lattice QCD Calculation of the $\rho$ Meson Decay Width. *Phys. Rev.*, D76:094506.

[20] Aoki, S. et al. (2009). 2+1 Flavor Lattice QCD toward the Physical Point. *Phys. Rev.*, D79:034503.

[21] Aoki, S. et al. (2011). $\rho$ Meson Decay in 2+1 Flavor Lattice QCD. *Phys. Rev.*, D84:094505.

[22] Arnold, P. B. and Moore, G. D. (2001). Monte Carlo simulation of O(2) $\phi^4$ field theory in three-dimensions. *Phys. Rev.*, E64:066113. [Erratum: Phys. Rev.E68,049902(2003)].

[23] Athenodorou, A. and Teper, M. (2019). On the spectrum and string tension of U(1) lattice gauge theory in 2 + 1 dimensions. *JHEP*, 01:063.

[24] Babich, R., Brannick, J., Brower, R. C., Clark, M. A., Manteuffel, T. A., McCormick, S. F., Osborn, J. C., and Rebbi, C. (2010). Adaptive multigrid algorithm for the lattice Wilson-Dirac operator. *Phys. Rev. Lett.*, 105:201602.

[25] Bai, Z. et al. (2015). Standard Model Prediction for Direct CP Violation in $K \to \pi\pi$ Decay. *Phys. Rev. Lett.*, 115(21):212001.

[26] Bali, G. S., Collins, S., Cox, A., Donald, G., Göckeler, M., Lang, C. B., and Schäfer, A. (2016a). $\rho$ and $K^*$ resonances on the lattice at nearly physical quark masses and $N_f = 2$. *Phys. Rev.*, D93(5):054509.

[27] Bali, G. S., Collins, S., Richtmann, D., Schäfer, A., Söldner, W., and Sternbeck, A. (2016b). Direct determinations of the nucleon and pion $\sigma$ terms at nearly physical quark masses. *Phys. Rev.*, D93(9):094504.

[28] Basak, S., Edwards, R., Fiebig, R., Fleming, G. T., Heller, U. M., Morningstar, C., Richards, D., Sato, I., and Wallace, S. J. (2004). Baryon operators and spectroscopy in lattice QCD. *Nucl. Phys. Proc. Suppl.*, 128:186–192. [,186(2003)].

[29] Basak, S., Edwards, R., Fleming, G. T., Heller, U. M., Morningstar, C., Richards, D., Sato, I., and Wallace, S. J. (2005a). Clebsch-Gordan construction of lattice interpolating fields for excited baryons. *Phys. Rev.*, D72:074501.

[30] Basak, S., Edwards, R. G., Fleming, G. T., Heller, U. M., Morningstar, C., Richards, D., Sato, I., and Wallace, S. (2005b). Group-theoretical construction of extended baryon operators in lattice QCD. *Phys. Rev.*, D72:094506.

[31] Beringer, J. et al. (2012). Review of Particle Physics (RPP). *Phys. Rev.*, D86:010001.

[32] Bernard, V., Hoja, D., Meissner, U. G., and Rusetsky, A. (2012). Matrix elements of unstable states. *JHEP*, 09:023.

[33] Bernard, V., Lage, M., Meissner, U.-G., and Rusetsky, A. (2008). Resonance properties from the finite-volume energy spectrum. *JHEP*, 08:024.

[34] Bečirević, D., Kruse, M., and Sanfilippo, F. (2015). Lattice QCD estimate of the $\eta_c$ (2S) $\to J/\psi\gamma$ decay rate. *JHEP*, 05:014.

[35] Bhattacharya, B., Hill, R. J., and Paz, G. (2011). Model independent determination of the axial mass parameter in quasielastic neutrino-nucleon scattering. *Phys. Rev.*, D84:073006.

[36] Bhattacharya, B., Paz, G., and Tropiano, A. J. (2015). Model-independent determination of the axial mass parameter in quasielastic antineutrino-nucleon scattering. *Phys. Rev.*, D92(11):113011.

[37] Bijnens, J., Bramon, A., and Cornet, F. (1990). Three Pseudoscalar Photon Interactions in Chiral Perturbation Theory. *Phys. Lett.*, B237:488–494.

[38] Bjorken, J. D. (1967). CURRENT ALGEBRA AT SMALL DISTANCES. *Conf. Proc.*, C670717:55–81.

[39] Bjorken, J. D. (1967). Theoretical Ideas on Inelastic Electron and Muon Scattering. In *Electron and Photon Interactions at High Energy*, page 109.

[40] Bjorken, J. D. and Paschos, E. A. (1969). Inelastic Electron Proton and gamma Proton Scattering, and the Structure of the Nucleon. *Phys. Rev.*, 185:1975–1982.

[41] Blanton, T. D., Romero-López, F., and Sharpe, S. R. (2019). Implementing the three-particle quantization condition including higher partial waves. *JHEP*, 03:106.

[42] Bloom, E. D. et al. (1969). High-Energy Inelastic e p Scattering at 6-Degrees and 10-Degrees. *Phys. Rev. Lett.*, 23:930–934.

[43] Blossier, B., Della Morte, M., von Hippel, G., Mendes, T., and Sommer, R. (2009). On the generalized eigenvalue method for energies and matrix elements in lattice field theory. *JHEP*, 04:094.

[44] Blum, T. et al. (2012). The $K \to (\pi\pi)_{I=2}$ Decay Amplitude from Lattice QCD. *Phys. Rev. Lett.*, 108:141601.

[45] Bourrely, C., Caprini, I., and Lellouch, L. (2009). Model-independent description of B —> pi l nu decays and a determination of |V(ub)|. *Phys. Rev.*, D79:013008. [Erratum: Phys. Rev.D82,099902(2010)].

[46] Boyd, C. G., Grinstein, B., and Lebed, R. F. (1995). Constraints on form-factors for exclusive semileptonic heavy to light meson decays. *Phys. Rev. Lett.*, 74:4603–4606.

[47] Boyd, C. G. and Savage, M. J. (1997). Analyticity, shapes of semileptonic form-factors, and anti-B —> pi lepton anti-neutrino. *Phys. Rev.*, D56:303–311.

[48] Briceno, R. A., Dudek, J. J., Edwards, R. G., and Wilson, D. J. (2017). Isoscalar $\pi\pi$ scattering and the $\sigma$ meson resonance from QCD. *Phys. Rev. Lett.*, 118(2):022002.

[49] Briceno, R. A., Dudek, J. J., and Young, R. D. (2018). Scattering processes and resonances from lattice QCD. *Rev. Mod. Phys.*, 90(2):025001.

[50] Briceño, R. A., Hansen, M. T., and Walker-Loud, A. (2015). Multichannel $1 \to 2$ transition amplitudes in a finite volume. *Phys. Rev.*, D91(3):034501.

[51] Briceño, R. A. (2014). Two-particle multichannel systems in a finite volume with arbitrary spin. *Phys. Rev.*, D89(7):074507.

[52] Briceño, R. A., Dudek, J. J., Edwards, R. G., Shultz, C. J., Thomas, C. E., and Wilson, D. J. (2015). The resonant $\pi^+\gamma \to \pi^+\pi^0$ amplitude from Quantum Chromodynamics. *Phys. Rev. Lett.*, 115:242001.

[53] Briceño, R. A., Dudek, J. J., Edwards, R. G., Shultz, C. J., Thomas, C. E., and Wilson, D. J. (2016). The $\pi\pi \to \pi\gamma^\star$ amplitude and the resonant $\rho \to \pi\gamma^\star$ transition from lattice QCD. *Phys. Rev.*, D93(11):114508.

[54] Briceño, R. A. and Hansen, M. T. (2015). Multichannel $0 \to 2$ and $1 \to 2$ transition amplitudes for arbitrary spin particles in a finite volume. *Phys. Rev.*, D92(7):074509.

[55] Briceño, R. A. and Hansen, M. T. (2016). Relativistic, model-independent, multichannel $2 \to 2$ transition amplitudes in a finite volume. *Phys. Rev.*, D94(1):013008.

[56] Briceño, R. A., Hansen, M. T., and Sharpe, S. R. (2017). Relating the finite-volume spectrum and the two-and-three-particle *S* matrix for relativistic systems of identical scalar particles. *Phys. Rev.*, D95(7):074510.

[57] Broecker, P., Carrasquilla, J., Melko, R. G., and Trebst, S. (2017). Machine learning quantum phases of matter beyond the fermion sign problem. *Scientific Reports*, 7(1):8823.

[58] Brommel, D., Crompton, P., Gattringer, C., Glozman, L. Ya., Lang, C. B., Schaefer, S., and Schafer, A. (2004). Excited nucleons with chirally improved fermions. *Phys. Rev.*, D69:094513.

[59] Brueckner, K. A. (1952). Meson-Nucleon Scattering and Nucleon Isobars. *Phys. Rev.*, 86:106–109.

[60] Bulava, J., Donnellan, M., and Sommer, R. (2012). On the computation of hadron-to-hadron transition matrix elements in lattice QCD. *JHEP*, 01:140.

[61] Bulava, J., Fahy, B., Hörz, B., Juge, K. J., Morningstar, C., and Wong, C. H. (2016). $I = 1$ and $I = 2$ $\pi - \pi$ scattering phase shifts from $N_f = 2 + 1$ lattice QCD. *Nucl. Phys.*, B910:842–867.

[62] Cardy, J. (1996). *Scaling and Renormalization in Statistical Physics*. Cambridge Lecture Notes in Physics. Cambridge University Press.

[63] Chatrchyan, S. et al. (2012). Observation of a new boson at a mass of 125 GeV with the CMS experiment at the LHC. *Phys. Lett.*, B716:30–61.

[64] Chen, H.-X. and Oset, E. (2013). $\pi\pi$ interaction in the $\rho$ channel in finite volume. *Phys. Rev.*, D87(1):016014.

[65] Chollet, F. et al. (2015). Keras. https://keras.io.

[66] Christ, N. H., Feng, X., Martinelli, G., and Sachrajda, C. T. (2015). Effects of finite volume on the $K_L$-$K_S$ mass difference. *Phys. Rev.*, D91(11):114510.

[67] Christ, N. H., Kim, C., and Yamazaki, T. (2005). Finite volume corrections to the two-particle decay of states with non-zero momentum. *Phys. Rev.*, D72:114506.

[68] Chung, S. U. (1971). SPIN FORMALISMS.

[69] Chung, S. U., Brose, J., Hackmann, R., Klempt, E., Spanier, S., and Strassburger, C. (1995). Partial wave analysis in $K$-matrix formalism. *Annalen Phys.*, 4:404–430.

[70] Chung, Y., Dosch, H. G., Kremer, M., and Schall, D. (1982). Baryon Sum Rules and Chiral Symmetry Breaking. *Nucl. Phys.*, B197:55–75.

[71] Cohen, T. D. and Ji, X.-D. (1997). Chiral multiplets of hadron currents. *Phys. Rev.*, D55:6870–6876.

[72] Colangelo, G., Hoferichter, M., Kubis, B., Procura, M., and Stoffer, P. (2014). Towards a data-driven analysis of hadronic light-by-light scattering. *Phys. Lett.*, B738:6–12.

[73] Cornwell, J. F. (1985a). *GROUP THEORY IN PHYSICS. VOL. 1*.

[74] Cornwell, J. F. (1985b). *GROUP THEORY IN PHYSICS. VOL. 2*.

[75] Cossu, G., Del Debbio, L., Giani, T., Khamseh, A., and Wilson, M. (2018). Machine learning determination of dynamical parameters: The Ising model case.

[76] Cotton, F. A. (2003). *Chemical applications of group theory*. John Wiley & Sons.

[77] Crisafulli, M. and Lubicz, V. (1992). A Lattice study of electromagnetic decays of vector mesons. *Phys. Lett.*, B278:323–329.

[78] Davies, C. T. H., Follana, E., Kendall, I. D., Lepage, G. P., and McNeile, C. (2010). Precise determination of the lattice spacing in full lattice QCD. *Phys. Rev.*, D81:034506.

[79] DeGrand, T. A., Ng, Y. J., and Tye, S. H. H. (1977). Jet Structure in e+ e- Annihilation as a Test of QCD and the Quark-Confining String. *Phys. Rev.*, D16:3251.

[80] Detmold, W. and Flynn, M. (2015). Finite-volume matrix elements in multiboson states. *Phys. Rev.*, D91(7):074509.

[81] Detmold, W., Lin, C. J. D., and Meinel, S. (2012). Calculation of the heavy-hadron axial couplings $g_1$, $g_2$ and $g_3$ using lattice QCD. *Phys. Rev.*, D85:114508.

[82] Detmold, W. and Nicholson, A. (2016). Low energy scattering phase shifts for meson-baryon systems. *Phys. Rev.*, D93(11):114511.

[83] Dowdall, R. J. et al. (2012). The Upsilon spectrum and the determination of the lattice spacing from lattice QCD including charm quarks in the sea. *Phys. Rev.*, D85:054509.

[84] Duane, S., Kennedy, A. D., Pendleton, B. J., and Roweth, D. (1987). Hybrid Monte Carlo. *Phys. Lett.*, B195:216–222.

[85] Dudek, J. J., Edwards, R., and Thomas, C. E. (2009). Exotic and excited-state radiative transitions in charmonium from lattice QCD. *Phys. Rev.*, D79:094504.

[86] Dudek, J. J., Edwards, R. G., and Thomas, C. E. (2012). $S$ and $D$-wave phase shifts in isospin-2 $\pi\pi$ scattering from lattice QCD. *Phys. Rev.*, D86:034031.

[87] Dudek, J. J., Edwards, R. G., and Thomas, C. E. (2013). Energy dependence of the $\rho$ resonance in $\pi\pi$ elastic scattering from lattice QCD. *Phys. Rev.*, D87(3):034505. [Erratum: Phys. Rev. D90, no.9, 099902 (2014)].

[88] Dudek, J. J., Edwards, R. G., Thomas, C. E., and Wilson, D. J. (2014). Resonances in coupled $\pi K - \eta K$ scattering from quantum chromodynamics. *Phys. Rev. Lett.*, 113(18):182001.

[89] Dudek, J. J., Edwards, R. G., and Wilson, D. J. (2016). An $a_0$ resonance in strongly coupled $\pi\eta$, $K\overline{K}$ scattering from lattice QCD. *Phys. Rev.*, D93(9):094506.

[90] Durr, S., Fodor, Z., Hoelbling, C., Katz, S. D., Krieg, S., Kurth, T., Lellouch, L., Lippert, T., Szabo, K. K., and Vulvert, G. (2011). Lattice QCD at the physical point: Simulation and analysis details. *JHEP*, 08:148.

[91] Ellis, J. R., Gaillard, M. K., and Ross, G. G. (1976). Search for Gluons in e+ e- Annihilation. *Nucl. Phys.*, B111:253. [Erratum: Nucl. Phys.B130,516(1977)].

[92] Englert, F. and Brout, R. (1964). Broken Symmetry and the Mass of Gauge Vector Mesons. *Phys. Rev. Lett.*, 13:321–323. [,157(1964)].

[93] Estabrooks, P. and Martin, A. D. (1975). $\pi\pi$ Partial Waves from 0.6 to 1.8 GeV. *Nucl. Phys.*, B95:322–346.

[94] Feng, X., Jansen, K., and Renner, D. B. (2011). Resonance parameters of the $\rho$ meson from lattice QCD. *Phys. Rev.*, D83:094505.

[95] Feynman, R. P. (1948). Space-time approach to nonrelativistic quantum mechanics. *Rev. Mod. Phys.*, 20:367–387.

[96] Feynman, R. P. (1949). Space - time approach to quantum electrodynamics. *Phys. Rev.*, 76:769–789. [,99(1949)].

[97] Feynman, R. P. (1969). Very high-energy collisions of hadrons. *Phys. Rev. Lett.*, 23:1415–1417. [,494(1969)].

[98] Finkenrath, J., Alexandrou, C., Bacchio, S., Charalambous, P., Dimopoulos, P., Frezzotti, R., Jansen, K., Kostrzewa, B., Rossi, G., and Urbach, C. (2018). Simulation of an ensemble of $N_f = 2 + 1 + 1$ twisted mass clover-improved fermions at physical quark masses. *EPJ Web Conf.*, 175:02003.

[99] Foreman, S., Giedt, J., Meurice, Y., and Unmuth-Yockey, J. (2018). Examples of renormalization group transformations for image sets. *Phys. Rev.*, E98(5):052129.

[100] Fortuin, C. M. and Kasteleyn, P. W. (1972). On the Random cluster model. 1. Introduction and relation to other models. *Physica*, 57:536–564.

[101] Frezzotti, R., Grassi, P. A., Sint, S., and Weisz, P. (2000). A Local formulation of lattice QCD without unphysical fermion zero modes. *Nucl. Phys. Proc. Suppl.*, 83:941–946.

[102] Frezzotti, R., Grassi, P. A., Sint, S., and Weisz, P. (2001). Lattice QCD with a chirally twisted mass term. *JHEP*, 08:058.

[103] Frezzotti, R. and Rossi, G. C. (2004). Chirally improving Wilson fermions. 1. O(a) improvement. *JHEP*, 08:007.

[104] Friedman, J. I. and Kendall, H. W. (1972). Deep inelastic electron scattering. *Ann. Rev. Nucl. Part. Sci.*, 22:203–254.

[105] Frison, J. et al. (2010). Rho decay width from the lattice. *PoS*, LATTICE2010:139.

[106] Fritzsch, H., Gell-Mann, M., and Leutwyler, H. (1973). Advantages of the Color Octet Gluon Picture. *Phys. Lett.*, 47B:365–368.

[107] Fu, Z. and Wang, L. (2016). Studying the $\rho$ resonance parameters with staggered fermions. *Phys. Rev.*, D94(3):034505.

[108] Funai, S. S. and Giataganas, D. (2018). Thermodynamics and Feature Extraction by Machine Learning.

[109] Furman, V. and Shamir, Y. (1995). Axial symmetries in lattice QCD with Kaplan fermions. *Nucl. Phys.*, B439:54–78.

[110] Gattringer, C. and Lang, C. B. (2010). Quantum chromodynamics on the lattice. *Lect. Notes Phys.*, 788:1–343.

[111] Gell-Mann, M. (1964). A Schematic Model of Baryons and Mesons. *Phys. Lett.*, 8:214–215.

[112] Gockeler, M., Horsley, R., Lage, M., Meissner, U. G., Rakow, P. E. L., Rusetsky, A., Schierholz, G., and Zanotti, J. M. (2012). Scattering phases for meson and baryon resonances on general moving-frame lattices. *Phys. Rev.*, D86:094513.

[113] Gottlieb, S. A., MacKenzie, P. B., Thacker, H. B., and Weingarten, D. (1986). Hadronic Couplings Constants in Lattice Gauge Theory. *Nucl. Phys.*, B263:704.

[114] Green, J., Hasan, N., Meinel, S., Engelhardt, M., Krieg, S., Laeuchli, J., Negele, J., Orginos, K., Pochinsky, A., and Syritsyn, S. (2017). Up, down, and strange nucleon axial form factors from lattice QCD. *Phys. Rev.*, D95(11):114502.

[115] Green, J., Meinel, S., Engelhardt, M., Krieg, S., Laeuchli, J., Negele, J., Orginos, K., Pochinsky, A., and Syritsyn, S. (2015). High-precision calculation of the strange nucleon electromagnetic form factors. *Phys. Rev.*, D92(3):031501.

[116] Greenberg, O. W. (1964). Spin and Unitary Spin Independence in a Paraquark Model of Baryons and Mesons. *Phys. Rev. Lett.*, 13:598–602.

[117] Gross, D. J. and Wilczek, F. (1973). Ultraviolet Behavior of Nonabelian Gauge Theories. *Phys. Rev. Lett.*, 30:1343–1346. [,271(1973)].

[118] Guo, D., Alexandru, A., Molina, R., and Döring, M. (2016). Rho resonance parameters from lattice QCD. *Phys. Rev.*, D94(3):034501.

[119] Guo, P., Dudek, J., Edwards, R., and Szczepaniak, A. P. (2013). Coupled-channel scattering on a torus. *Phys. Rev.*, D88(1):014501.

[120] Guralnik, G. S., Hagen, C. R., and Kibble, T. W. B. (1964). Global Conservation Laws and Massless Particles. *Phys. Rev. Lett.*, 13:585–587. [,162(1964)].

[121] Gérardin, A., Green, J., Gryniuk, O., von Hippel, G., Meyer, H. B., Pascalutsa, V., and Wittig, H. (2018). Hadronic light-by-light scattering amplitudes from lattice QCD versus dispersive sum rules. *Phys. Rev.*, D98(7):074501.

[122] Göckeler, M., Horsley, R., Lage, M., Meissner, U. G., Rakow, P. E. L., Rusetsky, A., Schierholz, G., and Zanotti, J. M. (2012). Scattering phases for meson and baryon resonances on general moving-frame lattices. *Phys. Rev.*, D86:094513.

[123] Göckeler, M., Horsley, R., Nakamura, Y., Pleiter, D., Rakow, P. E. L., Schierholz, G., and Zanotti, J. (2008). Extracting the $\rho$ resonance from lattice QCD simulations at small quark masses. *PoS*, LATTICE2008:136.

[124] Güsken, S., Low, U., Mutter, K. H., Sommer, R., Patel, A., and Schilling, K. (1989). Nonsinglet Axial Vector Couplings of the Baryon Octet in Lattice QCD. *Phys. Lett.*, B227:266–269.

[125] Haar, A. (1933). Der massbegriff in der theorie der kontinuierlichen gruppen. *Annals of Mathematics*, 34(1):147–169.

[126] Hall, J. M. M., Hsu, A. C. P., Leinweber, D. B., Thomas, A. W., and Young, R. D. (2013). Finite-volume matrix Hamiltonian model for a $\Delta \to N\pi$ system. *Phys. Rev.*, D87(9):094510.

[127] Han, M. Y. and Nambu, Y. (1965). Three Triplet Model with Double SU(3) Symmetry. *Phys. Rev.*, 139:B1006–B1010. [,187(1965)].

[128] Hannah, T. (2001). The Anomalous process gamma pi —> pi pi to two loops. *Nucl. Phys.*, B593:577–595.

[129] Hansen, M. T. and Sharpe, S. R. (2012). Multiple-channel generalization of Lellouch-Lüscher formula. *Phys. Rev.*, D86:016007.

[130] Hanson, G. et al. (1975). Evidence for Jet Structure in Hadron Production by e+ e- Annihilation. *Phys. Rev. Lett.*, 35:1609–1612.

[131] Higgs, P. W. (1964). Broken Symmetries and the Masses of Gauge Bosons. *Phys. Rev. Lett.*, 13:508–509. [,160(1964)].

[132] Hinton, G. E., Srivastava, N., Krizhevsky, A., Sutskever, I., and Salakhutdinov, R. R. (2012). Improving neural networks by preventing co-adaptation of feature detectors.

[133] Hoferichter, M., Kubis, B., Leupold, S., Niecknig, F., and Schneider, S. P. (2014). Dispersive analysis of the pion transition form factor. *Eur. Phys. J.*, C74:3180.

[134] Hoferichter, M., Kubis, B., and Sakkas, D. (2012). Extracting the chiral anomaly from gamma pi –> pi pi. *Phys. Rev.*, D86:116009.

[135] Hoferichter, M., Kubis, B., and Zanke, M. (2017). Radiative resonance couplings in $\gamma\pi \to \pi\pi$. *Phys. Rev.*, D96(11):114016.

[136] Hu, B., Molina, R., Döring, M., and Alexandru, A. (2016). Two-flavor Simulations of the $\rho(770)$ and the Role of the $K\bar{K}$ Channel. *Phys. Rev. Lett.*, 117(12):122001.

[137] Hu, W., Singh, R. R. P., and Scalettar, R. T. (2017). Discovering phases, phase transitions, and crossovers through unsupervised machine learning: A critical examination. *Phys. Rev. E*, 95:062122.

[138] Ioffe, B. L. (1981). Calculation of Baryon Masses in Quantum Chromodynamics. *Nucl. Phys.*, B188:317–341. [Erratum: Nucl. Phys.B191,591(1981)].

[139] Ishii, N., Aoki, S., Doi, T., Hatsuda, T., Ikeda, Y., Inoue, T., Murano, K., Nemura, H., and Sasaki, K. (2012). Hadron–hadron interactions from imaginary-time Nambu–Bethe–Salpeter wave function on the lattice. *Phys. Lett.*, B712:437–441.

[140] Ishizuka, N., Ishikawa, K. I., Ukawa, A., and Yoshié, T. (2015). Calculation of $K \to \pi\pi$ decay amplitudes with improved Wilson fermion action in lattice QCD. *Phys. Rev.*, D92(7):074503.

[141] Jaeger, G. (1998). The ehrenfest classification of phase transitions: introduction and evolution. *Archive for history of exact sciences*, 53(1):51–81.

[142] Jansen, K., McNeile, C., Michael, C., and Urbach, C. (2009). Meson masses and decay constants from unquenched lattice QCD. *Phys. Rev.*, D80:054510.

[143] Jansen, K. and Schmaltz, M. (1992). Critical momenta of lattice chiral fermions. *Phys. Lett.*, B296:374–378.

[144] Johnson, R. C. (1982). Angular momentum on a lattice. *Phys. Lett.*, 114B:147–151.

[145] Kaiser, N. and Friedrich, J. M. (2008). Cross-sections for low-energy pi- gamma reactions. *Eur. Phys. J.*, A36:181–188.

[146] Kaplan, D. B. (1992). A Method for simulating chiral fermions on the lattice. *Phys. Lett.*, B288:342–347.

[147] Kasteleyn, P. W. and Fortuin, C. M. (1969). Phase Transitions in Lattice Systems with Random Local Properties. *Physical Society of Japan Journal Supplement, Vol. 26. Proceedings of the International Conference on Statistical Mechanics held 9-14 September, 1968 in Koyto., p.11*, 26:11.

[148] Kennedy, A. D. (2006). Algorithms for dynamical fermions.

[149] Kim, C. H., Sachrajda, C. T., and Sharpe, S. R. (2005). Finite-volume effects for two-hadron states in moving frames. *Nucl. Phys.*, B727:218–243.

[150] Landsberg, L. G. (1985). Electromagnetic Decays of Light Mesons. *Phys. Rept.*, 128:301–376.

[151] Lang, C. B., Mohler, D., Prelovsek, S., and Vidmar, M. (2011). Coupled channel analysis of the $\rho$ meson decay in lattice QCD. *Phys. Rev.*, D84(5):054503. [Erratum: Phys. Rev.D89,no.5,059903(2014)].

[152] Lang, C. B. and Verduci, V. (2013). Scattering in the $\pi N$ negative parity channel in lattice QCD. *Phys. Rev.*, D87(5):054502.

[153] Lasscock, B. G., Hedditch, J. N., Kamleh, W., Leinweber, D. B., Melnitchouk, W., Williams, A. G., and Zanotti, J. M. (2007). Even parity excitations of the nucleon in lattice QCD. *Phys. Rev.*, D76:054510.

[154] Leinweber, D. B., Melnitchouk, W., Richards, D. G., Williams, A. G., and Zanotti, J. M. (2005). Baryon spectroscopy in lattice QCD. *Lect. Notes Phys.*, 663:71–112. [,71(2004)].

[155] Lellouch, L. and Luscher, M. (2001). Weak transition matrix elements from finite volume correlation functions. *Commun. Math. Phys.*, 219:31–44.

[156] Lepage, G. P. (1994). Lattice QCD for small computers. In *High-energy phenomenology. Proceedings, 42nd Scottish Universities Summer School in Physics, NATO Advanced Study Institute, St. Andrews, UK, August 1-21, 1993*.

[157] Lepage, G. P. and Mackenzie, P. B. (1993). On the viability of lattice perturbation theory. *Phys. Rev.*, D48:2250–2264.

[158] Lepage, G. P., Magnea, L., Nakhleh, C., Magnea, U., and Hornbostel, K. (1992). Improved nonrelativistic QCD for heavy quark physics. *Phys. Rev.*, D46:4052–4067.

[159] Leskovec, L., Alexandrou, C., Koutsou, G., Meinel, S., Negele, J. W., Paul, S., Petschlies, M., Pochinsky, A., Rendon, G., and Syritsyn, S. (2016). A study of the radiative transition $\pi\pi \to \pi\gamma^*$ with lattice QCD. *PoS*, LATTICE2016:159.

[160] Leskovec, L., Alexandrou, C., Meinel, S., Negele, J. W., Paul, S., Petschlies, M., Pochinsky, A., Rendon, G., and Syritsyn, S. (2018a). A Lattice QCD study of the $\rho$ resonance. In *13th Conference on the Intersections of Particle and Nuclear Physics (CIPANP 2018) Palm Springs, California, USA, May 29-June 3, 2018*.

[161] Leskovec, L., Alexandrou, C., Meinel, S., Negele, J. W., Paul, S., Petschlies, M., Pochinsky, A., Rendon, G., and Syritsyn, S. (2018b). Calculating the $\rho$ radiative decay width with lattice QCD. In *36th International Symposium on Lattice Field Theory (Lattice 2018) East Lansing, MI, United States, July 22-28, 2018*.

[162] Leskovec, L. and Prelovsek, S. (2012a). Scattering phase shifts for two particles of different mass and non-zero total momentum in lattice QCD. *Phys. Rev.*, D85:114507.

[163] Leskovec, L. and Prelovsek, S. (2012b). Scattering phase shifts for two particles of different mass and non-zero total momentum in lattice QCD. *Phys. Rev.*, D85:114507.

[164] Liddle, J. and Teper, M. (2008). The Deconfining phase transition in D=2+1 SU(N) gauge theories.

[165] Lin, C. J. D., Martinelli, G., Sachrajda, C. T., and Testa, M. (2001). K –> pi pi decays in a finite volume. *Nucl. Phys.*, B619:467–498.

[166] Lin, H.-W. et al. (2009). First results from 2+1 dynamical quark flavors on an anisotropic lattice: Light-hadron spectroscopy and setting the strange-quark mass. *Phys. Rev.*, D79:034502.

[167] Llewellyn Smith, C. H. (1971). INELASTIC LEPTON SCATTERING IN GLUON MODELS. *Phys. Rev.*, D4:2392.

[168] Long, B. and van Kolck, U. (2010). $\pi N$ Scattering in the $\Delta(1232)$ Region in an Effective Field Theory. *Nucl. Phys.*, A840:39–75.

[169] Luscher, M. (1977). Construction of a Selfadjoint, Strictly Positive Transfer Matrix for Euclidean Lattice Gauge Theories. *Commun. Math. Phys.*, 54:283.

[170] Luscher, M. (2006). The Schrodinger functional in lattice QCD with exact chiral symmetry. *JHEP*, 05:042.

[171] Lüscher, M. (1991). Two particle states on a torus and their relation to the scattering matrix. *Nucl. Phys.*, B354:531–578.

[172] Lüscher, M. and Weisz, P. (1985). Computation of the Action for On-Shell Improved Lattice Gauge Theories at Weak Coupling. *Phys. Lett.*, B158:250–254.

[173] Lüscher, M. and Wolff, U. (1990). How to Calculate the Elastic Scattering Matrix in Two-dimensional Quantum Field Theories by Numerical Simulation. *Nucl. Phys.*, B339:222–252.

[174] Maiani, L. and Testa, M. (1990). Final state interactions from Euclidean correlation functions. *Phys. Lett.*, B245:585–590.

[175] Matthews, P. T. and Salam, A. (1954). The Green's functions of quantized fields. *Nuovo Cim.*, 12:563–565.

[176] Matthews, P. T. and Salam, A. (1955). Propagators of quantized field. *Nuovo Cim.*, 2:120–134.

[177] McNeile, C. and Michael, C. (2003). Hadronic decay of a vector meson from the lattice. *Phys. Lett.*, B556:177–184.

[178] McNeile, C. and Michael, C. (2006). Decay width of light quark hybrid meson from the lattice. *Phys. Rev.*, D73:074506.

[179] McNeile, C., Michael, C., and Pennanen, P. (2002). Hybrid meson decay from the lattice. *Phys. Rev.*, D65:094505.

[180] Meinel, S. (2010). Bottomonium spectrum at order $v^6$ from domain-wall lattice QCD: Precise results for hyperfine splittings. *Phys. Rev.*, D82:114502.

[181] Meissner, U.-G. (2011). The Beauty of Spin. *J. Phys. Conf. Ser.*, 295:012001.

[182] Meyer, A. S., Betancourt, M., Gran, R., and Hill, R. J. (2016). Deuterium target data for precision neutrino-nucleus cross sections. *Phys. Rev.*, D93(11):113015.

[183] Meyer, H. B. (2011). Lattice QCD and the Timelike Pion Form Factor. *Phys. Rev. Lett.*, 107:072002.

[184] Michael, C. (1985). Adjoint Sources in Lattice Gauge Theory. *Nucl. Phys.*, B259:58–76.

[185] Mildred Dresselhaus, Gene Dresselhaus, Ado Jorio (2008). *Group Theory: Application to the Physics of Condensed Matter*. Springer-Verlag Berlin Heidelberg, 1 edition.

[186] Montvay, I. and Munster, G. (1997). *Quantum fields on a lattice*. Cambridge Monographs on Mathematical Physics. Cambridge University Press.

[187] Moore, D. C. and Fleming, G. T. (2006a). Angular momentum on the lattice: The Case of non-zero linear momentum. *Phys. Rev.*, D73:014504. [Erratum: Phys. Rev. D74, 079905 (2006)].

[188] Moore, D. C. and Fleming, G. T. (2006b). Multiparticle States and the Hadron Spectrum on the Lattice. *Phys. Rev.*, D74:054504.

[189] Morningstar, A. and Melko, R. G. (2017). Deep learning the ising model near criticality.

[190] Morningstar, C., Bulava, J., Fahy, B., Foley, J., Jhang, Y. C., Juge, K. J., Lenkner, D., and Wong, C. H. (2013). Extended hadron and two-hadron operators of definite momentum for spectrum calculations in lattice QCD. *Phys. Rev.*, D88(1):014511.

[191] Morningstar, C. and Peardon, M. J. (2004). Analytic smearing of $SU(3)$ link variables in lattice QCD. *Phys. Rev.*, D69:054501.

[192] Namekawa, Y. et al. (2004). Light hadron spectroscopy in two-flavor QCD with small sea quark masses. *Phys. Rev.*, D70:074503.

[193] Narayanan, R. and Neuberger, H. (1993). Infinitely many regulator fields for chiral fermions. *Phys. Lett.*, B302:62–69.

[194] Narayanan, R. and Neuberger, H. (1995). A Construction of lattice chiral gauge theories. *Nucl. Phys.*, B443:305–385.

[195] Neuberger, H. (1998a). Exactly massless quarks on the lattice. *Phys. Lett.*, B417:141–144.

[196] Neuberger, H. (1998b). More about exactly massless quarks on the lattice. *Phys. Lett.*, B427:353–355.

[197] O'Donnell, P. J. (1981). Radiative decays of mesons. *Rev. Mod. Phys.*, 53:673.

[198] Orginos, K. and Richards, D. (2015). Improved methods for the study of hadronic physics from lattice QCD. *J. Phys.*, G42(3):034011.

[199] Osborn, J. C., Babich, R., Brannick, J., Brower, R. C., Clark, M. A., Cohen, S. D., and Rebbi, C. (2010). Multigrid solver for clover fermions. *PoS*, LATTICE2010:037.

[200] Osterwalder, K. and Schrader, R. (1973). AXIOMS FOR EUCLIDEAN GREEN'S FUNCTIONS. *Commun. Math. Phys.*, 31:83–112.

[201] Osterwalder, K. and Seiler, E. (1978). Gauge Field Theories on the Lattice. *Annals Phys.*, 110:440.

[202] Owen, B., Kamleh, W., Leinweber, D., Menadue, B., and Mahbub, S. (2015a). Light Meson Form Factors at near Physical Masses. *Phys. Rev.*, D91(7):074503.

[203] Owen, B. J., Kamleh, W., Leinweber, D. B., Mahbub, M. S., and Menadue, B. J. (2015b). Transition of $\rho \to \pi\gamma$ in lattice QCD. *Phys. Rev.*, D92(3):034513.

[204] Parisi, G. (1973). Deep inelastic scattering in a field theory with computable large-momenta behaviour. *Lett. Nuovo Cim.*, 7S2:84–88. [Lett. Nuovo Cim.7,84(1973)].

[205] Pascalutsa, V. and Vanderhaeghen, M. (2006). Chiral effective-field theory in the Delta(1232) region: I. Pion electroproduction on the nucleon. *Phys. Rev.*, D73:034003.

[206] Patrignani, C. et al. (2016a). Review of Particle Physics. *Chin. Phys.*, C40(10):100001.

[207] Patrignani, C. et al. (2016b). Review of Particle Physics. *Chin. Phys.*, C40(10):100001.

[208] Paul, S., Alexandrou, C., Leskovec, L., Meinel, S., Negele, J. W., Petschlies, M., Pochinsky, A., Suzuki, J. G. R., and Syritsyn, S. (2018a). $\pi\pi$ P-wave resonant scattering from lattice QCD. *EPJ Web Conf.*, 175:05022.

[209] Paul, S. et al. (2018b). Towards the P-wave nucleon-pion scattering amplitude in the $\Delta(1232)$ channel. In *36th International Symposium on Lattice Field Theory (Lattice 2018) East Lansing, MI, United States, July 22-28, 2018*.

[210] Pelaez, J. R. and Yndurain, F. J. (2005). The Pion-pion scattering amplitude. *Phys. Rev.*, D71:074016.

[211] Pelissier, C. and Alexandru, A. (2013). Resonance parameters of the $\rho$-meson from asymmetrical lattices. *Phys. Rev.*, D87(1):014503.

[212] Peskin, M. E. and Schroeder, D. V. (1995). *An Introduction to quantum field theory*. Addison-Wesley, Reading, USA.

[213] Politzer, H. D. (1973). Reliable Perturbative Results for Strong Interactions? *Phys. Rev. Lett.*, 30:1346–1349. [,274(1973)].

[214] Prelovsek, S., Skerbis, U., and Lang, C. B. (2017). Lattice operators for scattering of particles with spin. *JHEP*, 01:129.

[215] Rendon, G., Leskovec, L., Meinel, S., Negele, J., Paul, S., Petschlies, M., Pochinsky, A., Silvi, G., and Syritsyn, S. (2018). $K\pi$ scattering and the $K^*(892)$ resonance in 2+1 flavor QCD. In *36th International Symposium on Lattice Field Theory (Lattice 2018) East Lansing, MI, United States, July 22-28, 2018*.

[216] Rummukainen, K. and Gottlieb, S. A. (1995). Resonance scattering phase shifts on a nonrest frame lattice. *Nucl. Phys.*, B450:397–436.

[217] Shamir, Y. (1993a). Chiral fermions from lattice boundaries. *Nucl. Phys.*, B406:90–106.

[218] Shamir, Y. (1993b). Constraints on the existence of chiral fermions in interacting lattice theories. *Phys. Rev. Lett.*, 71:2691–2694.

[219] Shanahan, P. E., Trewartha, D., and Detmold, W. (2018). Machine learning action parameters in lattice quantum chromodynamics. *Phys. Rev.*, D97(9):094506.

[220] Sheikholeslami, B. and Wohlert, R. (1985). Improved Continuum Limit Lattice Action for QCD with Wilson Fermions. *Nucl. Phys.*, B259:572.

[221] Shindler, A. (2008). Twisted mass lattice QCD. *Phys. Rept.*, 461:37–110.

[222] Shrestha, M. and Manley, D. M. (2012). Multichannel parametrization of $\pi N$ scattering amplitudes and extraction of resonance parameters. *Phys. Rev.*, C86:055203.

[223] Shultz, C. J., Dudek, J. J., and Edwards, R. G. (2015). Excited meson radiative transitions from lattice QCD using variationally optimized operators. *Phys. Rev.*, D91(11):114501.

[224] Sint, S. (1994). On the Schrodinger functional in QCD. *Nucl. Phys.*, B421:135–158.

[225] Sint, S. (2007). Lattice QCD with a chiral twist. In *Workshop on Perspectives in Lattice QCD Nara, Japan, October 31-November 11, 2005*.

[226] Stathopoulos, A. and Orginos, K. (2010). Computing and deflating eigenvalues while solving multiple right hand side linear systems in quantum chromodynamics. *SIAM J. Sci. Comput.*, 32:439–462.

[227] Sterman, G. F. and Weinberg, S. (1977). Jets from Quantum Chromodynamics. *Phys. Rev. Lett.*, 39:1436.

[228] Streater, R. F. and Wightman, A. S. (1989). *PCT, spin and statistics, and all that*.

[229] Swendsen, R. H. and Wang, J.-S. (1987). Nonuniversal critical dynamics in Monte Carlo simulations. *Phys. Rev. Lett.*, 58:86–88.

[230] Symanzik, K. (1973). A field theory with computable large-momenta behavior. *Lett. Nuovo Cim.*, 6S2:77–80. [Lett. Nuovo Cim.6,77(1973)].

[231] Symanzik, K. (1983a). Continuum Limit and Improved Action in Lattice Theories. 1. Principles and phi**4 Theory. *Nucl.Phys.*, B226:187.

[232] Symanzik, K. (1983b). Continuum Limit and Improved Action in Lattice Theories. 2. $O(N)$ Nonlinear Sigma Model in Perturbation Theory. *Nucl. Phys.*, B226:205–227.

[233] Symanzik, K. (1983c). Improved lattice actions for nonlinear sigma model and nonabelian gauge theory. In *Workshop on Non-perturbative Field Theory and QCD Trieste, Italy, December 17-21, 1982*, pages 61–72. [,61(1983)].

[234] 't Hooft, G. (1971). Renormalization of Massless Yang-Mills Fields. *Nucl. Phys.*, B33:173–199.

[235] Terent'ev, M. V. (1972). Process pi+- –> pi0 pi+- in Coulomb field and anomalous divergence of neutral axial vector current. *Phys. Lett.*, 38B:419–422.

[236] Toussaint, D. (2017). private communication.

[237] Truong, T. N. (2002). Study of gamma pi —> pi pi below 1-GeV using integral equation approach. *Phys. Rev.*, D65:056004.

[238] van Nieuwenburg, E., Liu, Y.-H., and Huber, S. (2017). Learning phase transitions by confusion. *Nature Physics*, 13:435 EP –.

[239] Verduci, V. (2014). *Pion-nucleon scattering in lattice QCD*. PhD thesis, Graz U.

[240] Vincent, P., Larochelle, H., Bengio, Y., and Manzagol, P.-A. (2008). Extracting and composing robust features with denoising autoencoders. In *Proceedings of the 25th international conference on Machine learning*, pages 1096–1103. ACM.

[241] Vincent, P., Larochelle, H., Lajoie, I., Bengio, Y., and Manzagol, P.-A. (2010). Stacked denoising autoencoders: Learning useful representations in a deep network with a local denoising criterion. *Journal of machine learning research*, 11(Dec):3371–3408.

[242] Von Hippel, F. and Quigg, C. (1972). Centrifugal-barrier effects in resonance partial decay widths, shapes, and production amplitudes. *Phys. Rev.*, D5:624–638.

[243] Wang, J.-S. and Swendsen, R. H. (1990). Cluster monte carlo algorithms. *Physica A: Statistical Mechanics and its Applications*, 167(3):565 – 579.

[244] Wang, L. (2016). Discovering phase transitions with unsupervised learning. *Phys. Rev. B*, 94:195105.

[245] Watson, K. M. (1952). The Effect of final state interactions on reaction cross-sections. *Phys. Rev.*, 88:1163–1171.

[246] Wetzel, S. J. (2017). Unsupervised learning of phase transitions: From principal component analysis to variational autoencoders. *Physical Review E*, 96(2):022140.

[247] Wetzel, S. J. and Scherzer, M. (2017). Machine Learning of Explicit Order Parameters: From the Ising Model to SU(2) Lattice Gauge Theory. *Phys. Rev.*, B96(18):184410.

[248] Wikipedia (2019). Particle physics — Wikipedia, the free encyclopedia. http://en.wikipedia.org/w/index.php?title=Particle%20physics&oldid=892192821. [Online; accessed 09-May-2019].

[249] Wilson, D. J., Briceno, R. A., Dudek, J. J., Edwards, R. G., and Thomas, C. E. (2015a). Coupled $\pi\pi, K\bar{K}$ scattering in $P$-wave and the $\rho$ resonance from lattice QCD. *Phys. Rev.*, D92(9):094502.

[250] Wilson, D. J., Dudek, J. J., Edwards, R. G., and Thomas, C. E. (2015b). Resonances in coupled $\pi K, \eta K$ scattering from lattice QCD. *Phys. Rev.*, D91(5):054008.

[251] Wilson, K. G. (1974). Confinement of Quarks . *Phys.Rev.*, D10:2445–2459. Legen ... Wait for it ... Dary.

[252] Wilson, K. G. (1975). Quarks and Strings on a Lattice. In *New Phenomena in Subnuclear Physics: Proceedings, International School of Subnuclear Physics, Erice, Sicily, Jul 11-Aug 1 1975. Part A*, page 99. [,0069(1975)].

[253] Woloshyn, R. M. (1986). VECTOR MESON RADIATIVE DECAY IN LATTICE QCD. *Z. Phys.*, C33:121.

[254] Yang, Y.-B., Liang, J., Bi, Y.-J., Chen, Y., Draper, T., Liu, K.-F., and Liu, Z. (2018). Proton Mass Decomposition from the QCD Energy Momentum Tensor. *Phys. Rev. Lett.*, 121(21):212001.

[255] Yoon, B., Bhattacharya, T., and Gupta, R. (2018). Machine Learning Estimators for Lattice QCD Observables.

[256] Zhang, W., Liu, J., and Wei, T.-C. (2018). Machine learning of phase transitions in the percolation and XY models. *arXiv e-prints*, page arXiv:1804.02709.

[257] Zweig, G. (1964a). An SU(3) model for strong interaction symmetry and its breaking. Version 1.

[258] Zweig, G. (1964b). An SU(3) model for strong interaction symmetry and its breaking. Version 2. In Lichtenberg, D. and Rosen, S. P., editors, *DEVELOPMENTS IN THE QUARK THEORY OF HADRONS. VOL. 1. 1964 - 1978*, pages 22–101.

# Appendix A

# Murray Gell-Mann matrices

The generators $T^b$ of the Lie group SU(3) are proportional to the 8 Gell-Mann matrices, $T^b = \frac{1}{2}\lambda^b$ , which are listed below:

$$\lambda^1 = \begin{pmatrix} 0 & 1 & 0 \\ 1 & 0 & 0 \\ 0 & 0 & 0 \end{pmatrix}, \qquad \lambda^2 = \begin{pmatrix} 0 & -i & 0 \\ i & 0 & 0 \\ 0 & 0 & 0 \end{pmatrix}, \qquad \lambda^3 = \begin{pmatrix} 1 & 0 & 0 \\ 0 & -1 & 0 \\ 0 & 0 & 0 \end{pmatrix},$$

$$\lambda^4 = \begin{pmatrix} 0 & 0 & 1 \\ 0 & 0 & 0 \\ 1 & 0 & 0 \end{pmatrix}, \qquad \lambda^5 = \begin{pmatrix} 0 & 0 & -i \\ 0 & 0 & 0 \\ i & 0 & 0 \end{pmatrix}, \qquad \lambda^6 = \begin{pmatrix} 0 & 0 & 0 \\ 0 & 0 & 1 \\ 0 & 1 & 0 \end{pmatrix},$$

$$\lambda^7 = \begin{pmatrix} 0 & 0 & 0 \\ 0 & 0 & -i \\ 0 & i & 0 \end{pmatrix}, \qquad \lambda^8 = \frac{1}{\sqrt{3}} \begin{pmatrix} 1 & 0 & 0 \\ 0 & 1 & 0 \\ 0 & 0 & -2 \end{pmatrix}.$$

The generators further satisfy the commutation relation known as Lie Brackets:

$$[T^a, T^b] = f^{abc} T^c, \tag{A.1}$$

where $f^{abc}$ are structure constants given by,

| $f_{abc}$ | $abc$ |
|---|---|
| 1 | 123 |
| $\frac{1}{2}$ | 147, 246, 257, 345 |
| $-\frac{1}{2}$ | 156, 367 |
| $\frac{\sqrt{3}}{2}$ | 458, 678 |

(A.2)